Inaugural dissertation
for
obtaining the doctoral degree
of the
Combined Faculty of Mathematics, Engineering and Natural Sciences
of the
Ruprecht - Karls - University
Heidelberg

Presented by

M.Sc. Alberto Diaz Jimenez

born in: Madrid, Spain 19th of April 1995

Oral examination: 16th of May 2024

Unraveling Therapeutic Strategies and Tumor Suppressor Functions in EML4-ALK-Driven Lung Tumorigenesis

Referees: Prof. Dr. Sergio P. Acebron

Dr. Michael Milsom

A mi familia.
Separados, que no distanciados.

TABLE OF CONTENT

INTRODUCTION 21

CANCER 21

The complexity of cellular dysfunction and proliferation 21

Cancer, a global disease 21

LUNG CANCER 22

Epidemiology of lung cancer 22

Histopathological and molecular classification of lung cancer 22

Genetic drivers of NSCLC 24

ALK tyrosine kinase: a driving force in lung cancer pathogenesis 25

Protein structure of ALK 25

ALK signaling 26

The physiological role of ALK 27

Oncogenic activation of ALK 27

ALK activation by gene amplification 27

ALK activation by gain-of-function mutations 28

ALK activation following chromosomal rearrangements 28

EML4-ALK-driven lung cancer: from mechanisms to therapies 29

EML4-ALK variants: protein structure and biology 29

EML4-ALK subcellular location and signaling. 31

Clinical aspects of ALK-positive patients 32

EML4-ALK lung cancer patient profiles 32

Clinical impact of EML4-ALK variants: incidence and outcomes. 33

Co-occurring genomic alterations in EML4-ALK tumors 34

Advancements in ALK inhibitors: targeted therapies for ALK-positive patients 35

Crizotinib: a first-generation ALK inhibitor. 36

Alectinib: revolutionizing the treatment of ALK-positive cancer. 37

Brigatinib: a potent second generation ALK inhibitor 37

Lorlatinib: a leading ALK inhibitor 38

ALK inhibitor resistance: challenges and strategies. 39

On-target resistance mechanisms. 40

Mechanisms of ALK-independent resistance 42

a) Bypass pathway alterations 42

b) The enigma of histological transformation in therapy resistant-ALK tumors 44

Emerging trends in ALK-positive lung cancer management 44

The next generation of TKIs to address on-target resistance 44

Enhancing therapeutic outcomes: combinatorial treatment strategies 45

Immunotherapy approaches in ALK-positive lung cancer 45

Modeling *EML4-ALK* lung cancer: tools and approaches 46

AIMS OF THE THESIS 49

RESULTS 51

Chapter 1: Understand the therapeutic response to ALK inhibitors in EML4-ALK variant 1 and variant 3-driven tumor cells 51

Development of a preclinical mouse model for investigating EML4-ALK driven lung tumors 51

Generation of *Eml4-Alk* mouse tumor-derived cells 53

Characterization of *Eml4-Alk* variant 1 and variant 3 mTDCs at the proteomic level 55

EML4-ALK V1 and V3 show different sensitivity to ALK inhibitors 56

Chapter 2: Identify novel therapeutic opportunities using drug combinatorial strategies 59

Inhibition of the MAPK signaling pathway enhances the therapeutic response to ALK inhibitors *in vitro* 59

Inhibition of SRC synergize with ALK inhibitors....61
Enhanced sensitivity of patient-derived ALK resistant cells to co-inhibition of ALK and SRC 65
Inhibition of ALK and SRC impacts the (phospho)proteomic profile of Eml4-Alk variant 3 mTDCs 66
Enhanced brigatinib cytotoxicity by suppressing the PI3K/AKT/mTOR axis....71
Pharmacological inhibition of ALK and SRC reduced EML4-ALK V3-driven tumorigenesis *in vivo*.74
Chapter 3: Investigate the role of key tumor suppressor genes in EML4-ALK-driven lung tumorigenesis 77
A novel EML4-ALK-driven mouse model to investigate co-occurring genomic alterations....78
Generation of a triple sgRNA lentiviral vector 80
Tumor barcoding allows investigation of V1 and V3 oncogenicity....83
Setd2 and *Lkb1* are suppressors of V3-driven tumors 86
Tumor barcoding allows for large genomic screenings in EML4-ALK-driven tumors 88
Comparative V1 vs V3 and comparative vs other oncogenes .... **Error! Bookmark not defined.**
Tumor suppressor gene inactivation modulates tumor growth and mouse survival in a *Eml4-Alk* variant-specific-manner 95
Tumor suppressor gene disruption leads to histologically distinct EML4-ALK-driven lung tumors97
Transcriptomic analysis of EML4-ALK-driven *Setd2*-deficient lung tumors....99
Therapeutic response of multiple EML4-ALK tumor genotypes 101
DISCUSSION....105
Optimizing therapeutic outcomes: exploring treatment responses in EML4-ALK variants and the potential of combinatorial approaches. 105
Refining preclinical modeling of *EML4-ALK*: current limitations and future perspective....105
EML4-ALK variant responses to ALK inhibitors 106
Synergizing therapeutic approaches: EML4-ALK and combinatorial treatments....106
Role of mTOR in treatment responses to ALK and SRC inhibitor combination 108
Tumor suppressor dynamics: modeling EML4-ALK V1 and V3 genotypic responses.....109
Generation of a novel EML4-ALK-driven mouse model to investigate concurrent genomic alterations 109
EML4-ALK V1 and V3 lung tumors cooperate with different tumor suppressor genes....110
Future considerations 112
CONCLUSIONS....115
Therapeutic response to ALK inhibitors in variant 1 and variant 3 EML4-ALK-driven tumor cells and 115
Identify novel therapeutic opportunities using combinatorial strategies....116
Investigate the role of key tumor suppressor genes in EML4-ALK lung tumorigenesis 117
CONTRIBUTIONS....119
MATERIALS AND METHODS 121
Mouse models 121
Mouse genotyping....121
Eml4-Alk adenovirus and lentivirus 122
Cloning of sgEGFP, sg*Eml4*$^{V1\ or\ V3}$, sg*Alk* in Lenti-PGK-Cre backbone....122
Analysis of human lung tumor data and tumor suppressor genes selection....125
Cloning of specific sgRNA for each tumor suppressor gene. 126
Barcoding of lentiviral vectors 129
Lentiviral plasmid isolation 131
Production, purification and titration of lentivirus 132
Intratracheal instillation of viral particles 133
Mouse dissection....133
Sample cryopreservation....133
Single cell suspension from cryopreserved tumors 133
DNA extraction from sorted tumor cells....134
Sorted tumor cell genotyping 135
RNA extraction and RNA library preparation from sorted tumor cell genotyping....135
RNA sequencing analysis 136

Establishment of *Eml4-Alk* mouse tumor-derived cells 136
Culture of ALK-patient derived cells....136
Histology and immunohistochemistry 137
Histological analysis 138
Macroscopic quantification of lung tumors 138
Western blot 139
Inhibitors used *in vitro* 140
Determination of IC50 and cell viability....141
Drug interaction assay 141
Clonogenicity assays 141
Determination of ROS levels by CellRox assay 141
Determination of antioxidant enzymes levels by RT-PCR....142
In vivo treatments....142
Cell cycle analysis....143
Generation of ALK-resistant cells....143
Sample preparation for proteomics analysis 144
Phosphopeptide enrichment 146
LC-MS/MS Analysis 146
Database search and Data Analysis 148
Pre-processing and quality control of the proteomic and phosphoproteomic data....149
Statistical and bioinformatic analysis....149
Mouse lung tissue homogenization for Tuba-seq 150
Phenol-Chloroform extraction of genomic DNA from tumor bearing lungs 150
Library preparation for tumor barcoding sequencing....151
Tumor barcoding analysis 152
Analysis of sgID-BC sequencing data 152
Removal of contaminating barcodes 153
Removal of mice with low tumor number....154
Filtering of vectors with insufficient titer from analysis 154
Adaptive sampling of tumors for statistical comparison of tumor genotypes....155
Analyses of correlation in tumor suppressive effects across oncogenic contexts 159
ACKNOWLEDGMENTS 161
References 165

LIST OF FIGURES

Figure 1 | Annual incidence of different cancer entities per 100,000 habitant 22
Figure 2 | Lung cancer classification 23
Figure 3 | ALK signaling 26
Figure 4 | Gene and protein structure of EML4-ALK 30
Figure 5 | Mechanisms of resistance to ALK inhibitors 41
Figure 6 | *Eml4-Alk* chromosomal rearrangement 52
Figure 7 | Adenoviral sg*Eml4*-sg*Alk*/Cas9-mediated lung tumor initiation in *Trp53*$^{Flox/Flox}$;*Rosa26*$^{mT/mG}$;*CCSP-Cre* mice 52
Figure 8 | *Eml4-Alk* mouse tumor-derived cells 54
Figure 9 | *Eml4-Alk* variant 1 and variant 3 cells display different proteomic profiles 56
Figure 10 | *Eml4-Alk* variant 3 cells show lower sensitivity to brigatinib and lorlatinib 58
Figure 11 | Inhibition of ERK1/2 enhances ALK inhibitors activity 60
Figure 12 | Inhibition of ERK1/2 does not improve therapeutic response to brigatinib *in vivo* 61
Figure 13 | Inhibition of SRC enhances ALK inhibition response 64
Figure 14 | *EML4-ALK* resistant patient-derived cells show increased sensitivity to co-inhibition of ALK and SRC 65
Figure 15 | Dual inhibition of ALK and SRC impacts the Eml4-Alk cell (phospho)proteome 67
Figure 16 | Pharmacological co-inhibition of ALK and SRC halts ALK driven oncogenesis 70
Figure 17 | Co-inhibition of ALK and SRC downregulates proteins associated with brigatinib resistance 71
Figure 18 | Dual inhibition of ALK and SRC do not impact on ROS levels 71
Figure 19 | Suppression of the PI3K/AKT/mTOR axis by co-inhibition of ALK and SRC 72
Figure 20 | Inhibition of mTOR sensitizes EML4-ALK-driven cells to ALK inhibitors 73
Figure 21 | Co-inhibition of ALK and SRC halts tumor growth 75
Figure 22 | Schematic of the cloning strategy 78
Figure 23 | Mouse model and lentiviral vectors 79
Figure 24 | Lentiviral CRISPR/Cas9-mediated initiation of EML4-ALK V1 and V3-driven lung tumors 80
Figure 25 | Triple sgRNA lentiviral vector efficiently targets specific genes and induce the *Eml4-Alk* rearrangement 82
Figure 26 | EML4-ALK V3 is a highly oncogenic fusion protein 84
Figure 27 | Tuba-seq demonstrates the superior oncogenic potential of V3 over V1 85
Figure 28 | Adaptive sapling and adaptive sapling mean methods 86
Figure 29 | V1 and V3 cooperates with different tumor suppressors genes. 87
Figure 30 | Cas9 is required for gene inactivation 88
Figure 31 | Prolonged survival and equitable tumor burden through reduced lentiviral dose in V1 and V3 mice 89
Figure 32 | Tumor suppressor gene effects are due to Cas9-activity 91
Figure 33 | Diverse outcomes of tumor suppressor gene inactivation on V1 and V3 lung tumors 91
Figure 34 | Tumor suppressive effect is different for each *Eml4-Alk* variant 92
Figure 35 | Spearman's rank correlation coefficient 93
Figure 36 | The tumor suppressor landscapes of *Eml4-Alk* V1 and V3 resemble distinct oncogenes 93
Figure 37 | Survival impact of tumor suppressor gene inactivation in V1 and V3 mice 96
Figure 38 | Tumor suppressor gene inactivation modulates tumor size in a *Eml4-Alk* variant-specific-manner 97
Figure 39 | Metastatic events in V1 and V3 mice 97
Figure 40 | Loss of tumor suppressor genes might drive histological transformations 98
Figure 41 | Inactivation of *Setd2* impact the V3-transcriptomic profile 100
Figure 42 | EML4-ALK-driven tumors respond to lorlatinib 103
Figure 43 | sgID-BC structure 129

LIST OF TABLES

Table 1 | Management of ALK positive patients 35
Table 2 | PCR primers 122
Table 3 | Lentiviral and U6-donor plasmids 122
Table 4 | PCR primers used in Step 1 123
Table 5 | sgRNA sequences 123
Table 6 | PCR primers used in Step 2 124
Table 7 | PCR primers used in Step 3 125
Table 8 | Sanger sequencing primers 125
Table 9 | Mutation frequency of putative tumor suppressor genes selected for investigation 126
Table 10 | sgRNAs targeting tumor suppressor genes 127
Table 11 | Used PCR primers 129
Table 12 | sgRNA-specific barcoded primers 130
Table 13 | Antibodies used for sorting EGFP tumor cells 134
Table 14 | Used PCR primers for TSG genotyping 135
Table 15 | Antibodies for immunohistochemistry 138
Table 16 | RIPA buffer for protein extraction 139
Table 17 | 2X Laemmli buffer 139
Table 18 | Western blot antibodies 140
Table 19 | RT-qPCR primers 142
Table 20 | Cell cycle solution 143
Table 21 | Primers used to amplify the most frequently mutated *Alk* region 144
Table 22 | Tuba-seq lysis cocktail 150
Table 23 | Number of sgNT1 tumors sampled in V1 cohort (Ni=basal,j=basal) rounded to the nearest hundred 157

LIST OF ABBREVIATIONS

Abbreviation	Meaning
AKT	RAC(Rho family)-alpha serine/threonine-protein kinase
AKT1	AKT Serine/Threonine Kinase 1
ALCL	Anaplastic Large Cell Lymphoma
ALEX	Automated Laboratory Experimentation
ALK	Anaplastic Lymphoma Kinase
ALKAL	Anaplastic Lymphoma Kinase Amplification
ALTA	A Study of Brigatinib Versus Crizotinib in Anaplastic Lymphoma Kinase Positive
ALUR	Alectinib compared with chemotherapy in previously treated patients with ALK-positive NSCLC
AMG510	Sotorasib, an AntiCancer Medication
ANOVA	Analysis of Variance
APC	Allophycocyanin, fluorochrome
ARID1A	AT-rich interactive domain-containing protein 1A
ASM	Adaptively sampled log-normal mean size
ASR	Age-standardized
AT2	Alveolar Type 2 cell
ATP	Adenosine Triphosphate
AXL	AXL Receptor Tyrosine Kinase
BC	Barcode
BRAF	v-Raf Murine Sarcoma Viral Oncogene Homolog B
CCSP	Club Cell Secretory Protein
CD11	Cluster of Differentiation 11
CD31	Platelet Endothelial Cell Adhesion Molecule
CD45	Leukocyte Common Antigen
CDK1	Cyclin Dependent Kinase 1
CDK6	Cyclin Dependent Kinase 6
CDKN2A	Cyclin Dependent Kinase Inhibitor 2A
CI	Confidence Interval
CLTA	Clathrin Light Chain A
CMTR2	Cap Methyltransferase 2
CNS	Central Nervous System
COPS6	COP9 Signalosome Subunit 6
CRISPR	Clustered Regularly Interspaced Short Palindromic Repeats
CT	Computed Tomography
DMSO	Dimethyl Sulfoxide
DNA	Deoxyribonucleic Acid
DUSP6	Dual Specificity Phosphatase 6
E2F	E2 Promoter Binding Factor
EA	EML4-ALK
EGF	Epidermal Growth Factor
EGFP	Enhanced Green Fluorescent Protein
EGFR	Epidermal Growth Factor Receptor
EMA	European Medicines Agency
EML	Echinoderm Microtubule Associated Protein Like
EMT	Epithelial Mesenchymal Transition
ERK	Extracellular Signal Regulated Kinase
ERK1	Extracellular Signal Regulated Kinase 1
ETS	E26 Transformation Specific
FACS	Fluorescence Activated Cell Sorting
FC	Fold Change
FDA	Food and Drug Administration
FDR	False Discovery Rate
FGFR	Fibroblast Growth Factor Receptor
FISH	Fluorescence In Situ Hybridization

FRS2	Fibroblast Growth Factor Receptor Substrate 2
GENIE	Genomics Evidence Neoplasia Information Exchange
GFP	Green Fluorescent Protein
GOS	Geostationary Operational Satellite
GRB2	Growth Factor Receptorm Bound Protein 2
GSEA	Gene Set Enrichment Analysis
GSK3B	Glycogen Synthase Kinase 3 Beta
GTP	Guanosine Triphosphate
H202	Hydrogen Peroxide
H3K36	Histone H3 Lysine 36
HBNF	Hepatocyte Growth Factor B
HELP	Hydrophobic motif in EML proteins
HER2	Human Epidermal Growth Factor Receptor 2
HSP90	Heat Shock Protein 90
IC50	Half Maximal Inhibitory Concentration
IFN	Interferon
IFU	Instructions For Use
IHC	Immunohistochemistry
IL6	Interleukin 6
IRS	Insulin Receptor Substrate
JAK	Janus Kinase
JASPAR	Joint Assessment of Scientific and Policy Advice on Radiation
JEB	Junctional Epidermolysis Bullosa
JNK	c-Jun N Terminal Kinase
KDM6A	Lysine Demethylase 6A
KEGG	Kyoto Encyclopedia of Genes and Genomes
KIF5B	Kinesin Family Member 5B
KIT	Tyrosine Protein Kinase KIT
KLC1	Kinesin Light Chain 1
KMT2D	Lysine Methyltransferase 2D
KRAS	Kirsten Rat Sarcoma Viral Oncogene Homolog
KRT5	Keratin 5
LC	Liquid Chromatography
LDL	Low Density Lipoprotein
LFQ	Label Free Quantification
LKB1	Liver Kinase B1
LN	Lymph Node
LSL	Lox-Stop-Lox
LTK	Leukocyte Receptor Tyrosine Kinase
LUAD	Lung Adenocarcinoma
LUSC	Lung Squamous Cell Carcinoma
MAM	Meprin, A5 protein and receptor protein tyrosine phosphatase mu
MAPK	Mitogen-Activated Protein Kinase
MAPK1	Mitogen-Activated Protein Kinase 1
MEK	MAPK/ERK Kinase
MET	MET Proto-Oncogene, Receptor Tyrosine Kinase
MK	Midkine
MS	Mass Spectrometry
mTDC	Mouse tumor-derived-cells
MYCN	MYC Proto Oncogene, BHLH Transcription Factor
NCT	National Clinical Trial
NES	Nuclear Export Signal
NF1	Neurofibromatosis Type 1
NF2	Neurofibromatosis Type 2
NGS	Next Generation Sequencing
NIH3T3	NIH 3T3 Mouse Embryo Fibroblast Cells
NKX2	NK2 Homeobox
NMRI	National Medical Research Institute
NPM	Nucleophosmin

NR	Nuclear Receptor
NRG1	Neuregulin 1
NS	Nonsmall Cell
NSCLC	Nonsmall Cell Lung Cancer
NT	Nucleus Tractus
NTRK	Neurotrophic Receptor Tyrosine Kinase
NVL	Nuclear Vascular Layer
OF	Olfactory
OSF	Open Science Framework
P40	Podoplanin
P63	Tumor Protein 63
PARVB	Parvin Beta
PCA	Principal Component Analysis
PCR	Polymerase Chain Reaction
PF	Pulmonary Fibrosis
PFS	Progression Free Survival
PI3K	Phosphoinositide 3-kinases
PIK3CA	Phosphatidylinositol-4,5-bisphosphate 3-kinase catalytic subunit alpha
PKB	Protein Kinase B
PLC	Phospholipase C
PTEN	Phosphatase and Tensin Homolog
PTN	Pleiotrophin
PTPN11	Protein Tyrosine Phosphatase Nonreceptor Type 11
R26	Rosa26 Locus
RAF	Rapidly Accelerated Fibrosarcoma
RAS	Rat Sarcoma Viral Oncogene Homolog
RASA1	RAS P21 Protein Activator 1
RB1	Retinoblastoma Protein 1
RBM10	RNA Binding Motif Protein 10
RET	Rearranged During Transfection, proto-oncogene
RNA	Ribonucleic Acid
ROI	Region of Interest
ROS	Reactive Oxygen Species
ROS1	ROS Proto-Oncogene 1, Receptor Tyrosine Kinase
RT	Reverse Transcription
RTK	Receptor Tyrosine Kinase
S6K	Ribosomal Protein S6 Kinase
SCC	Squamous Cell Carcinoma
SCLC	Small Cell Lung Cancer
SD	Standard Deviation
SEM	Scanning Electron Microscopy
SETD2	SET Domain Containing 2, Histone Lysine Methyltransferase
SHC	SHC Adaptor Protein
SHP099	SHP2 Inhibitor
SHP2	SH2-Containing Protein Tyrosine Phosphatase 2
SLC7A1	Solute Carrier Family 7 Member 1
SOS1	Son of Sevenless Homolog 1
SPC	Pulmonary-associated surfactant protein C
SRC	SRC Proto-Oncogene, Non-Receptor Tyrosine Kinase
STAG2	STAG2 Cohesin Complex Component
STAT	Signal Transducer and Activator of Transcription
STAT3	Signal Transducer and Activator of Transcription 3
STK	Serine/Threonine Kinase
STK11	Serine/Threonine Kinase 11
TAPE	Transcript Assembly, Processing, and Exploration
TD	Trimerisation domain
TER119	Transmembrane Protein 119
TF	Transcription Factor
TFBS	Transcription Factor Binding Site

TGF	Transforming Growth Factor
TGFBR2	Transforming Growth Factor Beta Receptor 2
TK	Tyrosine Kinase
TKI	Tyrosine Kinase Inhibitor
TOR	Target of Rapamycin
TORC1	TOR Complex 1
TORC2	TOR Complex 2
TP53	Tumor Protein 53
TPX	Targeted Protein Degradation
TRANSFAC	Transcription Factor Database
TSG	Tumor Suppressor Gene
TTF1	Thyroid Transcription Factor 1
U6	U6 Small Nuclear RNA
UMAP	Uniform Manifold Approximation and Projection
USP15	Ubiquitin-Specific Peptidase 15
VEGF	Vascular Endothelial Growth Factor
WD	Tryptophan-aspartic acid
WHO	World Health Organization
WNT	Wingless and Int-1
XAB2	XPA Binding Protein 2
YAP1	Yes-Associated Protein 1
YFP	Yellow Fluorescent Protein

SUMMARY

EML4-ALK is an oncogenic chromosomal rearrangement found in 5% of non-small-cell lung cancer. This fusion involves the echinoderm microtubule-associated protein-like 4 (EML4) and the anaplastic lymphoma kinase (*ALK*) genes. Interestingly, up to 15 different *EML4-ALK* variants have been described, with variant 1 and variant 3 accounting for over 70% of the cases. The discovery of the *EML4-ALK* oncogene represents a critical milestone in precision medicine, providing important insights into targeted therapies. However, despite exhibiting a favorable prognosis, EML4-ALK-driven tumors become resistant to available ALK inhibitors. Additionally, co-occurring genetic alterations can often shape tumor development and treatment response. Beyond the role of *TP53* in therapy response, very little is known about the impact of other genetic alterations. Therefore, this thesis aims to improve the therapeutic response of EML4-ALK tumor cells and to uncover the fitness landscape of EML4-ALK lung tumors across various genetic alterations.

To investigate the therapeutic response of variant 1 and variant 3, I established cell lines derived from corresponding murine lung tumors. These cell lines accurately reproduce histopathological markers of lung adenocarcinomas and respond to ALK inhibitors, rendering them appropriate as a preclinical tool. The results indicate that variant 3 exhibits lower sensitivity to brigatinib and lorlatinib, two potent ALK inhibitors used as standard-of care for the treatment. Importantly, this enhanced resistance could be overcome by the use of SRC inhibitors. In-depth (phospho)proteomic analyses revealed a synergistic effect primarily driven by a strong inhibition of pathways crucially linked to lung cancer, particularly inhibiting the mTOR pathway.

Due to the genomic heterogeneity of cancer and its impact on patient outcomes, I coupled CRISPR/Cas9 gene editing with tumor barcoding sequencing to the impact of 29 tumor suppressor genes in an *Eml4-Alk* variant-specific manner. This work identified unexpectedly diverse genetic interactions that strongly and specifically influence tumorigenesis driven by either EML4-ALK variant 1 or variant 3. These findings suggest that the underlying biology of V1 and V3-driven lung tumors is very different and show that different variants can significantly alter the effects of other pathways on tumor progression. Furthermore, I demonstrated that loss of *Lkb1* or *Setd2* significantly enhanced V3-tumor growth, reducing mouse survival. These findings highlight the essential role of these genes in cancer progression in an EML4-ALK variant-specific manner. Finally, this mouse model is a valuable preclinical tool for investigating pharmacological responses in various tumor genotypes.

ZUSAMMENFASSUNG

EML4-ALK ist ein onkogenes chromosomales Rearrangement, das bei 5 % der nicht-kleinzelligen Lungenkarzinome auftritt. Diese Fusion betrifft die Gene für das Mikrotubuli-assoziierte Protein 4 (EML4) und die anaplastische Lymphomkinase (ALK). Es sind bis zu 15 verschiedene *EML4-ALK* Varianten beschrieben worden, von denen Variante 1 und Variante 3 über 70 % der Fälle ausmachen. Die Entdeckung des *EML4-ALK* Onkogens stellt einen wichtigen Meilenstein in der Präzisionsmedizin dar und liefert Erkenntnisse für gezielte Therapien. Trotz der günstigen Prognose entwickeln EML4-ALK Tumore jedoch oft eine Resistenz gegenüber verfügbaren ALK-Inhibitoren. Zudem können gleichzeitig auftretende genetische Veränderungen die Tumorentwicklung und das Ansprechen auf die Behandlung beeinflussen. Neben der Rolle von *TP53* für das Ansprechen auf die Therapie ist nur sehr wenig über die Auswirkungen anderer genetischer Veränderungen bekannt. Diese Arbeit zielt darauf ab, das therapeutische Ansprechen von EML4-ALK-Tumorzellen zu verbessern und die Fitnesslandschaft von EML4-ALK Lungentumoren durch verschiedene genetische Veränderungen aufzudecken.

Um das therapeutische Ansprechen von Variante 1 und Variante 3 zu untersuchen, wurden Zelllinien aus entsprechenden murinen Lungentumoren hergestellt. Diese Zelllinien geben die histopathologischen Marker von Lungenkarzinomen genau wieder und sprechen auf ALK-Inhibitoren an. Diese Voraussetzungen/Bedingungen machen sie zu einem geeigneten präklinischen Werkzeug. Die Ergebnisse zeigen, dass Variante 3 eine geringere Empfindlichkeit gegenüber Brigatinib und Lorlatinib, zwei potente ALK-Inhibitoren, aufweist. Es ist wichtig zu erwähnen, dass die erhöhte Resistenz durch den Einsatz von SRC-Inhibitoren überwunden werden konnte. Die (Phospho-)Proteomanalysen ergaben einen synergistischen Effekt, der hauptsächlich auf die starke Hemmung von Signalwegen zurückzuführen ist, die entscheidend mit Lungenkrebs in Verbindung stehen. Insbesondere wurde der mTOR-Signalweg gehemmt.

Aufgrund der genomischen Heterogenität von Krebs und ihrer Auswirkungen auf die Behandlungsergebnisse habe ich CRISPR/Cas9-Gene Editing mit Tumor-Barcoding-Sequenzierung gekoppelt, um gleichzeitig die Auswirkungen von 29 Tumorsuppressorgenen in einer *Eml4-ALK*-Varianten-spezifischen Weise zu untersuchen. Dabei wurden unerwartet vielfältige genetische Interaktionen identifiziert, die die Tumorentstehung entweder durch die EML4-ALK Variante 1 oder die Variante 3 spezifisch beeinflussen. Die Ergebnisse deuten darauf hin, dass die zugrunde liegende Biologie von V1- und V3-Lungentumoren sehr

unterschiedlich ist. Verschiedene Varianten können die Auswirkungen anderer Signalwege auf den Tumorphänotyp erheblich verändern. Außerdem konnte nachgewiesen werden, dass der Verlust von *Lkb1* und *Setd2* das Wachstum von V3-Tumoren deutlich verstärkt und die Überlebensrate der Mäuse verringert. Diese Ergebnisse heben die wichtige Rolle dieser Gene bei der Krebsentwicklung in einer EML4-ALK-Varianten spezifischen Weise hervor. Dieses Mausmodell ist/dienst als ein wertvolles präklinisches Instrument zur Untersuchung pharmakologischer Reaktionen bei verschiedenen Tumor-Genotypen.

INTRODUCTION

CANCER

In the labyrinthine landscape of cellular biology, where the intricate dance of genes and proteins orchestrates life's symphony, cancer emerges as a disruptive crescendo.

The complexity of cellular dysfunction and proliferation

Cancer, also known as neoplasm, refers, literally, to a new growth, a disorder denoted by two fundamental characteristics: uncontrollable expansion, and the ability to invade and colonize (Alberts, B. 2020). Cancer is a multi-stage process instigated by physical, chemical or biological carcinogens, which provoke an initial mutation in a still normal cell. However, transformation into a cancerous entity holds a selective advantage given by a wide range of aberrant biological capabilities (Alberts, B. 2020). These hallmarks of cancer were firstly reviewed by Douglas Hanahan and Robert A. Weinberg, and include the dysregulation of cell signaling pathways, evasion of cell growth suppressors, activation of invasion and metastasis, enabling of replicative immortality, induction of angiogenesis, and resistance to cell death (Hanahan 2022).

Cancer, a global disease

The term of cancer encompasses a spectrum of complex disorders brought together under a common label. Cancer is a major worldwide public health burden and the second most-frequent cause of death globally accounting for one out of every six deaths. On average, 18,094,716 cases of cancer are diagnosed per year (WHO report, 2022). In recent decades, substantial efforts have been devoted to cancer prevention and early detection. Thus, the implementation of various cancer screening programs, such as those for prostate, colorectal, or breast cancer, has genuinely increased the cancer incidence due to the increase number of screening efforts. Denmark has the highest cancer rate, with 334.9 cases per 100,000 inhabitants. This heightened awareness, coupled with the expansion of healthcare initiatives and the influence of multi-generational shifts in diet, lifestyle, and environmental factors, collectively contribute to the ongoing efforts in decreasing the cancer burden (WHO report, 2022).

^Incidence of cancer varies widely among countries due to numerous risk factors, including geographical distribution, air pollution, or lifestyle. In central and south America, breast cancer has one of the highest incidences, while prostate is more prevalent in Canada. Lung cancer

is a significant concern in Eastern European countries and Asia. Additionally, prostate, colorectal and breast cancers remain a major health issue in Western European countries (**Figure 1**).

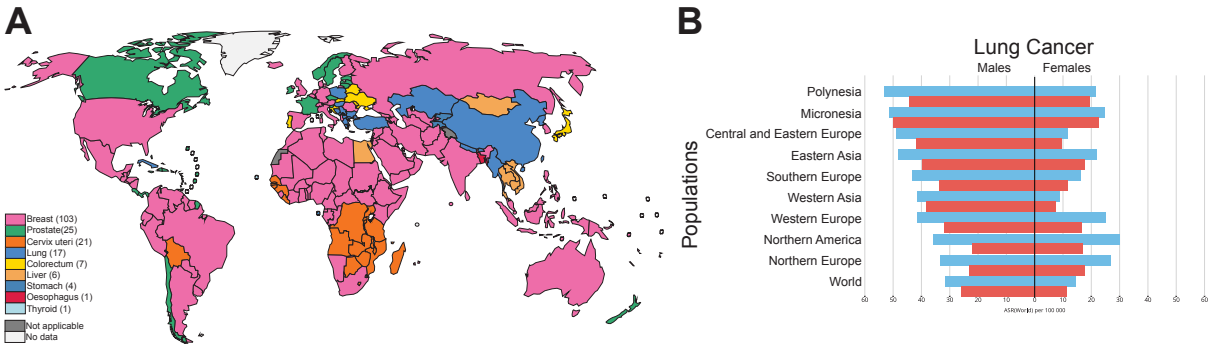


Figure 1 | Annual incidence of different cancer entities per 100,000 habitants. A) Top cancer types per country, estimated crude incidence rates in 2020, both sexes, all ages. Non-melanoma skin cancers are excluded. Numbers represent cases per 100,000 habitants. **B)** Lung cancer cases per 100,000 habitants. Cases are age-standardized (ASR). Data and figure adapted from WHO report, 2022.

LUNG CANCER

Epidemiology of lung cancer

Lung cancer is the second most frequently diagnosed cancer type worldwide in men and women and the deadliest cancer with an estimated of 2.2 million new cases of lung cancer worldwide (WHO report, 2022). Due to the deficiencies in the adoption of screening initiatives, a significant proportion of lung cancer patients are diagnosed at an advanced stage of the disease. The five-year overall survival rate is reported as 80% for the early stages (stage I), but declines to less than 60% for later stages (stage II and III) (Thai et al. 2021). This situation is anticipated to shift due to the projected reduction in lung cancer incidence, mirroring the global trend of gradual tobacco cessation (Thai et al. 2021). Nevertheless, despite the common thought of smoking as the sole cause of lung cancer, 25% of patients have no history of tobacco use (Sun et al. 2007).

Histopathological and molecular classification of lung cancer

Lung cancer is classified into two broad categories: small cell lung cancer (SCLC) and non-small cell lung cancer (NSCLC), which accounts for 85% of total diagnoses. A third less prevalent form of lung cancer is referred to as carcinoid. This histopathological categorization is continuously evolving, especially in the context of lung tumors with limited differentiation (**Figure 2**) (Sun et al. 2007; Kerr and López-Ríos 2016; Rotow and Bivona 2017; Thai et al. 2021; Gay et al. 2021).

SCLC represents a high-grade neuroendocrine carcinoma characterized by an elevated proliferation of malignant cells, synchronous metastases, and an unfavorable prognosis. Given the absence of a defined oncogenic driver and limited comprehension of the signaling pathways, treatment options rely on platinum-based chemotherapeutics, with some advances in immunotherapy. SCLC is genetically defined by the inactivation of the tumor suppressors *TP53* and *RB1* (Olsen et al. 2021; Thai et al. 2021; Gay et al. 2021; Aldana et al. 2022; Lee et al. 2023). This genetic profile contrasts with NSCLC, where the presence of activating oncogenic mutations appears to play a critical role in tumorigenesis.

NSCLC is morphologically categorized into two main subtypes: squamous cell carcinoma (LUSC), accounting for approximately 30% of cases, and non-squamous cell carcinoma. Within the non-squamous category, NSCLC is predominantly composed of adenocarcinomas (LUAD), constituting 90% of the cases, while the remaining 10% includes large-cell carcinomas (Sun et al. 2007; Rotow and Bivona 2017; Thai et al. 2021).

LUADs exhibit distinct histological features characterized by glandular differentiation, presenting in various patterns such as lepidic, acinar, papillary, or micropapillary structures. Solid LUAD tumors consistently stain strongly positive for thyroid transcription factor 1 (TTF1, also referred to as NKX2-1), alongside with mucin accumulation. On the other hand, LUSCs are positive for cytokeratin 5/6, P40 and P63 while being TTF1 negative. LUAD often exhibits genomic activation of oncogenic drivers such as *KRAS*, *EGFR*, *ALK* or *BRAF* (Skoulidis and Heymach 2019). Unlike LUAD, LUSC has an absence of molecular drivers, with often genetic alterations in *TP53, CDKN2A, PTEN, and PIK3CA* (Kim et al. 2013; Pan et al. 2023).

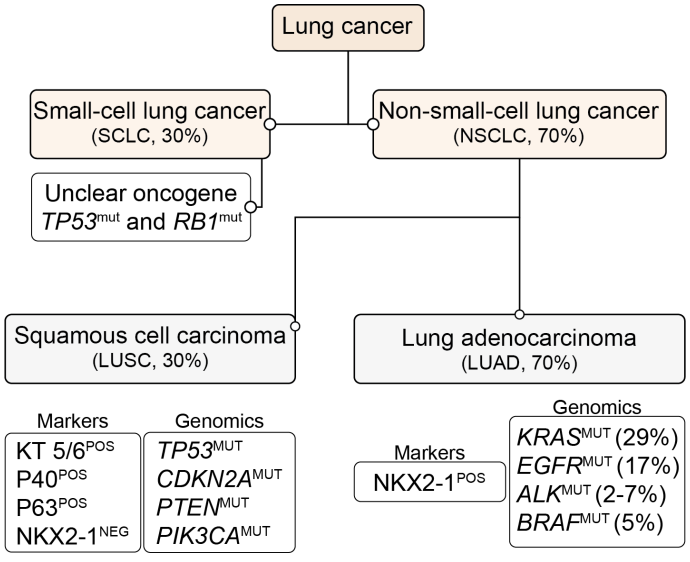


Figure 2 | Lung cancer classification. Diagram depicting lung cancer subtypes, with numbers indicating frequency, showcasing the correlation between genomic and histopathological markers.

Genetic drivers of NSCLC

Advances in genomic profiling of NSCLC samples have contributed to unravel the intricate pathways underlying tumorigenesis. Importantly, a major breakthrough has been the identification of driver oncogenic genomic alterations (Gridelli et al. 2015; Herbst et al. 2018). These drivers have not only facilitated the genetic classification of NSCLC patients, but has also provided the rationale for the implementation of targeted therapeutic strategies. These genetic lesions encompass a spectrum of alterations including activating mutations, rearrangements, insertions, or deletions (in specific repressor domains as *EGFR* exon 19 deletion) within key oncogenes. The majority of these alterations affect kinases, resulting in constitutive activation of signaling cascades that normally require ligand-dependent activation (Sun et al. 2007; Rotow and Bivona 2017; Cooper et al. 2022). This persistent signaling contributes to cellular transformation and potentially lays the groundwork for the development of cancer.

Among the oncogenes implicated in the development of lung cancer, Kirsten rat sarcoma viral oncogene homolog (*KRAS*) mutations hold significant incidence, accounting for 25% to 30% of lung cancer patients (Thai et al. 2021). Missense mutations in the *KRAS* gene affect codons 12, 13, 61, and 146, resulting in the sustained activation of KRAS due to the loss of its intrinsic GTPase activity. These *KRAS* mutations effectively trigger the action of the oncogenic rapidly accelerated fibrosarcoma kinase/mitogen-activated protein kinase/ phosphatidylinositol 3-kinase (RAF/MEK/PI3K) pathway (Salgia et al. 2021; Drosten and Barbacid 2022). As traditionally considered as “undruggable” due to its protein conformation, patients with *KRAS* mutations were treated using chemotherapeutic agents, resulting in a poor overall survival of 22 months (Salgia et al. 2021). However, recent developments in the field of small molecule therapeutics have yielded remarkable breakthroughs in the management of *KRAS*-mutated patients. KRAS (G12C) inhibitors like AMG510 (sotorasib) and MRTX849 (adagrasib) have demonstrated promising outcomes in clinical trials, overturning the historical challenges associated with KRAS-targeted treatments (Thai et al. 2021).

While *KRAS* mutations occur more frequently among smokers, activation of epidermal growth factor receptor (EGFR) and anaplastic lymphoma kinase (ALK) drivers occur primarily in never-smokers (Sun et al. 2007; Cooper et al. 2022). EGFR is a member of the ErbB family of receptors tyrosine kinase (RTK). EGFR is activated by the binding of the ligand epidermal growth factor (EGF) to its extracellular domain, driving cell growth and survival through RAS/MAPK, PI3K/AKT and JAK/STAT pathways (Gridelli et al. 2015; Cooper et al. 2022). Activating mutations are detected in approximately 15% of LUADs being the most common the exon 19 deletion, the exon 21 (L858R) and exon 18 (G719C, G719S, G719A) substitutions

(Gridelli et al. 2015). Although *EGFR* mutant tumors have a very high fractional response rate, tumors eventually acquire resistance. *EGFR*-mutant-treated tumors usually relapse through secondary mutations on exon 20 (T790M) after an initial response to gefitinib or erlotinib. Still relapsed $EGFR^{T790M}$ tumors are sensitive to the EGFR inhibitor osimertinib (Soria et al. 2017; Tsuboi et al. 2023).

ALK tyrosine kinase: a driving force in lung cancer pathogenesis

The *ALK* gene is located in the short arm of chromosome 2 (2p23) and encodes for a classical RTK. *ALK* gene was discovered in 1994 through the identification of the chromosomal translocation nucleophosmin *(NPM)-ALK* in anaplastic large-cell non-Hodgkin's lymphoma (Morris et al. 1994). Besides this disease, *ALK* plays an important role in several human cancers, including lung cancer, neuroblastoma and inflammatory myofibroblastic tumors (Corte et al. 2018). The activation of ALK can occur through fusion with other genes beside *NPM*, such as *EML4*, or *TIM*, in addition to gene amplification, mutation or overexpression (Palmer et al. 2009; Hallberg and Palmer 2013; Corte et al. 2018). The differences in the partner genes often determine the malignant capabilities of these tumors. In homeostasis, ALK acts as a transmembrane protein with a great similarity to the insulin receptor kinase superfamily. *ALK* is usually expressed in the small intestine, testis, and brain with a described role in neurogenesis (Palmer et al. 2009; Hallberg and Palmer 2013; Sabir et al. 2017). Understanding the role of *ALK* in cancer biology is key to optimizing therapeutic strategies for ALK-positive diseases.

Protein structure of ALK

The *ALK* gene, as many other RTKs, encodes for an extracellular ligand-binding domain, a transmembrane domain, and an intracellular tyrosine kinase domain. The extracellular domain encompasses a signal peptide, two MAM segments (meprin, A5 protein and receptor protein tyrosine phosphatase mu), as well as a LDLa (low density lipoprotein class a) domain. While LDLa domain potentially facilitates binding to LDL, the MAM domains are postulated to play a role in cell-to-cell interaction (Palmer et al. 2009) (**Figure 3**).

The initiation of ALK signal transduction is triggered by the binding of extracellular -ALK-ligands (ALKALs) to the receptor. JEB (jelly belly) serves as a ligand in *D. Melanogaster* embryos, triggering the extracellular signal-regulated kinase (ERK) signaling. Similar to JEB, Hen-1 (hesitation-1) ligand activates the mitogen-activated protein kinase (MAPK) pathway in *C. Elegans*. In mammals, ALK is proposed to be activated by the ligands PTN (pleiotrophin), OSF-1 (osteoblast-specific factor-1), HARP (heparin affinity regulatory peptide), HBNF

(heparin-binding neurotrophic factor), or MK (midkine) (Palmer et al. 2009; Roskoski 2013; Hallberg and Palmer 2013).

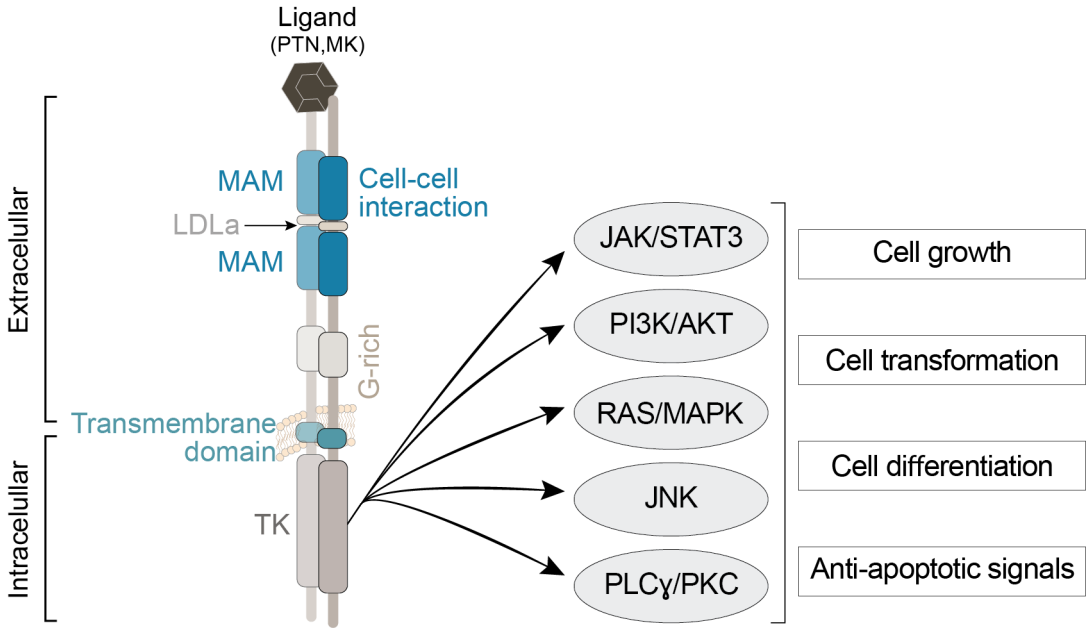


Figure 3 | ALK signaling. Extracellular and intracellular ALK protein domains are shown. ALK signaling occurs upon binding of the ALK ligands. Ligand-mediated ALK dimerization triggers auto-phosphorylation of the tyrosine kinase domain (TK) and subsequent activation of downstream pathways.

ALK signaling

Subsequently after ligand binding to the extracellular domain, activation of the kinase activity likely occurs similar to other RTKs (**Figure 3**). Ligand-mediated dimerization of ALK brings together both tyrosine kinase domains, resulting in transphosphorylation and activation of ALK kinase activity (Tartari et al. 2008; Palmer et al. 2009). Phosphorylated tyrosine residues recruit docking proteins that mirror the functionality of second-phase RTK autophosphorylation. These docking proteins typically activate downstream signaling molecules, thereby amplifying intricate signaling networks. Notably, adaptors like SHC (Src homology and collagen protein), FRS2 (fibroblastic growth factor substrate 2), IRS-1 (insulin receptor substrate 1), GRB2 (growth factor bond 2), among others, contribute to the amplification of ALK signaling (Palmer et al. 2009; Hallberg and Palmer 2013; Golding et al. 2018).

Creating a compressive map of the ALK pathway presents challenges. Our current understanding is derived from studies wherein ALK is activated through various alterations such as activating mutations, gene fusions, and gene amplifications. Moreover, these alterations originate from diverse tumor entities such as anaplastic large cell lymphoma, neuroblastoma, and NSCLC, which significantly complicates the analysis. Overall, it is

essential to note that the ALK pathway operates from well-recognized pathways as (1) RAS/RAF/MEK/ERK (MAPK), (2) Janus kinase (JAK)/signal transducer and activator of transcription (STAT), (3) PI3K/AKT/mTOR, (4) phospholipase Cɣ (PLCɣ), (5) c-Jun N-terminal kinase (JNK) pathways. These pathways collectively influence critical cellular processes such as cell growth, transformation, and antiapoptotic signaling.

The physiological role of ALK

The physiological role of ALK remains a topic of ongoing discussion. Insights from non-mammal model organisms such as *D. melanogaster*, *C. elegans,* and *D. rerio* have highlighted the role of ALK during sensory, developmental, and neural processes. In murine models, ALK-ligands MK and PTN have been linked to neural development, cell migration, and angiogenesis (Palmer et al. 2009; Hallberg and Palmer 2013). While not fundamentally indispensable, *Alk* deficient mice exhibit age-dependent alterations in brain function and in behavioral tests that align with its neurobiological role (Bilsland et al. 2008; Christova et al. 2023). Similarly, two potent ALK inhibitors, known for their penetration of the central nervous system, have side effects (e.g., neuropathy, cognitive dysfunction, myalgia) closely related to the ALK inactivation within this system (Gadgeel et al. 2014; Shaw et al. 2016; Shaw et al. 2017; Solomon et al. 2018).

Oncogenic activation of ALK

The relevance of *ALK* mutations in human diseases is predominantly confined to cancer. Since its identification in 1994 as a driver in anaplastic large cell lymphoma, *ALK* alterations have been described across numerous tumor entities, such as *EML4-ALK* chromosomal rearrangements in lung cancer (Soda et al. 2007), *ALK* amplification and gene fusion in colorectal cancers (Lipson et al. 2012) and activating point mutations in neuroblastoma (Chen et al. 2008).

ALK activation by gene amplification

The amplification of the *ALK* locus leads to consequent overexpression of the ALK protein, which has been identified as a driver in certain tumor samples. This phenomenon is particularly notable in neuroblastomas, where it is frequently co-amplified with MYCN (Janoueix-Lerosey et al. 2008; Mossé et al. 2008; Bresler et al. 2014). Furthermore, a study has shown an increase in the number of *ALK* copies in patients with EML4-ALK-driven lung cancer who experienced disease progression while receiving ALK inhibitors (Katayama et al. 2012).

ALK activation by gain-of-function mutations

Genetic analyses have unveiled activating point mutations characterized by single amino acid missense substitutions. These mutations specifically affect the tyrosine kinase domain of *ALK*, leading to the continuous and ligand-independent activation of the receptor. Such *ALK* mutations are detected in approximately 8% of both sporadic and hereditary neuroblastoma patients (Mossé et al. 2008), along with isolated cases of anaplastic thyroid carcinoma (Chen et al. 2008; Bresler et al. 2014).

In the context of neuroblastoma, biochemical and computational studies have enabled the correlation of these sequence variations with their transforming activity. Although *ALK* is susceptible to silent mutations, the oncogenic activating mutations, such as ALK^{F1174L} or ALK^{R1275Q}, significantly accelerates the autophosphorylation of the tyrosine kinase domain (Bresler et al. 2014). With the advances in precision medicine and the development of potent ALK inhibitors, the acquisition of gain-of-function mutations emerges as a common mechanism for oncogenic ALK activation (Cooper et al. 2022; He and Dar 2022).

Notably, ALK^{R1275Q} mutations are predicted to be sensitive to crizotinib, a first generation ALK inhibitor (Infarinato et al. 2016). Conversely, ALK^{L1196M}, ALK^{I1171}, or ALK^{F1174} mutations are expected to reduce the inhibitor binding due to steric hindrance or structural changes alterations that enhance the ATP-binding affinity of the kinase, thereby reducing the efficacy of these inhibitors (Gainor et al. 2016).

ALK activation following chromosomal rearrangements

The catalog of fusion partners identified in ALK-positive tumors has considerably expanded, encompassing over 90 different genes solely in the case of NSCLC. Among these partners, 28 genes are located on the short arm of chromosome 2 (2p21-25), aligning with ALK's genomic location (2p23.2-p23.1) (Ou et al. 2020). Importantly, the variety of partner genes greatly influence the spatial and temporal regulation of the ALK-fused product. This aberrant regulation can affect dimerization and substrate specificity, and consequently its oncogenic potential (Hallberg and Palmer 2013; Sabir et al. 2017; Ou et al. 2020). This ectopic expression results in ALK-rearranged proteins being active in diverse cellular environments, including the nucleolus, cytoplasm, or membraneless cytoplasmic protein granules, potentially interacting with distinct signaling molecules (Gouzi et al. 2005; Woo et al. 2016; O'Regan et al. 2020; Sampson et al. 2021; Tulpule et al. 2021). As a consequence of this altered configuration, the ALK-rearranged protein acquires ligand-independence and sustains

constitutive activation through homodimerization of its partner protein, each with distinct oncogenic potentials (Childress et al. 2018).

In addition to its presence in *NPM-ALK*-associated anaplastic large cell lymphomas, *ALK* fusions have been identified in other malignancies, including inflammatory myofibroblastic tumor, LUSC, diffuse large B cell lymphoma, and renal cell carcinoma and notably, NSCLC, where the most frequent partner gene for *ALK* fusion is *EML4* (Rikova et al. 2007; Soda et al. 2007; Huang 2018).

EML4-ALK-driven lung cancer: from mechanisms to therapies

The initial discovery of *ALK* rearrangements dates back to 1994, with the identification of *NPM-ALK* fusion in a subset of anaplastic large cell lymphomas (Morris et al. 1994). Thirteen years later, a significant breakthrough in the field of lung cancer occurred when a novel *ALK* fusion gene was described within the Japanese population (Soda et al. 2007). This particular chromosomal rearrangement involves the fusion of the echinoderm microtubule-associated protein-like 4 (*EML4*) gene with the tyrosine kinase domain of *ALK*, resulting in the formation of the fusion gene known as *EML4-ALK* (Rikova et al. 2007; Soda et al. 2007). *EML4-ALK* is the most prevalent fusion in lung cancer and is detected in approximately 3-7% of NSCLC patients (Schneider et al. 2023). Beside *EML4-ALK*, several other *ALK* fusions have been also reported in the context of lung cancer, including *KIF5B-ALK*, *TFG-ALK*, or *KLC1-ALK* (Shaw and Engelman 2013; Noh et al. 2017).

EML4-ALK variants: protein structure and biology

In 2007, Soda and colleagues characterized the first two *EML4-ALK* variants (variant 1 and variant 2), marking a significant milestone in the field of lung cancer genomics and targeted therapy. Their report identified an amplified cDNA, which corresponds to the amino-terminal portion of the *EML4* gene. Interestingly, this amplified cDNA also encoded for a carboxy-terminal portion identical to the tyrosine kinase domain of *ALK* gene, suggesting that the cDNA encoded for the fusion protein *EML4-ALK* (Soda et al. 2007).

The EML family encompasses six different human EML proteins, denoted as *EML1* to *EML6*. These proteins participate in the precise regulation of microtubules during the mitotic process. *EML4* begins with an N-terminal coil-coiled domain (basic region), followed by a hydrophobic echinoderm microtubule-associated protein-like protein (HELP) domain. Further downstream, *EML4* exhibits variable tryptophan-aspartic acid (WD) repeats. The coil-coiled region, referred to as the trimerization domain (TD), facilitates the formation of trimeric

oligomers. Notably, this TD domain establishes direct interactions with microtubules. Furthermore, *EML4* exhibits the ability to bind soluble α/β-tubulin heterodimers. This interaction is facilitated by the TAPE domain, which is characterized by a tandem arrangement of β-propellers (**Figure 4A**) (Heuckmann et al. 2012; Richards et al. 2014; Richards et al. 2015; Sabir et al. 2017).

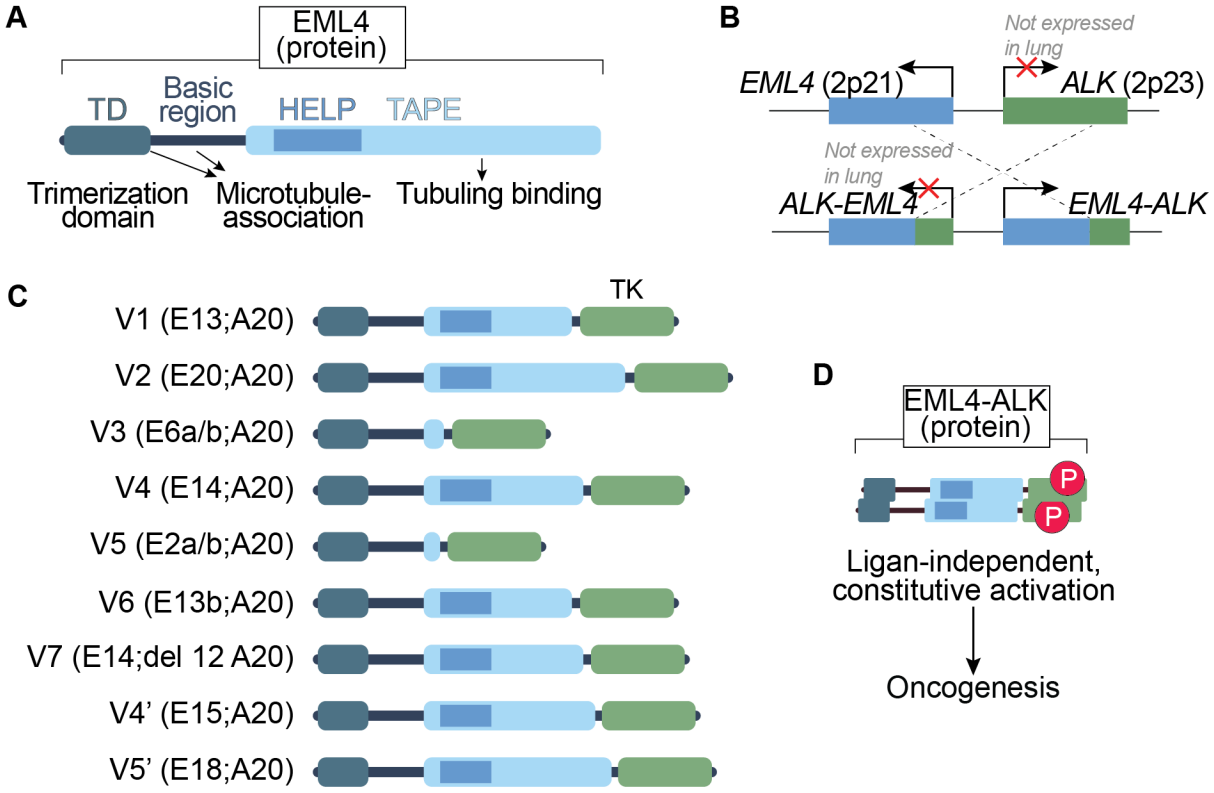


Figure 4 | Gene and protein structure of EML4-ALK. A) EML4 protein structure. EML4 domains and their main function are illustrated. **B)** Chromosomal location of *EML4*, *ALK* and the rearranged products *EML4-ALK* and *ALK-EML4*. Gene promoters and direction of the gene expression are indicated. **C)** Protein structure of different EML4-ALK variants. "E" referred to EML4 intron, "A" refers to ALK intron, and "TK" refers to ALK-tyrosine kinase. **D)** Schematic showing ligand-independent and constitutive activation of EML4-ALK.

The chromosomal rearrangement resulting in *EML4-ALK* fusion involves distinct domains of the *EML4* gene, leading to the creation of a fusion protein with altered functionality. This rearrangement stems from a paracentric inversion [inv(2)(p21p23)] occurring in the short arm of chromosome 2, where both *EML4* and *ALK* genes are located (**Figure 4B**). To date, researchers have catalogued at least 15 different *EML4-ALK* variants. All these variants share the tyrosine kinase of *ALK*, which spans exons 20 to 29, but they greatly differ in the point of fusion with the *EML4* gene (**Figure 4C**).

EML4-ALK variants 1 (V1), and 3a/b (V3) are the most prevalent, accounting for 33% and 29% of the patients respectively. Subsequently, variant 2 (V2) is observed at a frequency of 9%, while variant 4 (V4) and variant 5 each exhibit a 2% occurrence rate (Soda et al. 2007;

Choi et al. 2008; Noh et al. 2017). Importantly, all *EML4-ALK* variants encode for the TD domain of *EML4*, which plays a crucial role in protein homodimerization and the subsequent constitutive autophosphorylation of ALK (Richards et al. 2015) (**Figure 4C,D**). Notably, some variants also exhibit differences in the length of their TAPE domain. The presence of an incomplete TAPE domain within *EML4-ALK* variants 1, 2, and 4 renders a notable instability to the resulting fusion protein. To counteract this inherent instability, EML4-ALK variants 1, 2, and 4 rely on the chaperone protein HSP90 for their stability (Heuckmann et al. 2012; Richards et al. 2014; Woo et al. 2016). This discovery unveiled a potential therapeutic avenue, where specific variants could be targeted through co-inhibition of ALK and HSP90. However, despite the initial response, clinical trials evaluating this strategy did not yield discernible benefits for *EML4-ALK*-positive lung cancers (Lee et al. 2016). On the other hand, *EML4-ALK* variants 3 and 5 are classified as short variants since they entirely lack the C terminal TAPE domain (Choi et al. 2008; Takeuchi et al. 2008) (**Figure 4C**).

Owing to the notable the structural protein differences among EML4-ALK variants, there is a prevailing hypothesis that they exhibit different biological and molecular attributes (Heuckmann et al. 2012; Hrustanovic et al. 2015; Woo et al. 2016; Sabir et al. 2017; O'Regan et al. 2020). In the aim of pinpointing the specific protein domains of EML4 crucial for EML4-ALK activity, Soda et al. demonstrated that the removal of WD repeats had no discernible impact on tumor formation; however, it did influence tumor growth. Notably, tumors exhibited reduced size in the absence of the HELP domain or remained undetectable when the basic domain was absent (Soda et al. 2007). Nevertheless, this early study presents limitations due to the individual removal of EML4 domains, potentially not reflecting the complex interplay of C-terminal domains in EML4-ALK. Furthermore, recent evidence contradicts these findings, notably showcasing that variant 5, despite lacking the basic domain, exhibits transforming activity (Takeuchi et al. 2008).

EML4-ALK subcellular location and signaling.

The subcellular localization of EML4-ALK has remained a topic of debate within the scientific community. Valuable insights have emerged from experimental studies involving the overexpression of recombinant *EML4-ALK* protein in NIH3T3 fibroblast cells. While in variant 1 and variant 2, EML4-ALK predominantly localized to the cytoplasm; variant 3, exhibited a more evenly distribution between the cytoplasm and nucleus (Heuckmann et al. 2012). Subsequent research conducted by R. Bayliss, employing YFP-tagged *EML4-ALK* in HeLa cells, unveiled further nuances. Specifically, it was observed that variant 3 uniquely co-localized with microtubules, whereas variants 1, 2, and 5 displayed a diffuse cellular

distribution pattern (Richards et al. 2015). Furthermore, in 2021, three groups independently reported EML4-ALK protein aggregates in form of cytoplasmic foci or lipid membraneless cytoplasmic protein granules (Qin et al. 2021; Sampson et al. 2021; Tulpule et al. 2021). These lipidic structures were found to actively signal by concentrating components of the RAS-MAPK signaling, including the RAS activating complex GRB2/SOS1 (Qin et al. 2021; Sampson et al. 2021; Tulpule et al. 2021).

The involvement of the RAS-MAPK pathway in the EML4-ALK signaling appears to be variant-specific. Within the HELP domain lies a hydrophobic region that could facilitate access to the lipid structures and potentially engage with RAS isoforms. However, this interaction was not observed in a patient-derived variant 3 cell line, where the activation of EML4-ALK appeared to be independent of RAS and separate from the MAPK signaling pathway (Hrustanovic et al. 2015; Tulpule et al. 2021).

Beside the MAPK pathway, EML4-ALK is thought to drive lung cancer through critical signaling networks such as PI3K/AKT and JAK/STAT (Camidge and Doebele 2012; Hallberg and Palmer 2013). Initial studies have shown that chemical inhibition of ALK leads to decreased phosphorylation of AKT and ERK, indicating its influence in these pathways (Koivunen et al. 2008; McDermott et al. 2008). Additionally, STAT3 emerged as a potential downstream target of EML4-ALK, as inhibition of ALK showed to reduce STAT3 phosphorylation (Hrustanovic et al. 2015; Yanagimura et al. 2022).

It is crucial to note that many of these findings have primarily relied on *in vitro* overexpression systems along with a restricted panel of patient-derived cell lines. Disruption of the normal *EML4-ALK* expression may exert a significant impact on downstream signaling pathways and the malignant characteristics of cells, potentially leading to misconceptions. These advancements emphasize the evolving understanding of *EML4-ALK* biology, underscoring the requirement for further research to elucidate the precise function and cellular localization of EML4-ALK protein.

Clinical aspects of ALK-positive patients

EML4-ALK lung cancer patient profiles

EML4-ALK-positive lung cancer patients often have a history of light smoking (<10 pack-years) or are non-smokers. With a higher incidence observed among women, *EML4-ALK*-positive patients tend to be diagnosed at a younger age than the average for other lung cancers (Cooper et al. 2022; Schneider et al. 2023). Unfortunately, by the time of diagnosis,

the disease is often at an advanced stage with 20% of patients showing brain metastases, due to the high tropism of EML4-ALK-driven tumors for the central nervous system (CNS) (Gadgeel et al. 2014; Solomon et al. 2014; Cooper et al. 2022).

At the genomic level, *EML4-ALK* alterations are typically mutually exclusive with other drivers of LUAD, such as *KRAS* or *EGFR* mutations (Skoulidis and Heymach 2019; Elshatlawy et al. 2023). In terms of histopathological classification, *EML4-ALK*-postive lung tumors are predominantly identified as LUADs, with occasionally signet cell features, a characteristic associated with a less favorable prognosis (Rodig et al. 2009). In rare instances, *ALK*-positivity has been also reported in LUSC and large cell carcinomas (Boland et al. 2014; Sagawa et al. 2018).

In clinical practice, the diagnosis of *EML4-ALK* rearrangements relies on four different detection methods (Kerr and López-Ríos 2016; Xiang et al. 2022). Among these, fluorescence in situ hybridization (FISH) is the preferred approach, although it is not variant-specific. Immuno-histochemistry (IHC) serves as a screening tool for tumor biopsies, utilizing the FDA-approved antibody (Ventana D5F3) to identify ALK positivity, irrespective of its partner gene. In contrast, reverse transcription polymerase chain reaction (RT-PCR) enables the detection of specific variants. Additionally, next-generation sequencing (NGS) offers the advantage of not only detecting *ALK* fusions but also determining the specific fusion type and other co-occurring mutations. Besides, later efforts have demonstrated the effectiveness of NGS techniques in detecting ALK rearrangements in circulating tumor DNA (ctDNA) and circulating free DNA (cfDNA) (Angeles et al. 2021). However, it is important to note that the implementation of NGS can lead to increased diagnosed cost.

Clinical impact of EML4-ALK variants: incidence and outcomes.

The relative incidence of the *EML4-ALK* variants varies across studies due to the discrepancies in patient numbers, molecular screening platform, and participant ethnicity. For instance, in a study lead by Jessica J. Lin involving 123 *EML4-ALK* patients, variant 1 accounted for 43%, followed by variant 3 at 40%, and variant 2 at 6%. In an independent cohort of 577 ALK-positive NSCLCs sequenced at Foundation Medicine, the most prevalent fusions were variant 3 (32%) and variant 1 (32%), with variant 2 at 8% (Lin et al. 2018). Jin Kang reported that variant 3 was the most frequent *EML4-ALK* fusion, detected in 36% of the patients, followed by variant 1 at 17% (Kang et al. 2018). More recent findings from the sequencing of 1387 *EML4-ALK* patients across two independent datasets revealed that variant 3 represented 42% of the patients, while variant 1 comprised 37% (Zhang et al. 2021).

Co-occurring genomic alterations in EML4-ALK tumors

As cancer cells are evolving, they must break the normal rules governing cell growth and cell division. Tumor suppressor genes (TSG) have antagonist function to oncogenes and therefore prevent the formation of cancer. While the mutation of a single copy of an oncogene has a dominant and growth-promoting effect, both copies of the TSG need to be lost or inactivated before an effect is seen. Some exceptions have been reported for haploinsufficient TSGs (i.e., *PTEN*), where the product of the intact allele is insufficient to control cell homeostasis (Alberts et al. 2007). Importantly, alterations in multiple TSG were found in oncogene-negative tumors, a mechanism to amplify growth signaling deriving in cancer formation (Yousefi et al. 2022). TSG as *TP53* and *RB1* are widely inactivated in SCLC (Gay et al. 2021). Mutations in *TP53* are the most common genetic lesions found in NSCLC (Skoulidis and Heymach 2019). TP53 is a transcription factor for genes that regulates apoptosis and DNA damage responses. Besides this, NSCLC often inactivates genes that capture a wide range of different aspects of biology including suppressors of canonical signaling pathways (e.g., *NF1*, *STK11* (*LKB1*), *PTEN*), chromatin regulators (e.g., *ARID1A*, *STAG2, SETD2*), epigenomic regulation (e.g., *ARID1A*, *KDM6A*), and regulators of differentiation and splicing (e.g. *RBM10*) (Skoulidis and Heymach 2019; Cai et al. 2021).

In the context of *EML4-ALK* lung cancer tumors, these cell-intrinsic alterations remain largely unknown. Similar to other NSCLC cohorts, *TP53* is the most frequently inactivated TSG and is mutated in ~30% of *EML4-ALK* patients (GENIE Cohort v14, 2023; Kron et al. 2018; Christopoulos et al. 2018; Zhang et al. 2021). Consistent with other never-smoking drivers such as *EGFR* (Huang et al. 2011), the loss of *TP53* impacts the response to tyrosine kinase inhibitors and significantly impact the overall survival (Kron et al. 2018; Wang et al. 2018; Christopoulos et al. 2018). Interestingly, large discrepancies have emerged when studying the impact of *TP53* mutations in different EML4-ALK variants. A retrospective study of 102 ALK-positive patients revealed that variant 3 *TP53*-mutated patients had a higher number of metastases and shorter progression-free survival (PFS) (Christopoulos et al. 2018). An observation that was supported by Tanimoto and colleagues (Tanimoto et al. 2021). In contrast, Kron found that *TP53* mutations were prognostically negative in variant 1 and variant 3 patients, reaching statistical significance solely in variant 1 (Kron et al. 2018). Of note, the small number of variant-annotated patients is an important limiting factor in these studies that could influence the conclusions.

Importantly, while the impact of *TP53* mutations *in EML4-ALK* tumors has been elucidated, the consequences of inactivating other TSGs remain largely unexplored,

underscoring the need for further comprehensive investigations to unravel the intricate molecular landscape of *EML4-ALK* tumorigenesis.

Advancements in ALK inhibitors: targeted therapies for ALK-positive patients

ALK-positive tumors are characterized by the dependency on ALK signaling for their growth and survival, often exhibiting a remarkable response to ALK inhibitors. This pronounced sensitivity has classified these malignancies as oncogene-addicted and represent a significant milestone in the field of pharmacogenomics (Solomon et al. 2014; Cooper et al. 2022; Schneider et al. 2023).

There are currently five ALK tyrosine kinase inhibitors approved by the European Medicines Agency (EMA) and the U.S. Food and Drug Administration (FDA) for the treatment of ALK-positive lung cancers (**Table 1**). The use of these inhibitors has dramatically improved the survival of ALK patients and provided invaluable insight into the design of targeted therapies.

ALK inhibitor	Generation	Approval Status	Median PFS (months)	Targeted ALK mutations
Crizotinib	First	FDA, EMA, first-line	10.9	L1198F
Alectinib	Second	FDA, EMA, first-line second after crizotinib	34.8	L1152P/R C1156Y/T F1174C/L/V L1196M S1206C/Y G1269A/S
Brigatinib	Second	FDA, EMA Second after crizotinib	16.7-34 Shaw 24	I1151Tins L1152P/R C1156Y/T F1174C/L/V L1196M G1202R G1269A/S
Lorlatinib	Third	FDA, EMA, second-line and third-line After two lines of ALK inhibitors or as a second-line	NR	I1151Tins L1152P/R C1156Y/T I1171T/N/S F1174C/L/V L1166M G1202R S1206C/Y E1210K G12691/S

Table 1 | Management of ALK positive patients. The table summarizes the current ALK inhibitors employed in the treatment of ALK patients. PFS: Progression Free Survival; EMA: European Medicines Agency; FDA: Food and Drug Administration of the United States; NR: Not Reached.

Crizotinib: a first-generation ALK inhibitor.

Crizotinib (PF-2341066) is a potent, orally available small molecule inhibitor with ATP-competitive activity. Although initially developed as a c-MET kinase inhibitor, early preclinical studies demonstrated that crizotinib effectively inhibits NPM-ALK fusion in human ALCL cell lines and *ROS1*-driven tumors (Zou et al. 2007; Cui et al. 2011).

Approximately one year after the identification of *EML4-ALK* as a lung cancer driver, McDermott conducted an extensive drug screening on a broad panel of human tumor-derived cell lines to identify genotype-specific sensitivities. Among the wide range of drug-genotype interactions observed, crizotinib demonstrated a robust antiapoptotic response in H3122, an *EML4-ALK* variant 1 patient-derived cell line. These findings suggested that a subset of lung cancer patients may potentially benefit from crizotinib treatment (McDermott et al. 2008).

Crizotinib pioneered the era of targeted therapy for patients with ALK-positive lung tumors (Eunice et al. 2010). In a phase 1 clinical trial involving ALK-positive stage III or IV patients who had received at least one prior therapy, crizotinib led to a marked tumor shrinkage or stable disease in most of the patients (Camidge et al. 2012) . Subsequently, in a phase 3 study, crizotinib outperformed the standard first-line pemetrexed-plus-platinum chemotherapy in previously untreated patients with locally advanced or metastatic ALK-positive lung patients (Solomon et al. 2014).

In the context of first-line treatment, crizotinib exhibited an impressive objective response rate of 74%, compared to 65% for the chemotherapy arm. Furthermore, it significantly prolonged PFS, with a duration of 10.9 months, as opposed to 7.7% in the chemotherapy arm (Solomon et al. 2014). These compelling evidences strongly advocate for the use of crizotinib as first-line therapy for patients who tested positive for *ALK*-rearrangements (Cooper et al. 2022; Schneider et al. 2023).

Despite these promising results, 25% of the patients who received extended treatment with crizotinib experienced disease progression in the brain (Camidge et al. 2012). This event is consistent with previous reports indicating the limited penetration of crizotinib into the cerebrospinal fluid, suggesting reduced efficacy of crizotinib in the CNS (Costa et al. 2011). In addition, nearly all patients within a year of starting treatment experienced tumor relapse, primarily due to acquisition of secondary resistance *ALK* mutations, *ALK* gene amplification, and activation of alternative bypass signaling pathways (Katayama et al. 2012; Ou et al. 2014; Kang et al. 2018). Together, these factors limit the long-term clinical benefits of crizotinib.

Alectinib: revolutionizing the treatment of ALK-positive cancer.

With the primary goal of overcoming resistance to crizotinib, the development of more potent second-generation ALK inhibitors became imperative. Alectinib (CH-5424802) emerged as a potent orally available inhibitor. Alectinib is a selective ALK inhibitor with cross-reactivity with leukocyte receptor tyrosine kinase (LTK) at concentrations five times higher. In comparison to crizotinib, alectinib shows superior activity in inhibiting ALK phosphorylation, consequently impacting downstream signaling pathways, including STAT3 or AKT. Alectinib also demonstrated high antitumor efficacy as compared with crizotinib in xenograft models expressing native *EML4-ALK* or the mutant ALK^{L1196M}, which is unresponsive to crizotinib (Sakamoto et al. 2011).

Alectinib was firstly approved as second-line after crizotinib failure. Moreover, in contrast to crizotinib, alectinib exhibits notably activity within the central nervous system, improving metastatic disease that had progressed on crizotinib (Ou et al. 2015). In a pivotal phase 2 study, alectinib induced remission of CNS metastases, achieving an overall response rate of 57%, a disease control rate of 83%, and notable complete responses in some patients (Ou et al. 2015). Furthermore, a single arm, a phase 1-2 clinical trial conducted in Japan reported a remarkable overall response rate of 93.5% in advanced *ALK*-rearranged patients treated with alectinib (Seto et al. 2013).

The largest global randomized study in the first-line setting, known as the ALEX clinical trial, compared a next-generation ALK inhibitor, alectinib, with crizotinib. Alectinib significantly extended the progression free survival to 34.8 months compared to 10.9 months with crizotinib. Importantly, the median overall survival had not yet been reached in the alectinib arm, in contrast to 57.4 months observed with crizotinib (Mok et al. 2020). This finding holds exceptional significance in the field, considering that the five-year relative survival rates for patients with NSCLC have historically remained low. These conclusions were supported by the ALUR study, a clinical trial with a more modest sample size. Remarkably, patients with baselines CNS metastases presented a progression free survival of 25.4 months with alectinib, compared to the 7.4 months with crizotinib (Wolf et al. 2022).

Brigatinib: a potent second generation ALK inhibitor

Brigatinib (AP-26113) is a second-generation inhibitor, developed by Sen Zhang to address resistance arising from *ALK* mutations following progression on crizotinib or alectinib treatments. Brigatinib demonstrates remarkable potency, being active at subnanomolar levels. Notably, it exhibits efficacy against several frequent *ALK* mutations, including ALK^{G1202R},

ALK^{L1196M}, and *ALK*^{F1174}. In addition, brigatinib has superior efficacy to crizotinib in various xenograft and intracranial tumor models, underscoring its promising clinical potential in the management of ALK-positive patients. Interestingly, brigatinib exhibited cross-reactivity against *EGFR* exon 19 deletion, or *EGFR*^{L858R} and *EGFR*^{T790M} mutations, while remaining inactive against wildtype *EGFR* (Zhang et al. 2016).

In clinical practice, patients with a refractory disease to crizotinib benefited from brigatinib treatment as they showed robust systemic and CNS responses. Notably, median PFS reached 16.7 months, indicating a superior performance than other ALK inhibitors in similar clinical scenarios (Camidge et al. 2018). Subsequent studies such as ALTA, assessed brigatinib as first line treatment. Its latest phase 3 clinical findings revealed that in advanced ALK-positive NSCLC patients who had not previously been treated with ALK inhibitors, brigatinib was associated with a remarkable 3-year progression free survival of 43% of the cases, a significant improvement over the 19% observed with crizotinib. Similar to alectinib, brigatinib also demonstrated a substantial improvement in the median intracranial PFS, in stark contrast to 21.2 months observed with crizotinib (Camidge et al. 2021).

The phase 3 ALTA-3 trial is currently evaluating the efficacy of alectinib and brigatinib in ALK-positive patients who had previously progressed crizotinib treatment. The preliminary results indicate that both treatment arms extended progression free survival to approximately 19 months. Additionally, both ALK inhibitors showed a notably intracranial objective response rate of 73% and 68% in the brigatinib and alectinib groups, respectively. These findings endorse brigatinib and alectinib as promising second line options for ALK-positive patients who have experienced disease progression when treated with crizotinib (Yang et al. 2023).

Preclinical studies have suggested that brigatinib may offer potential benefits for tumors that have developed resistance to alectinib due to its chemical structure (Zhang et al. 2016). However, a retrospective multicenter study that evaluated the response to brigatinib in alectinib-refractory ALK-positive patients showed limited clinical benefit (Lin et al. 2018). In this study half of the patients exhibited a stable disease and a median PFS of 4.4 months. In contrast and in line with the preclinical observations, a larger Japanese study demonstrated an extended survival of 7.3 months and disease stability in 79% of the patients when treated with brigatinib (Nishio et al. 2021).

Lorlatinib: a leading ALK inhibitor

Lorlatinib (PF-06463922) marked a significant advancement in the management of ALK-positive patients (Schneider et al. 2023). Chemically designed in 2014 to overcome a

wide spectrum of ALK resistant mutations, including the main gatekeeper mutations *ALK*^{L1196M} and *ALK*^{G1202R}, lorlatinib is a third generation, highly potent, and selective ALK/ROS1 inhibitor (Johnson et al. 2014; Zou et al. 2015). A preclinical study using a murine pro-B cell line, demonstrated that lorlatinib outperformed all other ALK inhibitors by inhibiting all *ALK*-mutated genotypes (including the ALK double-mutant D1203N+E1210K) (Gainor et al. 2016). Furthermore, given the metastatic incidence of ALK-positive patients, lorlatinib was intentionally designed to be accumulated in the CNS (Johnson et al. 2014; Zou et al. 2015).

In initial stages of clinical trials, lorlatinib showcased its capacity to improve progression free survival of ALK-positive patients who had previously received at least one ALK inhibitor. Remarkably, lorlatinib demonstrated a robust activity against *ALK*-mutations. These compelling clinical findings led to lorlatinib's accelerated approval by the FDA in 2018 and the conditional approval by the EMA in 2019 for ALK-positive patients with disease progression to at least two ALK inhibitors (Shaw et al. 2019; Shaw et al. 2020; Kuang and Leighl 2021; Solomon et al. 2023).

More recently, the CROWN study, an ongoing phase 3 clinical trial, evaluated the benefits of lorlatinib over crizotinib in treatment-naïve ALK-positive patients (Solomon et al. 2023). At data cutoff (2017-2021), the overall median PFS was not reached for lorlatinib and was 9.3 months for crizotinib. Importantly, the 3-year progression free survival was 64% in the lorlatinib group, the greatest benefit for the lung cancer field. In addition, despite the longer follow-up, the intracranial response to lorlatinib continued to be efficient, showing a complete intracranial response rate of 72% of the metastatic patients (Shaw et al. 2019; Solomon et al. 2023).

Interestingly, either after resistance to crizotinib, alectinib, or brigatinib a larger percentage of variant 1 patients, in contrast to variant 3, showed non-mutated *ALK*. This finding suggested the activation of ALK-independent resistance mechanisms within this subset of patients (Cooper et al. 2022; Schneider et al. 2023). This underscores the potential benefits of lorlatinib for *ALK*-mutant patients and implies that *EML4-ALK* variant 3 patients, with their higher incidence of *ALK* mutations, may experience longer PFS compared to variant 1 patients. Nonetheless, this clinical study faces limitations due to the low number of participants and more extensive trials may be necessary to provide further insights.

ALK inhibitor resistance: challenges and strategies

The development of ALK inhibitors has significantly improved the management of patients with advanced *ALK* lung tumors and achieved long-term treatment efficacy. However,

the emergence of resistance mechanisms remains a critical medical need. Ongoing research efforts have categorized resistance mechanisms as either "on-target" (alterations of the targeted kinase-coding gene) or "off-target" (activation of independent signaling proteins). Understanding these distinctions is critical because these mechanisms require tailored therapeutic strategies.

On-target resistance mechanisms

As the field progresses in treating ALK-positive patients, clinicians face a significant challenge in the form of on-target resistance mechanisms. Resistance to ALK inhibitors can arise from a variety of genetic alterations that occur within the *ALK* tyrosine kinase fraction of the *EML4-ALK* fusion gene (**Figure 5A**) (Cooper et al. 2022; Koopman et al. 2022).

An early study of the mechanisms of acquired crizotinib resistance showed that nearly 7% of the patients had high levels of *ALK* gene amplification (Katayama et al. 2012). In the same study, 22% of patients developed the ALK^{L1196M}, ALK^{G1202R} and ALK^{S1206} mutations. *ALK* mutations cause conformational changes or steric hindrance, making the kinase target less amenable to inhibition (**Figure 5A**). Specifically, these three mutations are clustered around the ATP-binding pocket of ALK (Katayama et al. 2012; Cooper et al. 2022).

Upon progression to second-generation inhibitors, nearly half of patients harbor *ALK* kinase mutations. Interestingly, each inhibitor is associated with specific *ALK* mutations (compound mutations). For example, ALK^{G1202R} is commonly found in patients treated with alectinib and brigatinib. The ALK^{G1202R} mutation leads to steric hindrance, which repels most ALK inhibitors by affecting the charge of the binding site (**Figure 5A** and **Table 1**). Other mutations have been shown to affect the C-terminus of the ALK protein, increasing its ATP-binding affinity (Kuang and Leighl 2021; Koopman et al. 2022; Schneider et al. 2023).

The different resistant mutations in the kinase domain of ALK appear to have a specific variant-dependent pattern. An analysis of the clinical outcomes in the treatment of *EML4-ALK* positive patients shed light on potential associations between specific *EML4-ALK* variants and the emergence of *ALK* resistance mutations. In a retrospective clinical analysis, ALK^{G1202R} mutations were more prevalent among patients with *EML4-ALK* variant 3. In contrast, variant 1 patients exhibited a higher incidence of ALK^{L1196M} and ALK^{F1174C} mutations after progression to crizotinib or second-generation ALK inhibitors (Lin et al. 2018).

Despite the promising clinical benefits of lorlatinib, lorlatinib-resistant *ALK* mutations are expected to emerge. An analysis of lorlatinib-resistant biopsies showed that more than

60% of these samples harbored dual or triple *ALK* resistance mutations. The majority of these mutations were *ALK*^{G1202R} or *ALK*$^{I1171N/S/T}$ mutations, which induce large alterations within the kinase domain, rendering patients unresponsive to ALK inhibitors (**Figure 5A**) (Shiba-Ishii et al. 2022).

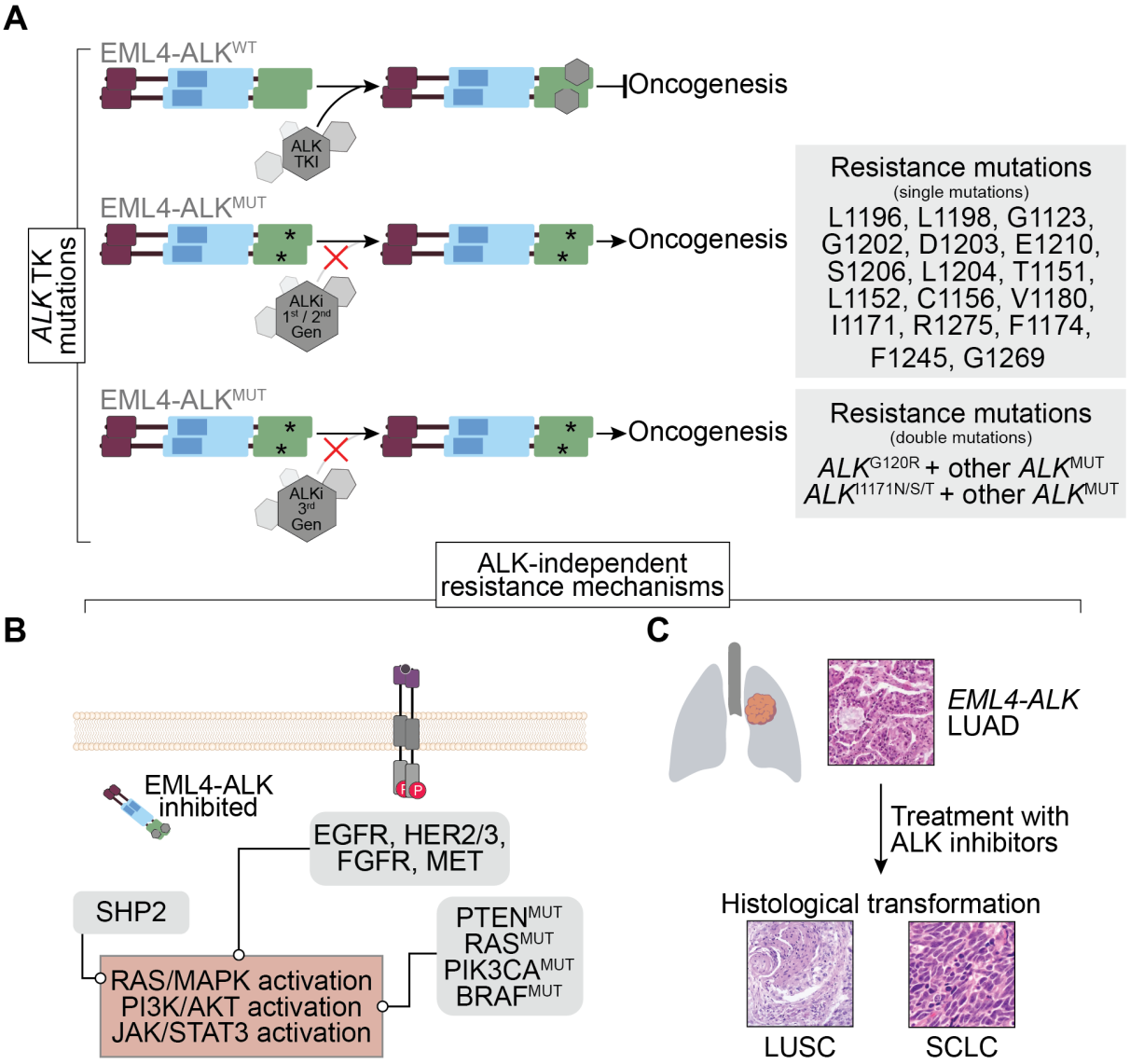


Figure 5 | Mechanisms of resistance to ALK inhibitors. A) ALK mutations cause steric hindrance or structural changes in the ALK protein, rendering tumor cells insensitive to ALK inhibitors. Single mutations are common resistance mechanisms to 1st and 2nd generation ALK inhibitors. *ALK*^{G120R} or *ALK*$^{I1171N/S/T}$ based mutations are often found after 3rd generation ALK inhibitors. ALK-independent resistance mechanisms are mediated by signal transduction activation (B) or histologic transformation (C). **B**) ALK-independent activation of bypass signaling is mediated by overactivation of receptor tyrosine kinases (EGFR, HER2/3, FGFR, MET) or tyrosine-protein phosphatases (SHP2/PTPN11) or genetic alterations (mutations in key signaling regulators). **C**) Lineage transformation may result from the selective pressure exerted by ALK inhibitors. Patients with histologic transformation often present with LUSC or SCLC histology. Adapted from Cooper, A. J. et al., 2022 and Schneider, J. L. et al., 2023.

Mechanisms of ALK-independent resistance

Although considerable research efforts have been directed toward unraveling the catalog of *ALK*-mutations, the complex landscape of resistance mechanisms extends far beyond kinase alterations. Surprisingly, nearly 50-70% of patients treated with crizotinib do not have detectable point mutations within the kinase domain of *EML4-ALK* (Katayama et al. 2012). In addition, approximately 50% of refractory patients treated with second-generation ALK inhibitors do not harbor on-target resistance mechanisms (Lin et al. 2018). Similarly, analysis of tissue biopsies following lorlatinib treatment showed that more than half of the samples did not harbor *ALK* mutations (Recondo et al. 2020; Shiba-Ishii et al. 2022).

These *ALK*-independent resistance mechanisms often encompass the activation of downstream or parallel signaling pathways or histological transformations.

a) *Bypass pathway alterations*

Off-target resistance mechanisms include a variety of signaling molecule alterations that allow cells to grow independently of ALK inhibition. These elusive mechanisms challenge the efficacy of TK inhibitors and require a tailored understanding to optimize therapeutic strategies. In this effort, the presence of *MET* amplification emerged as an actionable kinase in the analysis of *ALK*-rearranged samples that progressed to ALK inhibitors (Dagogo-Jack et al. 2020). However, combined inhibition of *ALK* and *MET* have shown limited benefits (Dagogo-Jack et al. 2023).

Significant advances have been made by using patient-derived cell lines, overexpression of *EML4-ALK* models or patient-derived xenograft models. These preclinical systems effectively mitigate the challenges posed by the limited availability of *EML4-ALK* biospecimens with similar clinical histories or genomic backgrounds. Early studies using crizotinib-resistant patient-derived cell lines and the variant 1 H3122 patient-derived cell line identified the aberrant activation of *KIT* or *EGFR* as a resistant mechanism (Katayama et al. 2012). Interestingly, activation of *EGFR* was independent of *EGFR* mutations or amplifications, suggesting a ligand or gene expression upregulation (**Figure 5B**).

Drug screenings also serve as a platform to uncover novel signaling pathways associated with acquired resistance to ALK inhibitors and to identify potential tumor vulnerabilities. In a study employing an FDA-approved drug library, Yun and colleagues identified the transcriptional co-regulator YAP as a key resistance mechanism. Interestingly, YAP was found to mediate the expression of oncogenic signaling molecules such as *AXL*,

EGFR or *TGFBR2* (Yun et al. 2019). Similarly, an independent study using unbiased proteomic characterization also highlighted the significance of YAP as a central protein in alectinib-resistant patient-derived cells (Tsuji et al. 2019). Importantly, the role of EGFR in eliciting PI3K/AKT and RAS/MAPK pathways was also demonstrated by analyzing the transcriptomic profile of lorlatinib-resistant cells (**Figure 5B**) (Redaelli et al. 2018).

Unbiased genomic screenings have been instrumental in identifying potential resistance mechanisms. In 2018, a research team led by Jeffrey A. Engelman performed a shRNA screening using *EML4-ALK* variant 1 cell lines derived from patients who had progressed on crizotinib (Dardaei et al. 2018). This approach led to the identification of SHP2 (PTPN11) as a targetable protein in resistant cells. SHP2 is a non-receptor protein tyrosine phosphatase that regulates oncogenic signaling by activating the RAS/MAPK pathways (**Figure 5B**). Subsequently, chemical inhibition of SHP2 and ALK effectively suppressed RAS and ERK activation, delaying therapeutic failure. The promising outcome of this combinatorial treatment have prompted the initiation of the clinical trials NCT04292119 and NCT04800822. C. Importantly, in this clinical trial, the inhibition of SHP2 showed a notable decrease in ERK phosphorylation and circulating tumor DNA in an *EML4-ALK* patient who had previously received crizotinib, ceritinib, alectinib, and lorlatinib (Drilon et al. 2023). However, it is important to note that this study is still in its early stages, and larger cohorts are needed to draw more robust conclusions.

Increased *KRAS* copy number or loss of expression of *DUSP6*, a MAPK phosphatase, have been established as drivers of RTK-mediated resistance in *ALK* patients. These ALK-independent alterations reactivate the MAPK signaling cascade leading to tumor growth. On this basis, preclinical *in vitro* studies have shown that co-inhibition of ALK and the downstream RAS effector MEK enhances therapeutic responses through PI3K/AKT/mTOR pathway ablation (Hrustanovic et al. 2015). These findings are the basis for ongoing clinical efforts (NCT02321501, NCT04005144). Interestingly, mTOR overactivation was found to mediate lorlatinib resistance through the loss of NF2, a negative regulator of mTOR (Recondo et al. 2020).

Other bypass pathways involve the non-receptor tyrosine kinase SRC. SRC was found to be an important signaling node in *in vitro* models of patients who had progressed to ALK tyrosine kinase inhibitors. In these upfront clinical settings, inhibition of ALK along the SRC kinase effectively disrupted the MAPK pathways, resulting in a profound response (Crystal et al. 2014; Yoshida et al. 2017; Recondo et al. 2020).

In summary, the diverse landscape of ALK-independent resistance mechanisms poses a significant challenge in the management for these patients. As we continue to unravel these intricate pathways, it will become increasingly important to identify signaling nodes that can serve as common therapeutic targets. By identifying common vulnerabilities, we can develop more comprehensive strategies to address the complex array of resistance mechanisms found in EML4-ALK-driven cancers.

b) *The enigma of histological transformation in therapy resistant-ALK tumors*

Lineage plasticity, the ability of cells to transition between distinct developmental stages, has emerged as a critical factor in cancer progression, drug resistance and metastasis (Quintanal-Villalonga et al. 2020).

While *EML4-ALK* tumors are primarily classified as LUADs (Rodig et al. 2009; Boland et al. 2014; Sagawa et al. 2018), the extent of tumor cell plasticity and the prevalence of histologic transformations within different molecular subsets of NSCLC remain largely underexplored. Sporadic reports of squamous transformation occurring in response to ALK inhibitors have been reported (**Figure 5C**) (Fujita et al. 2016; Shiba-Ishii et al. 2022). Furthermore, neuroendocrine SCLC transformations, known for their aggressive nature, have been implicated in refractory cases in both EGFR- and ALK-driven lung cancers (Niederst et al. 2015). In line, post-treatment re-biopsies in *EML4-ALK* patients have identified rare cases of neuroendocrine transformation (**Figure 5C**), typically associated with the concurrent loss of *RB1* and *TP53* genes (Takegawa et al. 2016). Understanding these complex transformations is crucial for advancing our strategies against ALK therapy resistance.

Emerging trends in ALK-positive lung cancer management

The next generation of TKIs to address on-target resistance

Ongoing research into novel ALK inhibitors aims to enhance treatment outcomes and address potential on-target resistance. Importantly, progression to several ALK inhibitors often results in a progressive disease with multiple mutations on the same *ALK* allele —an issue that current ALK inhibitors struggle to address effectively (Cooper et al. 2022; Schneider et al. 2023).

TPX-0131 is a CNS-penetrant and selective ALK inhibitor structurally designed to target the ATP-binding site of ALK. *In vitro* experiments have demonstrated TPX-0131 is the most potent ALK inhibitor. Importantly, TPX-0131 is active against challenging *ALK* mutations such as ALK^{G1202R} or ALK^{L1196M}, leading to complete tumor remission as compared to lorlatinib.

Strikingly, TPX-0131 has also proven its efficacy in reducing cell viability in cases involving *ALK*^{G1202R}-based double and triple mutations- a frequent genetic occurrence among ALK-positive patients treated with lorlatinib (Murray et al. 2021).

NVL-655 is also a fourth-generation, potent and brain-penetrant ALK inhibitor. Similar to TPX-031, NVL -655 demonstrates effectiveness against the typical *ALK*^{G1202R} mutation and shows promise in double mutant cells and *ALK*-resistant xenograft models (Pelish et al. 2021).

These two cutting-edge ALK inhibitors offer promising preclinical profiles, marking a promising chapter in the evolving landscape of targeted therapies. Notably, ongoing phase 1/2 clinical trials (NCT04849273, NCT05384626) are actively assessing the impact and efficacy of these inhibitors in patients with advanced ALK-positive NSCLC.

Enhancing therapeutic outcomes: combinatorial treatment strategies

Combinatorial therapies have emerged as promising alternative treatment strategies to address the complex challenges associated with resistance. The rationale behind combinatorial therapies lies in the multiple evasion mechanisms and cellular adaptations to TKI pressure (Neto et al. 2020; Settleman et al. 2021). By targeting ALK along with complementary signaling nodes, these therapies aim to efficiently induce tumor regression or delay the onset of resistance.

ALK rearranged patients might benefit from MET inhibitors when presenting *MET* amplifications (Dagogo-Jack et al. 2020). Besides, MEK inhibitors arose as a putative target to prevent RAS-MAPK reactivation upon ALK inhibition (Hrustanovic et al. 2015). In line, SHP2 inhibitors, currently in clinical trials (NCT04292119 and NCT04800822), aims to effectively abrogate the MAPK pathway by synergizing with ALK inhibitors (Dardaei et al. 2018; Sodir et al. 2023). Moreover, several clinical trials in early stage are combining ALK inhibitors with mTOR (NCT02321501) or VEGF (NCT04227028) inhibitors.

Immunotherapy approaches in ALK-positive lung cancer

Immunotherapies have revolutionized the treatment of various NSCLC subtypes, yet their impact on ALK-positive patients remains limited (Thai et al. 2021; Cooper et al. 2022). This is often attributed to the low mutational burden and limited neoantigen landscape of these patients (Thai et al. 2021; Cooper et al. 2022). To address this, current efforts are focused on the development of ALK-specific vaccines. In this regard, a research team led by Roberto Chiarle has pioneered a novel cancer vaccine against *ALK* rearranged lung tumors (Voena et

al. 2015; Mota et al. 2023). By employing mice with ectopic human EML4-ALK protein expression, they developed an ALK-vaccine that elicited a strong immune response. This innovative vaccine, focusing on the intracytoplasmic domain of ALK, has demonstrated a robust suppression of tumor growth when combined with ALK inhibitors. These advancements hold promise for enhancing the therapeutic options and outcomes in ALK-driven lung cancer.

Modeling *EML4-ALK* lung cancer: tools and approaches

The study of *EML4-ALK* lung cancer requires relevant models that faithfully recapitulate the pathophysiology of the disease. Preclinical modeling of *EML4-ALK* has proven critical in unraveling the complex biology of this oncogenic fusion and developing more effective treatment strategies.

Since the discovery of *EML4-ALK* and its multiple variants, *in vitro* systems have been extensively used to understand the biology and treatment responses of *EML4-ALK* tumors. The overexpression of the human oncogenic fusion *EML4-ALK* in untransformed cells has served as the basis for mutagenesis and ALK inhibitor screenings. However, many of these drug screens have been performed in Ba/F3 cells, a murine pro-B cell line (Soda et al. 2007; Choi et al. 2008; Zou et al. 2015; Gainor et al. 2016; Recondo et al. 2020; Shiba-Ishii et al. 2022), or in the mouse embryonic fibroblast cell line NIH3T3 (Soda et al. 2007; Choi et al. 2008; Zou et al. 2015; Shiba-Ishii et al. 2022). While these isogenic cell systems are popular for kinase and transformation screenings, they do not accurately recapitulate the lung origin of the disease. In addition, overexpression of *EML4-ALK* using artificial promoters can misrepresent the physiological levels of the oncoprotein, potentially leading to misleading experimental results.

Patient-derived xenografts and patient-derived cells have been instrumental in the understanding of ALK resistance mechanisms (Crystal et al. 2014; Hrustanovic et al. 2015; Gainor et al. 2016; Zhang et al. 2016; Yoda et al. 2018; Tangpeerachaikul et al. 2021). However, these models also have important limitations, such as the lack of an appropriate *in vivo* environment, being grown in non-orthotopic sites, and the obligate absence of the immune system.

The development of germline transgenic mouse models with lung tissue-specific expression of the human *EML4-ALK* (variant 1) transgene has provided preclinical models for *in vivo* studies and screening of ALK inhibitors (Soda et al. 2008; Pyo et al. 2017). Despite their importance, ectopic expression of human oncoproteins at non-physiological levels and the complex germline manipulation have proven challenging.

With the development of CRISPR/Cas9 genome editing, the possibility of modeling these complex genetic alterations became feasible. Simultaneously, two groups modelled the murine *Eml4-Alk* variant 1 chromosomal rearrangement through the delivered CRISPR/Cas9-containing viruses (Blasco et al. 2014; Maddalo et al. 2014). CRISPR/Cas9 provoke targeted double-strand breaks and intrachromosomal inversion to induce the murine *Eml4-Alk* variant 1 fusion in somatic lung cells. Importantly, these tumors exhibit histopathological and molecular features characteristic of ALK-positive human lung tumors and provided important preclinical tools for ALK inhibitor screenings and biological studies (Blasco et al. 2014; Maddalo et al. 2014; Chen et al. 2022; Mota et al. 2023).

AIMS OF THE THESIS

Over the last two decades, significant improvements in the field of lung cancer have been made. One major breakthrough in pharmacogenomics was the discovery of *EML4-ALK,* which has provided major milestones for targeted therapies. Despite their strong dependence on ALK signaling, nearly all *ALK*-positive tumors eventually develop resistance. Consequently, there is an urgent clinical need to identify novel therapeutic approaches.

In addition, concurrent genomic alterations serve as critical biomarkers for patient stratification. *TP53* mutations are known to adversely affect the outcome of *EML4-ALK* patients. However, whether alterations in other tumor suppressor genes may influence tumor growth or treatment response remains largely unknown.

In this regard, the objectives of this thesis are:

- To understand the therapeutic response to ALK inhibitors in EML4-ALK variant 1 and variant 3-driven tumor cells.
- To identify novel therapeutic opportunities using combinatorial strategies.
- To investigate the role of key tumor suppressor genes in EML4-ALK lung tumorigenesis.

RESULTS

Chapter 1: Understanding the therapeutic response to ALK inhibitors in EML4-ALK variant 1 and variant 3-driven tumor cells

Some of the results and figures presented in this chapter have been submitted in a manuscript (Diaz-Jimenez, A et al., 2024). The results and figures have been adapted accordingly.

Development of a preclinical mouse model for investigating EML4-ALK driven lung tumors

Since the discovery of *EML4-ALK*, *in vitro* systems have been extensively used to understand the biological features and therapeutic response of EML4-ALK-driven tumors. Nevertheless, those models do not closely recapitulate the lung origin of the disease. Major strives have been made by overexpressing the human EML4-ALK protein in a murine pro-B cell line or in a mouse embryonic fibroblast cell line using artificial promoters (Soda et al. 2007; Choi et al. 2008; Zou et al. 2015; Gainor et al. 2016; Recondo et al. 2020; Shiba-Ishii et al. 2022). As previously discussed, this can misrepresent the physiological levels of the oncoprotein, potentially leading to misleading experimental results. We, therefore, sought to generate a preclinical murine model that encompasses the lung origin and is driven by the endogenous *Eml4-Alk* chromosomal rearrangement. Within the spectrum of human *EML4-ALK* variants, our research focused on variant 1 and variant 3. Their notable prevalence underscores their significance as key targets for preclinical modeling.

To do so, our laboratory took advantage of the CRISPR/Cas9 methodology previously generated by Andrea Ventura (Maddalo et al. 2014), in which intratracheal instillation of adenoviral vectors induced the endogenous *Eml4-Alk* variant 1 (V1) chromosomal inversion (**Figure 6**). This adenovirus carries vectors encoding for two sgRNAs (sg*Eml4*^{V1} and sg*Alk*) and the Cas9 protein. Subsequent after cell transduction, the double chromosomal break induced by sg*Eml4*^{V1} (targeting *Eml4*$^{intron\ 14}$) and sg*Alk* (*Alk*$^{intron\ 19}$) provoke the intrachromosomal inversion and the consequent endogenous *Eml4-Alk* V1 rearrangement. Based on this technology, Sara Chocarro and Kalman Somogyi, members of the Sotillo Lab (DKFZ, Heidelberg), modified the original vector and replaced the sg*Eml4*^{V1} by sg*Eml4*^{V3} (targeting *Eml4*$^{intron\ 6}$) to induce the *Eml4-Alk* variant 3 (V3).

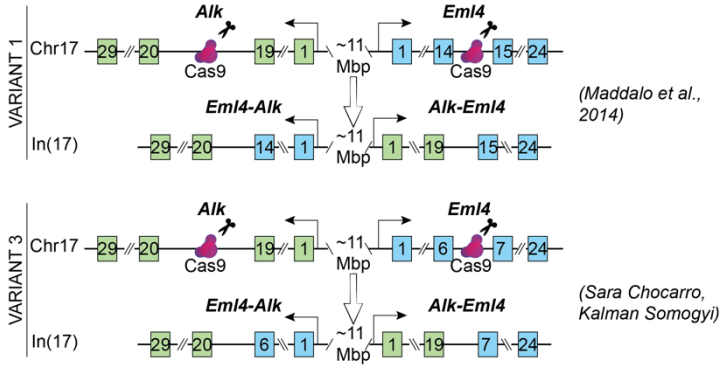


Figure 6 | *Eml4-Alk* chromosomal rearrangement. The murine *Eml4-Alk* chromosomal rearrangement results from a paracentric inversion between the *Eml4* and *Alk* genes. Both genes are located on chromosome 17 in the mouse genome (chromosome 2 in humans). sg*Eml4*^{V1} targets *Eml4*^{intron14}, sg*Eml4*^{V3} targets *Eml4*^{intron6}, sg*Alk* targets *Alk*^{intron19}.

To establish a preclinical *in vitro* model to understand the therapeutic response to different ALK inhibitors, I generated lung tumor-derived cells from *Trp53*$^{fllox/flox}$;*Rosa26*$^{mT/mG}$;*CCSP-Cre* mice (**Figure 7A**). A *Trp53*-deficient background (Marino et al. 2000) was employed as *TP53* is the most frequently mutated gene found in 30% of *EML4-ALK* patients (Kron et al. 2018; Christopoulos et al. 2018). Besides, loss of *TP53* has been demonstrated to reduce patient overall survival and increase the risk of therapeutic failure (Kron et al. 2018; Christopoulos et al. 2018). Of note, I failed to grow lung tumor-derived EML4-ALK-driven *Trp53*^{WT} cells from *Rosa26*$^{mT/mG}$;*CCSP-Cre* mice.

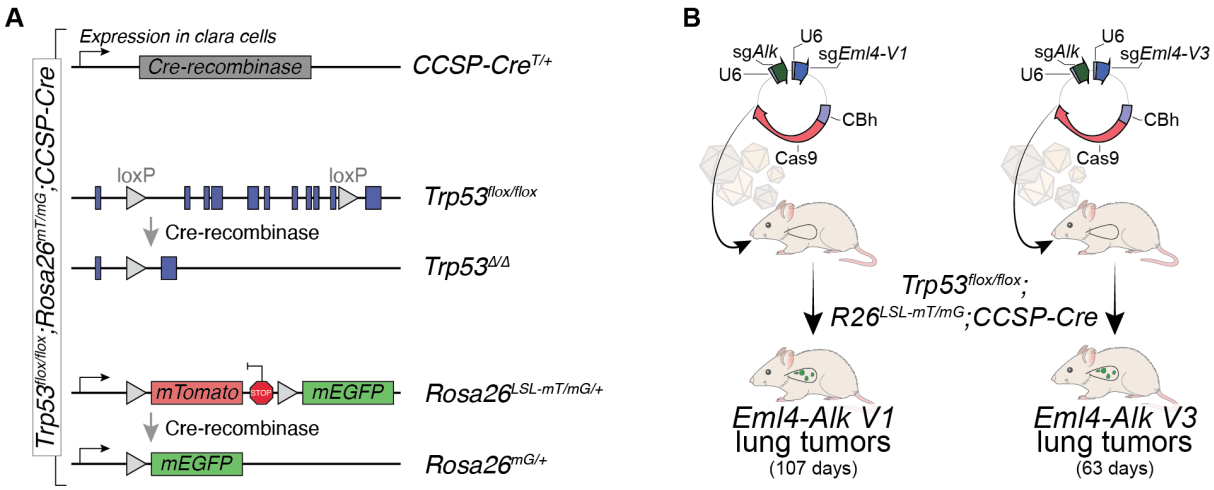


Figure 7 | Adenoviral sg*Eml4*-sg*Alk*/Cas9-mediated lung tumor initiation in *Trp53*$^{flox/flox}$;*Rosa26*$^{mT/mG}$;*CCSP-Cre* mice. A) Schematic of the *Trp53*$^{flox/flox}$, *Rosa26*$^{mT/mG}$ and *CCSP-Cre* alleles. In this model, Cre-recombinase is expressed in the club cells of the lung. Cre-recombinase allows the recombination of the membrane-Tomato-STOP cassette, leading to the expression of membrane-EGFP protein in club cells. Cre-recombinase inactivates *Trp53* in club cells. **B)** Intratracheal instillation of sg*Eml4*^{V1}-sg*Alk*/Cas9 or sg*Eml4*^{V3}-sg*Alk*/Cas9 induce lung tumors in *Trp53*$^{flox/flox}$;*Rosa26*$^{mT/mG}$;*CCSP-Cre* mice. Median survival for V1 mice is 107 days and 63 days for V3 mice (data from Sara Chocarro).

The *Rosa26*$^{mT/mG}$ (Muzumdar et al. 2007) and CCSP-Cre (Oikonomou et al. 2012) transgenes constitute a genetic system employed for tracing gene expression and cell lineage

within the respiratory system (**Figure 7A**). The *Rosa26*$^{LSL\text{-}mT/mG}$ allele facilitates the expression of a EGFP (mG) fluorescent protein, replacing the previously expressed Tomato (mT), upon Cre recombination. In this model, Cre recombinase is govern by the CCSP promoter, which is active in club cells. club cells have been established as the origin of *Eml4-Alk* lung adenocarcinomas (Chen et al. 2022). Consequently, the *Trp53*$^{flox/flox}$;*Rosa26*$^{LSL\text{-}mT/mG}$*; CCSP-Cre* mice serve as a suitable preclinical mouse mode, enabling the faithful reproduction of the *TP53*^{mut} background and EGFP-label of lung tumors.

Generation of *Eml4-Alk* mouse tumor-derived cells

To generate *Eml4-Alk* variant 1 and variant 3 lung tumor-derived cells, *Trp53*$^{flox/flox}$;*Rosa26*$^{mT/mG}$*;CCSP-Cre* mice over 8 weeks old were intratracheally instilled with either adeno-sg*Eml4*^{V1}-sg*Alk*/Cas9 or sg*Eml4*^{V3}-sg*Alk*/Cas9 vectors (**Figure 7B**). Variant 1 lung tumor bearing mice presented an overall survival of 107 days, while variant 3 injected-mice had an accelerated disease progression and an overall survival of 63 days (1.7 times lower*, P<0.0001;* data from Sara Chocarro).

I then microdissected individual lung tumors and generated mouse tumor-derived cells (mTDCs) from EML4-ALK variant 1 or variant 3-driven lung adenocarcinomas (see methods) (**Figure 8A**). mTDCs genotyping and Sanger sequencing confirmed the presence of the corresponding *Eml4-Alk* variant (**Figure 8B**). To confirm the homozygosity or heterozygosity of *Eml4-Alk*, I then genotyped the mTDCs for the *Alk* wildtype gene using primers surrounding the chromosomal breaking point (**Figure 8C**). Interestingly, two out of three variant 1 mTDCs were homozygous for *Eml4-Alk*, while all variant 3 mTDCs were heterozygous (**Figure 8C**). Histological examination of mTDCs confirmed the presence of LUAD markers (SPC^{+}, TTF1^{+}, CCSP^{-}) and demonstrated the absence of LUSC component (KRT5^{-}) (**Figure 8D**).

Despite attempts to confirm the presence of murine EML4-ALK protein using various anti-murine ALK antibodies, these efforts proved unsuccessful, as described in Sara Chocarro's MSc Thesis (2018). To validate the expression of EML4-ALK protein, I conducted Western blot analysis employing an anti-EML4 antibody. The immunoblot revealed the presence of both EML4-ALK variant 1 and variant 3 in the respective mTDCs. Furthermore, consistent with the genomic analysis of the *Eml4-Alk* variant 1 in mTDCs, no wildtype EML4 protein was detected in these cells (**Figure 8E**). Finally, to confirm the activity of EML4-ALK and the activation of downstream effectors, I evaluated the levels of MEK, ERK, and AKT and compare them with healthy lung tissue. Immunoblot of these kinases demonstrated the successful oncogenic activation of EML4-ALK and engagement of the MAPK and PI3K/AKT

pathways (**Figure 8E**). Interestingly, although V3 accelerated tumor progression, I found that all mTDCs presented similar proliferation rates in culture (**Figure 8F**).

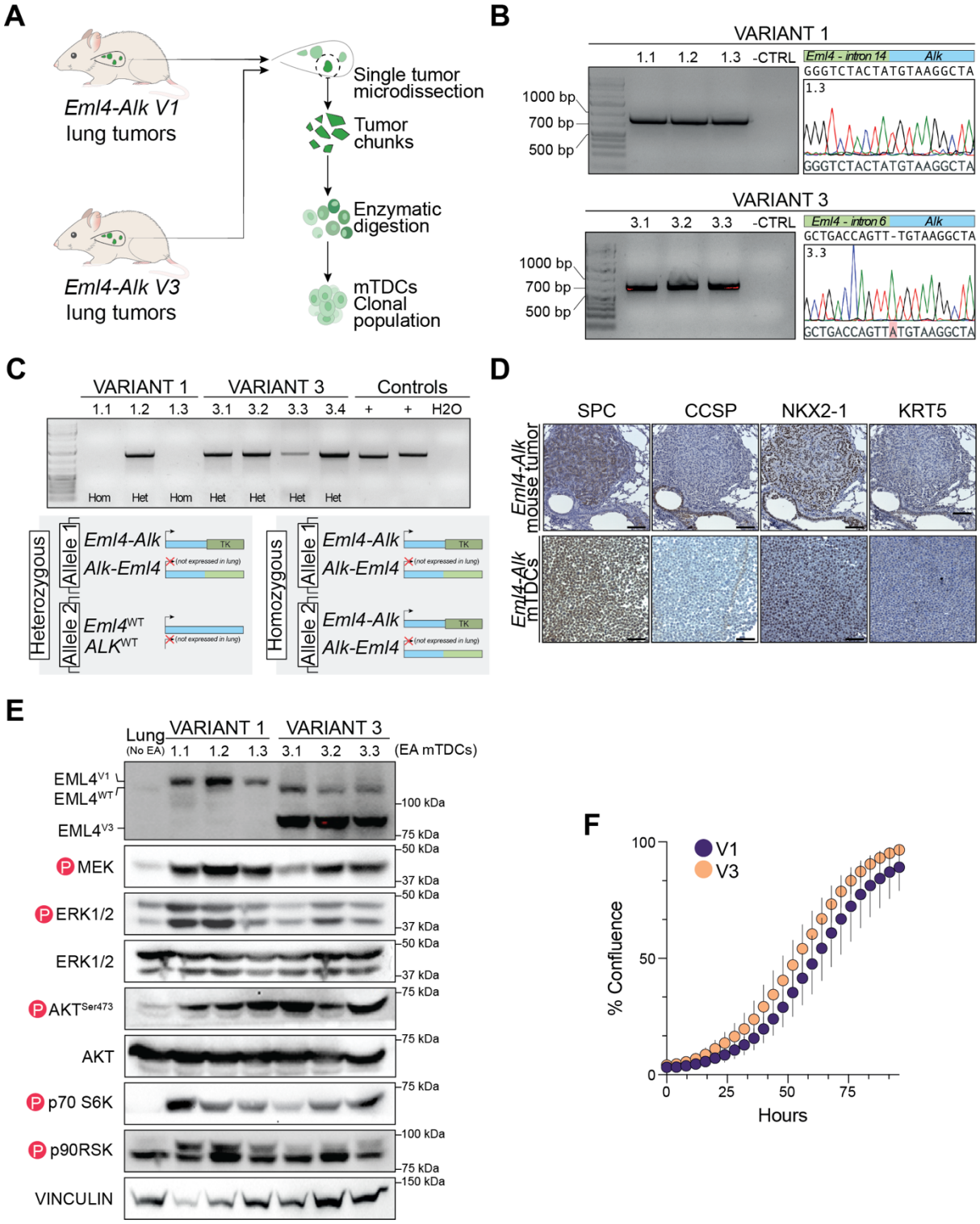


Figure 8 | *Eml4-Alk* mouse tumor-derived cells. A) Schematic of *Eml4-Alk* lung tumor cell derivation. **B)** PCR resolved bands showing the presence of *Eml4-Alk* variant 1 or variant 3. Each lane is a clonal cell population. Right panel shows a representative Sanger seq result from *Eml4-Alk* variant 1 or variant 3. **C)** PCR resolved bands showing the presence or absence of non-fused *Alk* alleles. A schematic of the genomic products is shown. **D)** Representative immunohistochemistry of Eml4-Alk mouse lung tumors and an *Eml4-Alk* mouse tumor-derived cell

line. **E)** Cell lysates from healthy lung (control) and *Eml4-Alk* mTDCs were assessed by immunoblotting with the indicated antibodies. Each lane is an independent clone. **F)** Cell growth of variant 1 and variant 3 cells over time. Experiment was performed using four V1 cells and three V3 cells.

Characterization of *Eml4-Alk* variant 1 and variant 3 mTDCs at the proteomic level

To characterize the molecular and cellular processes diversity along *Eml4-Alk* variants, I performed proteomic analysis with the help of Dr. Barbara Helm and Dr. Dario Lucas Frey (from the lab of Dr. Ursula Klingmüller, DKFZ, Heidelberg) and Junyan Lu (Heidelberg University, Heidelberg).

Unbiased proteomic profiling of four variant 1 and four variant 3 mTDCs identified 4843 proteins. To understand the variance among mTDCs and variants and to reduce the dimensionality of the dataset, I performed a Principal Component Analysis (PCA). Based on the proteomic profiles of the variant 1 and variant 3 mTDCs, samples clustered according to their *Eml4-Alk* variant (**Figure 9A**).

Identification of differentially expressed proteins from the proteomic data revealed discrete differences between variants (**Figure 9B**). Interestingly, COPS6, CLTA, CDK6, SLC7A1, PARVB, XAB2 or USP15 proteins were found exclusively in variant 3 mTDCs (**Figure 9C**). Gene set enrichment analysis (GSEA) revealed enriched pathways related to GTPase effectors, WNT and metabolic signaling in variant 3 mTDCs. These results may suggest that different *Eml4-Alk* variants may act through separate signaling cascades (**Figure 9D**).

To identify potential transcription factors that might be differentially influenced within a context-specific variant, I conducted a transcription factor binding motif analysis among the upregulated proteins (**Figure 9E**). Interestingly, variant 1 mTDCs showed enrichment in the ETS transcription factor family (ELF, TCF, ETS), which has been described in the process of cell survival and cell renewal (Yu et al. 2016; Zacharias et al. 2018). In contrast, variant 3 mTDCs presented an overrepresentation of the Sp/Klf-related motifs. These motifs have been demonstrated to govern cell proliferation and stemness (Yu et al. 2016; Zacharias et al. 2018), being related with WNT-signatures previously described in the GSEA analysis. Besides, Sp/Klf members have been described in WNT-responsive alveolar epithelial progenitors, suggesting that V3 may induce loss of differentiation (Sutherland et al. 2014; Zacharias et al. 2018).

Altogether, these results demonstrated that variant 1 and variant 3 mTDCs are a valuable preclinical tool, with a strong LUAD background and different enriched pathways.

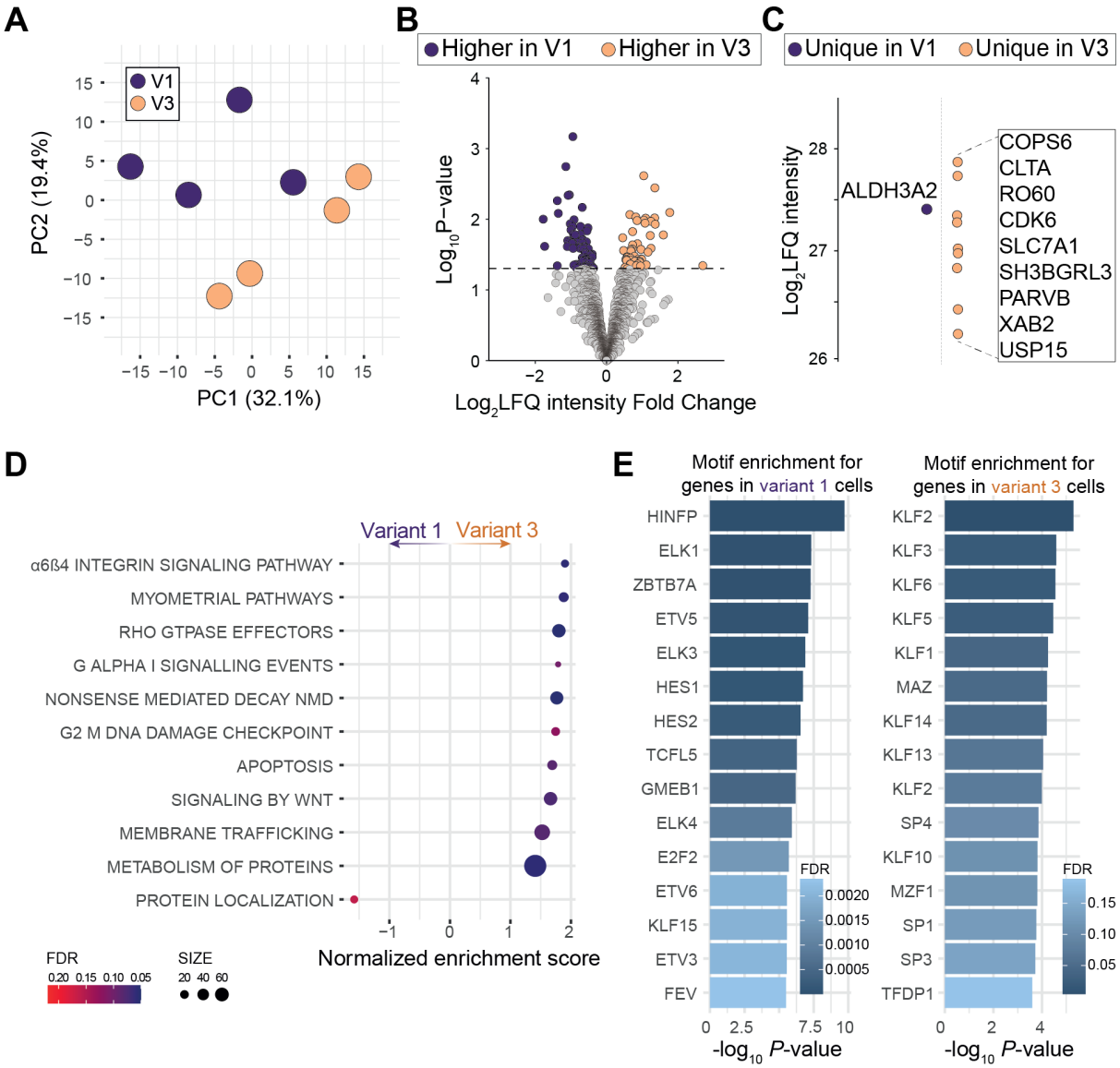


Figure 9 | *Eml4-Alk* variant 1 and variant 3 cells display different proteomic profiles. A) PCA of the proteomic profiles from variant 1 and variant 3 cells. The proportion of variance captured by each principal component is indicated. **B)** Label-free quantitation (LFQ)-based volcano plot showing the protein level changes between variant 1 (grey) and variant 3 (dark purple) mTDCs. Threshold at adjusted *P-Value*<0.25. **C)** LFQ- plot showing the unique proteins presented in variant 1 (grey) and variant 3 (dark purple) mTDCs. **D)** Gene Set Enrichment Analysis (GSEA) on overexpressed proteins comparing variant 3 vs variant 1 cells. The size of the dots refers to the number of core enrichment proteins and the color represents the FDR value. **E)** Transcription factor motifs enriched prediction (JASPAR 2018 non-redundant; −450 to +50 bp from transcription start site) in variant 1 and variant 3 cells. Threshold at LFQ>1 and adjusted P-Value<0.25. Transcription factors are colored based on FDR.

EML4-ALK V1 and V3 show different sensitivity to ALK inhibitors

Preclinical and clinical studies have suggested that the response to different ALK inhibitors is highly determined by the different *EML4-ALK* variants (Woo et al. 2016; Sabir et al. 2017; Christopoulos et al. 2018). However, there is no clear consensus among clinical studies due to the low patient homogeneity. In this regard, clinical studies tend to cluster *EML4-*

ALK variants according to the length of EML4, disempowering further analysis. To solve this issue, I employed a panel of variant 1 and variant 3 mTDCs with similar genetic background.

ALK inhibitors were chosen based on their usage and relevance in the current clinical context. Crizotinib (first-generation), alectinib and brigatinib (second-generation), and lorlatinib (third-generation) were therefore used.

I first performed a dose-response curve analysis to characterize cell viability at different drug concentrations. Consistent with previous reports, *Eml4-Alk* variant 1 mTDCs showed increased sensitivity to ALK inhibitors, while variant 3 mTDCs exhibited some degree of resistance (**Figure 10A,B**). I then investigated whether this V3-associated resistance might be due to an incomplete abrogation of the ALK signaling cascade. Immunoblotting of ALK downstream effectors showed incomplete inhibition of ALK when cells were treated with crizotinib. However, second-generation ALK inhibitors (alectinib or brigatinib) and third-generation ALK inhibitor (lorlatinib) effectively impaired ALK activity by reducing or suppressing ERK1/2 phosphorylation (**Figure 10C**). Nevertheless, this analysis was insufficient to determine why variant 1 had an enhanced response to ALK inhibitors.

To assess whether the initial response to ALK inhibitors could influence the development of resistance, mTDCs were exposed to two different concentrations (20 and 100 nM) of various ALK inhibitors (crizotinib, brigatinib, alectinib, and lorlatinib) for 14 days (**Figure 10D**). After this two-week treatment period, crizotinib exhibited incomplete inhibitory activity, resulting in the highest relative growth compared to other ALK inhibitors (**Figure 10C**). Both crizotinib and alectinib treatment led to similar growth patterns for variant 1 and variant 3 mTDCs, as evidenced by their comparable colony-forming abilities (**Figure 10C**). Interestingly, while variant 3 cells exhibited the ability to grow under low doses of lorlatinib, their resistance capabilities were significantly reduced at higher doses (**Figure 10C**). Notably, variant 3 cells displayed increased resistance to brigatinib, even at higher doses.

Taken together, these results suggest that mTDCs have different degrees of sensitivity to ALK inhibition. In particular, variant 3 mTDCs have a higher resistance capacity to brigatinib.

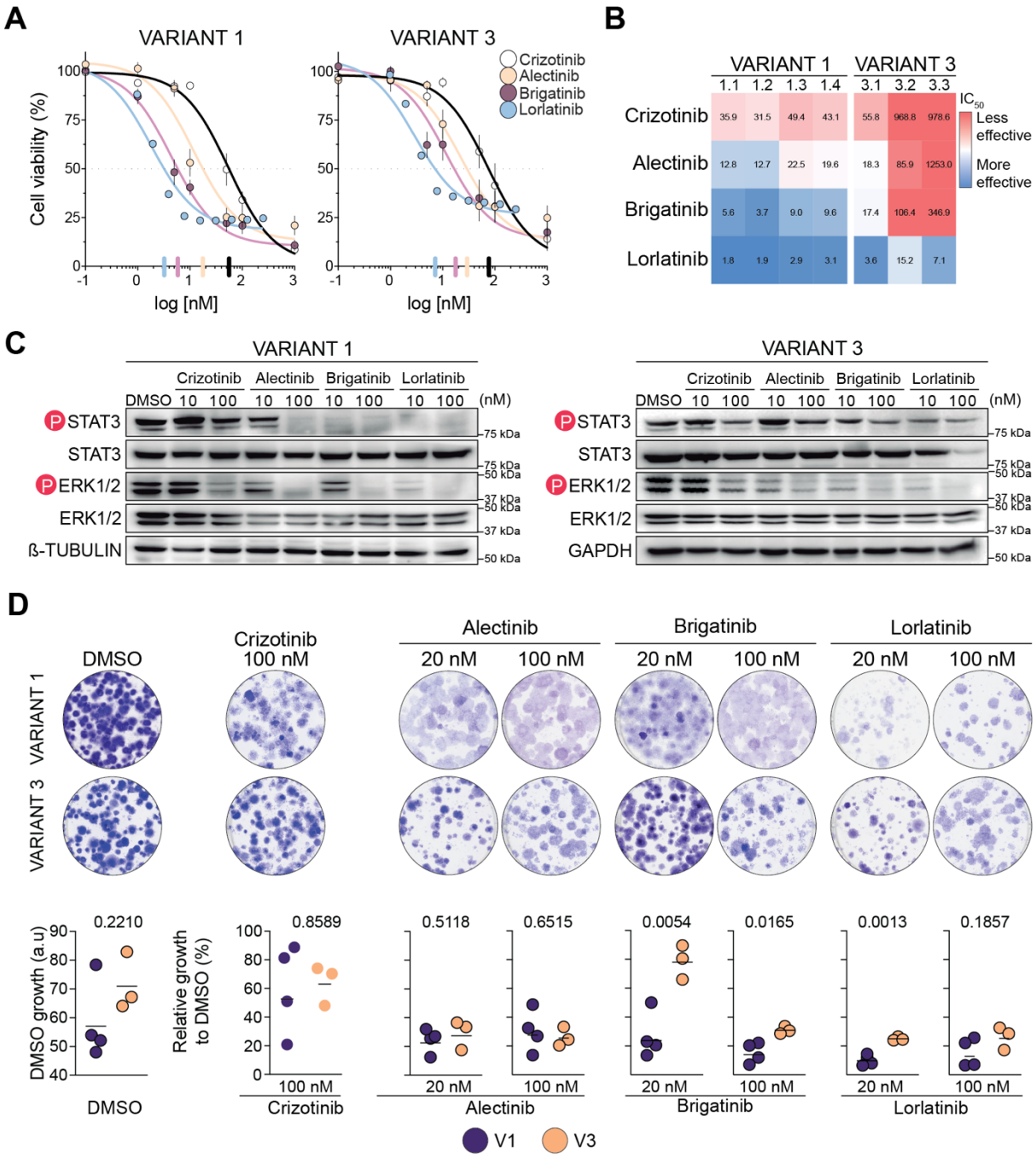


Figure 10 | *Eml4-Alk* variant 3 cells show lower sensitivity to brigatinib and lorlatinib. A) Cell viability analysis of variant 1 and variant 3 cells treated with increasing concentrations of the ALK inhibitors crizotinib, alectinib, brigatinib or lorlatinib. Vertical lines on the X-axis indicates the IC50 values. **B)** The mean of the half inhibitory concentration determined from A) and represented by cell line. **C)** Representative immunoblots from one variant 1 mTDC and one variant 3 mTDC treated with ALK inhibitors as indicated for 16 h. P means phosphorylated. **D)** Representative crystal violet results from variant 1 (purple) and variant 3 (orange) cells treated with ALK inhibitors at indicated doses for 15 days. Each dot is a cell line. Horizontal line indicates the mean. Nominal *P-values* are indicated.

Chapter 2: Identifying novel therapeutic opportunities using drug combinatorial strategies

Some of the results and figures presented in this section have been submitted in a manuscript (Diaz-Jimenez, A et al., 2024). The results and figures have been adapted accordingly.

Inhibition of the MAPK signaling pathway enhances the therapeutic response to ALK inhibitors *in vitro*

Despite the promising initial response to ALK inhibitors, almost all *EML4-ALK* lung cancer patients experience relapse (Gainor et al. 2016; Dagogo-Jack et al. 2019; Pailler et al. 2019). Similar to other TK-driven tumors, different resistance mechanisms may emerge in response to the high selective pressure exerted by TK inhibitors. These resistance mechanisms can mainly be classified as "on-target" -such as mutations in the ALK tyrosine kinase domain (~50% of ALK patients)- or "off-target" -such as bypass signaling cascades. To prevent the activation of bypass resistance mechanisms, some studies have focused on co-inhibition of the driver oncogene together with key downstream or parallel signaling cascades. In this regard, co-inhibition of different members of the EGFR signaling cascade has significantly reduced resistance development in an *EGFR*^{mut} NSCLC model (Neto et al. 2020). Therefore, we decided to investigate whether pharmacological co-inhibition of ALK and the MAPK member ERK could enhance the initial cytotoxicity of ALK inhibitors.

To evaluate the effect of ERK and ALK co-inhibition, I treated mTDCs with alectinib, brigatinib or lorlatinib, alone or in combination with the ERK-2 inhibitor VX11e (Aronov et al. 2009). Interestingly, chemical inhibition of ERK dramatically improved the response to all ALK inhibitors after two weeks of treatment (**Figure 11A,B**). In previous studies on KRAS-driven LUAD, it was observed that the simultaneous removal of both ERK-1 and ERK-2 had a more pronounced tumor-suppressive effect compared to the individual removal of either ERK-1 or ERK-2 (Blasco et al. 2011). In consequence, I decided to use the dual ERK inhibitor SCH772984, which has been proved efficient in BRAF and EGFR-driven tumor models (Morris et al. 2013). Given the initial low sensitivity to brigatinib in variant 3 mTDCs, I decided to investigate whether SCH772984 could synergize with brigatinib. To investigate potential synergy, a matrix assay was conducted using both inhibitors in escalating doses, alone and in combination. Results showed that the combination of both inhibitors had a synergistic antitumor effect, particularly in variant 3 mTDCs, with a Loewe score of over 10 (**Figure 11C**). These findings suggest that SCH772984 treatment enhances the antitumor efficacy of multiple ALK inhibitors, with variant 3 mTDCs exhibiting a particularly robust response to this combination.

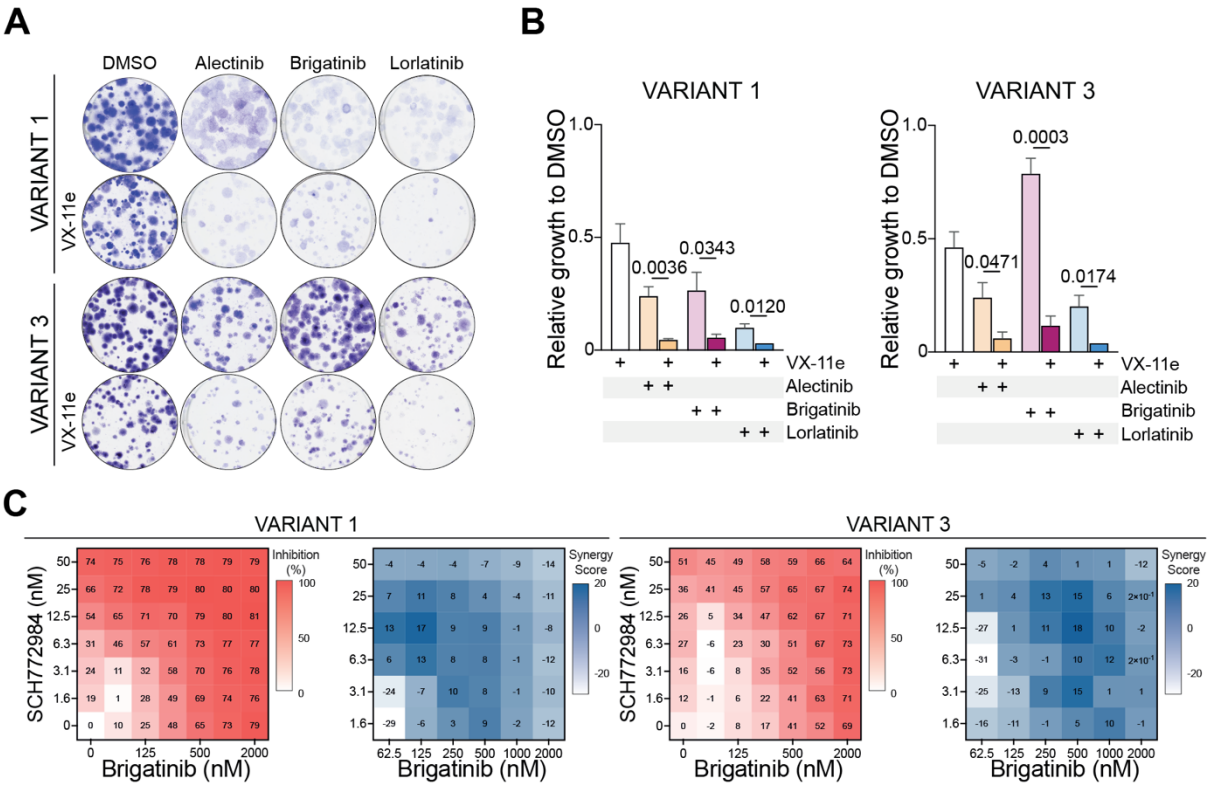


Figure 11 | Inhibition of ERK1/2 enhances ALK inhibitors activity. A) Representative colony formation assay of variant 1 and variant 3 cells treated with 20 nM of alectinib, brigatinib, or lorlatinib and 500 nM of the ERK inhibitor VX-11e, alone or in combination for 14 days. **B)** Bar plots showing the quantification of A). DMSO was used as reference. Mean ± SEM is represented. Student's t-test analysis was performed and nominal *P*-Values are shown. **C)** Drug-response matrix showing the percentage of inhibition and the synergy score of variant 1 and variant 3 cells treated as indicated. Synergy scores were calculated using the Loewe model (antagonist <-10; additive -10<x<10; synergistic >10).

Based on the *in vitro* response to the combination of brigatinib and SCH772984, we aimed to investigate the potential antitumor effects of co-inhibiting ALK and ERK-1/2 *in vivo*. Therefore, I subcutaneously injected variant 1 and variant 3 mTDCs into NMRI-*Foxn1*$^{nu/nu}$ mice (**Figure 12A**). All mTDCs successfully engrafted and gave rise to subcutaneous tumors without differences among variants (**Figure 12B**). After tumor onset (500 mm^3), mice were randomly allocated in vehicle, brigatinib or combo (brigatinib and SCH772984) arms. Brigatinib treatment led to a slight initial tumor response, resulting in extended overall survival compared to the control group (**Figure 12**). In stark contrast to our *in vitro* findings, variant 3 mTDCs did not exhibit greater resistance to brigatinib compared to variant 1 mTDCs (**Figure 12**). Additionally, the inclusion of SCH772984 failed to improve the antitumor effects of brigatinib or prolong survival in mice (**Figure 12**). This can be attributed to the insufficient inhibitory activity of SCH772984 caused by its pharmacokinetics and pharmacodynamics, as reported previously by other researchers (Neto et al. 2020).

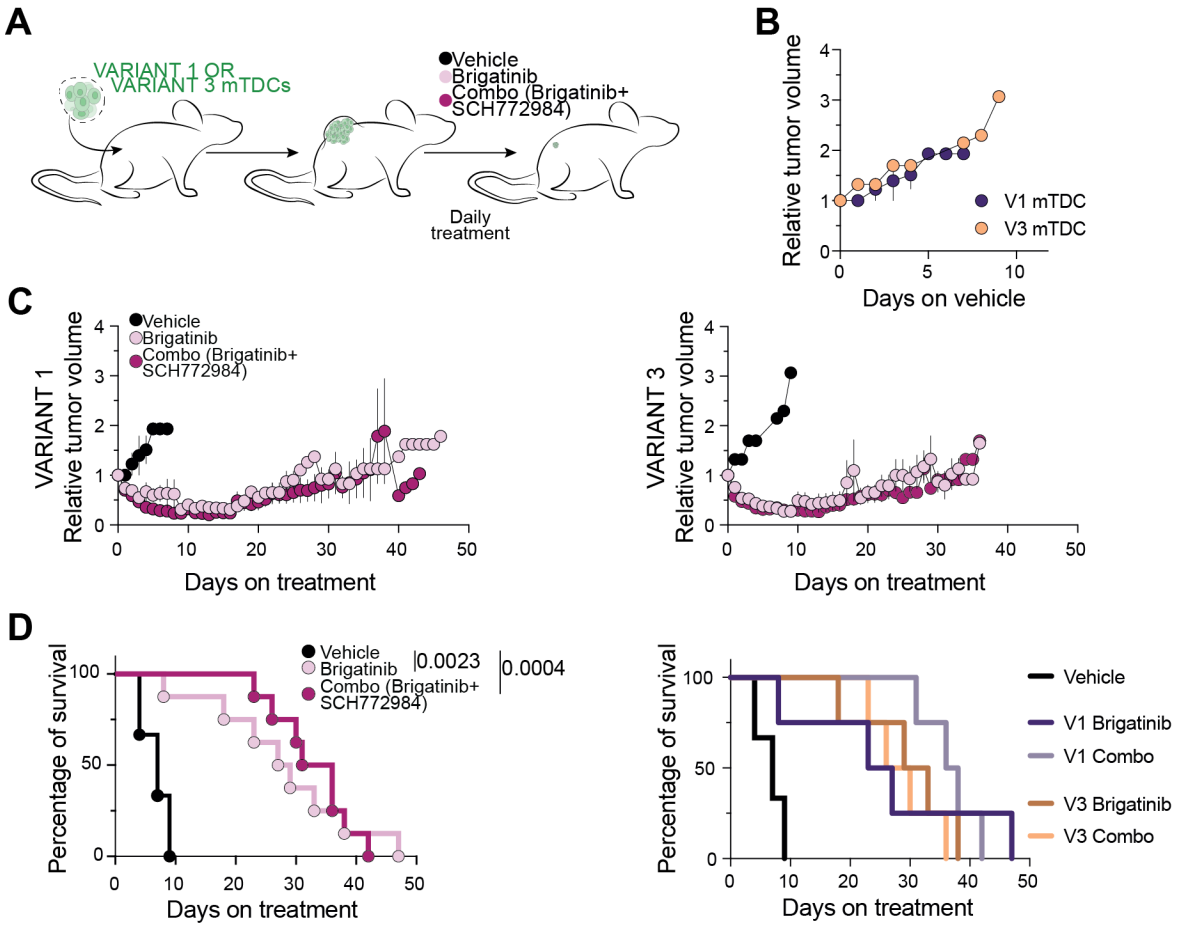


Figure 12 | Inhibition of ERK1/2 does not improve therapeutic response to brigatinib *in vivo*. **A)** Schematic of the *in vivo* experiment. Variant 1 or variant 3 cells were injected into the flank of NMRI-*Foxn1*$^{nu/nu}$ mice. Tumor bearing mice were allocated in vehicle, brigatinib or combo arms. **B)** Relative growth of subcutaneous tumors over time. **C)** Subcutaneous growth of variant 1 and variant 3 tumors. Each dot represents the mean ± SEM of six mice. **D)** Survival of variant 1 and variant 3 pooled mice by treatment. Mantel-Cox test, nominal *P-Values* are shown.

Inhibition of SRC synergize with ALK inhibitors

Building on our previous efforts, where co-inhibition of ALK and ERK-1/2 proved insufficient to halt tumorigenesis, we conducted an extensive proteomic study and literature review that led us to explore potential molecule effectors that could increase the cytotoxic activity of ALK inhibitors.

Working alongside Maria Ramos, Dr. Ursula Klingmüller and Dr. Junyan Lu, we conducted a thorough and unbiased proteomic analysis on variant 3 mTDCs subjected to brigatinib treatment over different time intervals. We focused our investigation on variant 3 mTDCs as they exhibited a higher resistance to ALK inhibitors, and in particular to brigatinib (**Figure 10A-D**). We narrowed our study down to effectors that could be pharmacologically inhibited and had treatments approved by medical agencies such as the FDA and EMA. In addition, we selected protein kinases based on their described role in ALK inhibitor-resistant tumors, focusing on those proteins that have not been previously investigated in untreated

cells. Among the effectors that can be targeted, we specifically investigated SRC, since it exhibited a substantial rise in protein levels as time progressed during brigatinib treatment (**Figure 13A**). In line, quantification of the phospho-SRC/total-SRC ratio as response to alectinib, brigatinib or lorlatinib demonstrated increased levels over time in both *Eml4-Alk* variants (**Figure 13B,C**). SRC is a non-receptor protein tyrosine kinase and protooncogene that interacts with a wide range of growth factor receptors, G protein-coupled receptors and integrins. SRC has been previously shown to promote the RAS pathway through inhibitory phosphorylation of RASA1 (Giglione et al. 2001). SRC also plays a significant role in regulating the internalization of EGFR (Donepudi and Resh 2008), and increasing its mitogenic activity. In the context of ALK, SRC has been shown to drive cell growth after ALK resistance onset (Yoshida et al. 2017). However, the relevance of SRC in untreated tumors and its biological implications remain unknown.

I then investigated the potential advantages of co-inhibiting SRC and ALK in untreated cells. To achieve this, variant 3 mTDCs that were exposed to brigatinib, dasatinib (a SRC inhibitor), or a combination of both inhibitors at various time points were analyzed (**Figure 13D**). Brigatinib caused an increase in SRC phosphorylation over the course of the experiment, an effect that was halted with the dasatinib treatment. Pharmacologic inhibition of SRC did not affect the ALK pathway, as no variation in the phosphorylation status of MEK, ERK, p90RSK, AKT, and p70 S6K was observed (**Figure 13D**). Conversely, brigatinib successfully decreased the phosphorylation of these downstream surrogates. However, after 24 hours of ALK inhibition, increased phosphorylation of p90RSK, AKT, and p70S6K was observed, indicating a potential pathway rebound (**Figure 13D**). Importantly, this rebound effect was mitigated by the combination treatment. Furthermore, a notable increase in cell apoptosis, indicated by elevated levels of cleaved-caspase 3, was evident due to the potent suppression of the ALK pathway resulting from the co-inhibition of ALK and SRC (**Figure 13D**).

Given the remarkable cytotoxic activity elicited by simultaneous inhibition of ALK and SRC, I performed a dose escalation assay to determine if the combination treatment has an additive or synergistic effect in variant 3 mTDCs. Cell proliferation was minimally impacted by monotherapies (0 to 8%). Strikingly, the combination treatment resulted in a high synergy score (>10 Loewe model score) at specific concentrations, with a 6-fold stronger inhibitory effect on variant 3 mTDCs (**Figure 13E**).

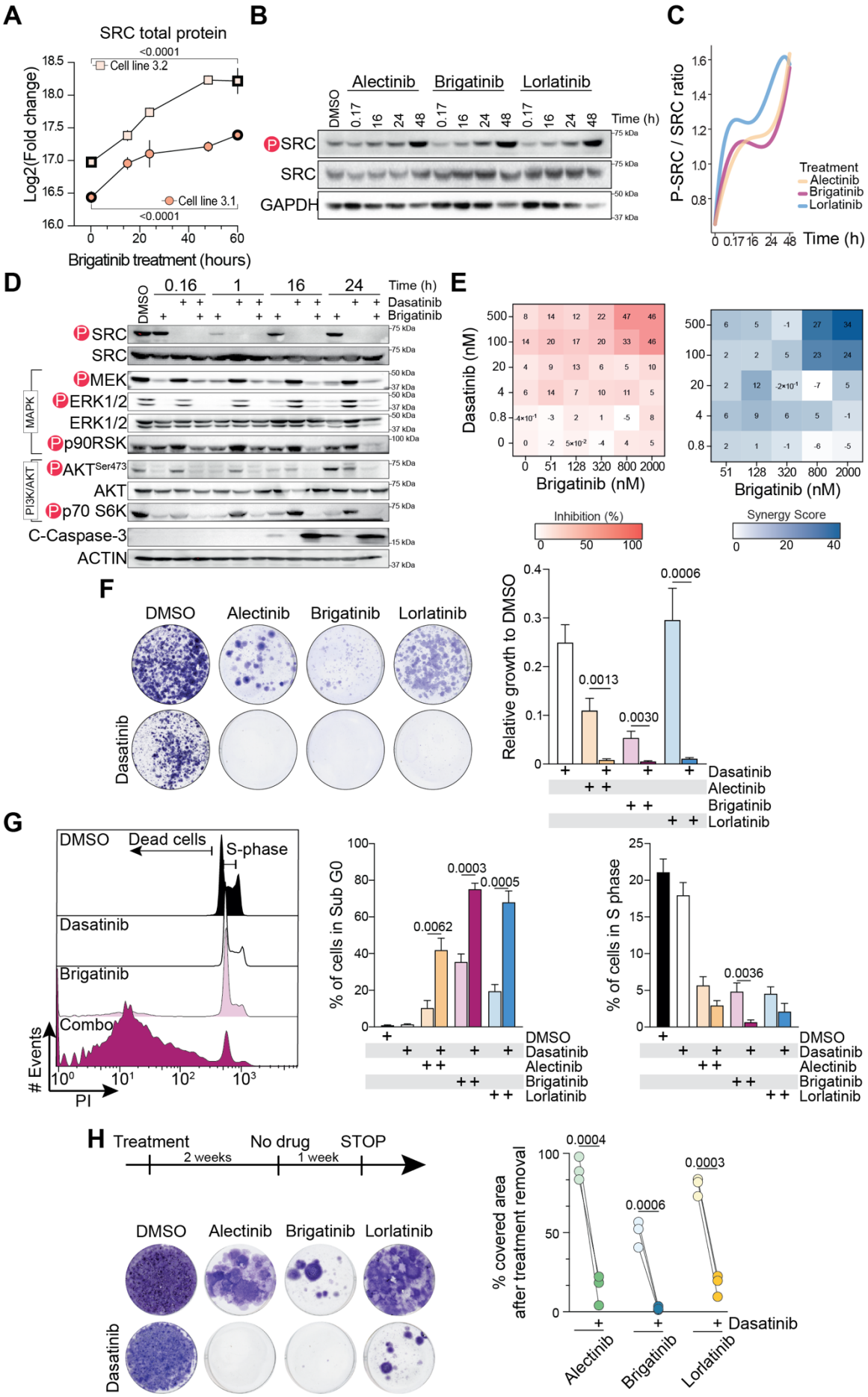

A
SRC total protein
<0.0001
Cell line 3.2
Cell line 3.1
<0.0001
Log2(Fold change)
Brigatinib treatment (hours)
B
Alectinib
Brigatinib
Lorlatinib
DMSO
Time (h)
PSRC
SRC
GAPDH
C
P-SRC / SRC ratio
Treatment
Alectinib
Brigatinib
Lorlatinib
Time (h)
D
Time (h)
Dasatinib
Brigatinib
PSRC
SRC
PMEK
PERK1/2
ERK1/2
Pp90RSK
PAKTSer473
AKT
Pp70 S6K
C-Caspase-3
ACTIN
MAPK
PI3K/AKT
E
Dasatinib (nM)
Brigatinib (nM)
Inhibition (%)
Synergy Score
F
DMSO
Alectinib
Brigatinib
Lorlatinib
Dasatinib
Relative growth to DMSO
0.0006
0.0013
0.0030
G
DMSO
Dead cells
S-phase
Dasatinib
Brigatinib
Combo
Events
PI
% of cells in Sub G0
0.0062
0.0003
0.0005
% of cells in S phase
0.0036
H
Treatment
2 weeks
No drug
1 week
STOP
% covered area after treatment removal
0.0004
0.0006
0.0003

Figure 13 | Inhibition of SRC enhances ALK inhibition response. A) Total levels of SRC protein imputed from variant 3 mTDCs treated with 1000 nM brigatinib during indicated time points. Student's t-test analysis was performed between the first and last time points and nominal *P*-Values are shown. **B)** Representative immunoblot for phospho-SRC and total-SRC from a variant 3 cell treated with 1000 nM of the indicated ALK inhibitors. Samples were collected at indicated time points. Experiment was repeated twice. **C)** Quantification of the phospho-SRC/total-SRC ratio over time from B). **D)** Representative immunoblot of SRC and surrogates of the ALK pathway from variant 3 mTDCs treated with 1000 nM brigatinib alone or in combination with 100 nM dasatinib. Samples were collected at indicated time points. The experiment was repeated twice. P-, phosphorylated. **E)** Drug response matrix showing the percentage of inhibition and the synergy score of variant 3 mTDCs treated with brigatinib, dasatinib or the combination of both inhibitors at increasing doses. Synergy scores were calculated using the Loewe model (antagonistic <-10; additive -10<x<10; synergistic >10). **F)** Representative crystal violet assay of variant 3 cells treated with 1000 nM alectinib, brigatinib or lorlatinib and 100 nM dasatinib, alone or in combination. For 14 days. Right panel shows quantification from the crystal violet assay using DMSO as the baseline growth. Mean ± SEM is represented. The experiment was performed twice using three individual variant 3 mTDCs. Mean ± SEM is represented, Student's t-test analysis was performed and nominal *P-Values* are shown. **G)** Representative cycle profile from a variant 3 mTDCs treated with 1000 nM brigatinib alone or in combination with 100 nM dasatinib for 24 hours. Percentage of cells in S-phase or SubGo-phase are shown. The experiment was performed twice using three individual variant 3 mTDCs. Mean ± SEM is represented, Student's t-test analysis was performed and nominal *P-Values* are shown. **H)** Schematic of the experimental workflow and representative crystal violet treated with 1000 nM brigatinib, 100 nM dasatinib, alone or in combination for 14 days. Cells were then grown for a week without treatment. Right panel shows the quantification relative to DMSO. Each dot is an individual cell line. Student's t-test analysis was performed and nominal *P-Values* are shown.

We examined whether co-inhibiting ALK and SRC would result in a prolonged suppression of cell proliferation. Besides, to assess whether the cytotoxic effect was brigatinib dependent, current clinically used ALK inhibitors, alectinib, brigatinib, and lorlatinib, were employed. After a 14-day treatment, the combination therapy suppressed clonogenicity significantly, independent of the ALK inhibitor used (**Figure 13F**). Moreover, analysis of cell cycle profiles 24 hours post-treatment revealed an increase of apoptosis (sub-G0) when dasatinib was used in combination with any ALK inhibitor, with brigatinib producing the most notable effect - consistent with the elevated levels of cleaved-caspase 3 observed in Figure 13D. Additionally, the combination of brigatinib and dasatinib resulted in a significant decrease in the proportion of cells undergoing proliferation (S-phase) (**Figure 13G**).

Based on our previous discoveries, which demonstrated a significant cytotoxic when employing the combination treatment, we aimed to determine the efficacy of this strategy in preventing the development of resistance. We treated variant 3 mTDCs with ALK inhibitors (alectinib, brigatinib, lorlatinib) or the SRC inhibitor, dasatinib, both alone and in combination (**Figure 13H**). After two weeks, the cells were allowed to grow without inhibitors for an additional week. Discontinuation of ALK inhibition led to regrowth of persistent cells. Notably, the combination of lorlatinib and dasatinib did not prevent cell regrowth, while alectinib or brigatinib in combination with dasatinib suppressed cell regrowth (**Figure 13H**). These findings demonstrate the potent cytotoxic effects of inhibiting ALK and SRC chemically.

Enhanced sensitivity of patient-derived ALK resistant cells to co-inhibition of ALK and SRC

We investigated the potential of simultaneous inhibition of ALK and SRC to treat *EML4-ALK* cell lines derived from human tumors. We used four different cell lines established from patients who had experienced disease progression after being treated with crizotinib, brigatinib, or alectinib (Bokhari et al. 2022; Chuang et al. 2023). As expected, alectinib, brigatinib, and lorlatinib produced negligible effects on ALK-resistant cells. Consistent with prior findings (Yoshida et al. 2017), co-inhibition of ALK and SRC notably influenced cell viability, particularly in case of brigatinib-treated cells. At the mitogenic pathway level, the combination of brigatinib and dasatinib efficiently reduced the phosphorylation levels of ALK surrogates, such as MEK, ERK-1/2, and p70 S6K. This suppressive effect counteracts brigatinib's low inhibitory activity on patient-derived cells that have progressed on ALK inhibitors.

A

	CUTO8	CUTO9	CUTO29	YU1077
***EML4-ALK* VARIANT**	V1	V1	V3	V3
TKI at time of biopsy	Crizotinib	Crizotinib	Brigatinib	Alectinib
ALK TKI resistance mutation	None	None	C1156Y	G1202R
***TP53* mutation**	G293fs*13	None	C277Y	R273C

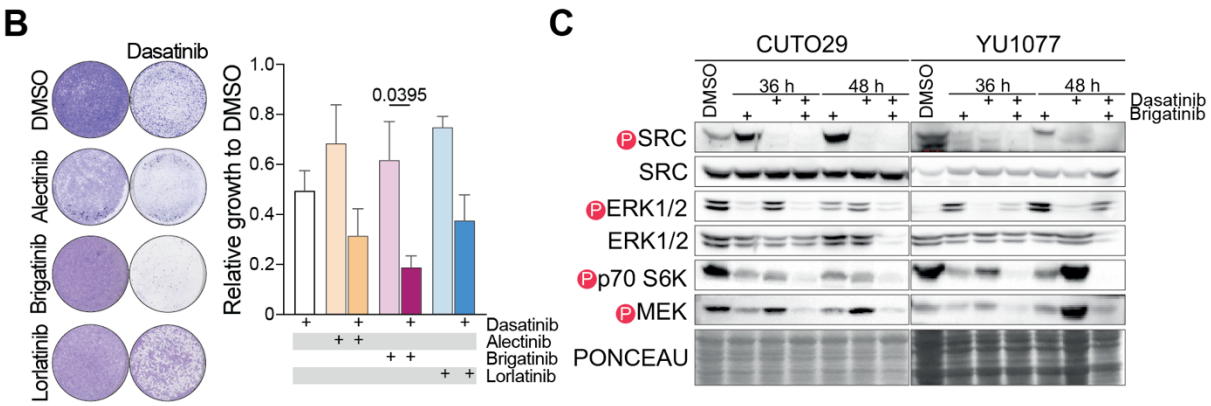


Figure 14 | *EML4-ALK* resistant patient-derived cells show increased sensitivity to co-inhibition of ALK and SRC. A) Summary of the main genomic alterations and patient treatment information from the *EML4-ALK* patient derived cells. **B)** Representative crystal violet assay of *EML4-ALK* patient derived cells (CUTO29 and YU1077) treated with 1000 nM alectinib, brigatinib or lorlatinib and 100 nM dasatinib, alone or in combination for 14 days. Right panel shows the quantification relative to DMSO. Data represent mean ± SEM. Student's t-test analysis was performed and nominal *P-Values* are shown. **C)** Western blot *EML4-ALK* patient derived cells (CUTO29 and YU1077) treated with DMSO, 1000 nM brigatinib or 100 nM dasatinib alone or in combination at indicated time points.

Inhibition of ALK and SRC impacts the (phospho)proteomic profile of *Eml4-Alk* variant 3 mTDCs

Our findings indicate that inhibition of SRC synergizes with ALK inhibitors by blocking the reactivation of downstream effectors of ALK. The mechanisms underlying the cooperative effect resulting from the inhibition of ALK and SRC remain unclear. We then sought to define the molecular characteristics that mediate the enhanced antitumor activity by ALK and SRC co-inhibition. In collaboration with Maria Ramos, Barbara Helm, Dario Lucas Frey, Ursula Klingmüller and Junyan Lu, we performed a comprehensive (phospho)proteomic analysis of variant 3 mTDCs treated with brigatinib and dasatinib, alone or in combination at different time points (**Figure 15A**). As a result, we compiled the most extensive (phospho)proteome dataset from lung cancer cells treated with various inhibitors at different time points. We detected 10,036 protein groups and 19,880 phosphorylation sites, with a false discovery ratio of 1% (**Figure 15B,C**). Notably, 65 proteins exhibited differential expression merely ten minutes after co-inhibition of ALK and SRC, whereas single treatments did not induce any alteration. This pattern was exacerbated at later time points, with an increase to over 4,374 proteins, emphasizing co-inhibition efficacy. Similarly, after 10 minutes, we detected a 10-fold increase in the number of affected phosphosites in the combinatorial treatment as compared to brigatinib (**Figure 15B,C**).

To identify any underlying patterns and connections within the (phospho)proteomic profiles of treated cells following drug treatment, I performed a PCA. Remarkably, mTDCs were observed to cluster as per their treatment and time points, where brigatinib and the combination treatment displayed clear segregation (**Figure 15D**). These data highlight the strong effect of ALK and SRC co-inhibition in disturbing the proteome of EML4-ALK-driven lung tumor cells.

I firstly evaluated the total protein levels of EML4-ALK and SRC in variant 3 mTDCs. We could not find sufficient aligned peptides of the junction region between EML4 and ALK to strictly measure the relative abundance of the fused protein (**Figure 15E**). We therefore aligned all peptides to the full length aminoacidic sequence of the ALK non-fused protein (**Figure 15E**). We found that all peptides mapped to the tyrosine kinase domain, indicating that ALK non-fused protein is probably not expressed. Strikingly, EML4-ALK and SRC proteins were found to be upregulated in response to brigatinib and dasatinib treatments. However, the interaction between these inhibitors resulted in a strong downregulation of these proteins. Importantly, we observed that in the combination treatment, EML4-ALK and SRC were slightly upregulated after 48 h (**Figure 15E**). This could be probably due to the *in vitro* half-life or stability of the inhibitors at extended time points.

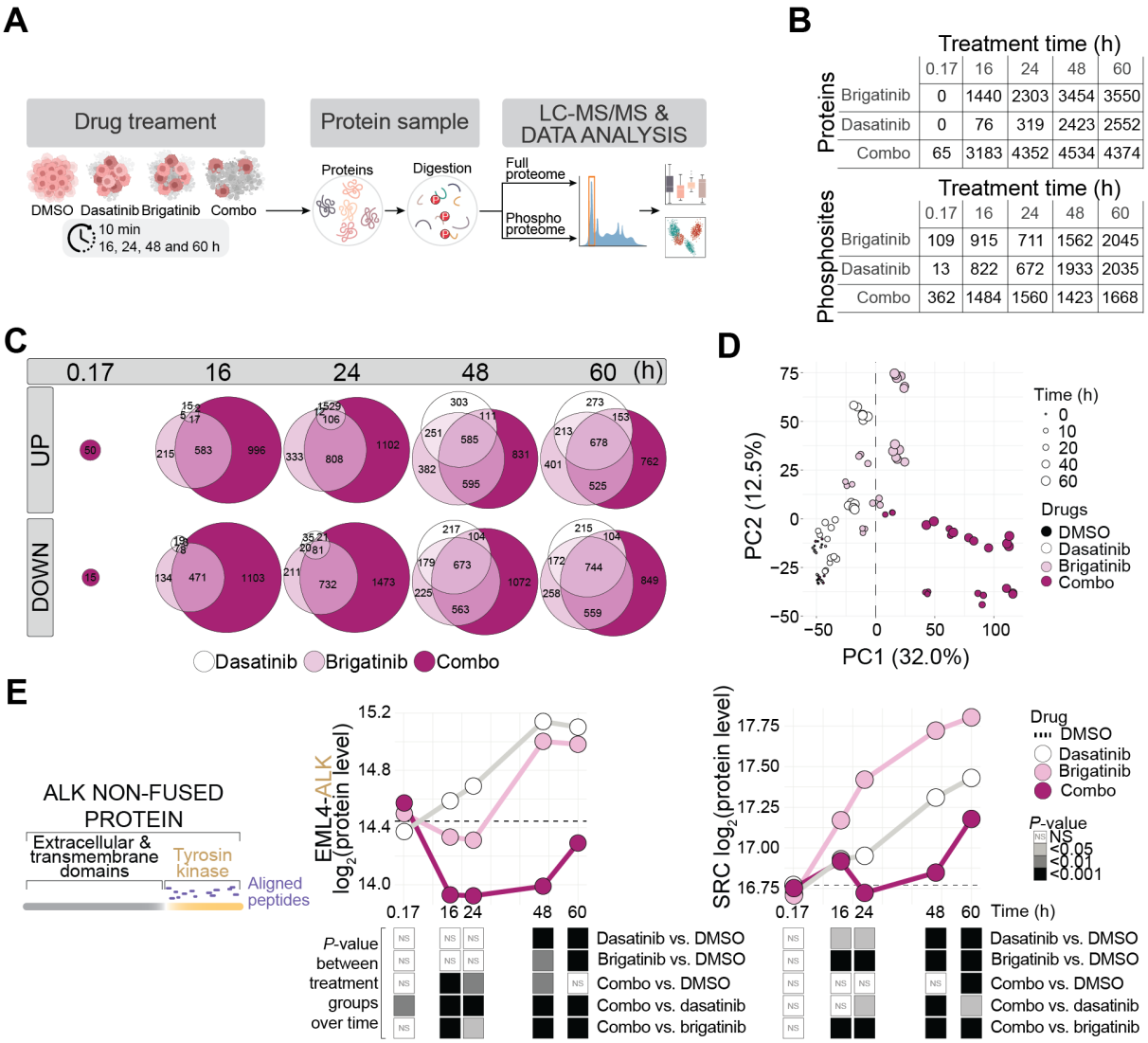


Figure 15 | Dual inhibition of ALK and SRC impacts the Eml4-Alk cell (phospho)proteome. A) Schematic of the experimental procedure. Variant 3 mTDCs were treated with 1000 nM brigatinib, 100 nM dasatinib alone or in combination for the indicated time points and subjected to LC-MS/MS. **B)** Number of differentially abundant proteins and phosphosites per time point and treatment**. C)** Euler plot of proteins and phosphosites showing common and exclusive proteins in each condition. **D)** PCA of the protein's values across the time points and drug treatments. **E)** Detected aligned EML4-ALK peptides and EML4-ALK and SRC protein quantification over time. *P*-Values were calculated by proDA package (see Methods) across all time points comparing treatment arms are shown as a grayscale underneath each graph. NS, not significant.

To understand the impact of the combination treatment on the downstream effectors of EML4-ALK, I conducted a protein level analysis by comparing it to brigatinib. The analysis revealed extensive downregulation of key proteins from the downstream signaling pathways including STATs, RAFs, and STKs (**Figure 16A**). Notably, the combination treatment resulted in lower levels of GRB2 (**Figure 16A,B**). Previous research has highlighted the essential role of GRB2 in triggering the RAS pathway in ALK-driven cells (Sampson et al. 2021; Tulpule et al. 2021). This suggests a broader effect on several major kinase proteins. Importantly, I also identified a reduction of YAP1 (Tsuji et al. 2019) and GSK3B (Shimizu et al. 2022), which had been previously implicated in ALK therapy resistance (**Figure 16B**). Additionally, the

phosphoproteomic analysis showed a similar pattern wherein there was a general downregulation of phosphosites upon co-inhibition of ALK and SRC (**Figure 16C**). The prolonged downregulation of total protein and phosphosites indicates that the combined treatment might considerably affect the status of significant signaling molecules and essential cellular processes, such as cell survival, proliferation, and apoptosis.

We aimed to gain a thorough understanding of the biological mechanisms that underlie the synergistic effect of co-inhibiting ALK and SRC. Pathway enrichment analysis demonstrated a significant impact on mRNA metabolism, mitochondria activity, signaling, cell cycle-related pathways, and oncogenic pathways (**Figure 16D**). In particular, we observed a strong alteration of RNA-associated pathways 10 minutes following treatment, which may account for the subsequent alterations in protein levels. Moreover, the analysis revealed evidence of overactive mitochondrial function and stress-inducing factors, such as reactive oxygen species and the unfolded protein response. This suggests a potential mitochondrial dysfunction and cell death triggered by an exacerbated cellular stress. Furthermore, several signaling cascades, including PI3K/AKT/mTOR, MAPK, and JAK/STAT, were observed to be downregulated (**Figure 16E**). Additionally, I observed that a large number of downregulated proteins shared motifs regulated by E2F transcription factors, providing further evidence of a significant cell cycle arrest (**Figure 16G,H**).

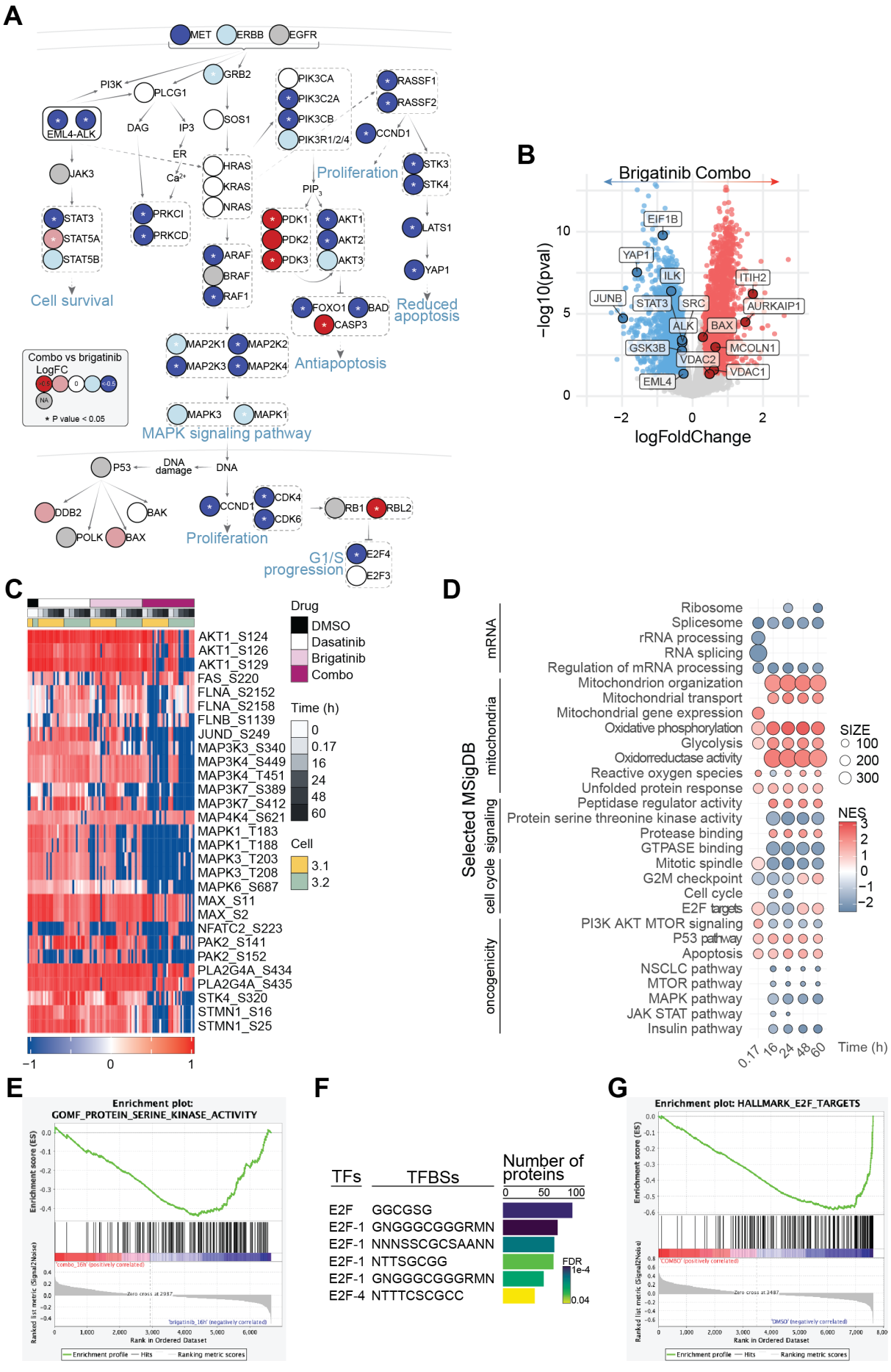

A
MET
ERBB
EGFR
PI3K
PLCG1
GRB2
PIK3CA
PIK3C2A
PIK3CB
PIK3R1/2/4
RASSF1
RASSF2
EML4-ALK
DAG
IP3
SOS1
CCND1
ER
JAK3
Ca2+
HRAS
KRAS
NRAS
Proliferation
STK3
STK4
PIP3
STAT3
STAT5A
STAT5B
PRKCI
PRKCD
PDK1
PDK2
PDK3
AKT1
AKT2
AKT3
LATS1
YAP1
ARAF
BRAF
RAF1
Cell survival
FOXO1
BAD
CASP3
Reduced apoptosis
MAP2K1
MAP2K2
MAP2K3
MAP2K4
Antiapoptosis
Combo vs brigatinib LogFC
* P value < 0.05
MAPK3
MAPK1
MAPK signaling pathway
P53
DNA damage
DNA
DDB2
BAK
POLK
BAX
CCND1
CDK4
CDK6
RB1
RBL2
Proliferation
G1/S progression
E2F4
E2F3
B
Brigatinib Combo
−log10(pval)
logFoldChange
EIF1B
YAP1
ILK
ITIH2
JUNB
STAT3
SRC
AURKAIP1
ALK
BAX
GSK3B
MCOLN1
VDAC2
VDAC1
EML4
C
Drug
DMSO
Dasatinib
Brigatinib
Combo
Time (h)
0
0.17
16
24
48
60
Cell
3.1
3.2
AKT1_S124
AKT1_S126
AKT1_S129
FAS_S220
FLNA_S2152
FLNA_S2158
FLNB_S1139
JUND_S249
MAP3K3_S340
MAP3K4_S449
MAP3K4_T451
MAP3K7_S389
MAP3K7_S412
MAP4K4_S621
MAPK1_T183
MAPK1_T188
MAPK3_T203
MAPK3_T208
MAPK6_S687
MAX_S11
MAX_S2
NFATC2_S223
PAK2_S141
PAK2_S152
PLA2G4A_S434
PLA2G4A_S435
STK4_S320
STMN1_S16
STMN1_S25
D
Selected MSigDB
mRNA
mitochondria
cell cycle signaling
oncogenicity
Ribosome
Splicesome
rRNA processing
RNA splicing
Regulation of mRNA processing
Mitochondrion organization
Mitochondrial transport
Mitochondrial gene expression
Oxidative phosphorylation
Glycolysis
Oxidorreductase activity
Reactive oxygen species
Unfolded protein response
Peptidase regulator activity
Protein serine threonine kinase activity
Protease binding
GTPASE binding
Mitotic spindle
G2M checkpoint
Cell cycle
E2F targets
PI3K AKT MTOR signaling
P53 pathway
Apoptosis
NSCLC pathway
MTOR pathway
MAPK pathway
JAK STAT pathway
Insulin pathway
SIZE
100
200
300
NES
Time (h)
E
Enrichment plot:
GOMF_PROTEIN_SERINE_KINASE_ACTIVITY
Enrichment score (ES)
Ranked list metric (Signal2Noise)
Rank in Ordered Dataset
Enrichment profile
Hits
Ranking metric scores
F
TFs
TFBSs
Number of proteins
E2F GGCGSG
E2F-1 GNGGGCGGGRMN
E2F-1 NNNSSCGCSAANN
E2F-1 NTTSGCGG
E2F-1 GNGGGCGGGRMN
E2F-4 NTTTCSCGCC
FDR
1e-4
0.04
G
Enrichment plot: HALLMARK_E2F_TARGETS
Enrichment score (ES)
Ranked list metric (Signal2Noise)
Rank in Ordered Dataset
Enrichment profile
Hits
Ranking metric scores

Figure 16 | Pharmacological co-inhibition of ALK and SRC halts ALK driven oncogenesis. A) Non-small cell lung cancer pathway adapted from KEGG (hsa05223). The circles and color code show the up- or downregulation of specific proteins comparing combo vs brigatinib at 16 hours after treatment. **B)** Volcano plot showing up- and downregulated proteins comparing combo versus brigatinib at 16 hours after treatment. Proteins are colored based on drug treatment and *P-value*. Relevant proteins are labeled. **C)** Heatmap representing the phosphosites that were down-regulated in combo compared to brigatinib treatment (*P-Value* < 0.05 and logFC < -0.15) and related to MAPK pathway (GSEA M13863, M10792). Phosphosites are colored based on phosphorylation abundance (normalized by protein abundance) linearly re-scaled from -1 (lowest abundance) to 1 (highest abundance) among samples. **D)** Differentially affected pathways (adjusted *P*-Value < 0.05) enriched in combo versus brigatinib at indicated time points. The circle size indicates the number of leading-edge proteins in the protein sets and the color indicates the normalized enrichment score (NES). **E)** Enrichment score of protein serine kinase activity-negatively regulated in combo treated cells after 16 hours of treatment. **F)** Putative E2F-transcription factor binding sites (TFBSs) from TRANSFAC database retrieved into g:GOSt (g:Profiler) downregulated in combo treated cells. **G)** Enrichment score of E2F TF activity-negatively regulated in combo treated cells after 16 hours of treatment.

Finally, I explored the impact of co-inhibiting ALK and SRC on proteins potentially associated with brigatinib resistance. To address this question, I generated brigatinib-resistant variant 3 mTDCs by subjecting them to prolonged exposure to high concentrations of brigatinib (**Figure 17A**). These resistant cells exhibited an enhanced proliferation capacity in the presence of brigatinib (**Figure 17B**).

Subsequently, I focused on proteins that were upregulated in brigatinib-resistant cells and could potentially drive brigatinib resistance (**Figure 17A**). By cross-referencing the status of these proteins with our previous dataset, I discovered that the co-inhibition of SRC and ALK kinases resulted in a profound downregulation of multiple proteins that could drive brigatinib resistance (**Figure 17B**). Overall, our (phospho)proteomic analysis provides a rationale for combining SRC and ALK inhibitors in the treatment of EML4-ALK-driven lung cancer.

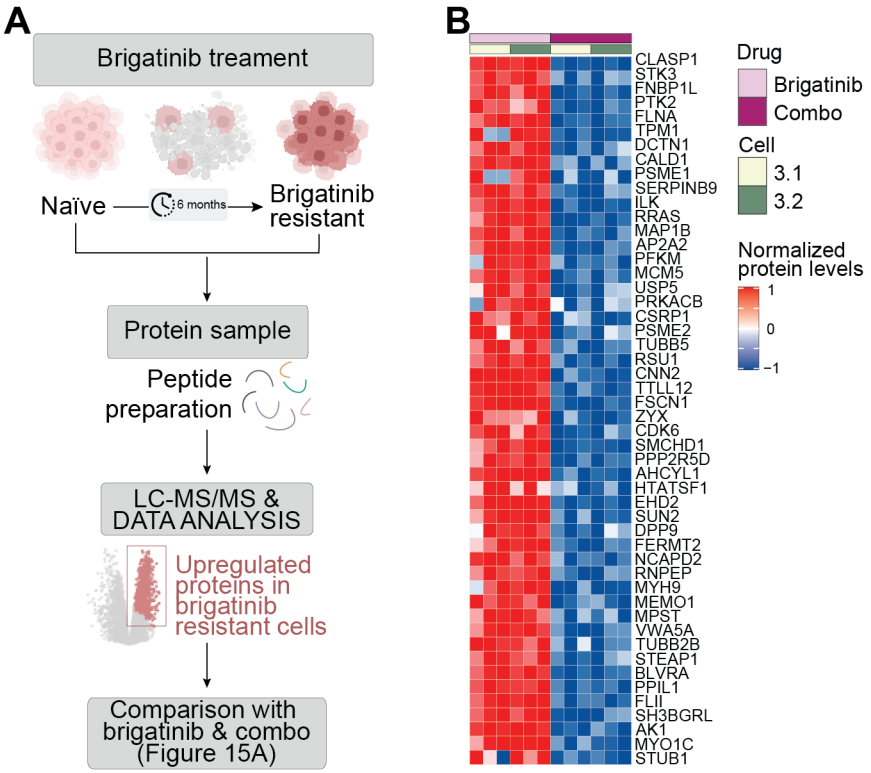


Figure 17 | Co-inhibition of ALK and SRC downregulates proteins associated with brigatinib resistance. A) Schematic of the analytical pipeline. Brigatinib-resistant cells were derived by exposing *Eml4-Alk* variant 3 cells to 2000 nM brigatinib for 6 months. The list of upregulated proteins from brigatinib-resistant cells was compared with the dataset in Figure 15A. **B)** Heatmap showing the status of upregulated proteins from brigatinib-resistant cells in brigatinib- and combo-treated cells from Figure 15A dataset. (*P-value* < 0.05). Protein abundance values were linearly rescaled from -1 (lowest abundance) to 1 (highest abundance) between samples.

Enhanced brigatinib cytotoxicity by suppressing the PI3K/AKT/mTOR axis

Maria Ramos and I collaboratively explored the underlying mechanisms driving cell death in response to co-inhibition of ALK and SRC. Our proteomic analysis uncovered increased mitochondrial activity, oxidative phosphorylation, and oxidoreductase activity. This heightened cellular activity could lead to cell death via accumulation of reactive oxygen species (ROS) (Sies and Jones 2020). Notably, ROS levels and antioxidant-related enzymes remained constant after concurrent inhibition of ALK and SRC, suggesting that antitumor activity does not rely on ROS.

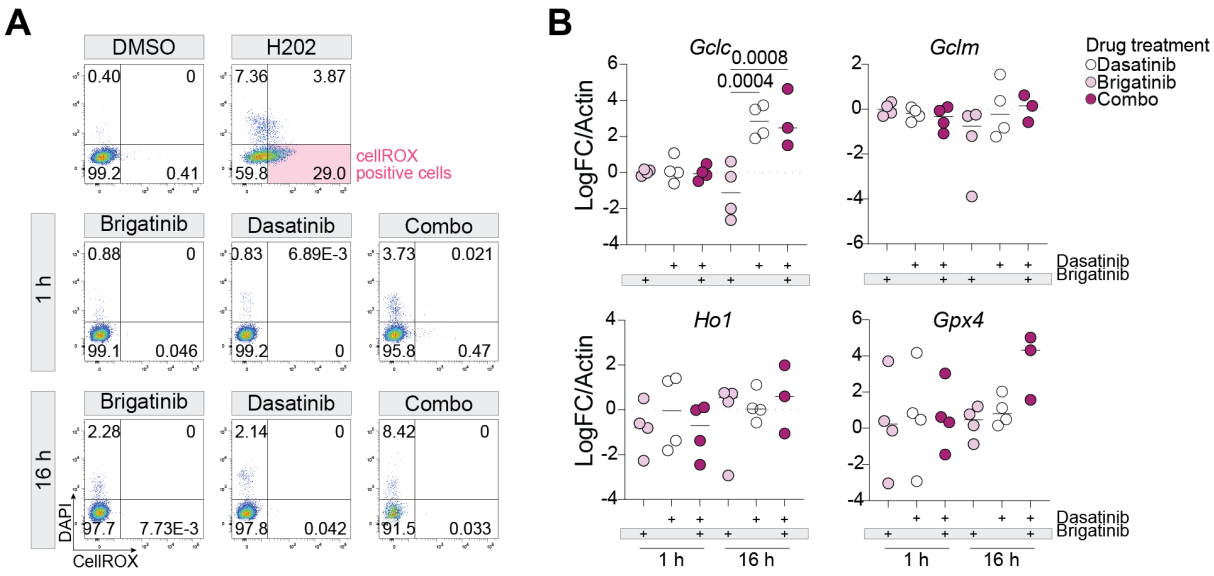


Figure 18 | Dual inhibition of ALK and SRC do not impact on ROS levels. A) Levels of ROS measured by flow cytometry (CellRox prove) in variant 3 mTDCs treated with indicated drugs. DMSO was used as vehicle and H202 was used as positive control. The experiment was performed twice using two different variant 3 mTDCs. **B)** mRNA levels of indicated ROS-related genes assessed by RT-PCR. The experiment was performed twice using two different variant 3 mTDCs.

To identify the biological process responsible for cell death resulting from ALK and SRC inhibition, Junyan Lu conducted a comprehensive analysis by integrating data on phosphorylation sites and protein abundance, and mapping kinase-substrate interactions to predict kinases that are likely impacted by the simultaneous inhibition of ALK and SRC (Yang et al. 2014; Yang et al. 2016). We found that single treatments efficiently affected GSK3B, mTOR, S6K, MAPK1, and CDK1 activity (**Figure 19A**). This effect was even more pronounced in the case of combination treatment. An in-depth assessment of the PI3K/AKT/mTOR pathway demonstrated a marked reduction in mTOR-related proteins in the combination

treatment (**Figure 19B-D**). In line, combinatorial treatment strongly reduced phosphorylation of S6K or 4EBP1 16 hours after treatment (**Figure 19E,F**). Collectively, brigatinib alone impacts MAPK as well as PI3K/AKT/mTOR pathways, whereas co-inhibition of SRC and ALK robustly restrains the PI3K/AKT/mTOR axis.

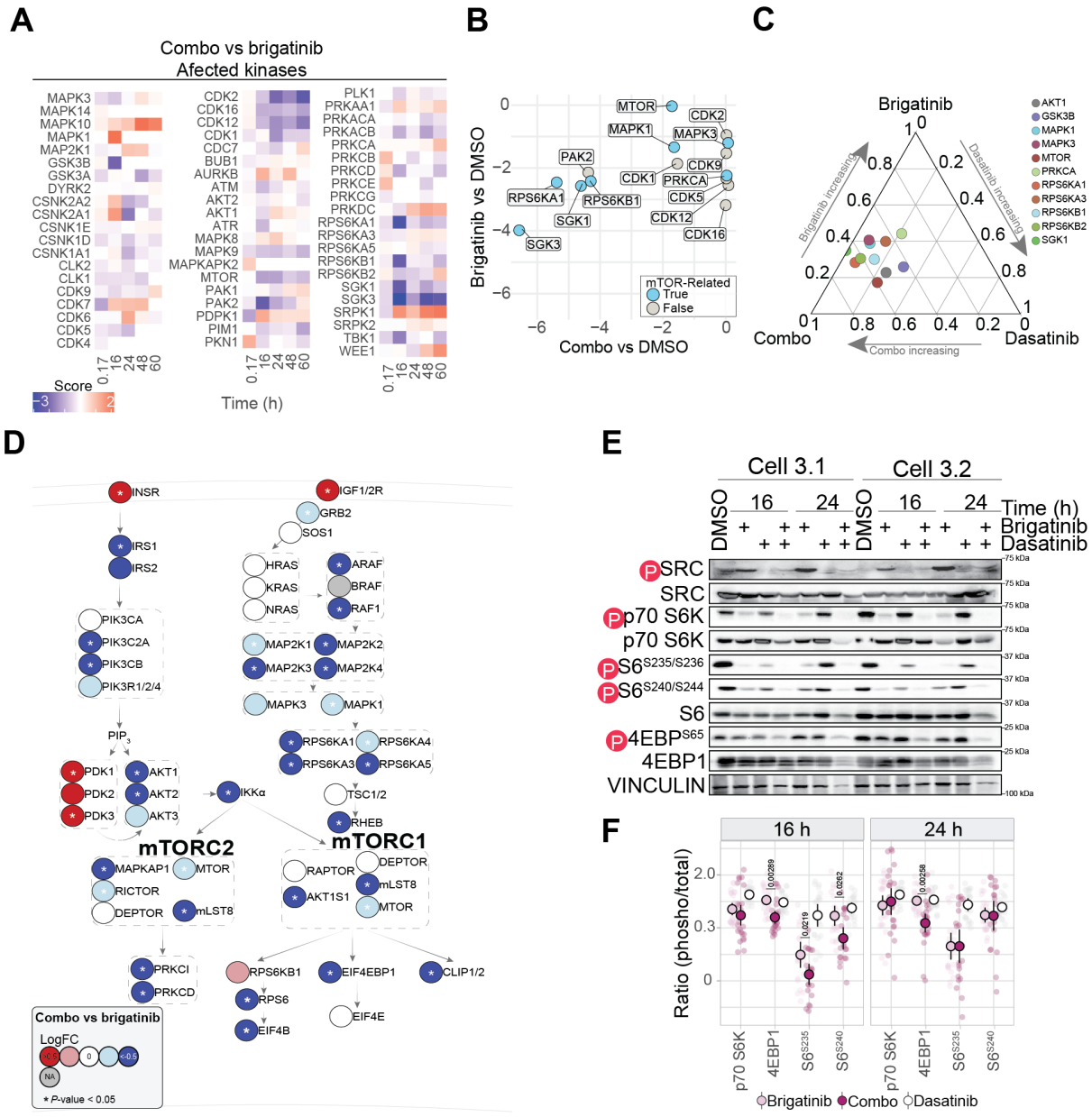


Figure 19 | Suppression of the PI3K/AKT/mTOR axis by co-inhibition of ALK and SRC. A) Predicted kinase activity over time comparing combo versus brigatinib treatment. Split into three blocks for visualization purposes; all blocks represent the same comparison. **B)** Kinase activity scores estimated by decoupleR (see Methods) for the cells treated with brigatinib or combo for 16 hours. Each point is a kinase colored based on its relation with the mTOR pathway (KEGG:04150). **C)** Ternary plot of mTOR-related proteins, comparing brigatinib, dasatinib and the combination of both versus DMSO. **D)** mTOR pathway adapted from KEGG (map04150). The circles show the up- or downregulation of specific proteins. **E)** Representative Western blot of mTOR-related proteins upon brigatinib and dasatinib treatment alone or in combination for 12 and 24 hours. The experiment was performed six times with two V3 mTDCs. **F)** Quantification of the ratio of phospho/total of mTOR-related proteins by Western blot. The experiment was repeated six times with two different cell lines. Points show the mean and CI. Student's t-test was performed and nominal *P-Values* are shown.

Based on our previous findings, suppression of the PI3K/AKT/mTOR axis would increase the cytotoxicity of brigatinib. Treatment of variant 3 mTDCs with rapamycin did not effectively reduce cell growth alone, probably due to its sole activity on mTORC1 (**Figure 20A**). Specific co-inhibition of mTORC1 and mTORC2 by Torin1 reduced cell growth to a similar extent as the simultaneous inhibition of ALK and SRC (**Figure 20A**).

We then investigated whether mTOR inhibition could be synergistic with brigatinib. To assess the impact of mTOR pathway inhibition while maintaining viable cell populations for further analysis, we deliberately employed concentrations of rapamycin and Torin1 that were 1000-fold lower than those typically used (**Figure 20B**). This reduced the extent of mTOR pathway suppression, resulting in increased cell survival. Consistent with our previous observations, inhibition of ALK and SRC strongly suppressed cell growth. Partial inhibition of mTOR in combination with brigatinib resulted in a similar suppression (**Figure 20B**). Taken together, our in-depth (phospho)proteomic analysis and *in vitro* studies suggest that variant 3 mTDCs may overcome ALK inhibition through the PI3K/AKT/mTOR axis, which can be effectively mitigated by the use of SRC or mTORC1/C2 inhibitors.

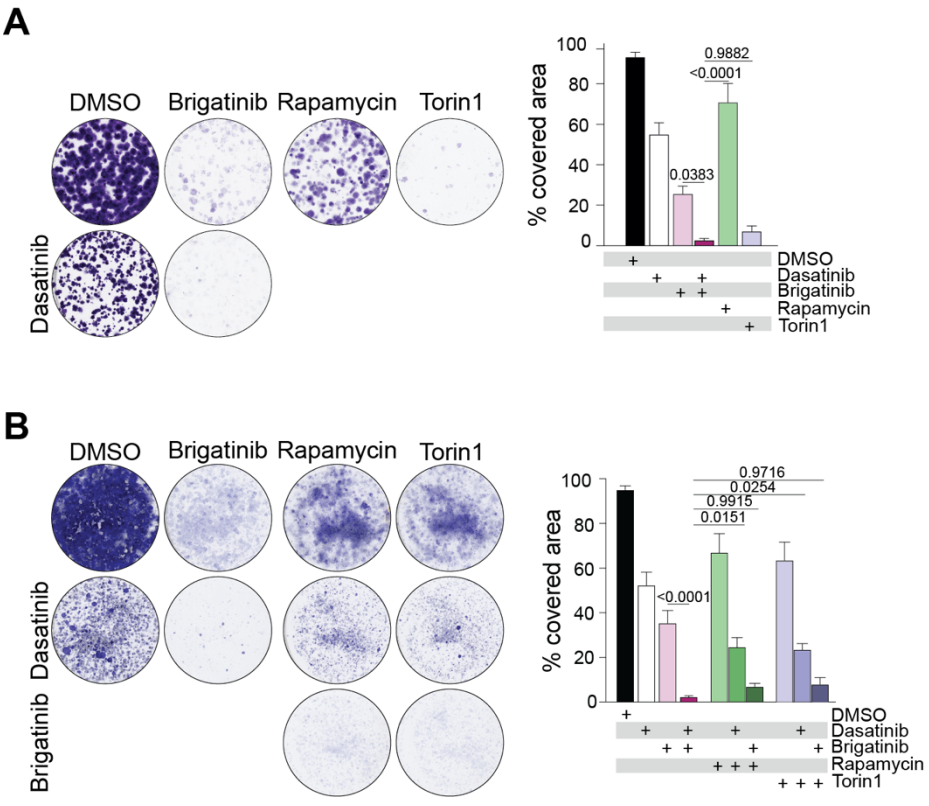


Figure 20 | Inhibition of mTOR sensitizes EML4-ALK-driven cells to ALK inhibitors. A) Representative crystal violet staining and corresponding quantification of V3 cells treated with brigatinib, dasatinib, rapamycin, or torin 1 alone or in combination for 10 days (left) and quantification of it (right). Data are shown as means ± SEM. Nominal P-Values are shown (One-way ANOVA with post-hoc Tukey multiple comparison test). **B)** Colony formation assay of V3 mTDCs treated with dasatinib, brigatinib, rapamycin or torin 1 (left) and quantification (right). Data are shown as means ± SEM. Nominal P-Values are shown (One-way ANOVA with post-hoc Tukey multiple comparison test.

Pharmacological inhibition of ALK and SRC reduced EML4-ALK V3-driven tumorigenesis *in vivo*

In collaboration with Maria Ramos, we evaluated the efficacy of concurrent ALK and SRC inhibition *in vivo* (**Figure 21A**). For this purpose, we chose the SRC inhibitor dasatinib instead of the mTORC1/C2 inhibitor Torin1. This choice was motivated by the observation that not only mTOR, but also several other key kinases were downregulated during brigatinib and dasatinib treatment. Importantly, the broader mechanism of action of dasatinib, targeting kinases upstream of the PI3K/AKT/mTOR axis, was considered a strategic approach to mitigate potential bypass mechanisms.

We firstly induced allografts by subcutaneously injecting variant 3 mTDCs into NMRI-*Foxn1*$^{nu/nu}$ mice. Once tumors reached 0.5 mm^3, mice were daily treated with vehicle, brigatinib, dasatinib, or the combination of both inhibitors for 21 days (**Figure 21A**). Single treatment with dasatinib had minimal effect on the growth of subcutaneous tumors (**Figure 21B,C**). Similar to our previous *in vivo* treatment, brigatinib treatment resulted in a transient and stable response with a slow tumor growth (**Figure 21B-D**). Notably, pharmacological inhibition of ALK and SRC resulted in a rapid tumor shrinkage followed by a stable disease during the time of the treatment (**Figure 21B-D**). I then performed immunohistochemistry analysis of tumor sections and revealed that ALK and SRC co-inhibition enhanced cell death (cleaved caspase 3) and mitigated cell proliferation (phospho-histone3). In contrast, refractory brigatinib-treated tumors showed no differences in cleaved-caspase 3 or phospho-histone 3 levels (**Figure 21E-G**).

Collectively, these results indicate that pharmacological co-inhibition of ALK and SRC has potent *in vivo* antitumor activity, enhancing the benefits of brigatinib as a single agent. Furthermore, our extensive *in vitro* pharmacological study and our comprehensive (phospho)proteomic analyses provide a rationale for using combined ALK and SRC inhibitors in the management of *EML4-ALK* untreated patients.

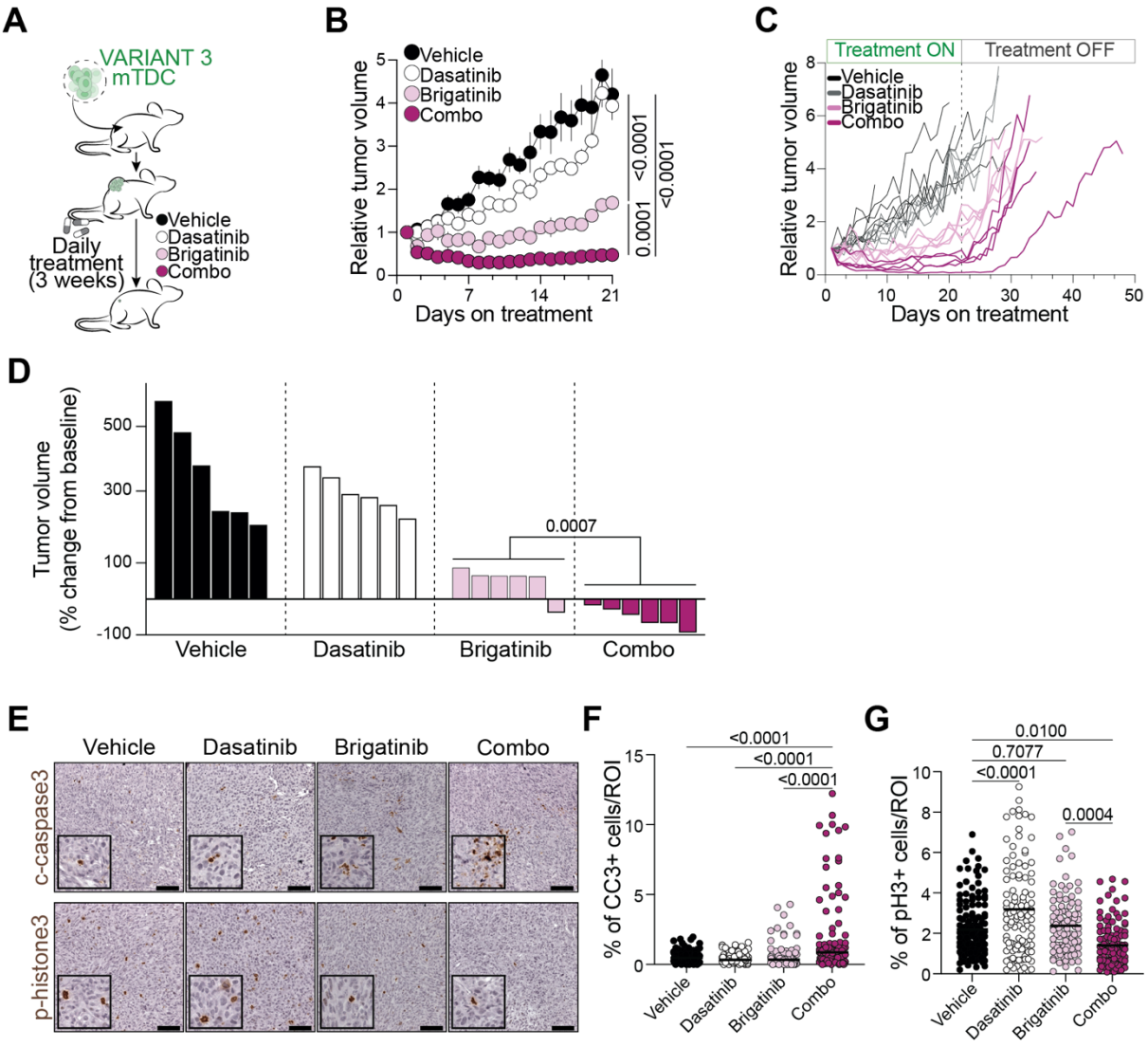


Figure 21 | Co-inhibition of ALK and SRC halts tumor growth. A) V3 subcutaneous tumors in nude mice following treatment with vehicle, brigatinib, dasatinib, or a combination of both inhibitors for 21 days. **B)** Relative tumor volume from treated mice. Points and connecting lines show the mean ± SEM from six mice per group. Two-way ANOVA followed by Tukey test was done*, P-Values* of significant comparisons are shown. **C)** Individual tumor volume over time. Each line is a tumor. Dashed line indicates the end of the treatment. **D)** Percentage of change from baseline of individual V3 mTDCs tumors grown in nude mice treated as indicated. Student's t-test analysis was performed and nominal *P-Values* are shown. **E)** Representative immunohistochemistry for cleaved-caspase3 and phospho-histone 3 from tumors treated with the indicated inhibitors. **F, G)** Percentage of cleaved-caspase3 and phospho-histone 3 from E. Each dot is a ROI (n=20 ROIs per mouse). Tukey's multiple comparisons test, P-Values of significant comparisons are shown.

Chapter 3: Investigate the role of key tumor suppressor genes in EML4-ALK-driven lung tumorigenesis

Some of the results and figures presented in this chapter have been submitted in a manuscript (Diaz-Jimenez, A et al., 2024). The results and figures have been adapted accordingly.

Extensive cancer genomic and biological studies have identified an array of genomic alterations that modulate the growth of neoplastic lesions by altering tumor suppressor gene activity (Alberts, B. 2020). Within this landscape of complex genetic alterations, alterations in tumor suppressor genes can directly impact the tumor fitness and therapeutic response (Alberts, B. 2020). However, besides our understanding of complex tumor genotypes, the practical interpretation of these findings in the context of EML4-ALK-driven lung cancer remains challenging due to the scarcity of available sequenced samples.

In 2018, two independent groups highlighted the association between *TP53* and a poor prognosis in EML4-ALK-positive patients. These analyses suggested that *TP53* mutations are associated with reduced responsiveness to ALK inhibitors and worsened prognosis (Kron et al. 2018; Christopoulos et al. 2018). In addition to these retrospective studies, no other study has focused on investigating the clinical relevance of co-occurring tumor suppressor gene mutations in EML4-ALK-positive patients.

Preclinical modeling of EML4-ALK-driven LUADs using autochthonous *in vivo* models has advanced our understanding of this disease. Current models rely on the conditional overexpression of the human EML4-ALK V1 transgene or adenoviral-mediated CRISPR/Cas9-driven generation of *Eml4-Alk* V1 rearrangement (Soda et al. 2008; Blasco et al. 2014; Maddalo et al. 2014). However, although clinically relevant, these mouse models have not been exploited to understand the impact of tumor suppressor pathways in EML4-ALK-driven lung tumorigenesis.

In order to investigate the role of multiple tumor suppressor genes and anticipate their clinical implications, I generated a novel mouse model of V1 and V3 EML4-ALK-driven LUAD. By coupling CRISPR/Cas9 gene editing and tumor barcoding, we uncover the genetic interactions of 29 tumor suppressor genes and demonstrated that V1 and V3 behave like different oncogenes.

A novel EML4-ALK-driven mouse model to investigate co-occurring genomic alterations

Integrating vectors, such as transposon or lentivirus, allow for high throughput and quantitative functional multiplexed genomics analysis *in vivo*. Contrary to our previously used adenoviral vectors, lentiviruses stably integrate into the transduced cell. In addition, mouse models of lung cancer have enabled barcode-based clonal and multiplexed analyses of the impact of different CRIPSR/Cas9-generated tumor genotypes in parallel (Cai et al. 2021; Foggetti et al. 2021; Lee et al. 2023).

To investigate the impact of several genomic alterations in a multiplexed manner, I firstly designed lentiviral vectors to induce EML4-ALK V1- and V3-driven LUAD in autochthonous mouse models. These lentiviral vectors encode for Cre-recombinase and, similarly to our adenoviral vectors (**Figure 6**), sgRNAs targeting the *Eml4* intron 14 (V1) or intron 6 (V3) and the *Alk* intron 19 (**Figure 22**) generate the fusion gene.

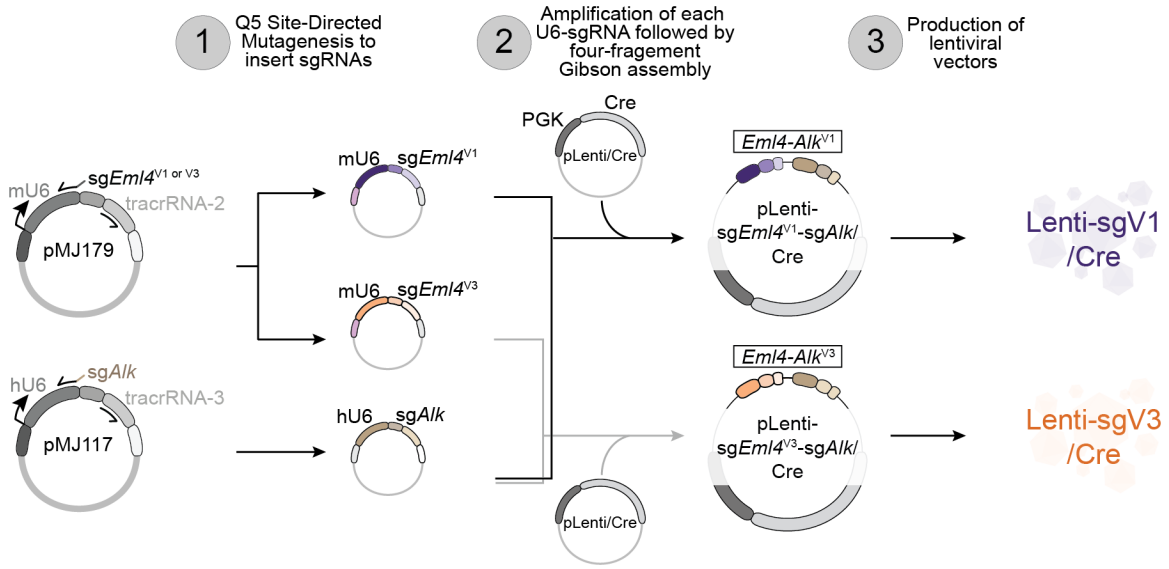


Figure 22 | Schematic of the cloning strategy. Individual sgRNAs (sg*Eml4*^{V1}, sg*Eml4*^{V3} and sg*Alk*) were cloned individually into U6 donor plasmids. Lenti-sgEgfp-sgV1/Cre and Lenti-sgEgfp-sgV3/Cre were then generated by Gibson assembly, combining U6 sgRNA plasmids with a pLenti/Cre donor plasmid.

Intratracheal delivery of these lentiviral vectors (V1: Lenti-sgV1/Cre and V3: Lenti-sgV3/Cre) into *R26*$^{LSL\text{-}Cas9\text{-}EGFP}$ mice (hereafter, *Cas9-EGFP* (Platt et al. 2014)) allows Cas9-induction by Cre-recombinase and expression of sg*Eml4* and sg*Alk* to create Cas9-mediated double-stranded DNA breaks, chromosomal inversion, and expression of the corresponding *Eml4-Alk* fusion oncogenes (**Figure 6, 23**).

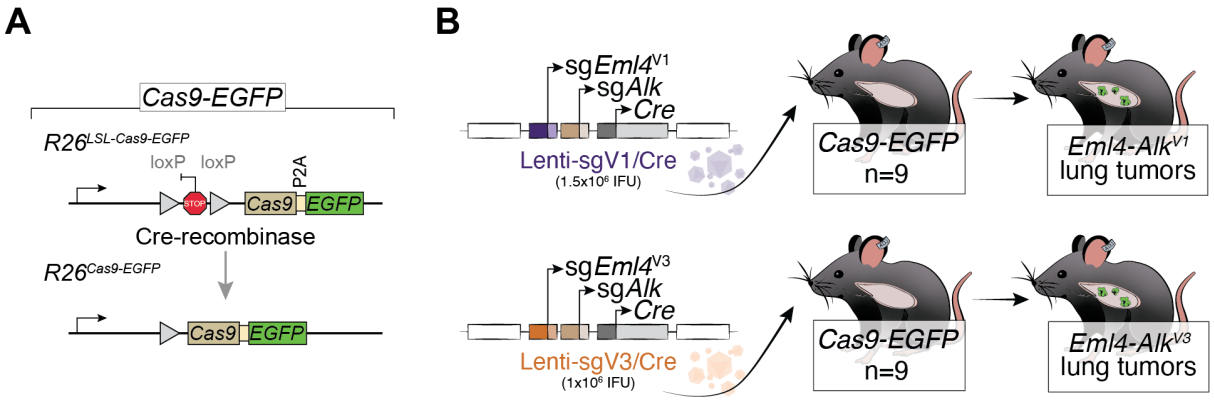


Figure 23 | Mouse model and lentiviral vectors. A) Diagram of the *R26*$^{LSL\text{-}Cas9\text{-}EGFP}$ mice (*Cas9-EGFP*) before and after Cre-mediated recombination. **B)** Schematic of the experimental pipeline. V1 and V3 lung tumors were initiated through intratracheal instillation of Lenti-sgV1/Cre and Lenti-sgV3/Cre vectors into *R26*$^{LSL\text{-}Cas9\text{-}EGFP/+}$ mice. Viral dose and number of mice is specified.

Lenti-sgV1/Cre and Lenti-sgV3/Cre vectors had 100% penetrance as all *Cas9-EGFP* mice developed lung tumors after intratracheal lentiviral delivery. However, V3-tumor bearing *Cas9-EGFP* mice had a significantly shorter survival (20 weeks) as compared to V1-transduced mice (46 weeks) (**Figure 24A**). Macroscopic examination revealed that although all mice died due to high tumor burden (**Figure 24B,C**), V3 tumors were significantly larger than V1-induced LUADs (**Figure 24D**) with a similar tumor number (**Figure 24E**). Histological characterization revealed that V1 and V3 tumors exhibited features similar to human EML4-ALK-driven lung cancers, ranging from adenomas to high-grade lung adenocarcinomas (**Figure 24F**). In addition, these tumors expressed the lung lineage-defining transcription factor NKX2-1/TTF1 and the surfactant protein C (proSP-C) (**Figure 24F**). To confirm the presence of the corresponding *Eml4-Alk* rearrangement, I sequenced the genomic DNA from sorted EGFP^{positive} tumor cells from V1 and V3 transduced mice, and confirmed the expected paracentric inversion (**Figure 24G**).

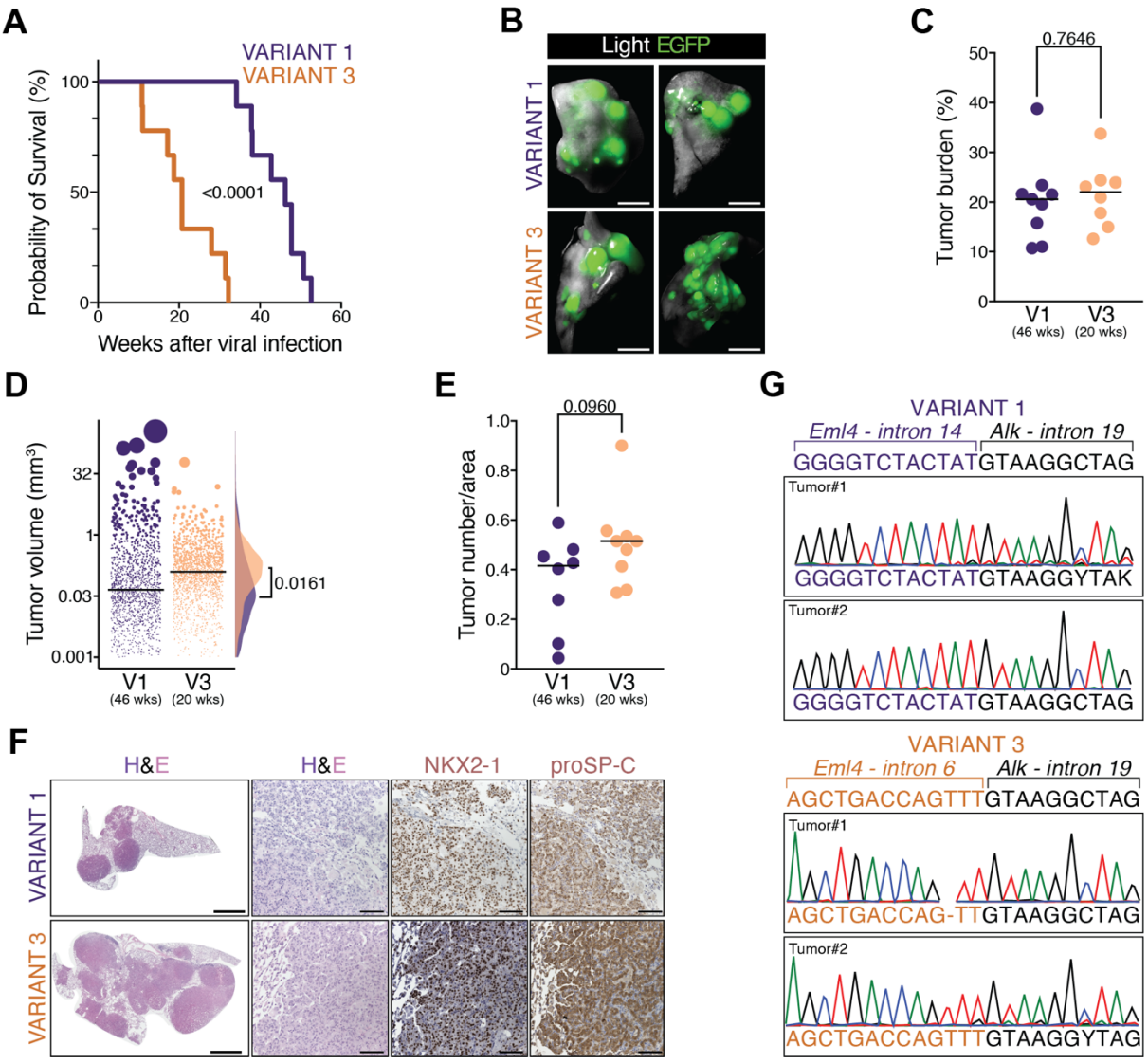


Figure 24 | Lentiviral CRISPR/Cas9-mediated initiation of EML4-ALK V1 and V3-driven lung tumors. A) Overall survival of Lenti-sgV1/Cre and Lenti-sgV3/Cre transduced *R26*$^{LSL\text{-}Cas9\text{-}EGFP/+}$ mice. Median survival of 46 weeks for V1 (n=9) and 20 weeks for V3 (n=9). A Log-rank (Mantel-Cox) test shows a p-value of <0.0001. **B)** Light and fluorescent images from EGFP^{positive} V1 and V3 lung tumors. Scales bars are 2 mm. **C)** Percentage of tumor burden (Tumor area/Total area, %) from end-point V1 and V3 mice. Each dot is a mouse. Unpaired t-test, nominal *P-value* is shown. **D)** Tumor volume (mm^3) from individual V1 and V3 lung tumors. The marginal plot represents the distribution of the V1 and V3 tumors along the Y-axis (tumor volume). Unpaired t-test, nominal *P-value* is shown. Each dot is a tumor. **E)** Tumor number from end-point V1 and V3 mice. Each dot is a mouse. Unpaired t-test, nominal *P-value* is shown. **F)** Representative H&E and immunohistochemistry for NKX2-1 and proSP-C of lung sections of end-point V1 and V3 mice. Scale bars are 1 mm, 100 µm, and 10 µm. **G)** Sanger sequencing chromatograms from genomic DNA of V1 and V3 individual tumors, showing the correct *Eml4-Alk* rearrangement.

These results highlighted the ability to induce *Eml4-Alk* V1 and V3 rearrangements using lentiviral vectors and somatic CRISPR/Cas9-mediated genome editing in autochthonous mouse models.

Generation of a triple sgRNA lentiviral vector

Traditional mouse models that inactivate specific genes using the Cre/loxP-based system are labor-intensive and require a large number of experimental animals to study

multiple tumor genotypes in parallel. In contrast, CRISPR-Cas9 and multiplexed studies allow multiple genes to be targeted simultaneously, significantly reducing the labor and time involved in the gene editing process (Kersten et al. 2017; Winters et al. 2018).

The inactivation of any gene of interest in parallel with the induction of the *Eml4-Alk* chromosomal rearrangement requires the addition of a third sgRNA to the original Lenti-sgV1/Cre and Lenti-sgV3/Cre vectors. During the generation of these vectors, we considered the chance for template switching between the U6 promoters and tracrRNAs. We employed U6 promoters from different species (bovine, murine and human), modified tracrRNAs, and ordered the sgRNAs to minimize recombination and lentiviral template switching (**Figure 25A** and **Methods**). Thereby, we decided to follow the following structure bU6-sg*TSG*-mU6-sg*Eml4*-hU6-sg*Alk*. Within this configuration, template switching would remove either sg*Eml4* or sg*Alk*, resulting in a non-oncogenic lentiviral vector because the *Eml4-Alk* inversion cannot be initiated. Possible template switching events could result in the following plasmid alterations (**Figure 25B**):

- Template switching among tracrRNA sequences:
  - *tracrRNA#1 and tracrRNA#2:* would remove sg*Eml4*, preventing the *Eml4-Alk* inversion and tumor development.
  - *tracrRNA#2 and tracrRNA#3*: would remove sg*Alk*, preventing the *Eml4-Alk* inversion and tumor development.
  - *tracrRNA#1 and tracrRNA#3*: would remove sg*Eml4* and sg*Alk*, preventing the *Eml4-Alk* inversion and tumor development.
- Template switching among U6-protmoter sequences:
  - U6#1 and U6#2: would remove sg*TSG*, allowing for the potential occurrence of *Eml4-Alk* inversion and tumor development, albeit with the inclusion of sgID for identifying sg*TSG*.
  - U6#2 and U6#3: would remove sg*Eml4*, preventing the *Eml4-Alk* inversion and tumor development.
  - U6#1 and U6#3: would remove sg*TSG* and sg*Eml4*, preventing the *Eml4-Alk* inversion and tumor development.

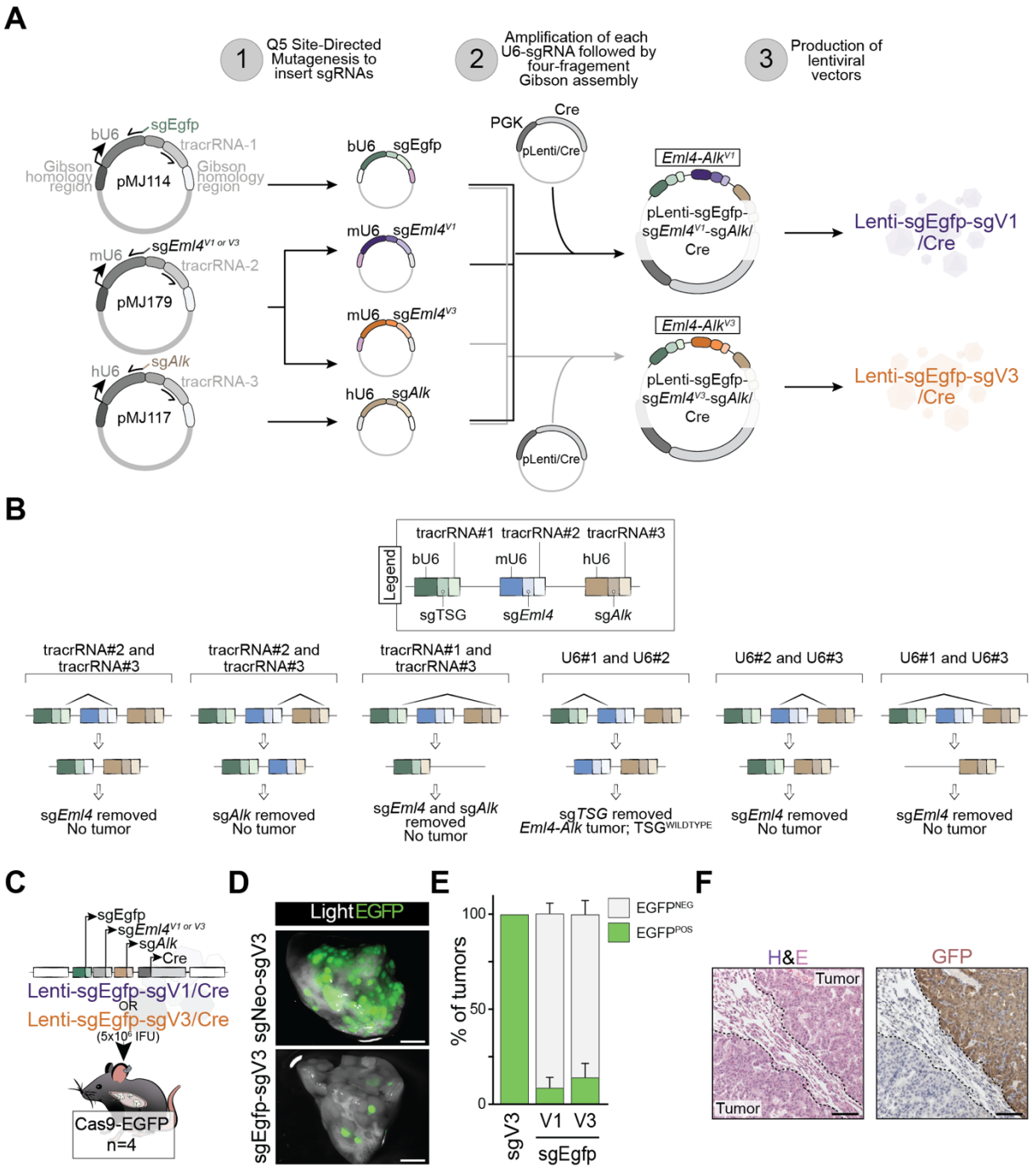


Figure 25 | Triple sgRNA lentiviral vector efficiently targets specific genes and induce the *Eml4-Alk* rearrangement. A) Schematic of the cloning strategy, donor plasmids, U6 promoters, sgRNAs, tracrRNAs, and gibson homology regions are highlighted. **B)** Outcomes of possible template switching events. U6 promoters, sgRNAs, and tracrRNAs regions are annotated. **C)** Schematic of Lenti-sgEgfp-sgV1/Cre and Lenti-sgEgfp-sgV3/Cre vectors intratracheally delivered into homozygous *Cas9-EGFP* mice *Rosa26*$^{LSL\text{-}Cas9\text{-}EGFP/LSL\text{-}Cas9\text{-}EGFP}$). **D)** Fluorescent images from V3-tumor bearing mice induced with Lenti-sgNeo-sgV3/Cre (only Eml4-Alk) or Lenti-sgEgfp-sgV3/Cre. Scale bars are 2 mm. **E)** Quantification of EGFP^{positive} and EGFP^{negative} tumors. **F**) Representative H&E and GFP immunohistochemistry showing one EGFP^{negative} and one EGFP^{positive} tumor. Scale bars 100 μm.

To quantify the functionality of our triple sgRNA lentiviral vector and to calculate how many tumors can escape biallelic inactivation of tumor suppressor genes, I transduced homozygous *Cas9-EGFP* mice (homozygous for the *Rosa26*$^{LSL\text{-}Cas9\text{-}EGFP/LSL\text{-}Cas9\text{-}EGFP}$ allele) with

a triple sgRNA vector that also targets the EGFP gene (Lenti-sgEgfp-sgV1/Cre and Lenti-sgEgfp-sgV3/Cre) (**Figure 25C,D**). As control, Lenti-sgNeo-sgV1/Cre and Lenti-sgNeo-sgV3/Cre were used. sgNeo targeted a "safe" region within the mouse genome (the Neomycin resistance cassette, Neo) that would only induce EML4-ALK driven lung tumors. Analysis of $EGFP^{positive}$ and $EGFP^{negative}$ tumors revealed that more than 80% of Lenti-sgEgfp-sgV1/Cre and Lenti-sgEgfp-sgV3/Cre-initiated lung tumors lacked EGFP expression (**Figure 25D-F**), confirming the efficient genomic intervention and the induction of the *Eml4-Alk* rearrangement.

In summary, this triple sgRNA configuration allows for highly multiplexed genome engineering while concurrently inducing the *V1* or *V3* rearrangements.

Tumor barcoding allows investigation of V1 and V3 oncogenicity

The scarcity of sequenced EML4-ALK-driven lung tumors and the lack of compression studies limit our understanding of how tumor suppressor gene alterations might affect EML4-ALK-driven tumors. A few studies have investigated the role of the well-established tumor suppressor gene *TP53* (Kron et al. 2018; Christopoulos et al. 2018), while other genomic analyses lack the clinical implication of other altered tumor suppressor genes. To evaluate in parallel the role of several tumor suppressor genes in EML4-ALK V1 and V3-driven lung cancer, we coupled CRISPR/Cas9 genome editing with high-throughput tumor barcode sequencing (Tuba-seq). Tuba-seq has two barcoding components that allow clonal labeling of genetically diverse tumors. This barcode region (sgID-BC) contains a characteristic sgRNA identifier (sgID, a known 8-nucleotide sequence that is variant specific and identifies each sgRNA) and a barcode sequence (BC, a random 20-nucleotide sequence that identifies each clonal expansion) (**Figure 26A,B** and **Methods**). PCR amplification and high-throughput sequencing of the sgID-BC region from DNA extracted from the bulk tumor-bearing lungs allows quantification of the number of reads from each sgID-BC and consequent estimation of the number of cells from each tumor genotype (**Figure 26C** and **Methods**).

With the help of Kalman Somogyi, I first generated two pools of barcoded lentiviral vectors encoding sgTSG (a variable sgRNA targeting genes of interest), sg*Eml4*^{V1} or sg*Eml4*^{V3} and Cre-recombinase (Lenti-sgTSG^{19}-sgV1-BC/Cre and Lenti-sgTSG^{19}-sgV3-BC/Cre) (**Figure 26D**). To increase the statistical power of our analysis and to minimize CRISPR/Cas9-off-target effects, we included two to three sgRNAs for each TSG. I prioritize genes that were frequently mutated in *EML4-ALK* human tumors, such as *TP53* and *SETD2*, or genes that, although not mutated, are relevant in other lung cancer models. This suggests mutual exclusivity with ALK tumors, such as *LKB1*. I also included five sgInert control vectors that either did not target the mouse genome (Non-Targeting, NT) or targeted a "safe" region within

the mouse genome (the Neomycin resistance cassette, Neo). Finally, a sgRNA targeting *Pcna* was included, an essential gene required to as positive control of CRISPR/Cas9 activity (**Figure 26B**).

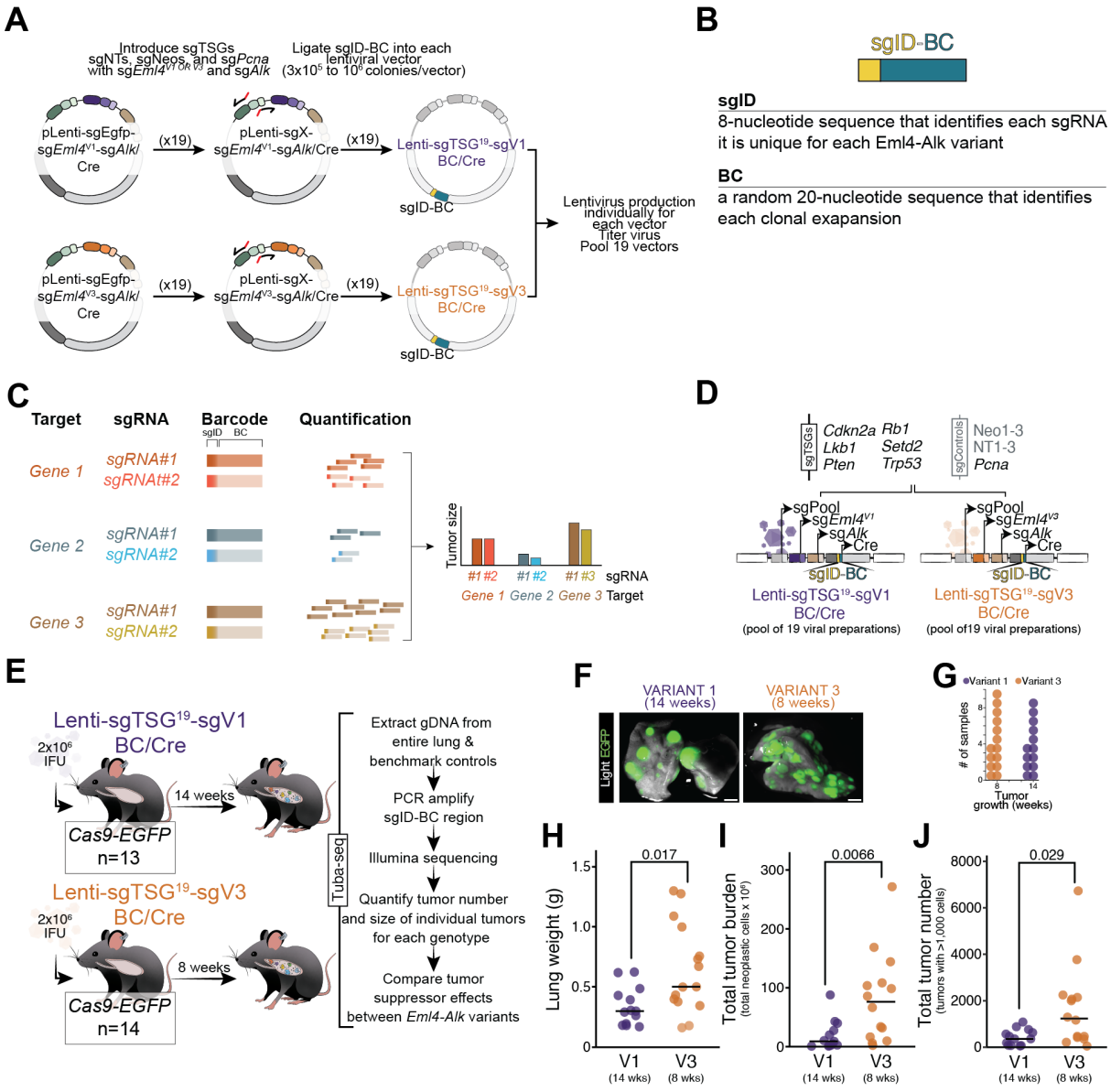


Figure 26 | EML4-ALK V3 is a highly oncogenic fusion protein. A) Schematic of the cloning strategy. Each barcoded lentiviral vector in the Lenti-sgTSG[19]-sgV1-BC/Cre and Lenti-sgTSG[19]-sgV3-BC/Cre pools was generated individually before pooling. **B)** Schematic showing sgID-BC structure. **C)** Schematic of the tuba-seq pipeline. For simplicity, only one BC was illustrated per sgRNA. Each gene is targeted by at least two sgRNAs. Each sgRNA has a unique sgID and multiple BC sequences, which identifies multiple clonal expansions caused by the same sgID but different lentiviral vector. By quantifying the number of reads, the number of neoplastic cells and the corresponding tumor size can be estimated. **D)** Schematic showing the targeted genes and the final lentivector structure. **E)** Experimental workflow. Lenti-sgTSG[19]-sgV1-BC/Cre and Lenti-sgTSG[19]-sgV3-BC/Cre vectors were intratracheally delivered into *Cas9-Egfp* (*R26* *LSL-Cas9-EGFG/ LSL-Cas9-EGFG* mice). Viral dose, number of mice and average time of sample collection are indicated. The right panel shows the workflow for tumor barcoding sequencing (Tuba-seq). **F)** Representative fluorescent images of V1 and V3 tumor bearing lungs. Scale bars are 2 mm. **G)** Number of V1 and V3 samples collected per time point. Each dot is a mouse. **H)** Lung weight (grams) from V1 and V3 tumor bearing lungs. Each dot is a mouse. **I)** Total tumor burden measured as total number of neoplastic cells assessed by Tuba-seq. Each dot is a mouse. **J)** Total number of tumors (tumors with more than 1000 cells) assessed by Tuba-seq. Each dot is a mouse.

To address the growth EML4-ALK V1 and V3-driven tumors while inactivating putative TSGs, I transduced independent cohorts of *Cas9-EGFP* mice with Lenti-sgTSG[19]-sgV1-BC/Cre or Lenti-sgTSG[19]-sgV3-BC/Cre (**Figure 26E**). I then sampled *Cas9-EGFP* mice when they exhibited symptoms associated with high tumor burden (~14 and ~8 weeks for V1 and V3 tumor-bearing mice, respectively; **Figure 26F,G**). In line with our previous observations (**Figure 24D**) and consistent with the assumption of EML4-ALK V3 being more oncogenic, V3 induced a greater tumor burden than V1 (**Figure 26H**).

Emily Shuldiner, PhD student from Dr. Monte Winslow's laboratory then quantified the size and number of each individual tumor. In line with the lung weight data, V3-tumor bearing lungs had a higher total number of neoplastic cells (**Figure 26I**) and higher tumor number (number of barcoded clonal expansions) as compared with V1-driven tumors (**Figure 26J**).

To compare the oncogenic potential of V1 and V3-driven lung tumors, we analyzed tumors that contained sgInert vectors (NT and Neo). These vectors lack the ability to inactivate TSGs, but still induce lung tumors driven by V1 or V3. sgInert-V3-driven tumors displayed significantly higher tumor burden as compared to sgInert-V1 tumors (**Figure 27A**). In addition, the increased tumor burden was a consequence of V3-driven larger and more numerous tumors than V1 (**Figure 27B**). Interestingly, tumors in both models attained similar maximum sizes (**Figure 27C**).

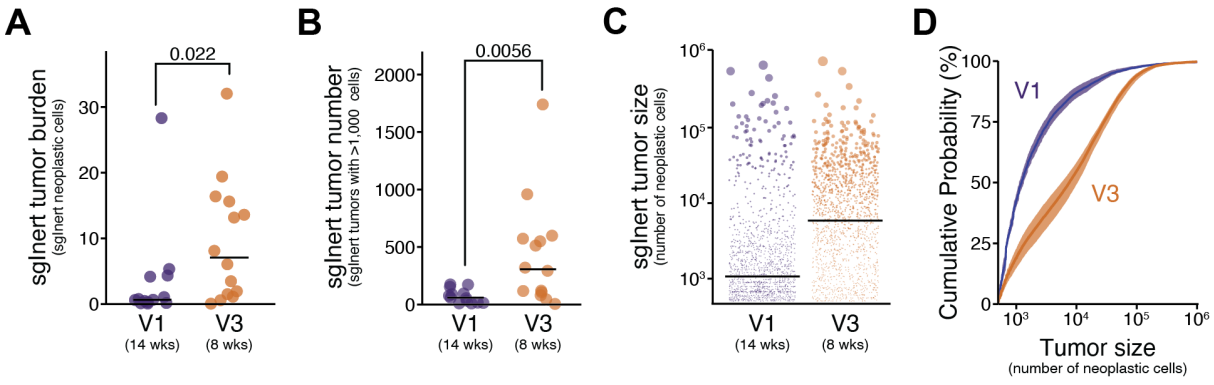


Figure 27 | Tuba-seq demonstrates the superior oncogenic potential of V3 over V1. A) Tumor burden from sgInert tumor cells measured as total number of sgInert-neoplastic cell per mouse. Each dot is a mouse. **B)** Total number of sgInert tumors with more than 1,000 cells. Each dot is a mouse. **C)** Individual size from sgInert-tumors. Each dot is a tumor. **D)** Cumulative probability distribution of tumor sizes, providing the likelihood of observing tumors of different sizes in V1 and V3 mice.

We then analyzed the tumor size distribution for each *Eml4-Alk* tumor genotype. The resulting metrics of tumor size can be highly sensitive to the cutoff used given by differences in the number of infectious units (**Figure 26C**). We therefore, directly compared the corresponding proportion of V1 and V3-induced tumors for each tumor size, adjusting the

metric to number of tumors per infectious unit of administered virus. This analysis reinforced that V3-driven tumors are substantially larger than V1 tumors, despite the differences in time and lentiviral doses (**Figure 27D**).

Setd2 and *Lkb1* are suppressors of V3-driven tumor growth

We then investigated the impact of inactivating putative tumor suppressor genes in the context of EML4-ALK V1 and V3-driving tumorigenesis. To this aim, Emily Shuldiner developed a novel quantitative metric (adaptive sampling mean, ASM) that considers equivalent proportions of the tumor size distribution for each sgRNA. This method accounts major variables as the number of mice, lentiviral dose, and the relative proportion of each sgRNA lentiviral vector used in each cohort (Lenti-sgTSG^{19}-sgV1-BC/Cre or Lenti-sgTSG^{19}-sgV3-BC/Cre) (**Figure 28A** and **Methods**). In the basis of this methodology, we calculated two metrics of V1 and V3-driven lung tumorigenesis: the adaptively sampled log-normal mean size (ASM) (**Figure 28B** and **Methods**). Importantly, these two metrics not only factor in the impact on tumor size but also take into account tumor initiation (number of tumors) owing to the adaptive sampling method.

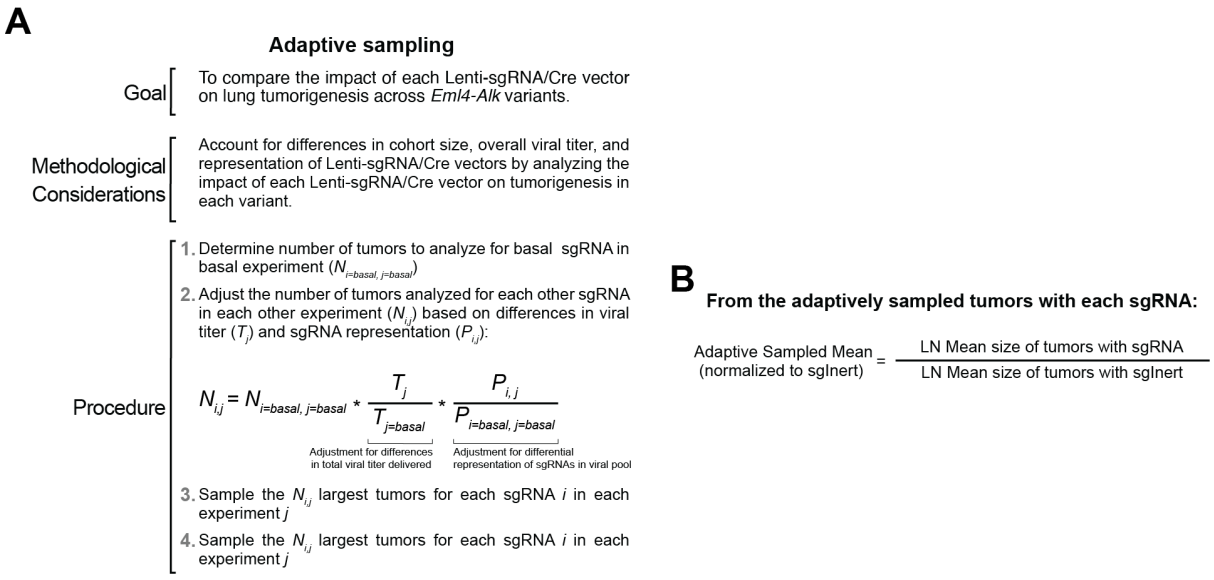


Figure 28 | Adaptive sapling and adaptive sapling mean methods. A) Explanation of the adaptive sampling method used to assess the impact of TSG inactivation in V1 and V3-driven lung tumors. ASM is a metric of tumorigenesis that integrates tumor size and tumor number (see Methods). **B)** The Adaptive Sampled Mean (ASM) statistic, normalized to sgInert, is based on the ratio of the natural logarithm (LN) mean size of a tumor with a specific sgRNA to the LN mean size of a tumor with sgInert. This statistic characterizes the advantage conferred by inactivation of putative tumor suppressor genes.

Inactivation of *Trp53* or *Cdkn2a*, which are frequently mutated or deleted in human *EML4-ALK* LUADs (GENIE, (Kron et al. 2018; Christopoulos et al. 2018)), increased V1 and V3-driven lung tumorigenesis. Interestingly, the inactivation of other tumor suppressor genes

differed among *Eml4-Alk* variants. Inactivation of *Pten*, a known tumor suppressor gene with function on cell metabolism, cell survival or genomic stability (Lee et al. 2018), markedly induced larger effects on the growth of V1 tumors as compared with V3-driven tumors (**Figure 29A**). Conversely, inactivation of *Lkb1* or *Setd2* genes had a positive effect on V3-driven tumors (**Figure 29C**), while remaining neutral or even detrimental in the context of V1 tumorigenesis (**Figure 29A**). Assessing the efficacy of individual sgRNAs revealed consistency and robustness across sgRNAs that target the same gene, across various tumorigenesis metrics, and in both sgRNA-level and gene-level analyses (**Figure 29B,D**).

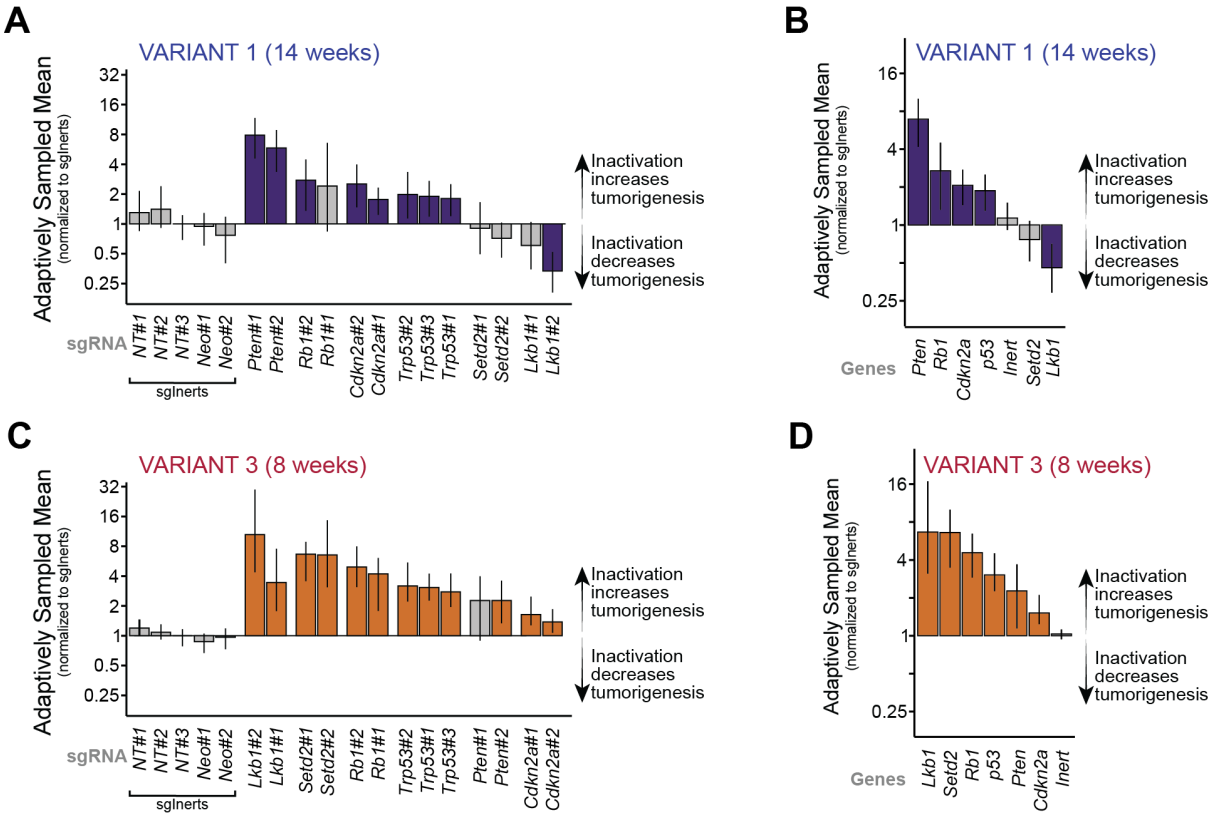


Figure 29 | V1 and V3 cooperates with different tumor suppressors genes. A,B) The adaptively sampled mean size (ASM) of each sgRNA was normalized to the ASM of sgInert tumors in V1 (A) and V3 (B) mice. Each bar represents a sgRNA, grouped by gene. The baseline tumor growth (Y=1) had no impact. sgRNAs that significantly increased or decreased ASM (two-sided FDR-adjusted *P-value*) are highlighted in color. *P-values* and confidence intervals were calculated using nested bootstrap resampling. **C,D)** Adaptively sampled mean tumor sizes were calculated at the gene level for V1 (C) and V3 (D) mice.

Finally, analysis of Cas9-negative *Kras*$^{LSL\text{-}G12D/+}$ mice intratracheally instilled with Lenti-sgTSG[19]-sgV1-BC/Cre or Lenti-sgTSG[19]-sgV3-BC/Cre pools (**Figure 30A,B**) exhibited nonsignificant differences across lentiviral vectors, confirming that the genomic interactions observed in *Cas9-EGFP* mice result from CRISPR/Cas9-mediated gene targeting (**Figure 30A,B**).

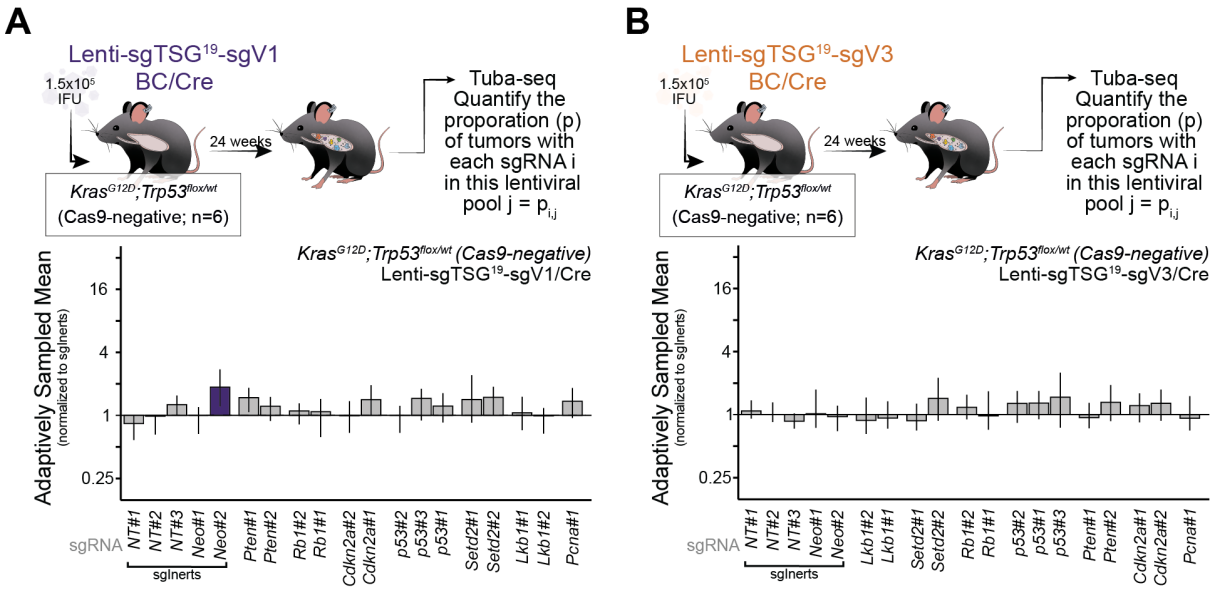


Figure 30 | Cas9 is required for gene inactivation. A,B) Schematic of tumor initiation in *Kras*$^{LSL\text{-}G12D/+}$;*Trp53*$^{flox/wt}$ (Cas9-negative) mice with Lenti-sgTSG^{19}-sgV1/Cre (A) and Lenti-sgTSG^{19}-sgV3/Cre (B) viral pools to determine representation of each lentivirus within the pools. Lower panels show the ASM metric for each sgRNA normalized to sgInerts. Baseline tumor growth (Y=1): no impact. Genes that significantly increased or decreased ASM (two-sided FDR-adjusted p-value) are in color. P-values and confidence intervals were calculated using nested bootstrap resampling.

Tumor barcoding allows for large genomic screenings in EML4-ALK-driven tumors

Our previous analysis encountered unexpected genetic interactions in the context of V1 and V3 lung tumors. Thereby, we decided to interrogate a larger and more diverse panel of tumor suppressor genes across main cancer-related pathways. I prioritized 29 tumor suppressor genes according to their mutation frequency in human EML4-ALK lung cancer (Noh et al. 2017), their role in KRAS^{MUT}- and EGFR^{MUT}-driven lung cancer mouse models (Cai et al. 2021; Foggetti et al. 2021), and their functionality in cancer cell biology. This gene panel accounts for a wide range of cellular processes including suppressors of canonical signaling pathways (*e.g. Nf1*, *Lkb1,* and *Pten*), chromatin regulators (*e.g. Arid1a*, *Stag2,* and *Suz12*), and regulators of differentiation and splicing (*e.g. Nkx2-1* and *Rbm10*) (**Figure 31A** and **Table 9**). In coordination with Kalman Somogyi, I generated additional Lenti-sgV1/Cre and Lenti-sgV3/Cre lentiviral vectors, targeting each of these 29 TSG with two to four sgRNAs. In addition to our previous sgInert control vectors (sgControls, three sgNTs and three sgNeo) and our sgRNA targeting *Pcna*. To diversify our lentiviral library, I barcoded each lentiviral vector with a unique sgID and a random BC region before lentiviral production. The vectors were then pooled at equal ratios to generate Lenti-sgTSG^{75}-sgV1-BC/Cre and Lenti-sgTSG^{75}-sgV3-BC/Cre pools (**Figure 31A**).

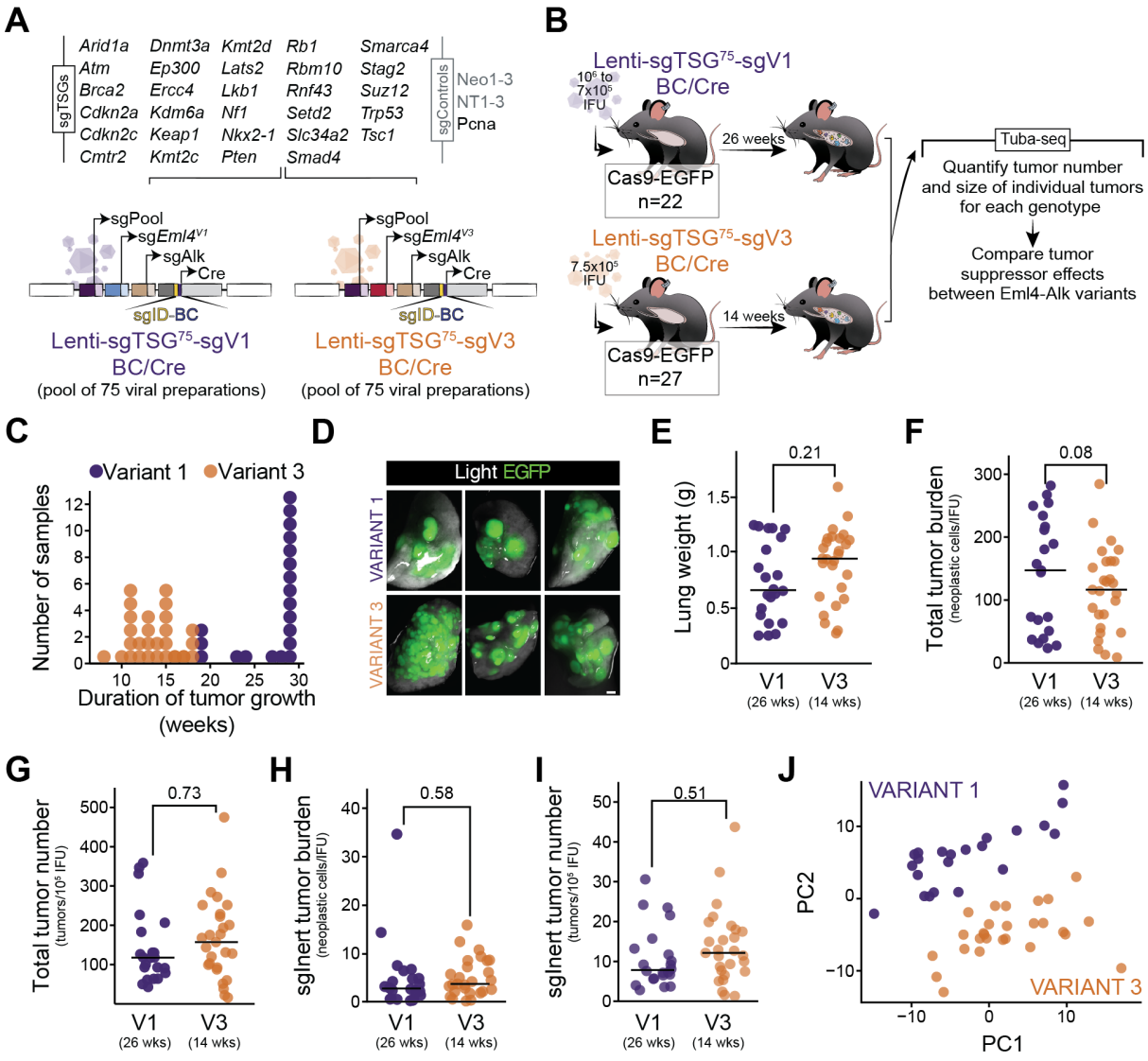


Figure 31 | Prolonged survival and equitable tumor burden through reduced lentiviral dose in V1 and V3 mice. A) Lenti-sgTSG^{75}-sgV1-BC/Cre and Lenti-sgTSG^{75}-sgV3-BC/Cre pools include two to four barcoded lentivector for each tumor suppressor gene, 6 sgControls, and a sgRNA targeting an essential gene (*Pcna*). All lentivectors were pooled in equal ratios prior to delivery. **B)** Schematic of the experimental workflow. Cas9-EGFP mice (*Rosa26*$^{LSL\text{-}Cas9\text{-}EGFP/LSL\text{-}Cas9\text{-}EGFP}$) were intratracheally instilled with Lenti-sgTSG^{75}-sgV1-BC/Cre and Lenti-sgTSG^{75}-sgV3-BC/Cre pools. Lungs were collected for Tuba-seq analysis. The lentiviral titer, median sample collection, and number of mice are indicated. **C)** Duration of tumor growth for mice in cohorts transduced with Lenti-sgTSG^{75}-sgV1/Cre and Lenti-sgTSG^{75}-sgV3/Cre pools. Each dot is a mouse. **D)** Representative light and fluorescent lung images from three V1 and three V3 mice. Scale bar is 2.5 mm. **E)** Lung weight (grams) from V1 and V3 mice. Each dot is a mouse. Unpaired t-test, nominal *P-value* is shown. **F)** Total tumor burden from V1 and V3 tumors calculated as total number of neoplastic cells relative to viral dose (IFU). Each dot is a mouse. Two-sided Wilcoxon rank sum test, nominal *P-value* is shown. **G)** Total tumor number of V1 and V3 tumors calculated as total number of neoplastic cells relative to IFU. Each dot is a mouse. Two-sided Wilcoxon rank sum test, nominal *P-value* is shown**. H)** Total tumor burden from V1 and V3 tumors relative to IFU. Each dot is a mouse. Two-sided Wilcoxon rank sum test, nominal *P-value* is shown. **I)** Total number of neoplastic cells summed across all sgInert tumors relative to IFU. Each dot is a mouse. Two-sided Wilcoxon rank sum test, nominal *P-value* is shown. **J)** Principal components analysis of tumor suppressive effects performed within each mouse. Each dot represents a mouse and is colored according to its *Eml4-Alk* variant.

To investigate the effects of inactivating each tumor suppressor gene on EML4-ALK-driven tumorigenesis, I transduced *Cas9-EGFP* cohorts as well as Cas9-negative *Kras*$^{LSL\text{-}G12D/+}$ mice with Lenti-sgTSG^{75}-sgV1-BC/Cre and Lenti-sgTSG^{75}-sgV3-BC/Cre pools (**Figure**

31B). A larger panel of genes may compromise the detection of weak genetic interactions. We, therefore, reasoned that reducing the lentiviral dose by up to 60% could increase the time to sample collection and improve the detection of genes with modest effects (**Figure 31B,C**). In this regard, we extended V1 survival by 12 weeks an V3 survival by 6 weeks. Once *Cas9-EGFP* mice exhibited symptoms associated with high tumor burden (~26 and ~14 weeks for V1 and V3 tumor-bearing mice, respectively), I collected the lungs for Tuba-seq (**Figure 31C,D**). I then extracted the genomic DNA from V1 and V3 tumor bearing lungs, amplified and high-throughput sequenced the sgID-BC region. Within this new experimental frame, the total tumor burden, sgInert tumor burden, total tumor number, and sgInert tumor number were similar in mice with V1 and V3-driven lung tumors (**Figure 31E-I**). Dimensionality reduction using principal component analysis of tumor size at 95th percentile clustered samples according to their *Eml4-Alk* variant, confirming general robustness across mouse cohorts and suggesting a distinct spectrum of tumor-genotype interactions (**Figure 31J**).

We then explored the tumorigenic potential of multiple tumor suppressor genes in a variant-specific manner. To do so, Emily Shuldiner performed the adaptively sampled log-normal mean size (ASM) for each sgRNA and gene in the Lenti-sgTSG^{75}-sgV1-BC/Cre and Lenti-sgTSG^{75}-sgV3-BC/Cre pools. Tumors generated by Lenti-sgTSG^{75}-sgV1-BC/Cre and Lenti-sgTSG^{75}-sgV3-BC/Cre pools in Cas9-negative *Kras$^{LSL\text{-}G12D/+}$* mice showed negligible differences among vectors, confirming that the tumor suppressive effects observed in the *Cas9-EGFP* mice are due to CRISPR/Cas9-mediated gene targeting (**Figure 32**).

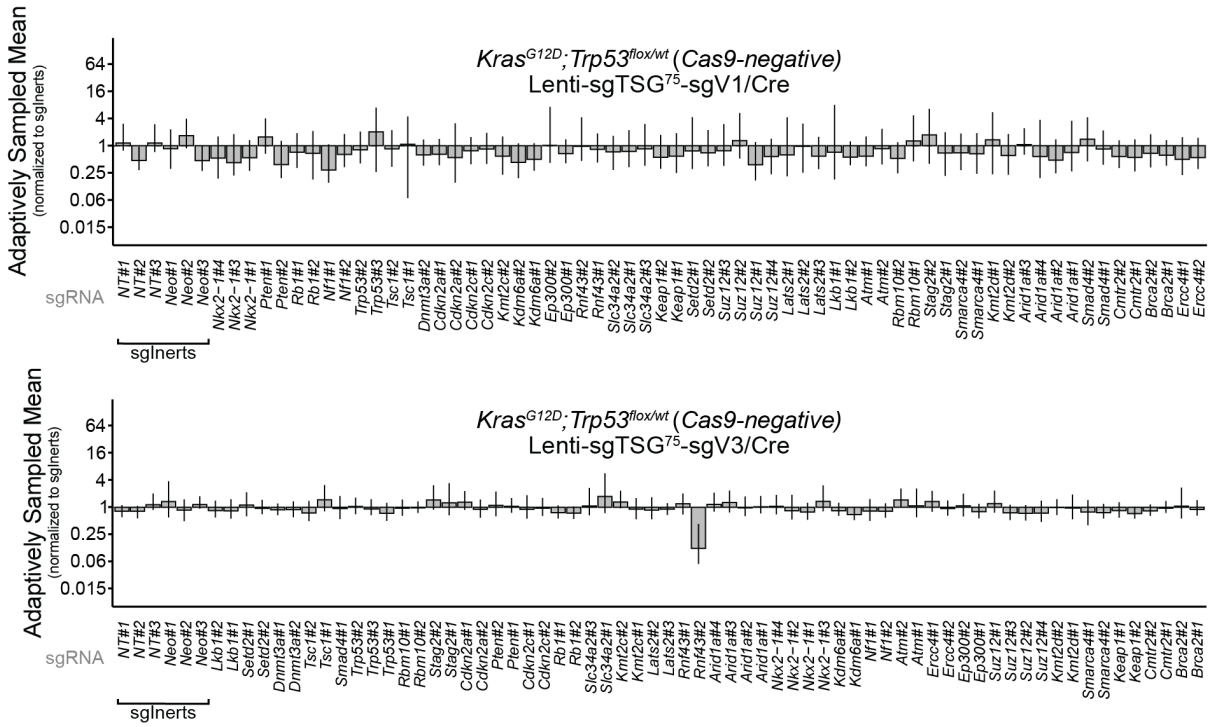


Figure 32 | Tumor suppressor gene effects are due to Cas9-activity. Adaptively Sampled Mean (ASM) tumor sizes relative to sgInert vectors for each sgRNA in theLenti-sgTSG[75]-sgV1/Cre (upper panel) and Lenti-sgTSG[75]-sgV3/Cre (lower panel) pools in Cas9-negative mice.

Analysis of *Cas9-EGFP* mice, by Emily Shuldiner, revealed that the tumorigenesis of V1 and V3 was largely impacted by different tumor suppressor genes. For each variant, specific tumor suppressor genes increased lung tumorigenesis, while others had a neutral or detrimental effect (**Figure 33**). In line with our previous observation, inactivation of *Trp53* or *Cdkn2a* increased V1- and V3-tumorigenesis (**Figure 32**). Functional suppressors whose inactivation is known to promote lung cancer (Concepcion et al. 2021; Cai et al. 2021; Lee et al. 2023), reduced EML4-ALK driven tumorigenesis. For example, deletion of *Smad4*, a known TGF-β signaling member, had a negative impact on V1-driven lung tumors; while inactivation of the methyltransferase *Cmtr2* was deleterious for both V1 and V3 tumors (**Figure 33**). Importantly, several genes, which were not evaluated in our initial screening, were found to be critical tumor suppressors. Inactivation of *Nkx2-1* (a lung development transcription factor) or *Nf1* (a negative regulator of the RAS pathways) cooperated with V1-tumorogenesis to a greater extent, while *Dnmt3a* (DNA methyltransferase) or *Tsc1* (negatively regulates mTORC1) increased V3-driven tumorigenesis (**Figure 33**).

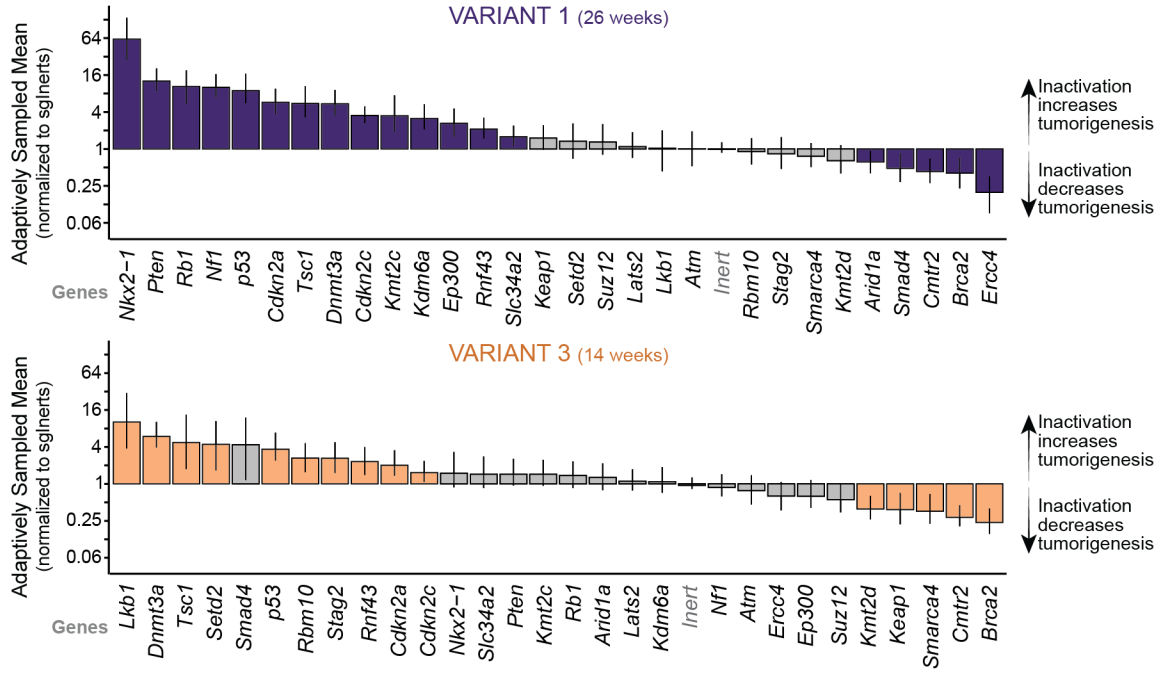


Figure 33 | Diverse outcomes of tumor suppressor gene inactivation on V1 and V3 lung tumors. Adaptively sampled mean tumor sizes were calculated at the gene level for V1 (upper panel) and V3 (lower panel) mice. Baseline tumor growth (Y=1): no impact. Genes that significantly increased or decreased ASM (two-sided FDR-adjusted p-value) are in color. *P-values* and confidence intervals were calculated using nested bootstrap resampling.

The tumor suppressive landscape of EML4-ALK V1 and V3 resembles distinct oncogenes

Our previous analysis highlighted significant variation in how specific variants interact with different tumor suppressor genes, with some suppressors showing contrasting effects. Emily Shuldiner performed statistical comparison of the ASMs calculated for each tumor genotype revealed that the tumor-suppressive landscape differed greatly in magnitude and/or rank between V1- and V3-driven tumors (**Figure 34A**). Deficiency of *Nkx2-1*, *Pten*, *Nf1* and *Ep300* had a positive effect on V1-driven lung cancer but did not affect V3 tumorigenesis, whereas loss of tumor suppressor genes such as *Lkb1*, *Setd2* and *Stag2* exclusively promoted V3 tumorigenesis (**Figure 34A,B**). Taken together, in contrast to the classical assumption that V1 and V3 are similar oncogenes with identical outcomes, these results indicate a significant restructuring of the tumor suppressor landscape between these two *Eml4-Alk* variants.

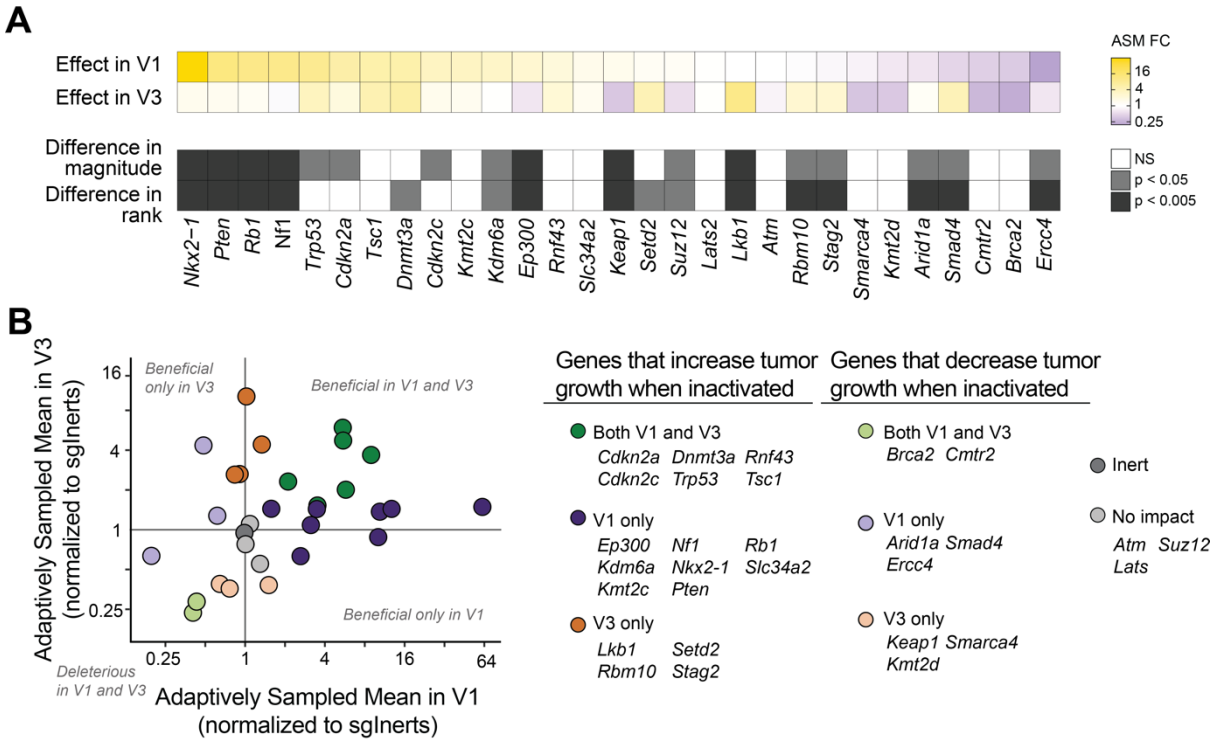


Figure 34 | Tumor suppressive effect is different for each *Eml4-Alk* variant. A) Heatmap showing the tumor suppressive effect of each gene in V1 and V3 tumors. Top: impact of inactivating each gene on tumor growth as measured by fold change in the adaptively sampled mean size (ASM) relative to control sgInert vectors. Color indicates both magnitude and direction of effect and genes are ordered by effect size in the V1 cohort. Bottom: significance of difference in impact of inactivating each gene in V1- and V3-driven lung tumors as measured by both magnitude and rank order of effects. **B)** Volcano plot depicting the tumor suppressive effect of the indicated genes on V1 and V3 tumors. Each point is a gene. Points are colored according to their effect.

To quantify the similarity between the ASMs for all putative tumor suppressor genes in the Lenti-sgTSG[75]-sgV1-BC/Cre and Lenti-sgTSG[75]-sgV3-BC/Cre pools, Emily Shuldiner calculated the Spearman's rank correlation coefficient (ρ). This coefficient provided a measure

of similarity, where -1 indicates complete disorganization, 0 signifies random reorganization, and 1 denotes complete equality (**Figure 35**).

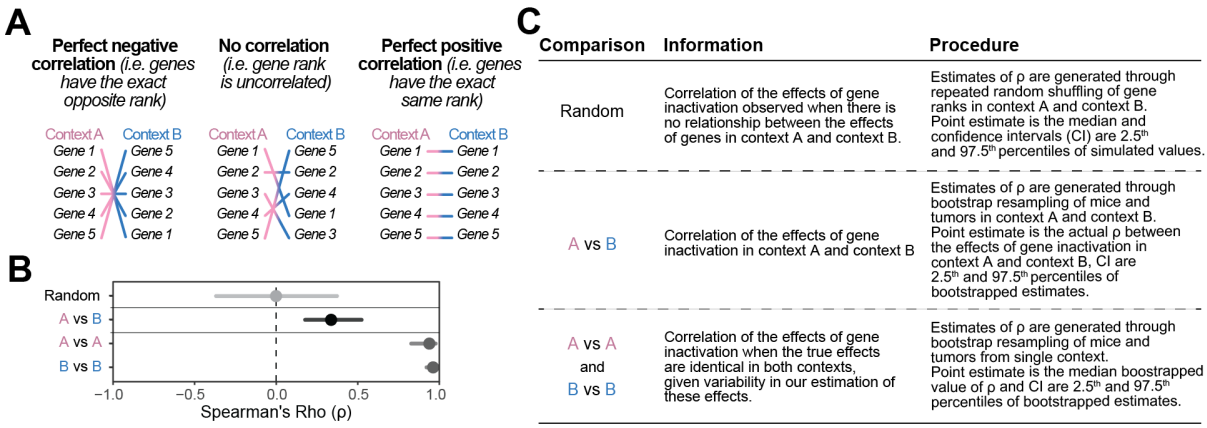


Figure 35 | Spearman's rank correlation coefficient (ρ). A) Example of ranked positions of five different genes in the context of A and B. **B**) example plot of correlation analysis contrasting A and B contexts. **C**) Accompanying explanation of the B) results.

As previously denoted by **Figure 34**, comparison of V1 and V3 tumor genotypes exhibited a nearly random degree of similarity (ρ=0.40) (**Figure 36A,C**). It is important to note that the intrinsic variability in our estimation of the tumor suppressor effect could influence the lower similarity among *Eml4-Alk* variants. This analysis confirmed the dissimilarity among *Eml4-Alk* variants, and rejected the hypothesis that the ranking of genes in V1 was random with respect to the ranking of genes in V3.

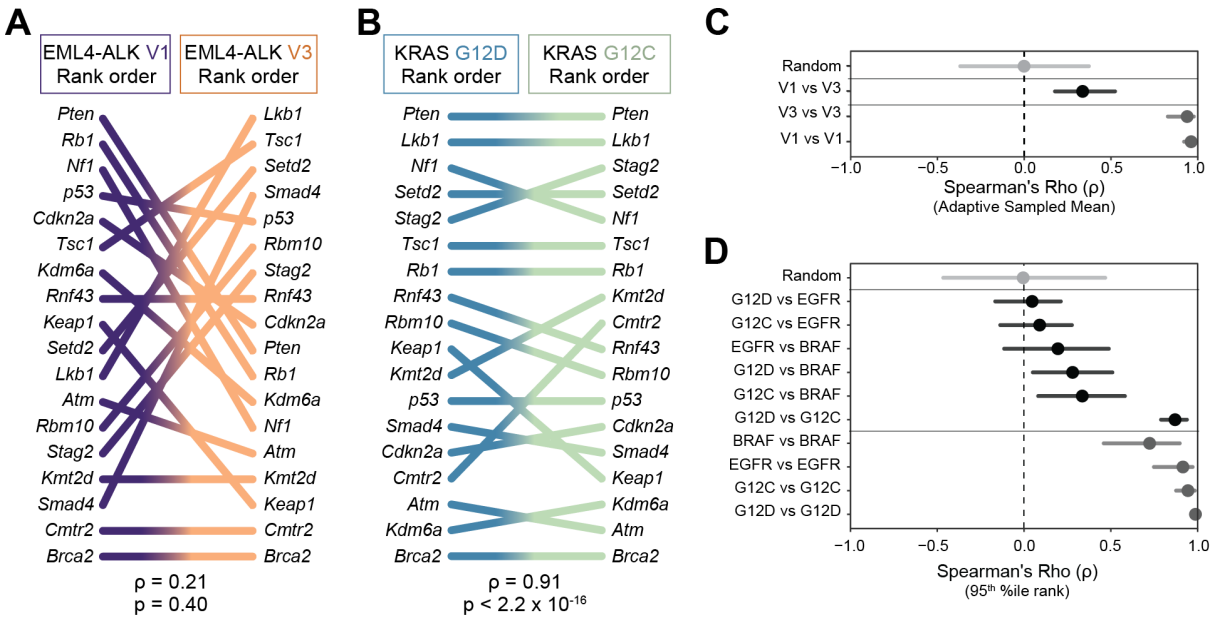


Figure 36 | The tumor suppressor landscapes of *Eml4-Alk* V1 and V3 resemble distinct oncogenes. A,B) Comparison of tumor suppressor genes between V1 and V3 lung tumors (A) and between $KRAS^{G12D}$ and $KRAS^{G12C}$ lung tumors (Blair et al. 2023) was conducted. Genes were ranked based on ASM metric relative to sgInerts in (A) and by fold change in 95th percentile tumor size relative to sgInerts. Only common genes assayed in the 4 cohorts

are displayed. **C**) Correlation in the rank order of tumor suppressive effects for all genes in V3 and V1 mice. **D**) Correlation in the rank order of tumor suppressive for all sgRNAs between $KRAS^{G12D}$, $KRAS^{G12C}$, BRAF, and EGFR mice from (Blair et al. 2023). Confidence intervals in panels (C) and (D) were generated through a nested bootstrap resampling procedure where tumor suppressive effects and ranks were repeatedly recalculated to quantify uncertainty in ρ. Points are median values across 10,000 bootstrap resampling. "Random" reflects the distribution of ρ observed when there is no relationship between two groups given the number of items being ranked and was produced through simulation.

To calculate the experimental noise, Emily Shuldiner resampled the dataset to perform "V1 vs V1" and "V3 vs V3" comparisons (**Figure 36C**). These intervariant comparisons serve as negative control to calculate the degree of correlation within the same variant and to calculate the experimental noise. Importantly, we found a high degree of correlation within the "V1 vs. V1" and "V3 vs. V3" comparisons, indicating the robustness of our data set.

The lack of similarity in the effects of simultaneous tumor suppressor inactivation in V1- and V3-driven tumors is remarkable, especially considering the general assumption of similarities between the two fusion proteins as oncogenic drivers. To contextualize these findings within the human lung cancer landscape, we compared other pairs of lung cancer oncogenes and different mutations from the same oncogene. We used a publicly available dataset that performed an analogous *in vivo* screening in oncogenic $KRAS^{G12D}$, $KRAS^{G12C}$, $EGFR^{L858R}$ and $BRAF^{V600E}$-driven lung tumors (**Figure 36B,D** and **Methods**) (Blair et al. 2023). We limited the analysis to the genes that are common to our *in vivo* screening. Similar to our previous analysis, Emily Shuldiner performed rigorous bootstrap resampling methods and assessed variability in each dataset and constructed confidence intervals around each estimate of ρ.

We firstly compared different pairs of oncogenes (*Kras* G12D or G12C with *Braf*, *Braf* with *Egfr*, or *Egfr* with a *Kras* G12D or G12C). As expected, given the different nature of the oncogenic signaling, the effects on tumor suppressor activity were weakly correlated (ρ ranging from 0.1-0.35) (**Figure 36D**). In contrast, comparison of the oncogenic variants $KRAS^{G12D}$ and $KRAS^{G12C}$ displayed a markedly high correlation (ρ=0.85) (**Figure 36B,D**). The high degree of correlation between the oncogenic $KRAS^{G12D}$ and $KRAS^{G12C}$ contrasts strikingly with the low similarity between the *Eml4-Alk* variants (**Figure 36A,B**). This is of high relevance since re-ordering of effects between V1 and V3 more closely resembles the extensive re-ordering observed between different oncogene comparisons.

In summary, our data on the epistatic interactions of EML4-ALK V1 and V3 with our broad panel of genes is more consistent with the EML4-ALK variant behaving like distinct oncogenes than to variants of the same oncogene.

Tumor suppressor gene inactivation modulates tumor growth and mouse survival in a *Eml4-Alk* variant-specific-manner

Pten and *Rb1* are tumor suppressor genes that limit the growth of EML4-ALK V1-driven lung tumors, while inactivation of *Lkb1* and *Setd2* increased growth in V3-driven lung tumors. These tumor suppressor genes affect important pathways, including cell metabolism (*Lkb1*, (Ji et al. 2007; Murray et al. 2019)), the AKT/PKB signaling pathway (*Pten*, (Cully et al. 2006; Song et al. 2012)), cell cycle (*Rb1*, (Dick and Rubin 2013; Walter et al. 2019; Aldana et al. 2022)), and epigenomic remodeling (*Setd2*, (Yuan et al. 2020; Leung et al. 2022; Xie et al. 2022)).

To validate our results, I induced *Lkb1*, *Pten*, *Rb1*, and *Setd2* deficient EML4-ALK V1- and V3-driven lung tumors individually (Lenti-sgTSG-sgV1/Cre or Lenti-sgTSG-sgV3/Cre; **Figure 37A**). Lentiviral vectors were delivered intratracheally into independent *Cas9-EGFP* mice cohorts to allow Cas9-mediated gene inactivation and *Eml4-Alk* V1 or V3 rearrangement. As controls, Lenti-sgNeo-sgV1/Cre and Lenti-sgNeo-sgV3/Cre were used to induce the corresponding *Eml4-Alk* rearrangement without altering any tumor suppressor gene (**Figure 37A**). Lentiviral vectors demonstrated an overall 96% penetrance after intratracheal delivery. The presence of the $R26^{LSL\text{-}Cas9\text{-}EGFP}$ transgene in mice that did not develop lung tumors was confirmed by PCR, indicative of a deficiency in the administration of lentiviral vectors (data not shown).

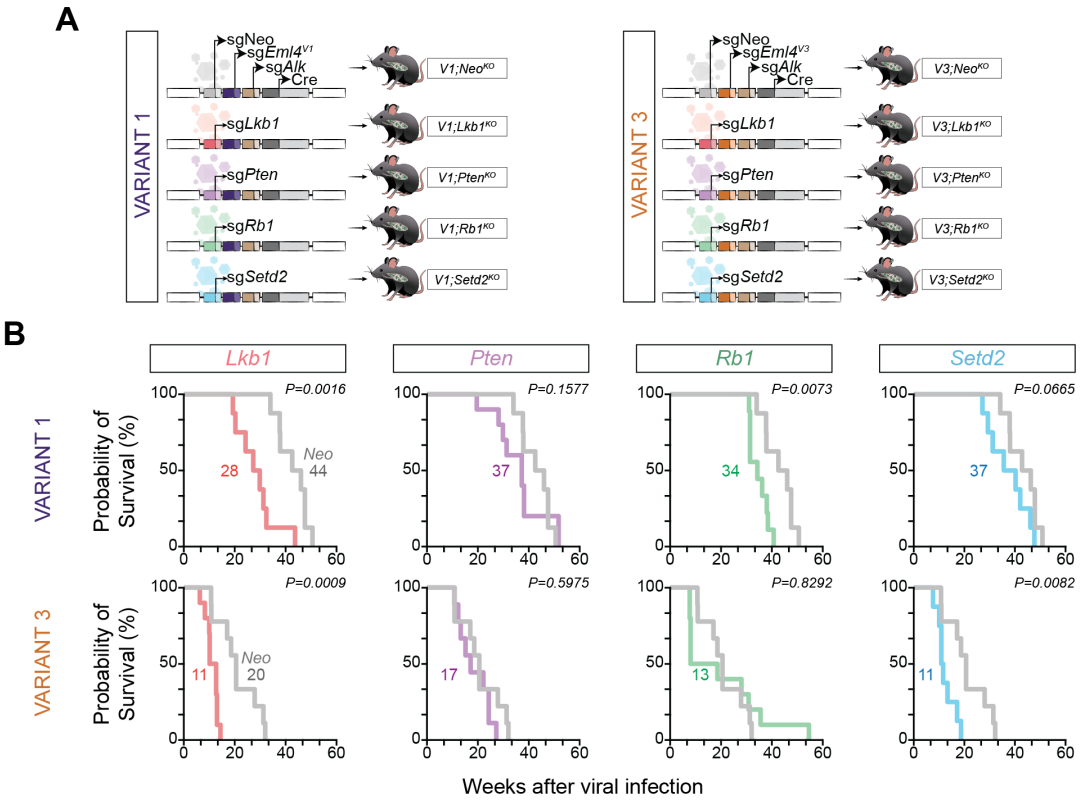


Figure 37 | Survival impact of tumor suppressor gene inactivation in V1 and V3 mice. A) Schematic of the experimental workflow. Cas9-EGFP mice (*Rosa26*$^{LSL\text{-}Cas9\text{-}EGFP/+}$) were intratracheally instilled with the indicated lentiviruses. Lenti-sgTSG-sgV1/Cre: 1.5x10^6 IFU/mouse and Lenti-sgTSG-sgV3/Cre: 1x10^6 IFU/mouse. N=10. **B)** Overall survival of Lenti-sgTSG-sgV1/Cre and Lenti-sgTSG-sgV3/Cre transduced *Cas9-EGFP* mice. Grey line indicates sgNeo-V1 or sgNeo-V3 mice, colored lines refer to sgTSG-V1 or sgTSG-V3 mice. Median survival for each group is indicated. Log-rank (Mantel-Cox) was performed and nominal *P-values* are indicated.

Macroscopic examination of lung tumors revealed that mice died due to a high tumor burden (**Figure 38A,B**), with the exception of V3;*Lkb1*-deficient mice that had a lower lung weight as compared with V3;*Neo* mice. Quantification of the surface tumor size confirmed variant-specific interactions. V1 oncogenesis was enhanced by the inactivation of *Pten* or *Rb1*, while V3 lung tumors grew larger when *Lkb1* or *Setd2* were inactivated. *Pten* inactivation only had a weak effect in V3 lung tumors (**Figure 38C,D**). Of note, the time since viral injection to sample collection may significantly impact group comparison. To address this potential confounding factor, I analyzed samples collected at comparable time points (V1: 36 to 39 weeks; V3:12 to 21 weeks; n=3 mice per group). Consistent with our previous findings, I observed significant differences in tumor size within these groups (**Figure 38E**).

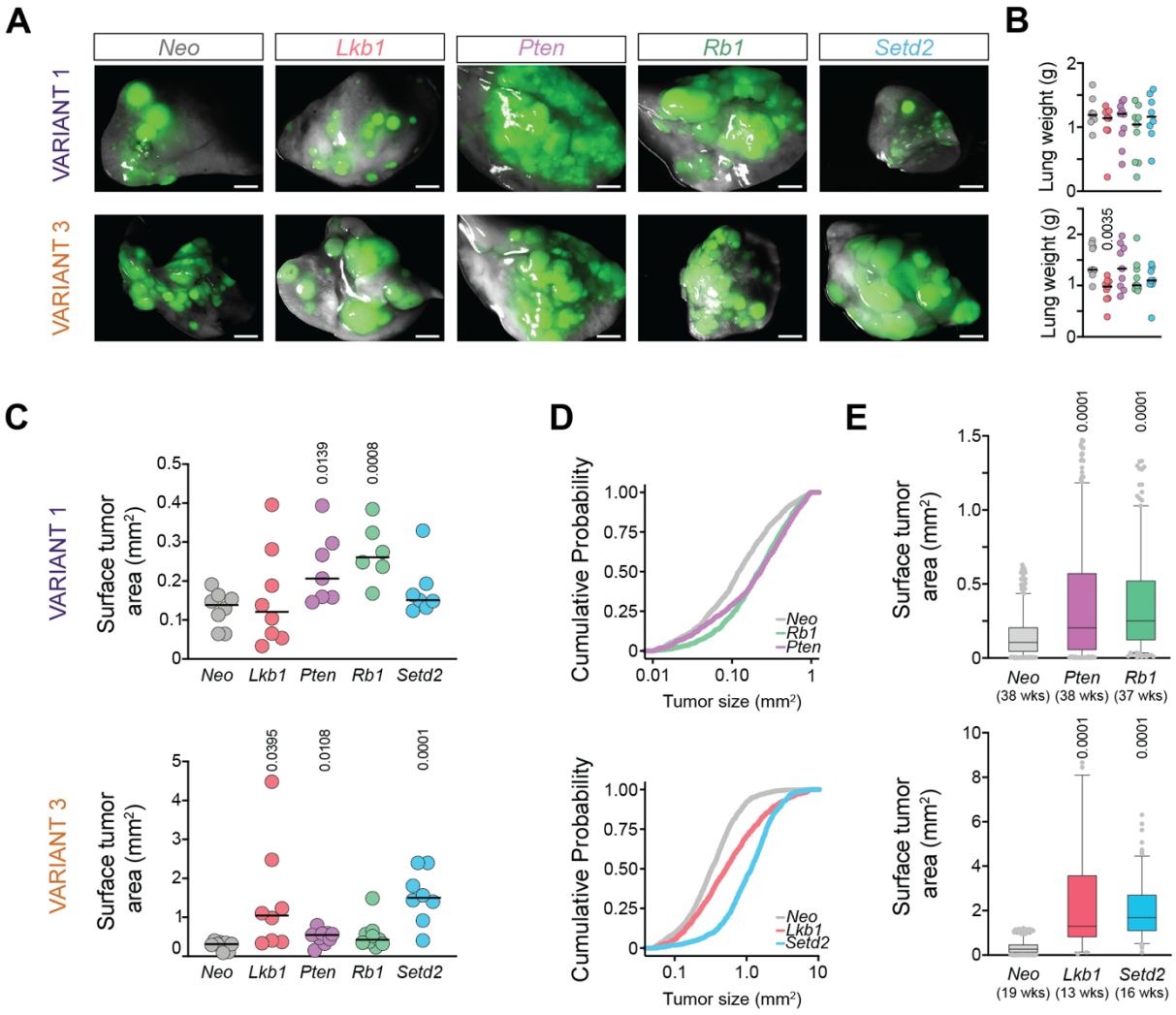


Figure 38 | Tumor suppressor gene inactivation modulates tumor size in a *Eml4-Alk* variant-specific-manner. A) Representative light and fluorescent lung images from Lenti-sgTSG-sgV1/Cre and Lenti-sgTSG-sgV3 induced lung tumors. Scale bar is 2 mm. **B)** Lung weight (grams) from Lenti-sgTSG-sgV1/Cre and Lenti-sgTSG-sgV3 induced lung tumors. Each point is a mouse. Horizontal line indicates the mean. Nominal *P-values* of significant comparison vs. *Neo* are indicated. **C)** Surface tumor area (mm^2) from indicated tumor genotypes. Each point represents the median tumor size of one mouse. Horizontal line indicates the mean. Nominal *P-values* of significant comparison vs. *Neo* are indicated. **D)** Empirical cumulative distribution of tumor size (mm^2) across different genotypes. **E)** Box-and-whisker plot displaying the 5-95 percentile range of tumor sizes (mm^2) by genotype. Time in weeks indicates the average of sample collection. Two-way ANOVA was performed. Nominal *P-values* of significant comparison vs. *Neo* are indicated.

Loss of tumor suppressor genes could enhance tumor aggressiveness and favor metastatic events (Jackson et al. 2005). Therefore, I conducted a thorough examination for metastatic events and discovered that the loss of *Lkb1* significantly affected the metastatic capability of both V1 and V3-driven tumors. This resulted in metastatic occurrences in approximately 40% of V1 mice (3 out of 8) and V3 mice (4 out of 10) (**Figure 39**). It is noteworthy that while loss of *Setd2* had a neutral impact on V1 tumor growth, its inactivation induced metastatic events in 20% of V1 mice. Besides, *Rb1*-deficient tumors exhibited the ability to metastasize, solely in V3-mice.

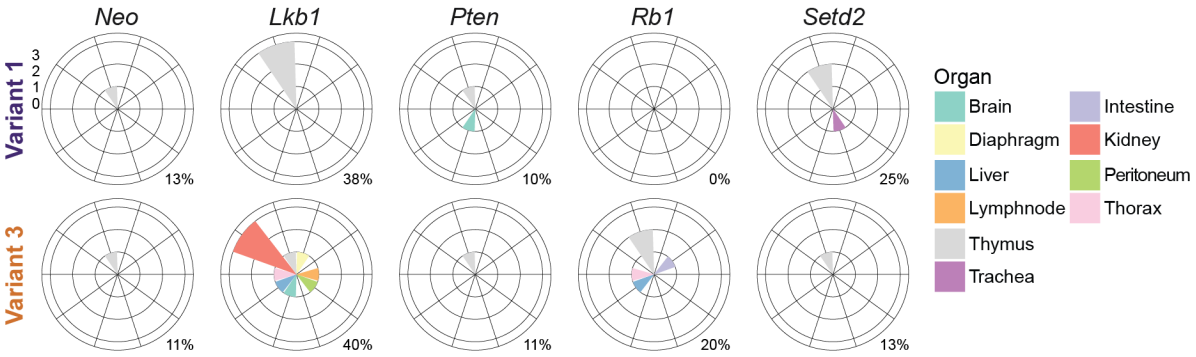


Figure 39 | Metastatic events in V1 and V3 mice. Radar chart of metastasis incidence in the specific organs of V1 and V3 mice harboring the indicated genotypes. The radius of each polygon indicates the number of metastases in the indicated organ across all mice. N=8-10 independent mice. Detailed percentages correspond to the fraction of mice with at least one metastasis.

Tumor suppressor gene disruption leads to histologically distinct EML4-ALK-driven lung tumors

Beyond driving uncontrolled cell growth, inactivation of tumor suppressor genes can significantly alter the structure of tumors (Jia and Zhao 2019; Hanahan 2022; Yang et al. 2022). To investigate the morphological effects of inactivating tumor suppressor genes, I performed a thorough histological analysis (grading) using hematoxylin and eosin (H&E) staining on our tumor models. Here, I used a cloud-based software that employs deep learning and artificial intelligence to automate and enhance histological analysis. This method classifies lung lesions from early adenomas (G1) to high-grade lung adenocarcinomas (G3), based on a previously described method (**Figure 40A**) (Jackson et al. 2005). Notably, EML4-ALK V3 tumors lacking

Setd2 exhibited a more aggressive histology compared to control EML4-ALK V3 Neo tumors (**Figure 40B**). Interestingly, V3-driven *Lkb1*-deficient tumors showed a significant increase in G2 tumors **Figure 40B**), in sharp contrast with the tumor promoting effect when inactivated in KRAS-driven LUAD (Ji et al. 2007; Nagaraj et al. 2017; Murray et al. 2019; Murray et al. 2022). However, histological analysis revealed that 50% of these mice had lung squamous cell carcinoma (LUSC), as reflected by their P63 expression, a well-established LUSC marker (**Figure 40C,D**). This suggests that the observed G2 enrichment could be partially due to undetected LUSC by the grading algorithm within these tumors. Remarkably, LUSC maintained NKX2-1 expression, a marker of LUAD, which may suggest a transdifferentiation from LUAD to LUSC (**Figure 40D**).

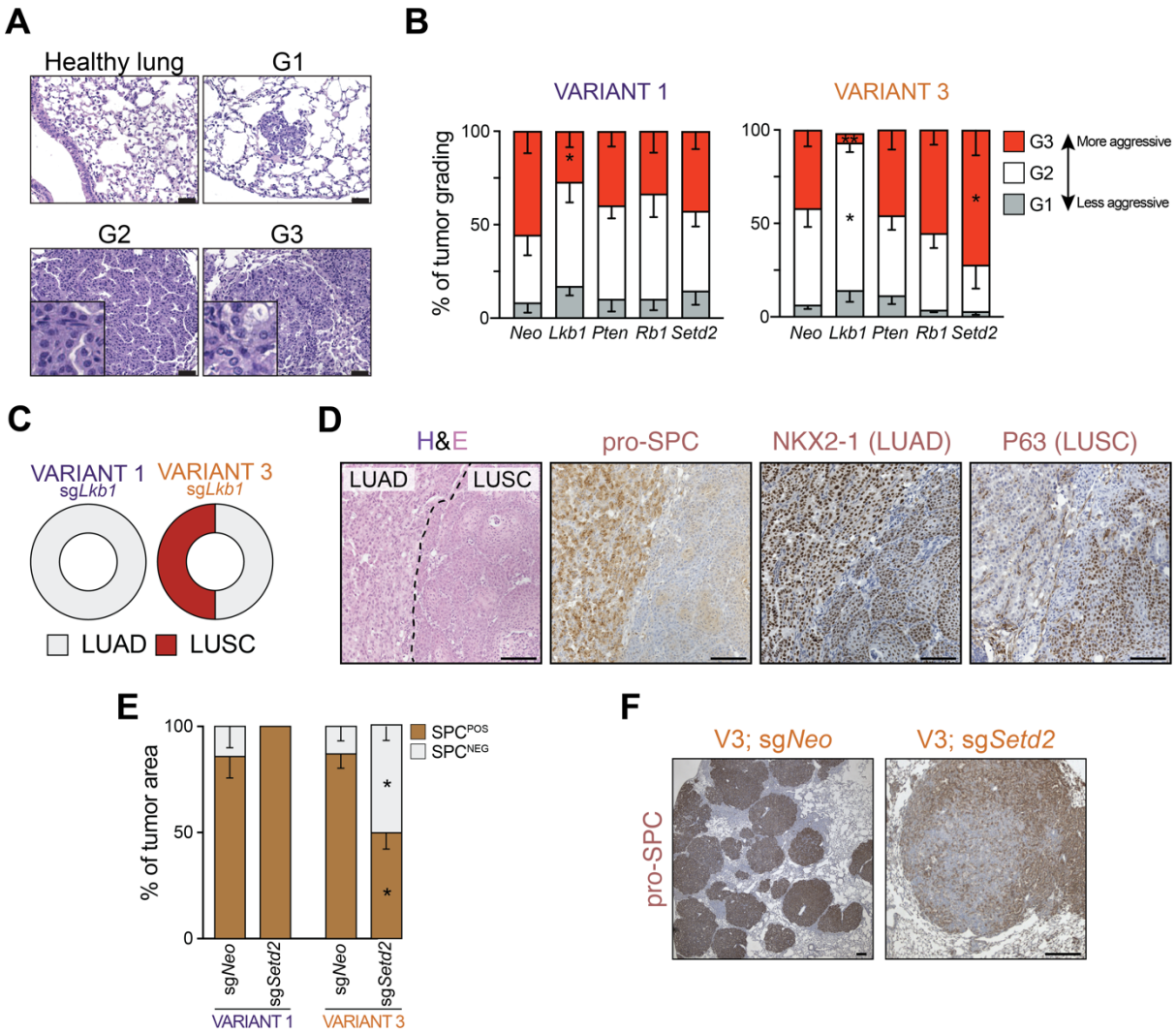


Figure 40 | Loss of tumor suppressor genes might drive histological transformations. A) Representative images of a healthy lung, grade 1 (G1), grade 2 (G2), and grade 3(G3). G1 indicates for early neoplastic lesions where cells exhibit an enlarged cytoplasm, accumulating in a solid tumor with a uniform nucleus. G2 include tumors which cells have slightly irregular nuclei and prominent nucleus. G3 tumors exhibit cells with pleomorphic nucleus. **B)** Stacked bars showing percentage of tumor grading per tumor genotype. Error bars indicate SEM. P-value <0.05 (*). **C)** Donut plot representing the frequency of LUAD and LUSC in EML4-ALK V1 and V3-driven *Lkb1*-deficient tumors. **D)** Representative H&E and SPC (pro-SPC), NKX2-1 and P63 staining. Scale bars are 100 µm. **E)** Stacked

bars showing percentage of SPC positive or negative tumor area. Error bars indicate SEM. One-way Anova, multiple comparison. P-value <0.05 (*) of comparing *Neo* vs *Setd2* conditions. **F)** Representative SPC (pro-SPC) staining in EML4-ALK V3-driven Neo (higher magnification) or *Setd2*-deficient tumors. Scale bars are 100 μm.

Overall, the majority of EML4-ALK V1 and V3 tumors were positive for both LUAD markers, SPC and NKX2-1/TTF1. Notably, some EML4-ALK V3-driven *Setd2*-deficient tumors exhibited tumor areas lacking expression of SPC, as compared with EML4-ALK V3 Neo tumors (**Figure 40E,F**).

Collective, my findings demonstrate that alterations in these tumor suppressor genes can significantly affect tumor histology, potentially increasing tumor plasticity and heterogeneity. This may have significant implications for patient prognosis and response to treatment (Marjanovic et al. 2020; Chen et al. 2022).

Transcriptomic analysis of EML4-ALK-driven *Setd2*-deficient lung tumors

Given the significant impact of *Setd2* inactivation on EML4-ALK V3-driven tumor growth, reduced survival in our mouse model, and its frequent mutation in cancer EML4-ALK-positive lung cancer patients (~6%), I decided to further investigate the role of *Setd2* in EML4-ALK-driven tumors. SETD2 is a histone methyltransferase that has been identified as a tumor suppressor in prostate, kidney, and lung cancer (Walter et al. 2017; Yuan et al. 2020; Zhu et al. 2021; Leung et al. 2022; Yang et al. 2022; Xie et al. 2023). However, no previous studies have suggested that SETD2 suppresses the growth of EML4-ALK V3-driven lung cancer.

To further investigate the tumor-suppressive effect of SETD2, I conducted immunohistochemical analysis of *Cas9-EGFP* mice transduced with either Lenti-sg*Setd2*-sgV1/Cre or Lenti-sg*Setd2*-sgV3/Cre, compared to a control group receiving Lenti-sg*Neo*-sgV1/Cre or Lenti-sg*Neo*-sgV3/Cre. To confirm the correct inactivation of *Setd2*, I firstly analyzed the presence of the trimethyl mark on H3K36 (H3K36me3), a mark of active transcription that is solely regulated by SETD2 (**Figure 41A**). Relative to controls, sg*Setd2* efficiently inactivated the targeted gene in V1 and V3-driven tumors (**Figure 41B**). In addition, H3K36me3 showed an inverse correlation with tumor size within individual mice. EML4-ALK V3 tumors lacking H3K36me3 (*Setd2*-deficient) were significantly larger compared to those expressing H3K36me3 (*Setd2*-proficient) within the same lung (**Figure 41C**), confirming our previous Tuba-seq results.

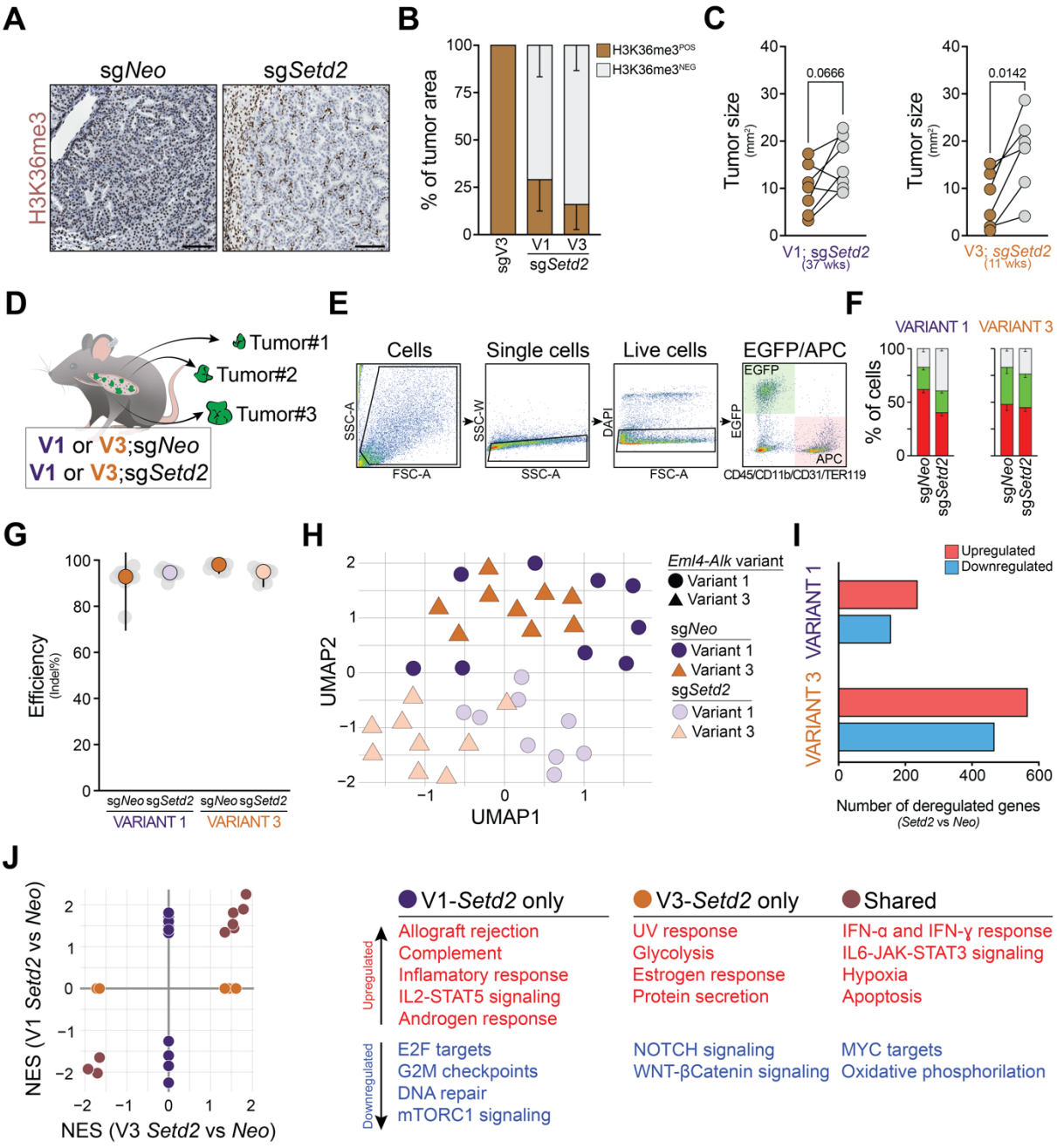


Figure 41 | Inactivation of *Setd2* impact the V3-transcriptomic profile. A) Representative immunohistochemistry of H3K36me3 of a EML4-ALK V3-driven *Neo*-deficient (left) and *Setd2*-deficient (right). Same pattern was observed in corresponding EML4-ALK V1-driven tumors. Scale bars are 100 µm. **B)** Percentage of H3K36me3 positive or negative tumor area. EML4-ALK V3-driven *Neo*-deficient is used as positive control. **C)** Size (mm^2) of H3K36me3 positive or negative tumors from Lenti-sg*Setd2*-sgV1/Cre (left) and Lenti-sg*Setd2*-sgV3/Cre (right) infected mice. Each dot is the mean of tumor size from one mouse. Connecting lines indicate matching samples. T-test on paired samples was performed and nominal P-values are shown. **D)** Schematic of the experimental workflow. *Cas9-EGFP* mice (*Rosa26*$^{LSL\text{-}Cas9\text{-}EGFP/+}$) were transduced with Lenti-sg*Neo*-sgV1/Cre, Lenti-sg*Neo*-sgV3/Cre, Lenti-sgSetd2-sgV1/Cre or Lenti-sgSetd2-sgV3/Cre as indicated in Figure 37A. Single tumors from each mouse were processed for fluorescence-activated cell sorting (FACS). **E)** FACS strategy for sorting neoplastic cells (EGFP$^+$/CD45$^-$/CD11b$^-$/CD31$^-$/TER119$^-$). **F)** Frequency of EGFP (green), CD45/CD11b/CD31/TER119 (APC, red) and double negative cells from (D-E). **G)** Percentage of insertion-deletion (indel) from sorted neoplastic cells. Each colored point is the mean of indels for that genotype. Grey points indicate individual tumors. Vertical lines indicate the coefficient of interval. **H)** UMAP plot normalized values Using 6,000 most variable genes. Each point is a tumor shaped and colored according to their *Eml4-Alk* variant and sgRNA. **I)** Number of deregulated genes when comparing *Setd2*-deficient versus *Neo*-deficient tumors for each variant. **J)** Pathway enrichment analysis of V1 and V3-driven *Setd2*-deficient tumors compared with corresponding V1 and V3-driven *Neo*-deficient tumors.

Since SETD2 is a significant epigenetic transcriptional activator (Sun et al. 2005), its inactivation is expected to have a significant impact on the transcriptomic profiles. Therefore, I conducted a transcriptomic analysis to better understand its role in suppressing EML4-ALK V3 lung tumor growth. To compare the transcriptional profiles of *Setd2*-deficient and proficient tumors, I sorted neoplastic cells ($EGFP^{POS}$ from the $Rosa26^{LSL\text{-}Cas9\text{-}EGFP/+}$ transgene) from single tumors initiated in Lenti-sg*Setd2*-sgV1/Cre or Lenti-sg*Setd2*-sgV3/Cre, as well as the controls Lenti-sg*Neo*-sgV1/Cre or Lenti-sg*Neo*-sgV3/Cre (**Figure 41D-F**). I evaluated the correct CRISPR/Cas9 gene edited by analyzing the percentage of insertion-deletion (Indel) and performed RNA sequencing on three tumor samples per mouse and a total of three mice per genotype (**Figure 41G**). Following bioinformatic analysis was then performed by Oscar Gonzalez, from Benedikt Brors' group, with constant discussion with me.

Uniform Manifold Approximation and Projection (UMAP) analysis revealed a segregation between *Setd2*-deficient and *Setd2*-proficient samples, indicating distinct transcriptional changes within these genotypes. In contrast, the EML4-ALK V1 and V3 samples clustered together, suggesting conserved transcriptional programs regardless of the EML4-ALK variant (**Figure 41H**). Besides, the inactivation of *Setd2* in V3 tumors largely affected the number of deregulated genes as compared with EML4-ALK V1-driven *Setd2*-deficient tumors (**Figure 41I**). Pathway enrichment analysis on EML4-ALK V1 and V3-driven *Setd2*-deficient tumors, highlighted exclusive EML4-ALK V1 and V3 programs, as well as shared deregulated pathways. Interestingly, EML4-ALK V1 and V3-driven *Setd2*-deficient tumors showed upregulation of IFN-α and IFN-ɣ response and IL6-JAK-STAT3 signaling which might suggest a complex interplay with their immune microenvironment (**Figure 41J**). Further analysis will elucidate the underlaying mechanisms behind these processes.

Therapeutic response of multiple EML4-ALK tumor genotypes

ALK patients eventually develop resistance to available ALK inhibitors due to refractory ALK mutations or heterogeneous ALK-independent resistance mechanisms (Gainor et al. 2016; Yoda et al. 2018; Shiba-Ishii et al. 2022). Alterations in tumor suppressor genes could drive these resistant mechanisms by activating bypass signaling pathways. Retrospective clinical studies highlighted that loss of *TP53* significantly limits the response to ALK inhibitors (Kron et al. 2018; Christopoulos et al. 2018). A different study highlighted the potential implication of mTOR activation through the loss of *NF2* in ALK-resistant samples (Recondo et al. 2020). However, there is a significant gap in understanding the potential influence of other concurrent genomic alterations on the response to EML4-ALK therapy.

To investigate the pharmacological response of multiple EML4-ALK-driven tumor genotypes, I prioritized tumor suppressor genes that were mutated in EML4-ALK-driven human tumors, exhibited strong cooperation in our Tuba-seq data, or were reported to be relevant in other tumor models (*Pten, Cdkn2a, Trp53, Kmt2d…*) (**Figure 42A**). Besides, genes (hereafter, pseudo-drug targets) that could potentially be inhibited alongside ALK inhibitors were included based on their involvement in oncogenic signaling pathways (*Egfr, cRaf, bRaf, Erk1, Stat3…*) (**Figure 42A**). This second panel is clinically relevant as inactivation of pseudo-drug targets may enhance therapeutic efficacy and potentially overcome resistance mechanisms in patients receiving solely ALK inhibitors.

In this experimental frame, we sought to explore the pharmacological response to the ALK inhibitor lorlatinib given its promising results in ongoing clinical trials (Kuang and Leighl 2021; Shiba-Ishii et al. 2022; Solomon et al. 2023). Besides, we included the SHP2 inhibitor SHP099 in combination with lorlatinib based on promising preclinical data demonstrating a synergistic effect of this combination (Dardaei et al. 2018; Drilon et al. 2023). This approach is currently being evaluated in clinical trials (NCT04292119 and NCT04800822), suggesting its potential for therapeutic application. By including both inhibitors, our study will not only identify tumor genotypes that do not respond to lorlatinib, but will also explore whether the combinatorial treatment has enhanced efficacy against aggressive tumors. Furthermore, pseudo-drug targets could illuminate promising combination therapies involving lorlatinib, either alone or in combination with SHP2 inhibitors, potentially paving the way for improved ongoing clinical efforts (**Figure 42B**).

Two pools of barcoded lentiviral vectors were generated with the help of Kalman Somogyi: Lenti-sgControls^{13}-sgV1-BC/Cre and Lenti-sgGenes^{104}-sgV3-BC/Cre (**Figure 42A**). The Lenti-sgControls^{13}-sgV1-BC/Cre pool includes only sgControls (sgInerts as *Neo* and *NT*, and sgRNA targeting essential genes *Pcna* and *Psma3*), while Lenti-sgGenes^{104}-sgV3-BC/Cre encodes sgRNAs targeting control genes, tumor suppressor genes, and pseudo-drug targets. Both lentiviral pools were mixed at a 1:2 ratio (V1 to V3) prior to mouse transduction (hereafter, Lenti-sgGenes^{117}-sgEA-BC/Cre). We exclusively used sgControls in V1-encoded lentivectors as they have a longer tumor development time compared to EML4-ALK V3-driven tumors, and therefore it is unlikely that V1-control tumors would be captured by Tuba-seq.

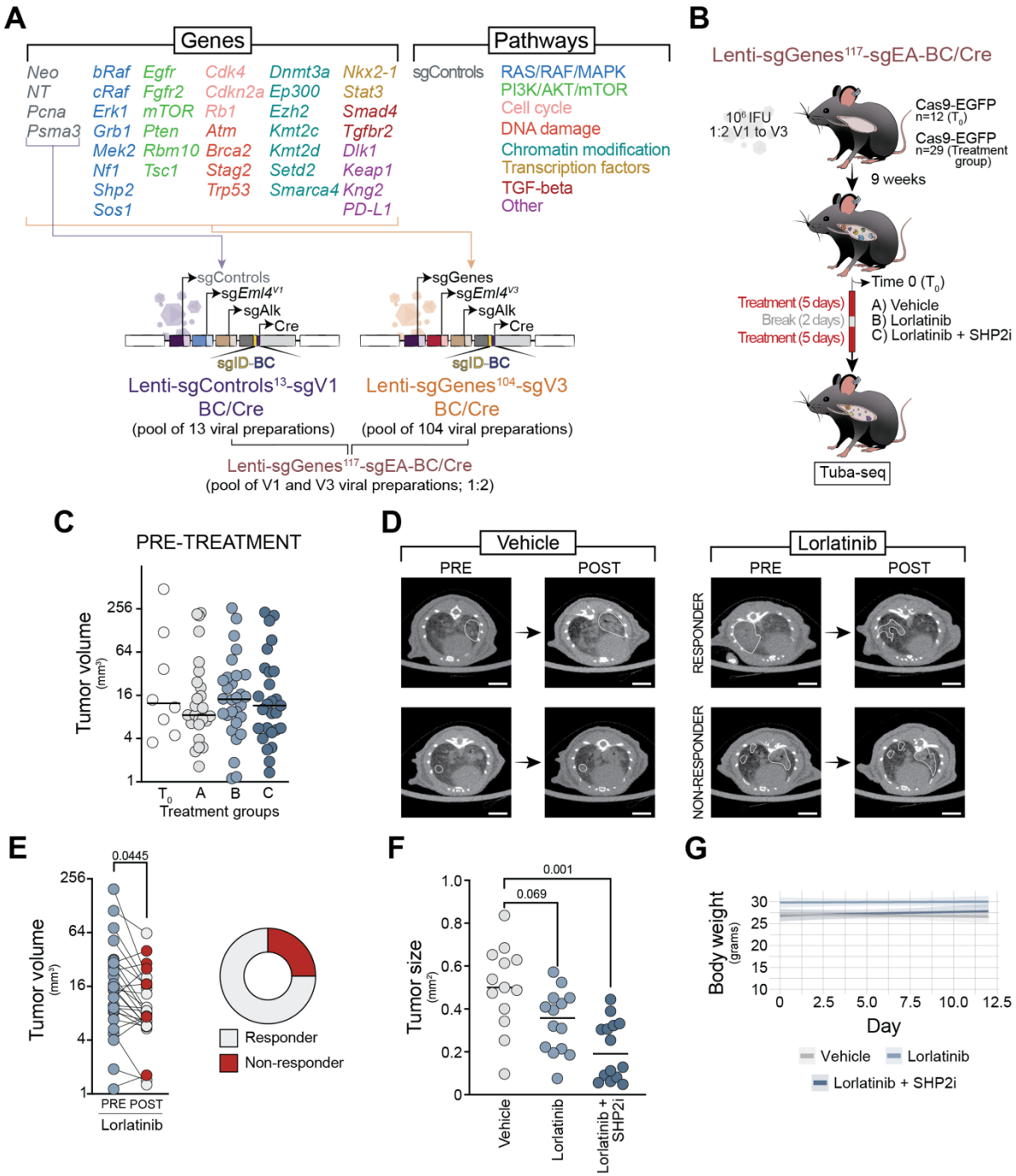


Figure 42 | EML4-ALK-driven tumors respond to lorlatinib. A) Lenti-sgGenes^{117}-sgEA-BC/Cre pool includes Lenti-sgControls^{13}-sgV1-BC/Cre and Lenti-sgGenes^{104}-sgV3-BC/Cre in a ratio 1:2. Each gene is targeted with 2 to 4 sgRNAs. **B)** Schematic of the experimental workflow. Cas9-EGFP mice (Rosa26$^{LSL\text{-}Cas9\text{-}EGFP/+}$) were intratracheal instilled with Lenti-sgGenes^{117}-sgEA-BC/Cre pool. Mice were assigned to T_0 (n= 12), vehicle (n=29), lorlatinib (n=29) or lorlatinib in combination with SHP2i (n=29). Mice were treated as indicated and lungs were collected for Tuba-seq analyses. **C)** Tumor volume (mm^3) measured by µCT before treatment of the indicated experimental groups. Each dot represents the median of tumor size per mouse. Group A was used as vehicle, group B as lorlatinib and group C as lorlatinib in combination with SHP2i. **D)** Representative µCT images from vehicle and lorlatinib mice before and after treatment. White lines indicate representative tumors that regress or progress upon treatment. Scale bars are 5 mm. **E)** Tumor volume (mm^3) of lorlatinib treated mice before and after treatment. Each dot represents the median of tumor volume per mouse. Connecting lines indicate matching samples. Paired T-test was performed, nominal P-value is indicated. Right panel show the percentage of responder and non-responder mice (Tumor volume pre-treatment < post-treatment). **F)** Tumor size (mm^2) from mice treated as indicated. Each dot represents the median of tumor volume per mouse. Multiple regression model analysis was performed with

vehicle as the reference level. Nominal P-values are indicated. **G)** Mouse body weight during treatment. Shadows indicate the confidence intervals.

I transduced independent cohorts of *Cas9-EGFP* mice with Lenti-sgGenes[117]-sgEA-BC/Cre (**Figure 42B**) and Cas9-negative control mice (*Kras*$^{LSL\text{-}G12D/+}$*; p53*$^{flox/flox}$). 9 weeks after viral injection, mice exhibited a mid to high tumor volume by µCT (median 10.9 mm^3, SD 76.2). I then assigned the mice to four treatment groups ensuring an initial equal distribution of tumor volume across all treatment arms (**Figure 42B,C**; multiple comparison one-way ANOVA, lowest *P-value* 0.3818). At the start of the treatment, I collected the lungs from 12 *Cas9-EGFP* transduced mice that will assess tumor size prior to treatment (Time 0; T_0). Lung monitoring by µCT in the vehicle and lorlatinib arms, demonstrated tumor regression after treatment (**Figure 42D,E**). Interestingly, despite the overall reduction by half in tumor volume ($\bar{x}$ vehicle= 26.07 mm^3, $\bar{x}$ lorlatinib =12.48 mm^3), comparison of pre- and post-treated tumors showed that 25% of lorlatinib-treated mice exhibited slight tumor growth (**Figure 42D,E**). Overall lung imaging assessment of tumor size showed that both lorlatinib and lorlatinib + SHP2i tend to reduce tumor size compared to the vehicle, with a higher effect in the lorlatinib + SHP2i arm (**Figure 42F**). Neither lorlatinib alone nor in combination with SPH2i caused any toxicity as measured by body weight loss (**Figure 42F,G**).

Future Tuba-seq analyses will determine which tumor suppressor genes affect lorlatinib activity. Additionally, ultra-deep sequencing of targeted *Alk* DNA regions will demonstrate if resistant tumors are driven by ALK kinase mutations or by the loss of specific tumor suppressor genes. Finally, by including pseudo-drug targets, this experiment will identify additional treatment opportunities to improve patient outcomes when used in combination with lorlatinib or lorlatinib and SHP2i.

DISCUSSION

Optimizing therapeutic outcomes: exploring treatment responses in EML4-ALK variants and the potential of combinatorial approaches.

The discovery of the *EML4-ALK* oncogene represents a critical milestone in precision medicine, providing important insights into targeted therapies across multiple tumor entities. In the last decades, a major progress has been made in the development of a new generation of ALK inhibitors, leading to the dramatic improvement of these patients (Kuang and Leighl 2021; Cooper et al. 2022; Schneider et al. 2023). However, ALK patients eventually develop resistance to available ALK inhibitors due to refractory ALK mutations or heterogeneous ALK-independent resistance mechanisms (Gainor et al. 2016; Yoda et al. 2018; Shiba-Ishii et al. 2022), which represent an urgent need to improve therapeutic responses. Beside this, different *EML4-ALK* variants have been proposed to exhibit differences in treatment responses, which can significantly impact the management of these patients.

Refining preclinical modeling of *EML4-ALK*: current limitations and future perspective

Understanding the distinct characteristics of the various *EML4-ALK* variants is crucial for tailoring targeted therapies and optimizing patient outcomes. In this regard, important knowledge was gained from *in vitro* studies (Katayama et al. 2012; Recondo et al. 2020; Shiba-Ishii et al. 2022). However, it is important to note that these studies were based on the overexpression of human *EML4-ALK* constructs. The overexpression of *EML4-ALK* using artificial promoters can misrepresent the physiological levels of the oncoprotein, potentially leading to misleading experimental results. Besides, studies involving mutagenesis and screening of ALK inhibitors rely on the overexpression of *EML4-ALK* in untransformed cells. Although fundamental, these drug screens have been performed in Ba/F3 cells (Soda et al. 2007; Choi et al. 2008; Zou et al. 2015; Gainor et al. 2016; Recondo et al. 2020; Shiba-Ishii et al. 2022), a murine pro-B cell line, or in the mouse embryonic fibroblast cell line NIH3T3 (Soda et al. 2007; Choi et al. 2008; Zou et al. 2015; Shiba-Ishii et al. 2022). While these isogenic cell systems are popular for kinase and transformation screens, they do not accurately recapitulate the lung origin of the disease.

To model the ALK disease preclinically, I generated several V1 and V3 cells derived from EML4-ALK-driven murine lung tumors that display classical LUAD features and responded to ALK inhibitors. These lung tumors were induced using CRISPR/Cas9 technology and therefore they carry the endogenous *Eml4-Alk* chromosomal rearrangement. The expression of this rearrangement is tightly regulated by the *Eml4* promoter, similar to ALK-positive patients, making them a suitable preclinical tool to study ALK therapeutic responses *in vitro*.

EML4-ALK variant responses to ALK inhibitors

Prior investigations have suggested a correlation between the presence of EML4-ALK V3 and an unfavorable prognosis (Woo et al. 2016; Christopoulos et al. 2018). Biochemical analyses have illuminated the underlying mechanism of this heightened aggressiveness, attributing it to the increased stability of the EML4-ALK V3 protein (Heuckmann et al. 2012; Woo et al. 2016; O'Regan et al. 2020). Nevertheless, due to the diversity among patients, the clarity of conclusions regarding the responses of different EML4-ALK variants remains uncertain. In this study, I discovered that V3 cells exhibited a lower sensitivity to brigatinib and lorlatinib, two potent ALK inhibitors. Biochemically, I did not find strikingly differences in the activation levels of the main ALK surrogates among both *Eml4-Alk* variants. It should be noted that the loss of *Trp53* in the cell lines may have influenced the results. In this study, I employed *Trp53* null, V1, and V3 cell models, as I failed to establish V1 and V3 cell lines from *Trp53*-proficient tumors. However, a *Trp53*-deficient background was employed based on clinical evidence showing *TP53* gene mutations in 30% of ALK-rearranged LUAD patients (GENIE, (Kron et al. 2018; Christopoulos et al. 2018)). In addition, recent clinical results highlighted that loss of *TP53* significantly limits the response to ALK inhibitors (Kron et al. 2018; Christopoulos et al. 2018). Importantly, alongside these advancements, contradictory findings have emerged when examining EML4-ALK patient outcomes stratified by specific EML4-ALK variants. Therefore, to refine therapeutic strategies, further research is needed to understand the responses observed in different EML4-ALK variants depending on *TP53* status. Furthermore, given the complexity of the tumor and its microenvironment, it would be interesting to evaluate the therapeutic response to ALK inhibitors using *Eml4-Alk in vivo* models.

Synergizing therapeutic approaches: EML4-ALK and combinatorial treatments

Combinatorial treatments have shown promise in several cancer types. Co-inhibition of EGFR and C-RAF results in complete regression of pancreatic tumors (Blasco et al. 2019).

Similarly, EGFR-driven lung cancer could benefit from the co-inhibition of EGFR and its downstream targets. In addition, these studies revealed that employing lower doses of each inhibitor not only reduces the risk of relapse but also mitigates associated toxicities (Neto et al. 2020; Settleman et al. 2021). This finding underscores the potential benefits of optimizing treatment regimens to achieve a delicate balance between therapeutic efficacy and minimizing adverse effects (Blasco et al. 2011; Sanclemente et al. 2018; Neto et al. 2020). However, this approach was not yet explored in the context of ALK-LUADs. In this regard, I reasoned that co-inhibition of ALK and ERK1/2 kinases could increase the therapeutic response to ALK inhibitors. Despite the success observed in increasing cell death *in vitro*, the translation of this strategy to *in vivo* models proved to be ineffective. A potential explanation for this discrepancy lies in the insufficient pharmacological activity of ALK and ERK1/2 inhibitors *in vivo*. In this regard main factors such as drug metabolism, biodistribution, and target engagement within the complex *in vivo*, could greatly affect the activity profiles of these inhibitors. Therefore, future experiments should aim to scrutinize the inhibitors' activities directly on tumor samples, considering factors such as drug stability, drug penetration or by biochemical analysis on signaling pathways.

In light of the limited success observed with the co-inhibition of ALK and ERK1/2, we turned our attention to the exploration of an alternative combinatorial approach. SRC was previously proposed as a potential bypass mechanism in already ALK resistant cells (Crystal et al. 2014; Yoshida et al. 2017), while its contribution to untreated tumors has not been addressed. Beyond this point, the potential interplay between the SRC and ALK pathways remains elusive. Proteomic analysis of V3 cells treated with brigatinib further supported this rationale, as treated cells exhibited a significant upregulation of SRC. Further supporting SRC role in cancer, interacting with receptor tyrosine kinases (RTKs) and non-RTKs which can contribute to tumorigenesis (Playford and Schaller 2004; Montero et al. 2011; Chen et al. 2014). Moreover, studies employing *ex vivo* cultures from BRAF and EGFR-driven colorectal tumors, demonstrated that SRC could act as a bypass mechanism (Higuchi et al. 2021; Gavert et al. 2022; Ruiz-Saenz et al. 2023). In line with this, I found that co-inhibition of ALK and SRC profoundly affects EML4-ALK-tumor cell growth *in vitro* and *in vivo*. In our study, inhibition of ALK and SRC synergize by disrupting the (phospho)proteomic profiles of EML4-ALK tumor cells. Previous studies have highlighted the role of SRC in already ALK-resistant cells, by activating critical signaling molecules of the MAPK and PI3K/ATK pathways or inducting an EMT phenotype (Crystal et al. 2014; Yoshida et al. 2017). In line with these reports, we further proved that co-inhibition of ALK and SRC strongly suppresses ALK surrogates and enhances cell apoptosis in previously untreated EML4-ALK driven tumor cells.

My thesis has revealed that chemical inhibition of SRC has a significant impact on GTPase activity and the phosphorylation of pivotal kinases, particularly AKT1. This finding suggests the existence of an SRC-AKT-driven drug-bypass mechanism. It is noteworthy that GTPases and ALK are recognized to organize into protein-based structures, actively participating in signaling cascades by engaging with the GRB2/SOS1 complex (Sampson et al. 2021; Tulpule et al. 2021). Interestingly, I found GRB2 to be downregulated upon SRC and ALK treatment, further suggesting a complete disruption of ALK signaling nodes. This disruption is reflected in the pronounced suppression of key oncogenic proteins in NSCLC, including STATs, RAFs, and STKs, as well as critical phosphorylation sites within the MAPK pathways. Notably, this effect probably arose from the downregulation of ALK protein levels, in sharp contrast to the compensatory increase observed with brigatinib treatment. These findings provide insights into potential compensatory pathways that may underlie resistance to ALK inhibition and extend our current knowledge on the role of SRC in ALK tumor cells.

Role of mTOR in treatment responses to ALK and SRC inhibitor combination

Concurrent targeting of ALK and SRC based on our (phospho)proteomic data had a profound inhibitory effect on the mTOR axis, a master regulator of cell metabolism (Liu and Sabatini 2020). Previous studies have implicated mTOR in lorlatinib resistance upon inactivation of *NF2*, a negative regulator of mTORC1 (Recondo et al. 2020). Other studies have exploited the benefit of using mTOR inhibitors in ALK-driven neuroblastoma (Marzec et al. 2007; Moore et al. 2014; Redaelli et al. 2016). In addition, SRC has previously been implicated in cell metabolism (Pelaz and Tabernero 2022). In our study, we observed that inhibition of mTORC1/C2 enhanced cell toxicity in combination with ALK inhibitors. An ongoing clinical trial (NCT02321501) is evaluating the feasibility of simultaneous ALK and mTOR inhibition in ALK-driven lung cancer patients, providing a clinical perspective within this promising scenario. In this regard, the preclinical studies of this thesis anticipate a positive therapeutic response. Nevertheless, I hypothesize that this heightened sensitivity is not only due to the direct regulatory effects on mTOR. Targeting SRC is a strategic approach due to its potential to impact multiple signaling pathways, surpassing the narrower focus on the mTOR pathway alone.

In summary, the work of my PhD Thesis supports the proposition that SRC plays a crucial role in enhancing the efficacy of ALK inhibitors, effectively delaying the onset of resistance. Furthermore, this study contributes to the existing understanding of SRC-mediated resistance by conducting an extensive (phospho)proteomic analysis, providing a comprehensive and robust interpretation of the significant antitumor effects achieved through

the concurrent inhibition of ALK and SRC. This outcome supports the use of combinatorial therapeutic approaches and highlights their potential as a primary treatment option.

Tumor suppressor dynamics: modeling EML4-ALK V1 and V3 genotypic responses

In the intricate and finely regulated landscape of human genomics, loss of tumor suppressor genes primes tumors for unrestrained growth and progression. The wide genomic diversity in cancer, even within tumors driven by the same oncogene, complicates the identification of driver and passenger mutations. Within this narrative, the emergence of EML4-ALK fusion-driven lung tumors and the discovery of its variants adds a layer of complexity to our understanding of the molecular mechanisms governing this phenomenon.

Generation of a novel EML4-ALK-driven mouse model to investigate concurrent genomic alterations

Previous mouse models of EML4-ALK-driven lung cancer have relied on transgenes to overexpress the EML4-ALK V1 fusion (Soda et al. 2008). Subsequent models of the disease have been based on lentiviruses or adenoviruses to induce *Eml4-Alk* V1 genomic rearrangement (Blasco et al. 2014; Maddalo et al. 2014). Although clinically relevant, these models have not been used to investigate the effect of concurrent genomic alterations in the context of EML4-ALK. To do so, I integrated CRISPR/Cas9-mediated gene editing and high-throughput tumor barcode sequencing (Tuba-seq, Rogers et al. 2018; Cai et al. 2021) to quantify EML4-ALK-variant oncogenicity and uncover the effect of 29 tumor suppressor genes on tumor growth. These mouse models represent a significant advancement in cancer genomics and disease modeling, achieving a challenging genomic intervention by simultaneously inactivating a tumor suppressor gene and inducing a paracentric chromosomal rearrangement.

This methodology involves the use of lentiviruses to ensure stable integration into the mouse genome, a critical requirement for subsequent barcoding analysis. Compared to other genetically engineered mouse models, our systems provide a rapid and scalable method to quantify hundreds of tumor genotypes (Winters et al. 2018). While this approach offers advantages, it is important to consider potential drawbacks. The integration of multiple lentiviruses into the same cell could potentially generate a single tumor with several genomic alterations, increasing the false positive error rate. To mitigate this, we reduced the lentivirus dose in our experiments and still found consistent results when comparing sgTSG[19] and

sgTSG^{75} pools. Furthermore, in later analyses, I validated V1 and V3-driven, *Lkb1*, *Pten*, *Rb1* and *Setd2*-deficient tumor phenotypes that align with our tumor barcoding analyses.

EML4-ALK driven lung tumors car arise from club cells and AT2 cells (Chen et al. 2022). Of note, previous studies have shown that lentiviruses have a preference for transducing AT2-cells, whereas adenoviruses have a broader cell tropism (unpublish data form the Lab). This distinction is relevant because it may influence cell-type specificity in the tumor-suppressive functions of certain genes. For example, loss of *Lkb1* or *Smarca4* enhances KRAS-driven tumorigenesis exclusively on club cells (Nagaraj et al. 2017; Concepcion et al. 2021). Further efforts using traditional lung cell-lineage tracing models are required to determine if the observed phenotypes are cell-type specific.

In addition, the use of a constitutive Cas9 expression mouse model ($R26^{LSL\text{-}Cas9\text{-}EGFP}$) can present challenges in achieving precise temporal control of genome editing, potentially leading to unintended off-target effects (Höijer et al. 2022; Guo et al. 2023). Moreover, sustained Cas9 expression can induce cellular responses that affect the overall physiological state of the system (Crudele and Chamberlain 2018). Future use of an inducible Cas9 mouse model may mitigate these disadvantages. Besides, it is crucial to account for the temporal aspects of human tumor development and the specific points in time when alterations in tumor suppressor genes may occur. However, since both *Eml4-Alk* rearrangement and tumor suppressor gene inactivation depend on CRISPR/Cas9 activity, I was challenged by the inability to induce these two events at different time points. Further experiments with inducible shRNAs may be required to inactivate tumor suppressor genes earlier or later than the oncogenic event. Finally, the use of a constitutive Cas9 model could potentially lead to homozygous inactivation of tumor suppressor genes, due to constant on-target Cas9-activity. This may be far from human genetics, where both or only one copy of a tumor suppressor gene is altered (Park et al. 2005; Song et al. 2012; Davoli et al. 2013; Schmutz et al. 2020). In this regard, *in vivo* experiments with traditional genetically modified mouse models employing the Cre-lox system could be crucial to address this issue.

EML4-ALK V1 and V3 lung tumors cooperate with different tumor suppressor genes

While previous studies have primarily focused on *TP53* mutations (Zhang et al. 2021), our methodology not only confirms these findings but also enhances our understanding by revealing the functionality of 28 additional genomic interactions. Furthermore, we identified unexpectedly diverse genetic interactions that strongly and specifically influence tumorigenesis in a EML4-ALK variant-specific manner. These findings indicate that the biology

underlying EML4-ALK V1 and V3-driven lung tumors is distinct, and that various fusion partner protein variants can significantly modify the effects of other pathways on tumor phenotypes.

The EML4-ALK fusion gene comprises various variants, all of which contain the tyrosine kinase of ALK (Sabir et al. 2017). However, they differ significantly in the proportion of the EML4 gene they include (Sabir et al. 2017). The EML4-ALK variants V1 and V3 differ particularly in the length of the TAPE domain and the presence of the HELP domain. V1 contains both domains, whereas V3 only harbors a small fraction of the TAPE domain (Sabir et al. 2017). In this regard, certain studies have indicated differences in tyrosine kinase activity, structural stability, and sensitivity to ALK inhibitors, resulting in distinct biological behaviors among EML4-ALK variants (Heuckmann et al. 2012; O'Regan et al. 2020). For this reason, it is reasonable to assume that tumor suppressor genes with similar effects in V1 and V3, impact pathways downstream of ALK kinase activity, while tumor suppressor genes with different effects are likely downstream of the HELP/TAPE domains. In line with this, a previous study conducted by Trever G Bivona found that EML4-ALK V1 interacts with RAS isoforms through the HELP domain, which is not observed in EML4-ALK V3 (Hrustanovic et al. 2015). Similarly, we discovered that the inactivation of *Nf1*, a negative regulator of RAS, only increased the size of EML4-ALK V1-driven lung tumors, coincident with its interaction with RAS isoforms.

The fitness landscape of EML4-ALK-driven lung tumors was significantly compromised by the inactivation of *Kmt2d*, *Cmtr2*, and *Brca2* genes in both V1 and V3. The biological function of KMT2D appears to be lung cancer driver specific. While it has a negative impact on EML4-ALK-driven tumors, loss of *Kmt2d* increases the growth of KRAS and $EGFR^{L858R}$ -driven tumors (Alam et al. 2020; Pan et al. 2023). Inactivation of *Kmt2d* has been also associated with the hyperactivation of receptor tyrosine kinases through chromatin remodeling, which leads to the enhancement of glycolysis and other mTOR-related outputs (Alam et al. 2020; Pan et al. 2023). Interestingly, others, as well as I, have shown that EML4-ALK tumor cells are sensitive to mTOR inhibition (Alam et al. 2020; Pan et al. 2023). In line with this, loss of *Tsc1*, a negative regulator of mTOR (Liu and Sabatini 2020), enhanced the growth of EML4-ALK-driven tumors, further highlighting the relevance of this pathway. Similar to *Kmt2d*, the loss of *Cmtr2* exhibits a deleterious effect on EML4-ALK-driven tumors, while it has a positive effect in the context of KRAS-driven tumors. CMTR2 modifies the 5'-cap of mRNAs and small nuclear RNAs (Werner et al. 2011). However, its specific mechanisms and implications in cancer need still to be elucidated. Inactivation of *Brca2*, resulting in a reduction of tumor growth, unveils novel avenues for assessing the susceptibility of EML4-ALK-driven tumors to genome instability. Although preliminary, these findings suggest that there is a

dependency of EML4-ALK on certain genes or pathways, which opens up new opportunities for combinational treatments.

The fitness of V1 and V3 tumors is significantly affected by various tumor suppressor genes, with specific variant-tumor suppressor gene interactions. Inactivation of *Nkx2-1, Pten* and *Rb1* largely increased the size of V1-driven tumors, while it had a neutral effect of V3 tumors. *Nkx2-1* mutations are rare in EML4-ALK patients, hinting at mutual exclusivity. Interestingly, *Nkx2-1* arose as a tumor suppressor gene in V1-driven tumors, aligning with other lung cancer models (Winslow et al. 2011; Snyder et al. 2013; Mollaoglu et al. 2018), while acting as a passenger mutation in V3-driven tumors. Loss of *Nkx2-1* induce mucinous lung tumors, which suggest that V1-tumors might benefit in transitioning to invasive mucinous adenocarcinoma. In contrast, inactivation of genes such as *Lkb1*, *Setd2*, *Smad4*, *Rbm10* or *Stag2* led to increased tumor growth of V3-driven tumors.

Single-gene validation not only solidified the robustness of the Tuba-seq method, but also revealed interesting results. Inactivation of *Lkb1* triggered transdifferentiation of LUAD to LUSC solely in EML4-ALK V3-driven tumors, echoing reports in KRAS-driven *Lkb1*-deficient settings (Han et al. 2014). While recent studies link EML4-ALK V1 to LUAD-to-LUSC transdifferentiation via JAK-STAT activation, further investigation is necessary to determine if EML4-ALK V3 follows a similar plasticity pathway or if requires *Lkb1*-inactivation (Qin et al. 2024). Notably, in line with this observed plasticity, loss of *Setd2* appears to cause down-regulation of SPC (a marker of LUAD) in EML4-ALK V3-driven tumors. These findings align with the concept of lung tumor plasticity, where phenotypic switching based on genotypic alterations can increase tumor aggressiveness (LaFave et al. 2020; Marjanovic et al. 2020; Concepcion et al. 2021; Naranjo et al. 2022; Yang et al. 2022). Transcriptomic profiling of EML4-ALK V1 and V3-driven *Setd2*-deficient tumors will elucidate the mechanisms behind this process. In addition, RNAseq analysis will also show why *Setd2*-deficient tumors are larger than EML4-ALK V3-driven tumors. One reason could be that EML4-ALK V1-driven *Setd2*-deficient tumors downregulate cell cycle and mTOR pathways, why they show upregulation in immune-activated pathways, further indicating the detrimental effect of *Setd2* inactivation in EML4-ALK V1-driven tumors.

Future considerations

The work of my thesis indicates that the impact on tumor growth varies depending on the EML4-ALK variant, highlighting the genotype-specific responses to alterations in tumor suppressor genes. Additional EML4-ALK variants can be categorized based on their EML4 domains, which may anticipate the tumor suppressor landscape of V1-like or V3-like tumors.

Notably, our quantitative and multiplexed system could be used to generate other EML4-ALK variants-driven lung cancers with inactivation of any panel of genes of interest, including other tumor suppressor genes, pathways of interest, or candidate drug targets. In this regard, it is imperative to search for mutations within the *Alk* sequencing, as they could be the driver of the resistant mechanisms. Furthermore, the broad application of similar general methods could be used to test the impact of TSG alterations on drug response *in vivo*.

Importantly, the highlighted differences among variants can impact therapy responses, as the inactivation of certain tumor suppressor genes in specific variants could activate bypass pathways. Anticipated consequences of *Nf1* mutations in EML4-ALK V1 tumors include the potential induction of resistance through RAS interaction with the HELP domain (Hrustanovic et al. 2015). It is important to note that only alterations that directly target ALK kinase activity and the signaling pathway downstream of ALK should be considered. Combination trials that fail to stratify EML4-ALK patients based on the variant and co-incident tumor suppressor alterations should be avoided due to the widespread effect of tumor suppressor genotype on drug responses in general.

In general, the importance of fusion partners and/or the difference between variants of the same fusion partner in oncogenic fusions in lung cancer (e.g. ROS1 and RET fusions) and in other carcinomas (e.g. NTRK, NRG1 and MET fusions) (Skoulidis and Heymach 2019; Consortium et al. 2020) remain largely unknown. Our data suggest that different variants of the same oncogenic fusion can be fundamentally different. Thus, beyond driving expression and multimerization of kinase domains, fusion partners that interact differentially with downstream signaling pathways will alter the molecular drivers of the disease, change how other genomic interactions impact tumorigenesis, and almost certainly modify treatment responses.

CONCLUSIONS

Therapeutic response to ALK inhibitors in variant 1 and variant 3 EML4-ALK-driven tumor cells and

- V3-driven tumor cells exhibit lower sensitivity to brigatinib and lorlatinib *in vitro*.
- No differences in the proteome were found downstream of V1 and V3 EML4-ALK that could explain the different response to brigatinib and lorlatinib.
- *In vivo* treatment of V1 and V3 tumors with brigatinib shows similar response rates.

This section of the thesis emphasizes the similar response to ALK inhibitors among EML4-ALK variants and highlights the differences between *in vitro* and *in vivo* systems. Further research is required to precisely elucidate the therapeutic response to ALK inhibitors using *in vivo* EML4-ALK models that recapitulate its tumor microenvironment.

Identify novel therapeutic opportunities using combinatorial strategies

- Dual inhibition of ALK and ERK1/2 presents benefits *in vitro*, but fails in *in vivo* model systems.
- Pharmacological inhibition of SRC synergizes with ALK inhibitors *in vitro* and *in vivo*.
- SRC and ALK inhibitors disrupt the (phospho)proteomic profile of V3-driven tumor cells.
- SRC and ALK inhibitors induce tumor cell death through sustained mTOR pathway inhibition.

The results of this section of the thesis emphasize the role of SRC in untreated ALK tumor cells. These findings suggest that EML4-ALK-driven tumor cells are dependent on SRC, which could be a potential therapeutic target in combination with ALK inhibitors. Additionally, this thesis expands on previous knowledge of the role of SRC and proposes a mechanism of action involving sustained mTOR pathway inhibition.

Investigate the role of key tumor suppressor genes in EML4-ALK lung tumorigenesis

- Lentiviral-induced EML4-ALK-driven lung tumors recapitulate the main characteristics of EML4-ALK human lung adenocarcinomas.
- EML4-ALK-V3 driven lung tumors exhibits higher oncogenic capabilities as compared with V1 EML4-ALK-driven lung tumors.
- Tumor suppressor genes cooperate differently with EML4-ALK V1- and V3.
- Loss of *Lkb1* or *Setd2* can induce loss of cell identity in EML4-ALK V3-driven tumors.
- EML4-ALK V1- and V3-driven tumors show similar transcriptomic profiles, while the loss of *Setd2* impacts the transcriptomic profile of EML4-ALK V3-driven tumors.
- Inactivation of certain tumor suppressor genes could impact lorlatinib response.

This work emphasizes the significance of coupling lentiviral vectors with CRISPR/Cas9 gene editing to investigate concurrent genomic alterations in the context of EML4-ALK tumorigenesis. Importantly, this thesis provides valuable insights into the genomic interactions among different EML4-ALK variants and offers a rationale for stratifying patients based on the EML4-ALK variant and co-occurring genomic alterations.

CONTRIBUTIONS

The design, conceptualization, and execution of the experiment were done by me, unless otherwise stated in the text. Prof. Dr. Rocio Sotillo contributed to the design and conceptualization of the experiments from all chapters. Dr. Monte Winslow contributed to the design and conceptualization of the experiments from chapter 3.

Dr. Sara Chocarro and Dr. Kalman Somogyi designed and cloned the Adeno-V3/Cas9 vector, which was then produced by Viraquest. EML4-ALK-driven cells were derived and characterized by me. Experiments shown in Figure 8 to Figure 12 were performed and analyzed by me. Experiments shown in Figure 13 to Figure 21 were performed and analyzed in collaboration with Maria Ramos.

Samples for Figure 9 were prepared in collaboration with technicians of Dr. Ursula Klingmüller. Samples for Figure 15 were prepared in collaboration with Maria Ramos and technicians of Dr. Ursula Klingmüller. Proteomic and (phospho)proteomic sequencing was performed by the group of Dr. Ursula Klingmüller (Dr. Barbara Helm, Dr. Dario Lucas Frey). The proteomic analyses for Figure 9 were performed by me, while the (phospho)proteomic analyses for Figure 15 and following were performed by Dr. Junyan Lu and myself in constant discussion with Maria Ramos, Prof. Dr. Rocio Sotillo, and Dr. Ursula Klingmüller's group (Dr. Barbara Helm, Dr. Dario Lucas Frey).

I, with the help of Dr. Kalman Somogyi, designed and cloned the lentiviral vectors used in this thesis, optimizing the available protocols from Dr. Monte Winslow's lab. Lentiviral production and corresponding *in vivo* experiments were performed by myself with technical support from Dr. Alicia Alonso de la Vega and Maria Ramos. Emily Shuldiner performed the bioinformatics analysis in constant discussion with Prof. Dr. Rocio Sotillo, Dr. Monte Winslow and myself. Cloning of lentiviral vectors from Figure 42 was performed by Dr. Kalman Somogyi and myself. Corresponding lentiviral production was done by myself, and tumor induction was performed by myself with technical support from Maria Ramos and Mulham Najajreh. *in vivo* treatment and tumor analysis from Figure 42 were performed by myself. I prepared the bulk-RNAseq libraries and Dr. Oscar Gonzalez Velasco analyzed the data with constant discussion with me.

Additional advice and technical assistance were provided by Filiz-Akkas, Dr. Sara Chocarro, Dr. Pan Fan, Dr. Sridhar Kandala.

This thesis has been proofread and corrected by Prof. Dr. Rocio Sotillo.

MATERIALS AND METHODS

Mouse models

All mouse experiments described in this thesis were approved by the local veterinary authorities and by the Regierungpräsidium Karlsruhe, Baden-Wurttemberg, Germany (animal license No. G265-19). The mice were kept in the DKFZ animal facilities free from specific pathogens, where they were exposed a consistent 12-hour light-dark cycle and were provided with a standard rodent diet and water ad libitum.

Trp53$^{flox/flox}$ mice (RRID:IMSR_JAX:008462) (Marino et al. 2000)were generously provided by Dr. Claudia Scholl at DKFZ, Heidelberg, Germany. The mT/mG mice (RRID:IMSR_JAX:007676) and the CCSP-Cre mice were kindly supplied by Dr. Georgios Stathopoulos from the University of Patras, Greece. These triple transgenic mice were backcrossed and maintained on the FBV background. Additionally, *Rosa26*$^{LSL\text{-}Cas9\text{-}EGFP}$ mice (RRID:IMSR_JAX:026179), obtained from Dr. Guoliang Cui at DKFZ, Heidelberg, Germany, were on a C57BL/6J background. *Kras*$^{LSL\text{-}G12D}$ mice (RRID:IMSR_JAX:008179) obtained from Dr. Claudia Scholl at DKFZ, were on a C57BL/6J background. *Trp53*$^{flox/flox}$ transgenes were used in homozygosity, while the others were utilized in either homozygosity or heterozygosity as required for the experiments.

Mouse genotyping

Mouse ear punches were digested in 1.5 mL centrifuge tubes using 100 µL of 0.05 M NaOH for 1 hour at 95°C and 800 rpm in a thermoblock. Following digestion, the reaction was neutralized with 1 M Tris HCl at pH 7.5. The genotyping reaction was prepared as follows: 1x Dream Taq Green Buffer (Life Technologies, B71), 0.25 pmol/µL of the forward primer, 0.25 pmol/µL of the reverse primer, 200 µM dNTPs mix, 1U/20µL Taq Polymerase enzyme, and 1 µL of DNA in a final volume of 20 µL. Specifically designed primers were used to amplify the transgenes (primer details are provided in **Table 2**). Amplicons were separated on a 1 to 2% agarose gel containing peqGreen DNA dye at 120 V and visualized using a Molecular Imager GelDocTM XR+ (Biorad, # 1708195EDU).

Table 2 | PCR primers

Transgene	Direction	Sequence	Product size (bp)
mT/mG	Forward	CTCTGCTGCCTCCTGGCTTCT	Wildtype = 330
	Reverse#1	CGAGGCGGATCACAAGCAATA	
	Reverse#2	TCAATGGGCGGGGGTCGTT	Mutant = 250
***Rosa*-$^{LSL\text{-}Cas9\text{-}EGFP}$ wildtype**	Forward	CAGGACAACGCCCACACA	Wildtype = 241
	Reverse	AAGGGAGCTGCAGTGGAGTA	
***Rosa*-$^{LSL\text{-}Cas9\text{-}EGFP}$ mutant**	Forward	CTTCTTCTT TGGGGCCATCT	Mutant =214
	Reverse	TCCCCATCAAGCTGATCC	
***Trp53* floxed**	Forward	GGTTAAACCCAGCTTGACCA	Wildtype = 270
	Reverse	GGAGGCAGAGACAGTTGGAG	Mutant = 390

Eml4-Alk adenovirus and lentivirus

The *Eml4-Alk* variant 1 adenovirus was designed by Dr. Andrea Ventura and commercialized by Viraquest (North Liberty, USA). The *Eml4-Alk* variant 3 adenovirus was engineered by Sara Chocarro and Kalman Somogyi at the Sotillo Lab (DKFZ, Heidelberg, Germany) and subsequently produced by Viraquest.

The *Eml4-Alk* variant 1 and variant 3 lentiviral vectors, along with the corresponding triple sgRNA vector configuration for targeting specific genes, were designed by me and Kalman Somogyi at the Sotillo Lab (DKFZ, Heidelberg, Germany). Detailed protocols for cloning, plasmid isolation, and lentivirus production are provided in separate sections.

Cloning of sgEGFP, sg*Eml4*$^{V1\text{ or }V3}$, sg*Alk* in Lenti-PGK-Cre backbone

To clone individual sgRNAs into shuttle vectors containing distinct U6 promoters and tracer regions we modified a protocol shared by Monte Winslow and published in (Murray et al. 2019).

pMJ179 plasmid was modified by Monte Winslow lab by reverting mU6 promoter in pMJ179 to wild-type sequence using side-directed mutagenesis. BamHI site at junction of homology region and mU6 promoter in pMJ179 were also destroyed by side-directed mutagenesis (**Table 3**).

Table 3 | Lentiviral and U6-donor plasmids

Reagent	Source	Identifier
pMJ117 (hU6 promoter)	Addgene	RRID:Addgene_85997
pMJ114 (bU6 promoter)	Addgene	RRID:Addgene_85995
pMJ179 (mU6 promoter)	Addgene	RRID:Addgene_85996
Lenti-sgNeo/cre (pLL3-Lenti/Cre backbone)	Addgene	RRID:Addgene_67594

We cloned sg*EGFP*, sg*Eml4*$^{V1\ or\ V3}$ and sg*Alk* in pMJ114 (bU6-driven cassette), pMJ179 (mU6-driven cassette) and pMJ117 (hU6-driven cassette) plasmids respectively (**Table 3**). To do so, we initially performed a site directed mutagenesis using Q5 High-Fidelity DNA Polymerase with specific forward primers that included the sgRNA sequence to be introduced. The following PCR program 98˚C 30s >> 30x (98˚C 10s >> Tm˚C 15s >> 72˚C 3m) >> 72˚C 5m >> 4˚C hold was used. PCR primers and primer melting temperature (Tm) are detailed in **Table 4**, sgRNA sequences are detailed in the **Table 5**. sgRNAs were designed to have a guanine as first base for efficient transcription from U6 promoters. sgRNAs containing or creating XmaI or BamHI recognition sites were excluded as these enzymes are used in following steps. PCR amplicons were then ligated using KLD reaction (1.50 µL 2x KLD Reaction Buffer + 0.33 µL 10x KLD Enzyme Mix + 0.33 µL Amplicon + 0.84 µL UltraPure DNase/RNase-Free Distilled Water) at room temperature for 5 minutes. Then 1 µL of KLD reaction product was used to transform 9 µL of DH5α by heat shock at 42°C for 45 seconds followed up by 30 minutes incubation in SOC medium at 37°C 220 rpm in a bacterial shaker. Finally, 100 µL of transformed bacteria were plated onto pre-warmed agar plates with 100 µg/mL carbenicillin. Then, PCR bacterial colony was performed to verify the successful insertion of the new sgRNAs. A final PCR reaction was prepared by combining 10 µL of HotStarTaq Master Mix, 0.5 µM of each primer, bacterial cells, and ultra-pure water, resulting in a total volume of 20 µL. Positive bacterial colonies were grown in LB medium supplemented with 100 µg/mL ampicillin for 16 hours at 37°C with agitation at 220 rpm on a horizontal shaker. DNAs from overnight cultures were isolated using QIAprep Spin Miniprep Kit (Qiagen, #27104).

Table 4 | PCR primers used in Step 1. The consecutive Ns in the provided Forward sequence represent any nucleotide and can be selectively replaced with the desired sgRNA sequence for inclusion within the construct.

Plasmid	Direction	Sequence	Product size (bp)	Primer Tm (°C)
pMJ117 (hU6 promoter)	Forward	NNNNNNNNNNNNNNNNNNNN GTTTCAGAGCTAAGCACAAGAGT	9135	65
	Reverse	CATGTTTCTGGCTTTCCACAAG		
pMJ114 (bU6 promoter)	Forward	NNNNNNNNNNNNNNNNNNNN GTTTAAGAGCTAAGCTGGAAACAG	9147	64
	Reverse	CATAAACATGGCCTCTCAAGAACT		
pMJ179 (mU6 promoter)	Forward	NNNNNNNNNNNNNNNNNNNN GTTTGAGAGCTAAGCAGAAAGCT	9192	66
	Reverse	CAACAAGGTGGTTCTCCAAGG		

Table 5 | sgRNA sequences

Target Gene	Variant	sgRNA_Sequence	Source
***Eml4* (intron 14)**	V1	TTTGTCGGGGTCTACTAGGA	Maddalo et al., 2014
***Eml4* (intron 6)**	V3	ACAAGAGCTGACCAGTTCAG	Sara Chocarro, Kalman Somogyi

***Alk* (intron 19)**		TCCTGGCATGTCTATCTGTA	Maddalo et al., 2014
EGFP		GACCAGGATGGGCACCACCC	Monte Winslow

Then, individual U6-sgRNA cassettes and flanking homology sites were amplified. Amplicons were generated using Q5 High-Fidelity DNA Polymerase with specific forward primers for each vector using the PCR program 98˚C 30s >> 30x (98˚C 10s >> Tm˚C 15s >> 72˚C 15s) >> 72˚C 5m >> 4˚C hold. PCR primers and primer melting temperature (Tm) are detailed in the **Table 6**. The resulting amplicons were then resolved by electrophoresis on a 0.75% agarose gel containing peqGreen DNA dye, with an applied voltage of 120V. PCR products were excised from the gel using a green LED light source and an Invitrogen iBright FL1500 Imaging System to prevent UV-induced mutations. The excised gel bands were further processed using the QIAquick Gel Extraction Kit (Qiagen, #28704) following the manufacturer's instructions.

Table 6 | PCR primers used in Step 2

Plasmid	Direction	Sequence	Product size (bp)	Primer Tm (°C)
pMJ117 (hU6 promoter)	Forward	GCTCGAATCTACACTCAGCTATG	426	66
	Reverse	ATAGGCGCGCCAAACAAAAAAAGCACCCGACTCGG		
pMJ114 (bU6 promoter)	Forward	AACTGTTTAAACTGTCGTGACCGAGCTTGTCTG	438	65
	Reverse	CATCGTGATAGTCAGACTGGAAAAA		
pMJ179 (mU6 promoter)	Forward	CCAGTCTGACTATCACGATTGA	468	64
	Reverse	GCTGAGTGTAGATTCGAGCAAA		

U6-driven cassette amplicons were then assembled into pLL3-Lenti/Cre backbone. Firstly, pLL3-Lenti/Cre backbone was linearized by PCR using Q5 High-Fidelity DNA Polymerase (98˚C 30s >> 30x (98˚C 10s >> 71˚C 15s >> 72˚C 3m) >> 72˚C 5m >> 4˚C hold). PCR primers are detailed in the **Table 7**. Linearized pLL3-Lenti/Cre backbone and U6-driven cassette amplicons were treated with DpnI (New England Biolabs, # R0176S) to digest the methylated parental DNA template and select for the newly synthesized DNA containing mutations. In brief, 16 µL amplicon, 2 µL 10x CutSmart Buffer and 2 µL DpnI were incubated at 37˚C for at least 30 minutes. Non-digested amplicons were then purified using QIAquick PCR Purification Kit (Qiagen, #28104) and eluted in 20 µL of UltraPure DNase/RNase-Free Distilled Water (Invitrogen, # 10977049). DNA concentrations were assessed using NanoDrop Lite Spectrophotometer and a Gibson Assembly reaction was prepared by mixing 25 ng linearized pLL3-Lenti/Cre backbone, 2.96 ng bU6 amplicon, 3.16 ng mU6 amplicon, and 2.87 ng hU6 fragment. Amplicons were then mixed 50% v/v with NEBuilder HiFi DNA Assembly Master Mix (New England BioLabs, #E2621S) in a final volume of 5-10 µL and incubated at 50°C for 15 minutes. Then 1 µL of Gibson reaction was used to transform 9 µL of DH5α by heat shock at 42°C for 45 seconds followed up by 30 minutes incubation in 390 µL SOC

medium at 37°C 220 rpm in a bacterial shaker. Finally, 100 µL of transformed bacteria were plated onto pre-warmed agar plates with 100 µg/mL carbenicillin. Individual bacterial colonies were grown in LB medium supplemented with 100 µg/mL ampicillin at 37°C with agitation at 220 rpm on a horizontal shaker. DNAs from overnight cultures were isolated using QIAprep Spin Miniprep Kit (Qiagen, #27104) and Sanger sequenced to confirm the successful assembly. The PGK promoter regulating Cre was also sequenced to confirm its integrity due to the presence of direct repeats that are susceptible to collapse. Sanger PCR primers are detailed in **Table 8**.

Table 7 | PCR primers used in Step 3

Plasmid	Direction	Sequence	Product size (bp)	Primer Tm (°C)
pLL3 Lenti-sgRNA/Cre	Forward	GTTTGGCGCGCCTATGGCTTAA	7410	71
	Reverse	ACAGTTTAAACAGTTCCTGCAGGGC		

Table 8 | Sanger sequencing primers

Region	Direction	Sequence	Expected outcome
b/mU6 promoters	Forward	GGGACAGCAGAGATCCAGTTTGG	~800 bp Sanger product that covers the bU6 and mU6-driven cassette promoters.
hU6 promoter	Forward	CCTTGGAGAACCACCTTGTTG	~800 bp Sanger product that covers the hU6-driven cassette promoter.
Cre	Reverse	TGCAGGCAAATTTTGGTGTACGG	~800 bp Sanger product that covers the PGK promoter.

Analysis of human lung tumor data and tumor suppressor genes selection

For the selection of tumor suppressor genes associated with EML4-ALK lung cancer, I used the AACR Project Genomics, Evidence, Neoplasia, Information, Exchange (GENIE) database was to analyze human lung tumor data. The genomic alterations of EML4-ALK lung cancer patients were examined with a focus on identifying genomic mutations that provide critical insights into this specific cancer subtype and/or have been identified as significant regulators of lung cancer in previous research. GENIE 14.0-public data were collected through the Synapse platform (syn7844529, www.synapse.org). Patient samples were filtered to only include those with cancer type lung adenocarcinoma, sample type primary tumor or metastasis and EML4-ALK positivity as per structural variant annotations. Furthermore, samples were annotated according to their mutation status, categorized as wild-type, mutated, or not screened for each gene, considering the corresponding gene panel. Genes that were mutated in at least 5 samples were considered. Additional genes of interest identified through a literature review were also included in the analysis. Genes are summarized in **Table 9**.

Table 9 | Mutation frequency of putative tumor suppressor genes selected for investigation. Mutant: altered gene, potentially linked to disease. Wildtype: normal gene, not disease-causing. Not analyzed: gene untested, impact unknown. All crucial for research and understanding health.

Hugo Symbol	Mutant	Wildtype	Not analyzed	Percentage	Pathway or function
TP53	13	138	0	8.61	DNA damage, cell cycle, many others
SETD2	9	142	0	5.96	Chromatin regulation; H3K36me3
KMT2D	8	143	0	5.3	Chromatin regulation; H3K4me
ATM	7	144	0	4.64	DNA damage
SMAD4	5	146	0	3.31	TGFbeta signaling
ARID1A	4	147	0	2.65	Chromatin remodeling
CDKN2A	3	148	0	1.99	Cell cycle
DNMT3A	3	148	0	1.99	DNA methylation
EP300	3	148	0	1.99	Histone acetylation
PTEN	3	148	0	1.99	PI3K signaling
RBM10	2	133	16	1.48	Splicing
ERCC4	2	135	14	1.46	DNA damage
BRCA2	2	149	0	1.32	DNA damage
NKX2-1 (TTF1)	2	149	0	1.32	Lung differentation
SMARCA4	2	149	0	1.32	Chromatin remodeling
STAG2	2	149	0	1.32	Cohesin
KMT2C	1	111	39	0.89	Chromatin regulation H3K4me
RNF43	1	134	16	0.74	Wnt signaling
SUZ12	1	141	9	0.7	Chromatin regulation; H3K27me
KEAP1	1	145	5	0.68	Stress response
KDM6A (UTX)	1	150	0	0.66	Chromatin regulation
NF1	1	150	0	0.66	RAS signaling
RB1	1	150	0	0.66	Cell cycle
CDKN2C	0	151	0	0	Cell cycle
CMTR2	0	25	126	0	Splicing
LATS2	0	102	49	0	Hippo/Yap signaling
SLC34A2	0	16	135	0	Ion homeostasis
STK11 (LKB1)	0	151	0	0	AMPK family signaling
TSC1	0	151	0	0	mTOR sigaling

Cloning of specific sgRNA for each tumor suppressor gene.

The sgEGFP from the previously generated sgEGFP,sg*Eml4*^{V1},sg*Alk*/Cre or sgEGFP,sg*Eml4*^{V3},sg*Alk*/Cre was replaced by specific sgTSG. The sgRNA sequence of each TSG is detailed in the **Table 10**.

Table 10 | sgRNAs targeting tumor suppressor genes. Different sgRNAs were used per gene of interest (#1, #2, #3…). sgRNA sequence and source are indicated.

Target	sgRNA sequence	Source
Arid1a#1	ATGGGTCCCAGACTCCACAG	Cai et al., 2021
Arid1a#2	CCTGCTGGCCATACGCACTG	Cai et al., 2021
Arid1a#3	CTAACGTTCATGGAAGAGAG	Cai et al., 2021
Arid1a#4	CAGAGCAGCCCATACCCAGG	Cai et al., 2021
Atm#1	CTTCTGTCTGGAGCTCTGTG	Cai et al., 2021
Atm#2	GTATCTCAGCAACAGTGGCT	Cai et al., 2021
Brca2#1	CTGAAAGGCGACTGGTCCAG	Cai et al., 2021
Brca2#2	GTACCCAAAGTCTCGTCAAG	Cai et al., 2021
Cdkn2a#1	CGGTGCAGATTCGAACTGCG	Cai et al., 2021
Cdkn2a#2	GCAGCTCTTCTGCTCAACTA	Cai et al., 2021
Cdkn2c#1	AAAGAATGGCCGAGCCTTGG	Cai et al., 2021
Cdkn2c#2	TGGCGTCCGCAGCTGCCAGG	Cai et al., 2021
Cmtr2#1	CCCACAGGAGAAGCTCTCCG	Cai et al., 2021
Cmtr2#2	GTAAGCCACTCGATAATGAG	Cai et al., 2021
Dnmt3a#1	ATGATTGAATGGGCCCTCGG	Cai et al., 2021
Dnmt3a#2	CAGGCCGAATTGTGTCTTGG	Cai et al., 2021
Ep300#1	AAGCTCGCTCTATAGAGCTG	Cai et al., 2021
Ep300#2	TTCACAGACCGCATGCCCTG	Cai et al., 2021
Ercc4#1	TATGAAGTCTACACGCAGGG	Cai et al., 2021
Ercc4#2	ACAAAGGGTCCAAGTAATGG	Cai et al., 2021
Kdm6a#1	AATTCGTGCTGCAAGTCCAG	Cai et al., 2021
Kdm6a#2	AGGTTGGATGCATCACACTG	Cai et al., 2021
Keap1#1	TCAAATACGACTGCCCGCAG	Cai et al., 2021
Keap1#2	GGTTCGGTTACCGTCCTGCG	Cai et al., 2021
Kmt2c#1	TTCTACGCCAACAGAGACCA	Cai et al., 2021
Kmt2c#2	AAGCACCCAGACAGCCTGTG	Cai et al., 2021
Kmt2d#1	TTGTGCTCTCTGTAACTGCG	Cai et al., 2021
Kmt2d#2	GAGCATCCGGCGCATCAATG	Cai et al., 2021
Lats2#1	GATTGCAAGAGATTCGAGAG	This work
Lats2#2	CATCCAAGGCTTCCACCCAG	This work
Lats2#3	CCCTGGATGCCAAAGTCCTG	This work
Lats2#4	ATAAGGTCCAAACTTCGGGG	This work
Lkb1 (Stk11)#1	GTGGTGGGCCGCAGTCACAA	Rogers et al., 2017
Lkb1 (Stk11)#2	CCACTCTCTGACCTACTCCG	Cai et al., 2021
Neo (inert)#1	TCATGGCTGATGCAATGCGG	Rogers et al., 2017
Neo (inert)#2	GATATTGCTGAAGAGCTTGG	Rogers et al., 2017
Neo (inert)#3	GAATAGCCTCTCCACCCAAG	Rogers et al., 2017
Nf1#1	CCAAACGTAAAGCAGCAGTG	Cai et al., 2021
Nf1#2	CTTCAACAACTCCCTCGATG	Cai et al., 2021
Nkx2-1#1	CGCCTTACCAGGACACCATG	This work
Nkx2-1#2	CGCCGCCTACCACATGACGG	This work
Nkx2-1#3	AGCGTACAGACAGGGCCAGG	This work
Nkx2-1#4	CTACAAGAAAGTGGGCATGG	This work
NT (non-targeting/inert)#1	GCGAGGTATTCGGCTCCGCG	Rogers et al., 2017

NT (non-targeting/inert)#2	GACGTAGCCTTCCGAAATAT	Cai et al., 2021
NT (non-targeting/inert)#3	GACTGAAATCCAAGGACTGT	Cai et al., 2021
Pcna1 (essential gene)	ATACGTGCAAATTCACCCGA	Cai et al., 2021
Pten#1	CCTCCAATTCAGGACCCACG	Cai et al., 2021
Pten#2	TCACCTGGATTACAGACCCG	Cai et al., 2021
Rb1#1	TCTTACCAGGATTCCATCCA	Rogers et al., 2017
Rb1#2	TACGTTCAGAATCCACGGGA	Cai et al., 2021
Rbm10#1	GTATTTCCTGAACAGATCCG	Cai et al., 2021
Rbm10#2	TGGGAACGAAAGCTCACCTG	Cai et al., 2021
Rnf43#1	GTAGACGAGCCCGAGCCGAG	Cai et al., 2021
Rnf43#2	TAGACAGATGGCACACACGG	Cai et al., 2021
Setd2#1	TCTCTAATCCATCTTCCCAG	Rogers et al., 2017
Setd2#2	CCGTCTCCTTCACTTAACTG	Cai et al., 2021
Slc34a2#1	TTGGCAGGTATGCTCGATTG	This work
Slc34a2#2	GGAGGGTAGCAGTTCAGTCT	This work
Slc34a2#3	TCATAGAGGAGCATCCCGAG	This work
Smad4#1	AGACGGGCATAGATCACATG	Cai et al., 2021
Smad4#2	GATGTGTCATAGACAAGGTG	Cai et al., 2021
Smarca4#1	GGGATGCAGGTCTTACCATG	Cai et al., 2021
Smarca4#2	CGGAGGAATCAGCTTCTGTG	Cai et al., 2021
Stag2#1	CGAGTCCTACAAGCATGACC	Cai et al., 2021
Stag2#2	GGTCAAGAAGCGCTATGTCC	Cai et al., 2021
Suz12#1	CTTCTTCACCGGCAACACCG	This work
Suz12#2	CTCGGCCTCCTCCTCCTCGG	This work
Suz12#3	TTGGTTTCTCAAAGGCCTGG	This work
Suz12#4	TTTCACAAGCAGGACTTCCA	This work
Trp53#1	AGGAGCTCCTGACACTCGGA	Rogers et al., 2017
Trp53#2	GAAGTCACAGCACATGACGG	Cai et al., 2021
Trp53#3	AACAGATCGTCCATGCAGTG	Cai et al., 2021
Tsc1#1	ACCTAAGATCCACATACCAG	Cai et al., 2021
Tsc1#2	ATCGTGTGGCTCCTGCAAGG	Cai et al., 2021

Each specific sg*TSG* was cloned by site directed mutagenesis using Q5 High-Fidelity DNA Polymerase with specific forward primers that included the sg*TSG* sequence to be introduced. Primer designed included 23 nt for vector backbone matching and 10 nt for the sg*TSG* sequence (**Table 11**). Site directed mutagenesis was performed using the following PCR program 98˚C 30s >> 30x (98˚C 10s >> Tm˚C 15s >> 72˚C 3m) >> 72˚C 5m >> 4˚C hold. Amplicons were ligated by KLD reaction as specified above and KLD products were purified using QIAquick PCR Purification Kit. sg*TSG*,sg*Eml4*^{V1},sg*Alk*/Cre or sg*TSG*,sg*Eml4*^{V3},sg*Alk*/Cre plasmids were eluted in 20 µL of UltraPure DNase/RNase-Free Distilled Water.

Table 11 | Used PCR primers. The consecutive Ns in the provided Forward sequence represent any nucleotide and can be selectively replaced with the desired sgRNA sequence for inclusion within the construct.

Primer	Sequence
Reverse primer	NNNNNNNNNNCATAAACATGGCCTCTCAAGAAC
Forward primer	NNNNNNNNNNGTTTAAGAGCTAAGCTGGAAACA

DH10alpha bacterial transformation was performed using 5 µL of the purified plasmid and 40 µL. After heat shock at 42°C for 45 seconds, cells were recovered in 500 µL of SOC medium at 37°C 220 rpm in a bacterial shaker for 0.5-1 hour. Finally, 100 µL of transformed bacteria were plated onto pre-warmed agar plates with 100 µg/mL carbenicillin. Four bacterial colonies for each sg*TSG* were grown in overnight cultures of LB supplemented with 100 µg/mL ampicillin and DNA was isolated using were isolated using QIAprep Spin Miniprep Kit. Finally, sg*TSG*,sg*Eml4*^{V1},sg*Alk*/Cre or sg*TSG*,sg*Eml4*^{V3},sg*Alk*/Cre plasmids were Sanger sequenced to ensure the integration of the sg*TSG* and the PGK promoter integrity.

Barcoding of lentiviral vectors

Each individual vector of the sg*TSG*,sg*Eml4*^{V1},sg*Alk*/Cre or sg*TSG*,sg*Eml4*^{V3},sg*Alk*/Cre collections were diversified by via cloning of sgID-BC cassettes.

Firstly, a defined pool of 8-bp sgRNA identifiers (sgID) with hamming distance of 2 bp to buffer for PCR or sequencing errors that occur over the course of library preparation or sequencing were designed. These sgID were specifically designed for each sgRNA, ensuring the uniqueness of each sgRNA for each the sg*TSG*,sg*Eml4*^{V1},sg*Alk*/Cre or sg*TSG*,sg*Eml4*^{V3},sg*Alk*/Cre collection. Oligos were ordered as represented in **Figure 43**, including a pre-defined sgID sequence followed by 20 nucleotides random barcode (random tumor barcode (BC)). Hand-mixed nucleotides at 1:1:1:1 ratio were requested to ensure even representation.



Figure 43 | sgID-BC structure. sgRNA ID (sgID) and random tumor barcode (BC) structures are highlighted. "N" refers to any nucleotide.

Unique sgID-BC were amplified by Q5 High-Fidelity DNA Polymerase reaction (5 ng of pLL3-Lenti/Cre backbone, 0.5 µM forward and 0.5 µM reverse primers, **Table 12**) using the PCR program: 98˚C 30s >> 30x (98˚C 10s >> 66˚C 15s >> 72˚C 15s) >> 72˚C 5m >> 4˚C hold.

Table 12 | sgRNA-specific barcoded primers. The consecutive Ns in the provided sequence represent any nucleotide and can be selectively replaced with the desired sgID and randomly replaced for the BC synthesis (see figure 43).

Backbone	Direction	Sequence
pLL3 Lenti-sgRNA/Cre	Forward	AGCTAGTCCGGANNNNNNNNGCNNNNNTANNNNNGCNNNNNTANNNNNGCATGCCCAAGAAGAAGAGGAAGGTGTC
	Reverse	AGCTAGGGATCCGCCGCATAACCAGTG

Amplicons were resolved by electrophoresis on a 1% agarose gel containing peqGreen DNA dye, with an applied voltage of 120V. Subsequently, the target bands were excised from the gel using a green LED light source and an Invitrogen iBright FL1500 Imaging System to prevent UV-induced mutations. The excised gel bands were further processed using the QIAquick Gel Extraction Kit (Qiagen, #28704) following the manufacturer's instructions. Prior to DNA elution, columns were incubated twice with 800 µL of PE buffer to reduce salt contamination. sgID-BCs were eluted in 18 µL UltraPure DNase/RNase-Free Distilled Water. Barcodes were then digested with BspEI/BamHI for 3 hours at 37˚C (2 µL Buffer 3.1, 1 µL BspEI, 1 µL BamHI, 16 µL barcoded insert).

Individual sg*TSG*,sg*Eml4*^{V1},sg*Alk*/Cre or sg*TSG*,sg*Eml4*^{V3},sg*Alk*/Cre vectors were digested overnight at 37°C (4 µl Cutsmart buffer, 2 µl XmaI, 2 µl, BamHI-HF (reduce star activity), 2 µg of the corresponding lentiviral plasmid). Digested sg*TSG*,sg*Eml4*^{V1},sg*Alk*/Cre or sg*TSG*,sg*Eml4*^{V3},sg*Alk*/Cre were resolved as indicated above. Prior to DNA elution, columns were incubated twice with 800 µL of PE buffer to reduce salt contamination. Digested vectors were eluted in 20 µL of UltraPure DNase/RNase-Free Distilled Water.

Both, sgID-BC and digested vectors were quantified using Qubit and ligated following the following reaction 75 ng digested plasmid, 25 ng digested barcode, 2 µL 10x T4 DNA Ligase Buffer, 1 µL T4 ligase (2,000,000 units/ml; New England BioLabs, #M0202T) and UltraPure DNase/RNase-Free Distilled Water in a final volume of 20 µL. sgID-BC and digested vectors were ligated overnight at 16°C and then purified using QIAquick PCR Purification Kit (Qiagen, #28104). Prior to DNA elution, columns were incubated twice with 800 µL of PE buffer to reduce salt contamination. Ligated barcoded plasmids were eluted in 20 µL of UltraPure DNase/RNase-Free Distilled Water (Invitrogen, # 10977049).

5 µL of purified barcoded plasmid were then used to electroporate 30 µL ElectroMAX DH10B Cells (Invitrogen, #18290015). DNA and bacterial mix were directly transferred to a pre-chilled 0.1-cm electroporation cuvette and electroporated at 2.0 kV, 200 Ω, 25 µF. Immediately after the electroporation, cells were resuspended in pre-warmed 550 µL of SOC medium and incubated for 1 hour at 37°C, 600 rpm on a thermoblock. Each barcoded plasmid was then plated onto pre-warmed agar plates (5 x 100 µL) with 100 µg/mL carbenicillin using

glass beads. A counting plate was prepared by diluting 11 µL of bacteria in 99 µL SOC and then mixing 10 µL of this dilution with 90 µL of SOC medium. Plates were incubated overnight at 37°C. Bacterial colony number was estimated from the counting plate. The bacterial library for each sgRNA was scraped off the agar and aggregated in 50 mL centrifuge tube (5 mL/plate of LB supplemented with 100 µg/mL ampicillin). Libraries were incubated at 37°C, 220 rpm for 30 minutes and pellet down at 14,000 rpm, 4°C for 30 minutes. DNA isolation was performed using PureLink HiPure Plasmid Midiprep Kit (Life Technologies, # K210004). DNA was resuspended in UltraPure DNase/RNase-Free Distilled Water and quantified using a NanoDrop Lite Spectrophotometer. An absorbance 260/280 ratio of approximately 1.8 indicated uncontaminated DNA. Libraries for each sgRNA were Sanger sequenced.

Resulting sg*TSG*,sg*Eml4*^{V1},sg*Alk*/Cre or sg*TSG*,sg*Eml4*^{V3},sg*Alk*/Cre diversified vectors were used for lentiviral preparation (see “Production, purification and titration of lentivirus” section).

Lentiviral plasmid isolation

Lentiviral plasmid DNA preparations were generated through DH10alpha bacterial transformation. The bacteria were cultured in Luria Broth (LB) supplemented with 100 µg/mL ampicillin and allowed to grow for 16 hours at 37°C with agitation at 220 rpm on a horizontal shaker. Following overnight growth, the bacterial culture was centrifuged at 4,000 rpm for 20 minutes and subjected to DNA isolation using either the PureLink HiPure Plasmid Midiprep Kit (Life Technologies, # K210004) or the PureLink Expi Endotoxin-Free Maxi Plasmid Purification Kit (Life Technologies, A31217) protocols.

In brief, the bacterial pellet was resuspended in ice-cold resuspension buffer and lysed for 5 minutes, followed by the addition of a neutralization buffer. The lysates were then clarified by centrifugation at 4,000 rpm for 15 minutes. Removal of endotoxins was achieved by adding endotoxin removal buffer, and the resulting lysates were loaded onto DNA-binding columns. After washing the columns with a washing buffer, DNA was eluted using prewarmed elution buffer at 55°C. Subsequently, DNA was precipitated by adding 0.7 volume of isopropanol and centrifuging at 4,000 rpm for 1 hour at 4°C. The DNA was further purified by washing with 70% ethanol and air-dried for 10 minutes. Finally, the DNA was resuspended in ultra-pure H2O and quantified using a NanoDrop Lite Spectrophotometer (Life Technologies, ND-LITE). An absorbance 260/280 ratio of approximately 1.8 indicated uncontaminated DNA.

Production, purification and titration of lentivirus

Lentivirus was produced following an optimized protocol for this thesis. Initially, 20 million Lenti-X 293T Cells (Takara, #632180) were seeded in a 150 mm dish containing DMEM supplemented with 10% FBS and 2 mM L-glutamine (Gibco, #25030024), without antibiotics (growth media). After 20 hours, the media were replaced with fresh growth media containing 5 M sodium butyrate (HDAC inhibitor) dissolved in DMEM.

Transfection was carried out 24 hours after cell seeding using the polyethylenimine (PEI) protocol. For each 150 mm dish, a mixture of 4.95 µg pCMV-dR8.2 plasmid (RRID:Addgene_8455), 1.9 µg of the VSV-G envelope-expressing plasmid (RRID:Addgene_8454), and 7.4 µg of the transfer plasmids in 200 µL of Opti-MEM I Reduced-Serum Medium (Gibco, #31985062) was prepared. This plasmid mix was diluted and vortexed with 74.25 µg of linear MW 25,000 Da PEI in 1 mL of Opti-MEM for 10 seconds. The mixture was then incubated for 20 minutes at room temperature before being added dropwise to the cells. Cells were incubated for 16-18 hours, after which the media was discarded and replaced with collection media (DMEM with 12% FBS, 4 mM L-glutamine, and 1 mM sodium pyruvate).

Individual lentivirus preparations were collected 24 and 48 hours after transfection, centrifuged at 1,000 rpm for 5 minutes at 4°C, and filtered through 0.45 µm PES or PVDF filters to remove cell debris. Subsequently, the virus was concentrated by ultracentrifugation for 1.5 hours at 25,000 rpm at 4°C. The resulting pellets were resuspended in PBS, pH 7.4 (Gibco, #10010023) overnight and stored at -80°C.

The concentration of lentiviral particles was determined by infecting Lox-Stop-Lox-YFP mouse embryonic fibroblasts (a gift from M. Winslow). Briefly, 200,000 cells were seeded in duplicates in 6-well plates 24 hours prior to lentiviral infection. One control well was counted before infection. Cells were then incubated with lentiviruses, vehicle, or a batch effect control. After 48 hours, cells were harvested, and the percentage of YFP-positive cells, excluding dead cells (using DAPI at 1 µg/ml; Life Technologies, 62248), was determined by flow cytometry. Viral particles per µL were calculated as follows:

$$x = \frac{\#\text{cells at 24 h} * \%\text{YFP}^{+}\text{cells}}{\mu\text{L of virus added}}$$

$$\text{Viral particles}/\mu\text{L} = \frac{x * \text{known } \%\text{YFP}^{+}\text{batch effect control}}{\text{actual } \%\text{YFP}^{+}\text{batch effect control}}$$

Intratracheal instillation of viral particles

Mice over 6 weeks old of both sexes were used for autochthonous lung tumor initiation. Intratracheal delivery of viral particles was conducted on anesthetized mice. Anesthesia was induced by intra-peritoneal injection of 100 µg/g ketamine and 14 µg/g xylazine in PBS. Mice were securely positioned in a supine orientation on an inclinable platform, and intratracheal instillation was performed following established protocols (DuPage et al. 2009; Chen et al. 2022). Briefly, 50 µL of *Eml4-Alk* variant 1 or variant 3 adenoviruses were pre-incubated in DMEM (Life Technologies, 41965039) with 2M CaCl2 for 20 minutes before inoculation. The final dose administered per mouse was 1.5 x 10E8 PFU. For studies involving tumor suppressor genes, lentiviral particles were diluted in PBS, with a maximum volume of 100 µL administered into the lungs at doses specified in the figure legends.

Mouse dissection

Mice were sampled at specific time points or at humane endpoint assessed by signs of respiratory distress or weight loss and euthanized if any morbidity criteria were met. Mice were euthanatized by cervical dislocation. The inferior vena cava was cut and intracardiac perfusion with PBS was performed to clear the erythrocytes from the lungs. Lungs were fixed with 10% formalin for 24 hours before paraffin embedding and processing. For DNA, RNA, or protein extraction, tissues were snap frozen in dry ice and stored at -80°C until further processing.

Sample cryopreservation

Single tumors were microdissected using a Leica stereomicroscope, placed into cryovials, and incubated in cell cryopreservation media (CryoStor-CS10, Sigma-Aldrich, #C2874) for 10 minutes on ice. Subsequently, the cryovials were gradually frozen in a freezing container over a period of 24-36 hours and then transferred to liquid nitrogen for long-term storage.

Single cell suspension from cryopreserved tumors

Cryopreserved individual tumors were thawed in a 37°C water bath and subsequently placed onto a 70 µm cell strainer. They were then thoroughly rinsed with 10 mL of Dulbecco's phosphate-buffered saline (DPBS, no calcium, no magnesium, Gibco, #14190144). Using sterile scissors, the single tumors were finely minced into pieces smaller than 0.5 mm^3, after which they were transferred into a 5 mL centrifuge tube containing 1.2 mL of pre-warmed digestion solution (Dispase (5 U/mL; Corning #354235), DNase I, Grade II (1 mg/mL; Sigma

#10104159001), Y-27632 ROCK inhibitor (0.5 mM; Stem Cell Technologies #72304) in Advanced DMEM/F-12 (Gibco #12634010)). The tumors were allowed to digest for 40 minutes at 37°C with gentle horizontal rotation at 80 rpm. Every 10-15 minutes during the digestion, the tumors were vigorously mixed by pipetting with a P200 tip attached to a P1000 tip, approximately 20 times.

After the 40-minute digestion, the tumors were mixed once more before the digestion solution was neutralized using blocking media (DMEM/F-12 (VWR International #392-0412), FBS (10%, Gibco #10270-106), HEPES (0.01 M, Gibco #15630056) with DNase I, Grade II (0.1 mg/mL), and ROCK inhibitor (0.05 mM)). The cell suspension was then centrifuged at 1,100 rpm for 7 minutes at 4°C, and the supernatant was carefully discarded. The resulting pellets were resuspended in 100 µL of red blood cell lysis buffer (Sigma-Aldrich, R7757) and incubated for 1 minute on ice. Next, 4 mL of blocking media was added to the tubes, and the samples were centrifuged again at 1,100 rpm for 7 minutes at 4°C. The supernatants were discarded, and the pellets were resuspended in an antibody cocktail (see **Table 13**), with the assumption of a final cell count of 125,000 for tumors initially measuring 1-2 mm². The cell suspensions were then transferred to round-bottom tubes with an attached 35 µm cell strainer cap (Falcon, #352235), which had been pre-wetted with 50 µL of FACS buffer. The cell suspensions were incubated for 30 minutes on ice, with gentle flicking every 10 minutes. Following this incubation, the cells were washed by adding 4 mL of FACS buffer and were subsequently centrifuged at 1,200 rpm for 5 minutes at 4°C. Finally, the cell pellets were resuspended in 150 µL of FACS buffer and stained with DAPI (1 µg/mL) before cell sorting. Sorted cells were collected in 1.5 mL tubes pre-filled with 150 µL of FACS buffer.

Table 13 | Antibodies used for sorting EGFP tumor cells

Antibody	Dilution	Source
APC anti-mouse CD45	1:1000	BioLegend Cat# 103112 RRID:AB_312977
APC anti-mouse TER-119/Erythroid Cells	1:200	BioLegend # 116212, RRID:AB_313713
APC anti-mouse CD31	1:200	BioLegend # 102409, RRID:AB_312904
APC anti-mouse/human CD11b	1:200	BioLegend # 101211, RRID:AB_312794
DAPI solution 1mg/ml	1:2000	Life Technologies #62248

DNA extraction from sorted tumor cells

Rapid purification of high-quality DNA from sorted tumor cells was performed using the QIAamp DNA Mini Kit (Qiagen, #51304) according to the manufacturing protocol. Briefly, sorted tumor cells were enzymatically lysed in 20 µL QIAGEN Proteinase K in a final volume of 200 µL PBS. The lysis solution was then mixed with 200 µL AL buffer and incubated at 56°C for 10 minutes at 800 rpm in a thermoblock. 100 µL absolute ethanol was then added, and the lysates were vortexed for 15 seconds and spun down briefly. The enteric lysate was then

transferred to a QIAamp MinElute column and spun down for DNA binding. The columns were then washed with Qiagen AW1 and AW2 buffers and finally spun at 14,000 rpm for 2 minutes to completely dry the membrane. DNA was eluted by adding 20 µL UltraPure DNase/RNase-Free Distilled Water and collected in a 1.5 mL centrifuge tube with low DNA binding. DNA purity was then measured using a NanoDrop Lite spectrophotometer. An absorbance 260/280 ratio of approximately 1.8 indicated uncontaminated DNA.

Sorted tumor cell genotyping

Purified DNA obtained from sorted tumor cells underwent PCR amplification targeting specific genomic coordinates using the HotStart Master Mix Kit (Qiagen, #203443). In summary, a final PCR reaction was prepared by combining 10 µL of HotStarTaq Master Mix, 0.5 µM of each primer, 0.5-1 ng of DNA, and ultra-pure water, resulting in a total volume of 20 µL. Detailed information about the primers and PCR settings can be found in **Table 14**.

The resulting amplicons were then resolved by electrophoresis on a 0.75% agarose gel containing peqGreen DNA dye, with an applied voltage of 120V. Subsequently, the target bands were excised from the gel using a green LED light source and an Invitrogen iBright FL1500 Imaging System to prevent UV-induced mutations. The excised gel bands were further processed using the QIAquick Gel Extraction Kit (Qiagen, #28704) following the manufacturer's instructions. The amplicons were then subjected to Sanger sequencing through Mycrosynth services, using forward primers. The base calling and overall DNA sequence quality assessment were conducted using Benchling [Biology Software] (2018-2024, https://benchling.com). TIDE was used to estimate the spectrum and frequency of small insertions and deletions (indels) (Brinkman et al. 2014).

Table 14 | Used PCR primers for TSG genotyping

Gene	Direction	Sequence	Product size (bp)	Primer Tm (°C)
***Eml4-Alk* V1**	Forward	GCTCAAGAGGTGGGTTGTGT	830	54
	Reverse	GGTCATGATGGTCGAGGTCC		
***Eml4-Alk* V3**	Forward	CTTTAATTGTAGACTGCAGCCCTGC	750	54
	Reverse	GGTCATGATGGTCGAGGTCC		
Neomycin	Forward	TGTTCTCCTCTTCCTCATCTCC	421	61
	Reverse	AAGGTGAGATGACAGGAGATCC		
Setd2	Forward	TCAATCACACTTAGTGGCATGG	556	54
	Reverse	CTTGCATTCTAGCTCACTAGTGAC		

RNA extraction and RNA library preparation from sorted tumor cell genotyping

RNA from sorted cells with the desired genotype was isolated using the PicoPure RNA Isolation Kit (Life Technologies, #KIT0204) according to the manufacturer's instructions.

Subsequently, RNA-sequencing libraries were constructed using the SMART-Seq mRNA library prep (Takara, #634768) and Unique Dual Index Kit (Takara, #634756) as per the manufacturer's protocol. Input included 1 ng of RNA and 1 ng of cDNA. Quality control was performed by assessing RNA, cDNA, and final library qualities using Tapestation. Libraries were analyzed in a NovaSeq 6k PE 150 S4.

RNA sequencing analysis

To identify gene expression changes, RNA-sequencing reads were mapped to the mouse genome (GRCm38) using the STAR aligner. Gender-related biases were then computationally removed from the data. Next, differentially expressed genes were obtained using the DESeq package, allowing for comparisons between groups. Finally, to unveil underlying biological processes associated with these gene expression changes, pathway analysis was conducted using GSEA.

Establishment of *Eml4-Alk* mouse tumor-derived cells

Single tumors obtained from independent *Trp53*$^{flox/flox}$; mT/mG; CCSP-Cre mice, which had previously undergone transduction with sg*Eml4*-sg*Alk*;Cas9-V1 (Maddalo et al. 2014) or sg*Eml4*-sg*Alk*;Cas9-V3 adenoviruses (Sara Chocarro, Kalman Somogyi), were subjected to digestion following the procedure outlined in the "Single tumor digestion" section. The cells derived from the digested tumors were subsequently plated in a 2D culture format at a concentration >50,000 cells/cm2. Tumor-derived cells were cultured in DMEM supplemented with 10% FBS and 2 mM L-glutamine. After several passages, monoclonal populations were established by initiating single-cell seeding in 96-well plates containing 100 µL of growth medium. Clonal populations were identified 24 hours after seeding, as wells containing one single cell.

Cell culture was done in incubators with a stable environment of 37°C, a relative humidity of about 95 percent and a CO_2 concentration of 5%. All studies involving these cell lines were conducted with cultures that had been maintained for fewer than thirty passages. Cell cultures were tested negative for mycoplasma contamination (Young et al. 2010).

Culture of ALK-patient derived cells

Cells derived from ALK patients were cultured as described in (Bokhari et al. 2022). In brief, ALK-patient derived cells were grown in RPMI 1640 Medium (ATCC modification, Gibco, #A1049101) supplemented with 10% FBS and 2 mM L-Glutamine. All studies were performed

on cells maintained in culture for less than thirty passages. All cell lines tested negative for mycoplasma (Young et al. 2010).

Histology and immunohistochemistry

Mouse tissue samples were fixed in 10% formalin (Sigma, HT501128) for 24 hours at room temperature prior to paraffin embedding and subsequent processing. For tumor-derived cells, cells were harvested, washed with PBS, resuspended in 100 µL HistoGel (Fisher Scientific, 12006679) according to the manufacturer's instructions, and fixed in 10% formalin overnight at 4°C.

Paraffin blocks were then cut into 3-µm thick slices using a microtome (Leica, #ASP300S). These paraffin sections were placed in a 40°C water bath containing distilled water to facilitate stretching. The sections were then transferred to Superfrost Plus slides (VWR International, 631-9483) and air dried in a 40°C oven overnight.

The samples were first deparaffinized by two successive washes with xylene for 10 minutes each. The tissues were then rehydrated by passing the slides through 100%, 95%, and 70% ethanol solutions for 3 minutes each and finally rinsed with distilled water for 5 minutes. Antigen retrieval was performed using 0.09% (v/v) unmasking solution (Vector Labs, #H-3300) in a steamer for 30 minutes. Slides were allowed to cool and rinsed with distilled water for 5 minutes. Endogenous peroxidase activity was then blocked by incubating sections in 3% H2O2 solution (Sigma, H1009) in distilled water for 10 minutes. Slides were then washed with PBS for 5 minutes and blocked with specific animal serum according to the type of primary antibody (VECTASTAIN Elite ABC kits (Vectors Lab, PK-6101; PK-6105; PK-6104)). After 20 minutes, sections were incubated with primary antibodies (**Table 15**) diluted in specific animal serum for 1.5 hours. Slides were washed twice with PBS for 5 minutes and secondary antibody incubation followed by avidin-biotin complex and DAB staining were performed using species-specific VECTASTAIN Elite ABC kits (Vector Labs, #PK-6101, #BMK-2202, and #SK-4100). Hematoxylin QS (Linaris, H-3404) was used for nuclear counterstaining. Samples were then dehydrated through 95% and 100% ethanol and finally incubated in xylene and mounted with DPX mounting medium (Sigma-Aldrich, #06522).

For hematoxylin and eosin (H&E) staining, after rehydration, sections were stained with hematoxylin to facilitate nuclear counterstaining, followed by rinsing in distilled water for 5 minutes. Tissues were then stained with acid eosin for an additional 5 minutes to achieve cytoplasmic counterstaining. Slides were then rinsed three times in distilled water, transferred

directly to 95% ethanol for 5 minutes, and finally dehydrated in 100% ethanol. Slides were transferred to xylene twice for 5 minutes and mounted as described above.

Table 15 | Antibodies for immunohistochemistry

Antibody	Dilution	Source
Rabbit Anti-Prosurfactant Protein C	1:500	Millipore Cat#AB3786, RRID:AB_91588
Rabbit Anti-Clara Cell Secretory Protein	1:1,000	Millipore Cat#07-623, RRID:AB_310759
Rabbit Anti-TTF1	1:200	Abcam Cat#ab76013,RRID:AB_1310784
Rabbit Anti-Cytokeratin 5	1:200	Abcam Cat# ab53121, RRID:AB_869889
Rabbit Anti-Phospho-Histone H3 (Ser10)	1:200	Cell Signaling Cat# 9701, RRID:AB_331535
Rabbit Anti-Cleaved Caspase-9 (Asp353)	1:200	Cell Signaling Cat# 9509, RRID:AB_2073476
Rabbit Anti-H3K36me3	1:2,000	Cell Signaling Cat# 4909, RRID:AB_1950412
Rabbit Anti-P63	1:200	Abcam Cat# ab124762, RRID:AB_10971840

Histological analysis

Samples were imaged using the TissueFAXS slide scanning platform (TissueGnostics), and subsequent analyses were performed using StrataQuest software (TissueGnostics) or QuPath (version 0.4.4). Regions of interest were annotated as individual lung tumors, lung lobes or by selecting random areas. Total cell count was determined by quantifying hematoxylin-positive nuclei with a defined inclusion criteria of sizes ranging from 5 to 20 µm. DAB-positive and DAB-negative cells were then quantified based on the intensity of DAB staining.

Evaluation of tumor burden was performed on hematoxylin and eosin-stained sections. Each individual tumor and the area of each lung lobe were delineated and annotated. Tumor burden was calculated as the percentage of lung area occupied by tumors.

Quantification of tumor grading was performed on hematoxylin and eosin-stained sections using an automated convolutional neural network (CNN) developed by Aiforia Technologies. This artificial intelligence analysis model was co-developed with Sara Chocarro and further enriched with annotations from myside and from the Peter M. K. Westcott and Tyler Jacks labs.

Macroscopic quantification of lung tumors

Rosa-LSL-Cas9-EGFP lungs were harvested as described in the "Mouse dissection" section. Tumor-bearing lungs perfused with sterile PBS were imaged using a Leica stereomicroscope to capture both bright field and EGFP images. Images were then analyzed using QuPath based on the fluorescence images. Individual tumors and lung lobes were manually annotated based on pixels with similar intensities and by performing manual corrections. Tumor and lung area was then measured corrected for a common scaling factor.

Western blot

Mouse tumor cells were collected by trypsinization and washed with ice-cold DPBS. Cells were lysed in ice-cold RIPA buffer (**Table 16**) and incubated at 4°C with agitation for 30 minutes. The lysates were then centrifuged at 14,000 rpm for 20 minutes at 4°C. The resulting supernatant was collected in fresh tubes, and the protein concentration was quantified using the Pierce BCA Protein Assay Kit (Thermo Scientific, #23225), using BSA as a standard reference. Samples were then prepared for electrophoresis by combining 40 µg of protein with 4X Laemmli loading buffer (**Table 16**) and Milli-Q water to a final volume of 30 µL. These sample mixtures were then boiled at 95°C for 5 minutes and briefly centrifuged. Proteins were then resolved on 1.5 mm thick 8-12% polyacrylamide gels at a constant voltage of 120-150 V until the desired separation was achieved. Proteins were then transferred to 0.2 µm nitrocellulose membranes (Bio-Rad, #1704270) using a Trans-Blot Turbo Transfer System (Bio-Rad, #1704150) following the standard "1.5 MM GEL" protocol (10 minutes at a constant 2.5 A; up to 25 V). To verify correct protein transfer, the membranes were washed with TBS-T buffer (137 mM NaCl, 2.7 mM KCl, 19 mM Tris-base, 0.1% Tween-20, pH 7.4 in Milli-Q water) and stained with reversible Ponceau S solution (Sigma-Aldrich, #P7170) for 5 minutes. The Ponceau S staining was then removed by sequential washing with TBS-T buffer. The membranes were then blocked in 5% BSA (Sigma, #SIALA7906) in TBS-T buffer for 1 hour at room temperature, followed by incubation with specific primary antibodies (**Table 18**) overnight at 4°C with gentle agitation. After primary antibody incubation, the membranes were washed with TBS-T buffer and incubated with appropriate secondary antibodies (**Table 18**) for 1 hour at room temperature with gentle shaking. Finally, protein detection was performed using an enhanced chemiluminescence (ECL) substrate (Thermo Scientific, #34094), and the resulting signal was visualized using an Invitrogen iBright FL1500 Imaging System.

Table 16 | RIPA buffer for protein extraction

Reagent	Final concentration
Tris HCl, pH 7.5	50 mM
NaCl	150 mM
EDTA, pH 8.0	2 mM
NP40	1%
PMSF	2 mM
Na3VO4	2 mM
EDTA-free complete protease inhibitor cocktail (Roche, #11873580001)	1X

Table 17 | 2X Laemmli buffer

Reagent	Final concentration
Tris-HCl, pH 6.8	0.125 M
Glycerol	20%
2-mercaptoethanol	20%

Bromophenol Blue	0.004%

Table 18 | Western blot antibodies

Antibody	Dilution	Source
Rabbit Anti-EML4	1:1,000	Cell Signaling Cat# 12156, RRID:AB_2797832
Rabbit Anti-Phospho-MEK1/2 (Ser217/221)	1:1,000	Cell Signaling Cat# 9154, RRID:AB_2138017
Rabbit Anti-Phospho-p44/42 MAPK (Erk1/2) (Thr202/Tyr204)	1:1,000	Cell Signaling Cat# 4376, RRID:AB_331772
Rabbit Anti-p44/42 MAPK (Erk1/2)	1:1,000	Cell Signaling Cat# 9102, RRID:AB_330744
Rabbit Anti-Phospho-Akt (Ser473)	1:1,000	Cell Signaling Cat# 3787, RRID:AB_331170
Rabbit Anti-Akt (pan)	1:1,000	Cell Signaling Cat# 4691, RRID:AB_915783
Rabbit Anti-Phospho-p70 S6 Kinase (Thr421/Ser424)	1:1,000	Cell Signaling Cat# 9204, RRID:AB_2265913
Rabbit Anti-p70 S6 Kinase	1:1,000	Cell Signaling Cat# 9202, RRID:AB_331676
Rabbit Anti-Phospho-p90RSK (Ser380)	1:1,000	Cell Signaling Cat# 11989, RRID:AB_2687613
Rabbit Anti-Phospho-Stat3 (Tyr705)	1:1,000	Cell Signaling Cat# 9145, RRID:AB_2491009
Rabbit Anti-Stat3α	1:1,000	Cell Signaling Cat# 8768, RRID:AB_2722529
Rabbit Anti-Phospho-Src Family (Tyr416)	1:1,000	Cell Signaling Cat# 2101, RRID:AB_331697
Rabbit Anti-Src	1:1,000	Cell Signaling Cat# 2109, RRID:AB_2106059
Rabbit Anti-Cleaved Caspase-3 (Asp175)	1:1,000	Cell Signaling Cat# 9661, RRID:AB_2341188
Rabbit Anti-Phospho-S6 Ribosomal Protein (Ser235/236)	1:1,000	Cell Signaling Cat# 4857, RRID:AB_2181035
Rabbit Anti-Phospho-S6 Ribosomal Protein (Ser240/244)	1:1,000	Cell Signaling Cat# 2215, RRID:AB_331682
Rabbit Anti-S6 Ribosomal Protein	1:1,000	Cell Signaling Cat# 2217, RRID:AB_331355
Rabbit Anti-Phospho-4E-BP1 (Ser65)	1:1,000	Cell Signaling Cat# 9451, RRID:AB_330947
Rabbit Anti- Phospho-4E-BP1 (Thr37 / Thr46)	1:1,000	Cell Signaling Cat# 2855, RRID:AB_560835
Rabbit Anti-4E-BP1	1:1,000	Cell Signaling Cat# 9644, RRID:AB_2097841
Mouse Anti-vinculin	1:1,000	Santa Cruz Cat# sc-25336, RRID:AB_628438
Rabbit Anti-Tubulin-β	1:1,000	Sigma-Aldrich Cat#SAB4500088, RRID:AB_10743647
Mouse Anti-GADPH	1:1,000	Millipore Cat# CB1001, RRID:AB_2107426
Sheep Anti-mouse IgG, HRP-linked Antibody	1:10,000	Cytiva Cat# NA931, RRID:AB_772210
Goat Anti-rabbit IgG, HRP-linked Antibody	1:10,000	Cell Signaling Cat# 7074, RRID:AB_2099233

Inhibitors used *in vitro*

The following ALK inhibitors were used in the study: crizotinib, alectinib (CH5424802, Hölzel Biotech, #S2762-5), brigatinib, (AP26113, Biozol Diagnostica, #SEL-S8229) and lorlatinib (PF-6463922, Biozol Diagnostica, #S7536-25). VX-11e (Biocat, #T3166) and SCH772984 (Hölzel Biotech, #A12824) were used to inhibit ERK activity. SRC inhibition was achieved with dasatinib (BMS-354825, Hölzel Biotech, #A10290-10mM). mTOR was inhibited with rapamycin (Biomol, #Cay13346-1) and torin1 (Cayman Chemical, #Cay10997-10). All inhibitors were dissolved in dimethyl sulfoxide (DMSO, Sigma-Aldrich, #D2650) and stored at -80°C for long-term storage. DMSO was used as a vehicle or control at the maximum concentration used for other inhibitors.

Determination of IC50 and cell viability

Mouse tumor cells were plated in 96-well plates with 2,000 cells per well. Duplicates were treated with serially diluted inhibitors in DMEM for 72 to 96 hours. After treatment, cell viability was assessed using CellTiter 96® AQueous One Solution (Promega, #G3580) according to the manufacturer's guidelines. After 4 hours of incubation, the absorbance at 490 nm was recorded using a 96-well plate reader. IC50 values were then determined using a three-parameter nonlinear dose-response fit using Graph Pad Prism software. These IC50 values were then normalized to control vehicle and/or crizotinib.

Drug interaction assay

The synergistic score for each drug combination was assessed as follows. Mouse tumor-derived cells were plated onto 96-well plates as previously described in the section "Determination of IC50 and Cell Viability." After 24 hours, cells were subjected to treatment with escalating concentrations of either individual drugs or drug combinations, as specified in figure legends. Subsequently, cell viability was evaluated using CellTiter 96® AQueous One Solution following the manufacturer's protocol. The assessment of drug interaction was then conducted using Synergy Finder in conjunction with the Loewe model.

Clonogenicity assays

1,000 mouse tumor cells were seeded per well of a 6-well plate 24 hours prior to treatment. The cells were then treated with specific inhibitors at the indicated doses. Media and inhibitors were refreshed three times per week and colonies were allowed to grow for two weeks. Wells were then gently rinsed with PBS and colonies were fixed with 100% methanol for 10 minutes at -20°C. Wells were then rinsed with PBS and stained with crystal violet working solution (0.5% crystal violet (Sigma, #V5265), 25% methanol, in distilled water) for 1 hour at room temperature or overnight at 4°C with gentle horizontal agitation. Plates were then rinsed with distilled water and colonies were imaged. Total covered area and crystal violet intensity were calculated using Fiji (version 2.9.0/1.53t).

Determination of ROS levels by CellRox assay

50,000 mouse tumor-derived cells were seeded per well of a 12-well plate. After 24 hours, cells were treated with specific drugs, concentrations and times as indicated in the figure legends. Reactive oxygen species (ROS) were measured using CellROX™ Deep Red (ThermoFisher, #C10491) according to the manufacturer's protocol. Briefly, ROS levels were

assessed by flow cytometry after excluding doublets and live cells (DAPI negative cells). H2O2 was used as a positive control at a final concentration of 5-20 µM.

Determination of antioxidant enzymes levels by RT-PCR

Mouse tumor-derived cells were first seeded and treated as described in the "Determination of ROS Levels by CellRox Assay" section. Total RNA was then extracted using the RNeasy Mini Kit (Qiagen, #74104) according to the manufacturer's instructions. The isolated RNA was quantified using a NanoDrop Lite spectrophotometer with an absorbance 260/280 ratio of approximately 2, indicating high quality RNA. To eliminate potential cDNA contamination, cDNA synthesis was performed using the QuantiTect Rev. Transcription Kit (Qiagen, #205313) according to the manufacturer's instructions. A 10 ng aliquot of cDNA was used for reverse transcription-quantitative polymerase chain reaction (RT-qPCR) using SYBR Green PCR Master Mix (2X) (Applied Biosystems, # 4364346) and primers listed in **Table 19**. The RT-qPCR procedure was performed using a LightCycler II 480 instrument (Roche, 05015243001). Data readouts were calculated using either the ΔCt or ΔΔCt quantification method and then normalized to housekeeping genes to estimate relative mRNA levels for the target genes.

Table 19 | RT-qPCR primers

Target gene	Direction	Sequence
Gclc	Forward	5' AGATGATAGAACACGGGAGGAG 3'
	Reverse	5' TGATCCTAAAGCGATTGTTCTTC 3'
Gclm	Forward	5' AGATGATAGAACACGGGAGGAG 3'
	Reverse	5' TGATCCTAAAGCGATTGTTCTTC 3'
Gpx4	Forward	5' CGCTCCATGCACGAATTCTC 3'
	Reverse	5' GCACACGAAACCCCTGTACT 3'
Hmox1	Forward	5' AGGCTAAGACCGCCTTCCT 3'
	Reverse	5' TGTGTTCCTCTGTCAGCATCA 3'

In vivo treatments

8-week-old Rj:NMRI-*Foxn1*$^{nu/nu}$ mice were purchased from Janvier-Labs. 250,000 mouse tumor cells resuspended in DMEM were injected subcutaneously into the right flank using an insulin syringe needle. Subcutaneous tumors were allowed to reach 0.50 cm3 (ERK inhibitor treatment) or 0.25 cm3 (SRC inhibitor treatment) and mice were randomly assigned to different arms of the experiment. Drugs were freshly prepared and mice were treated with brigatinib (10 mg/kg o.d., 0.5% CMC-Na (Sigma-Aldrich, #21902) + 0.5% Tween 20 (Sigma-Aldrich, #P9416)), an ERK inhibitor (15 mg/kg SCH772984 i.p., 10% DMSO + 40% PEG300 + 5% Tween 20 + 45% ddH2O), SRC inhibitor (5 mg/kg i.p., daily) as indicated in the figure legends. Vehicle groups received the maximum volume and concentration of drug solvents.

Animal weight and health status were assessed daily to determine drug-related side effects. Tumor length and width were measured daily using an electronic caliper, and tumor volume was calculated using the ellipsoidal formula (length × width^2)/2. Experimental endpoints were defined as a tumor exceeding 1.50 cm in length. The investigators were not blinded to treatment arm.

Cas9-EGFP mice underwent treatment as described in Figure 43. Treatment comprised 5 days followed by 2 days of no treatment, then 5 more days of treatment. Tumor burden was assessed via µCT lung scan before treatment. Only the lorlatinib group underwent µCT on the final treatment day. Lorlatinib and SHP099 were obtained from Selleckchem, dissolved in DMSO, 30% PEG, and water, and administered orally via gavage. Mice were monitored daily for lung tumor symptoms, weight loss, and treatment-related side effects.

Cell cycle analysis

A total of 200,000 mouse tumor-derived cells were seeded into each well of a 6-well plate. Following a 24-hour incubation period, cells were subjected to treatment with specific inhibitors, as described in the figure legend. Cells were incubated with these inhibitors for an additional 24 hours, after which both the supernatant and attached cells were collected into 1.5 mL centrifuge tubes. The cell suspension was washed with ice-cold PBS, and the resulting pellets were resuspended in 100 µL of ice-cold PBS. Subsequently, 1 mL of 70% ethanol was added drop-wise while gently vortexing the tubes. Cells were then fixed at -20°C for a minimum of 24 hours. After fixation, the cells underwent a PBS wash and were incubated with a cell cycle working solution (**Table 20**) for 30 minutes, at room temperature while gently agitating in dark conditions. Stained cells were washed with PBS, resuspended in FACS buffer and subsequently subjected to flow cytometry to measure propidium iodide intensity. The acquired data were analyzed using FlowJo software to assess cell profiling.

Table 20 | Cell cycle solution

Reagent	Final concentration
Propidium idodide, LIFE Technologies #BMS500PI	20 µg/mL
RNaseA, Sigma-Aldrich #10109142001	0.1 mg/ml
Tween 20, Sigma-Aldrich #P1379	0.1%
PBS	1X

Generation of ALK-resistant cells

Mouse tumor-derived cells were subjected to prolonged treatment with alectinib, brigatinib, and lorlatinib, each at a concentration of 2 µM, for a minimum of 6 months. To prevent over confluency, cells were periodically split and culture media and drug-conditions

were refreshed every other day. In parallel, control groups were treated with DMSO and maintained under identical aging conditions.

To assess the absence of mutations on the *Alk* kinase, targeted PCR amplification of the *Alk* kinase domain was performed (**Table 21**) on cDNA, followed by Sanger sequencing performed by Mycrosynth Services. Base calling and overall quality assessment of the DNA sequences were performed using Benchling [Biology Software] (2018-2024, https://benchling.com).

The development of resistance to the corresponding ALK inhibitor was confirmed using CellTiter 96® AQueous One Solution, as described in the "Determination of IC50 and cell viability" section.

Table 21 | Primers used to amplify the most frequently mutated *Alk* region

Primer	Sequence
Forward	TGGCAAGACTTCCTCCATCAG
Reverse	AGGTAAATATCCCTTCCATGAAGGC

Sample preparation for proteomics analysis

Sample preparation and further proteomic analysis was performed by myself and Maria Ramos in collaboration with members from the Klingmüller's group (Barbara Helm, Dario Lucas Frey) and Junyan Lu's group (Shubham Agrawal). This method section was described by Barbara Helm and Dario Lucas Frey.

"Initially, cellular lysis of tumor-derived cells was done by using RIPA buffer composed of 50mM Tris pH 7.4, 150mM NaCl, 4% SDS, 1µg/mL Aprotinin, and 0.1mg/mL 4-(2-Aminoethyl) benzene sulfonyl fluoride-hydrochloride. Next, cell lysates were sonicated on ice using a sonication probe (30 sec; 75% Amplitude; 0.1 on 0.5 off cycles). Then, the samples underwent centrifugation for ten minutes at a speed of 14,000 rpm and a temperature of 20°C. The resulting supernatant was transferred to a new vial with care. The BCA Assay was employed according to the manufacturer's instructions to determine the total protein concentration in each sample. For further processing, 10µg of protein was utilized.

The disulfide bonds in the proteins underwent reduction with 40 mM of Tris(2-carboxyethyl) phosphine (TCEP), followed by alkylation with 160 mM of chloroacetamide (CAA) for 5 minutes at 95°C. A modified version of the single-pot, solid-phase-enhanced sample-preparation protocol (SP3) that uses paramagnetic beads was employed to carry out

protein digestion and purification (61). Initially, Sera-Mag Speed Beads A and B from Ge Healthcare were mixed thoroughly by vortexing until the pellet had completely dissolved. Subsequently, 10µL of Bead A and 10µL of Bead B were mixed, and the solution was diluted to 200µL with MS-H2O. The mixture was then transferred to a magnetic rack and left for one minute, after which the supernatant was removed. The beads were then removed from the magnetic rack and washed with water three times. After the final wash, the volume was adjusted to 20µL using MS-H2O. Finally, 2µL of the bead preparation were added to each sample. Ethanol was added to achieve a final concentration of 50% (v/v), which enhanced protein binding to the beads. The samples were then incubated for 15 minutes at 800 rpm and room temperature.

After incubation, the samples were placed on the magnetic rack and the supernatant was discarded 3 minutes later. The magnetic rack was removed, and the samples were washed with 80% ethanol, repeating the process three times. Finally, the samples were reconstituted in a TEAB buffer with a concentration of 100mM, containing trypsin at an enzyme/protein ratio of 1:25. The samples were allowed to digest overnight on a shaker set at 37°C and 1000 rpm. Subsequently, the samples were placed on the magnetic rack once more, and the obtained supernatants were transferred to fresh tubes. The resulting peptides were then dried using vacuum centrifugation at 45°C and subsequently stored at -80°C until further use.

To analyze the (phospho)proteomics of *Eml4-Alk* variant 3 under the influence of ALK inhibitors, mTDCs were treated with dasatinib, brigatinib, or Combo for different time periods: 10 minutes, 16 hours, 24 hours, 48 hours, and 60 hours. At each specific time point, the cells were lysed using a buffer that comprised the following components. 25 mM Tris pH 7.6, 150 mM NaCl, 0.1% SDS, 1% NP40, 1% deoxycholic acid NA-salt, 1 mM Na3VO4, 10 mM NaF, 1 µg/mL aprotinin, 0.1 mg/mL 4-(2-aminoethyl) benzene sulfonyl fluoride-hydrochloride, 250 U/mL Benzonase, 10 U/mL DNase, and PhosSTOP (4906845001 Roche: 1x tablet/10 mL buffer) were used. The cell lysates were incubated and rotated for 30 minutes at 4°C following these steps. After the incubation period, the samples underwent centrifugation at 14,000 rpm and 20°C for 10 minutes. Afterwards, the supernatants were meticulously transferred to new vials. The BCA Assay was employed to determine protein concentration, using 55µg of total protein per sample for subsequent processing.

The modified automated paramagnetic bead-based single-pot, solid-phase-enhanced sample-preparation (Auto-SP3) protocol (62) was used to conduct protein digestion and purification on a Bravo liquid handling platform (Agilent). To begin with, the proteins' disulfide

bonds were reduced through the use of 10mM TCEP, and subsequently alkylated with 40mM CAA for 5 minutes at 95°C. To prepare the beads, Sera-Mag Speed Beads A and B from Ge Healthcare were vortexed until the pellet had completely dissolved. The bead suspension was placed onto a magnetic rack and removed the supernatant in a careful manner after one minute, repeating this magnetic bead washing procedure three times. Afterwards, 100µL of bead A was combined with 100µL of bead B, adjusting the final volume to 100µL using MS-H2O. Finally, a total of 5µL of the A+B bead mixture was added to each sample.

The Bravo liquid handling platform from Agilent was utilized, employing the "Auto-SP3" protocol provided by the same company. Protein digestion took place, utilizing a TEAB buffer that contained trypsin, with an enzyme/protein ratio of 1:25, and samples were incubated at 37°C overnight. After digestion and recovery, the peptides were separated into two separate aliquots, with one corresponding to 5 µg and the other to 50 µg, and then dried using vacuum centrifugation at 1,300 rpm at 45°C. These dried samples were later stored at -80°C for further analysis."

Phosphopeptide enrichment

This method section was described by Barbara Helm and Dario Lucas Frey.

"Phosphopeptide enrichment was carried out employing an AssayMAP head integrated with a Bravo liquid handling platform (Agilent) and 5µL Fe(III)-NTA cartridges, following a standard procedure provided by Agilent. In brief, 50 µg of digested peptides were initially reconstituted in 20 µL of H2O + 0.1% TFA and then sonicated for 5 minutes in a water bath. Subsequently, 80 µL of 100% ACN + 0.1% TFA buffer was added, and another 5-minute sonication step in a water bath followed. The cartridges were primed with a priming buffer consisting of 100 µL of 50% ACN + 0.1% TFA, at a flow rate of 300 µL/min, and subsequently equilibrated with 50 µL of 80% ACN + 0.1% TFA at a flow rate of 10 µL/min.

Following this, the peptides were loaded onto the cartridge at a flow rate of five µL/min. The Cup, internal cartridge, and stringent syringe wash steps were executed using the predefined values within the enrichment protocol. The phosphorylated peptides were eluted using 20 µL of 1% aqueous ammonia in a pH11 elution buffer, collected into a fresh collection plate. These samples were then subjected to drying via vacuum centrifugation (1,300 rpm at 45°C) and subsequently stored at -80°C until they were ready for analysis by LC-MS/MS."

LC-MS/MS Analysis

This method section was described by Barbara Helm and Dario Lucas Frey.

“For the Nano-flow LC-MS/MS analysis of the Eml4-Alk variant 1 and variant 3, an EASY-nLC 1200 was coupled to an Orbitrap Exploris 480 mass spectrometer (Thermo Fisher Scientific). Tryptic peptides were dissolved in 15 µL loading buffer (0.1% formic acid (FA), 2% ACN in MS-compatible H2O), and 2 µL were injected for each analysis. Peptides were delivered to an analytical column (75 µm × 30 cm, packed in-house with Reprosil-Pur 120 C18-AQ, 1.9 µm resin, Dr. Maisch) at a flow rate of 3 µL/min in 98% buffer A (0.1% FA in MS-compatible H2O). After loading, peptides were separated using an 84 min gradient from 2% to 38% of buffer B (0.1% FA, 80% ACN in MS-compatible H2O) at 350 nL/min flow rate. The Orbitrap Exploris 480 mass spectrometer was operated in data-dependent mode (DDA), automatically switching between full scan MS and MS2. Full scan MS spectra were acquired in the Orbitrap at 60 000 (m/z 200) resolution after accumulation to the set target value of 300% (100% = 1e6). Tandem mass spectra were generated for up to 20 peptide precursors in the orbitrap (isolation window 1.0 m/z) after fragmentation using higher energy collisional dissociation (HCD) at normalized collision energy (N)CE of 30%. MS2 spectra were acquired in the Orbitrap at a resolution of 15 000 with a target value of 100% (1e5) charges after accumulation for a maximum of 22 ms.

For the Nano-flow LC-MS/MS analysis of the (phospho)proteome of Eml4-Alk variant 3 upon drug treatments, an Ultimate 3000 HPLC (Thermo Fisher Scientific) was coupled to an Orbitrap Eclipse mass spectrometer (Thermo Fisher Scientific). For the full proteome analysis, peptides were dissolved in 15 µl loading buffer (0.1% formic acid (FA), 2% ACN in MS-compatible H2O), and 2 µL were injected for each analysis. For the phosphoproteome analysis, peptides were dissolved in 10 µl loading buffer (50mM Citric acid + 0,1% FA), and 5 µL were injected for each analysis. The samples were loaded onto a pre-column (PEPMAP 100 C18 5µm 0.3mmx5mm, Thermo Scientific) using a loading pump at a higher flow rate. After 5min, a valve was switched, and the peptides were delivered to an analytical column (75 µm × 30 cm, packed in-house with Reprosil-Pur 120 C18-AQ, 1.9 µm resin, Dr. Maisch) at a flow rate of 3 µL/min in 98% buffer A (0.1% FA in MS-compatible H2O). After loading, peptides were separated using a 140 min gradient from 2% to 38% of buffer B (0.1% FA, 80% ACN in MS-compatible H2O) at a 300 nL/min flow rate. The Orbitrap Eclipse was operated in data-independent mode (DIA), with an m/z range of 350-1400. Full scan spectra were acquired in the Orbitrap at 120 000 resolution after accumulation to the set target value of 300% (100% = 1e6) and maximum injection time of 45ms. DIA scans followed the full scans. Forty-seven isolation windows were defined, with an m/z range of 406-986 for full proteome and 421-1182 for phosphoproteome. Spectra were generated in the orbitrap (isolation window 1.6 m/z) after fragmentation using higher energy collisional dissociation (HCD) at normalized collision energy (N)CE of 28% for full proteome and 26% for phosphoproteomes and acquired at

30,000 resolution after accumulation to the set target value of 1000% (100% =1e5) and maximum injection time of 54ms."

Database search and Data Analysis

This method section was described by Barbara Helm and Dario Lucas Frey.

"MaxQuant version 1.6.3.3 processed all DDA raw files, enabling peak detection and quantification. Technical abbreviations are explained upon first use. The Andromeda search engine was used to search MS/MS spectra against the Uniprot Mus musculus reference proteome database, which was downloaded on February 2, 2021. This search involved contaminant detection and considering reversed sequences. The specified search parameters included carbamidomethylation of cysteine residues as a fixed modification and variable modifications of acetyl (Protein N-term) and oxidation (M). The proteolytic enzyme trypsin/P was implemented, allowing for up to three missed cleavages. To align replicates within the same group, matching between runs was permitted. MaxQuant's time-dependent recalibration algorithm was used to determine precursor ions' mass accuracy. The proteins and peptides were subject to a maximum false discovery rate (FDR) of 0.01, and required at least eight amino acids in length for analysis. All default parameters were retained.

The Spectronaut 16.3 software from Biognosys in Zurich, Switzerland was used for the direct DIA workflow analysis of all DIA raw data files. The study showed a noticeable decrease in reproducibility during later time points of the phosphoproteomic analysis, but consistently high reproducibility throughout. The mean R2 values were 0.9615 for full proteomic analysis and 0.7572 for phosphoproteomic analysis. The Pulsar search employed the Uniprot Mus musculus reference proteome database downloaded on February 21, 2023. The database parameters matched those of full-specificity trypsin digestion, encompassing a peptide range of 7-52 amino acids, with a maximum allowance of 2 missed cleavages. The protein database preprocessing involved eradicating N-terminal methionine. Carbamidomethylation at cysteine was specified as the fixed modification, with variable modifications covering protein N-terminal acetylation, methionine oxidation, and phosphorylation (STY) for phospho-enriched sample analysis. False discovery rates (FDRs) of 0.01 were applied for peptide-spectrum match (PSM), peptide, and protein identification. Technical term abbreviations were explained when first used. Quantification involved the use of identified (Qvalue) for precursor filtering and MS2 quantification, with area as the quantity type and no normalization selected. The writing adhered to principles of objectivity, comprehensibility, conventional structure, clear and objective language, format, formal register, balanced perspectives, precise word choice, and grammatical correctness."

Pre-processing and quality control of the proteomic and phosphoproteomic data

This method section was described by Junyan Lu.

“DDA and DIA data were processed by MaxQuant (version 1.6.3.3) and by Spectronaut (version 16.3) respectively. The report files generated by MaxQuant and Spectronaut underwent additional refinement and were subjected to analysis within R, version 4.2.0. The R/Bioconductor package DEP (version 64) was employed to handle the data concerning protein or phosphorylation abundance and to perform quality control procedures.

Proteins were considered suitable for further analysis if they were identified by at least one proteotypic peptide. This selection process yielded a dataset of 4843 proteins from the DDA data and 10036 proteins along with 19880 phosphorylation sites from the DIA data. Subsequently, the abundance data related to proteins and phosphorylation underwent background correction, scaling, and transformation using the variance stabilizing transformation method (Huber et al. 2002).

To pinpoint phosphorylation alterations that are independent of changes in protein abundance, the abundance of each phosphorylation site was additionally adjusted based on the abundance of the corresponding protein.”

Statistical and bioinformatic analysis

Statistical and bioinformatic analyses of the proteomics and phosphoproteomics data were conducted by Junyan Lu. Additional bioinformatic analyses were carried out by myself using the preprocessed data, supervision and guidance provided by Junyan Lu. This method section was described by Junyan Lu and myself.

Statistical analyses were carried out using GraphPad Prism 8 and R version 4.3.0, with specific details about the statistical tests provided in the corresponding figure legends. The results, figure legends, and methods sections contain comprehensive information on sample size, technical replicates, statistical methodologies, and measures of precision for all experiments conducted in this study.

To identify potential associations between protein or phosphorylation abundance and various conditions (such as V1 versus V3 variant or different treatments), the proDA package from Bioconductor was employed. This package utilizes a linear model and considers the presence of missing values through a detection model. Adjusted P-values were calculated

using the Benjamini-Hochberg method. Depending on the specific comparison type, proteins or phosphorylation sites meeting either an adjusted P-value < 0.1 (equivalent to a 10% false discovery rate) or a nominal P-value < 0.05 were reported.

For exploratory data analyses, which include techniques like principal component analysis and hierarchical clustering displayed in heatmap visualizations, missing values were imputed using the bpca (Bayesian PCA) method implemented within the DEP package.

Gene set enrichment analysis (GSEA) involved the use of the fgsea package against gene sets sourced from the Molecular Signature Database (MSigDB). Transcription factor enrichment analysis was conducted using Pscan.

To infer kinase activity based on the phosphoproteomic data, the decoupleR package was employed, utilizing prior knowledge of kinase-target relationships in mice from OmniPath. Kinase perturbation analysis (KinasePA) was performed using the DirectPA package. In both decoupleR and KinasePA analyses, differential abundant phosphorylation sites with a P-value < 0.05 were used as input data.

Mouse lung tissue homogenization for Tuba-seq

For tumor barcoding sequencing, lung lobes were snap frozen in clean 2 mL centrifuge tubes and stored at -80°C. After thawing, each lung lobe was treated with 1 mL of lysis cocktail (**Table 22**) and combined with three clean metal beads. In addition, 300,000 spike-in cells were added to each lung (a total of 5 lobes). The tubes were shaken vigorously for 2 minutes at 1,800 oscillations per minute using a Qiagen TissueLyser II. After a 2-minute rest, samples were shaken for an additional 2 minutes. If there was evidence of incomplete tissue disruption, this process was repeated. The samples were then incubated overnight at 55°C with constant horizontal shaking at 1,000 rpm. Digested lung lobes from the same mouse were aggregated in a 15 mL centrifuge tube and stored at 4°C.

Table 22 | Tuba-seq lysis cocktail

Stock	Final concentration
5 M NaCl	100 mM NaCl
1 M Tris, pH 7.6	20 mM Tris 7.6
0.5 M EDTA, pH 8.0	10 mM EDTA
20% SDS	0.5% SDS

Phenol-Chloroform extraction of genomic DNA from tumor bearing lungs

Lung lysates from section "*Mouse lung tissue homogenization for Tuba-seq*" were homogenized by applying vigorous vortex. 750 µL of the lysates were then mixed with 500 µL

of 5M NaCl and vortex-mixed. The samples were then centrifuged at 14,000 rpm, 4°C for 10 minutes. 1 mL was then transferred to a clean 2mL tube and mixed vigorously with 1 mL of UltraPure Phenol:Chloroform:Isoamyl Alcohol (25:24:1, v/v) (Invitrogen, #15593031). Samples were then spun down at 14,000 rpm, RT, for 5 minutes. 800 µL of the aqueous phase was transferred to a clean tube and vortex-mixed with 800 µL of chloroform. Samples were centrifuged at 14,000 rpm, RT, for 10 minutes. 550 µL of the aqueous phase were transferred to a clean tube and precipitated by adding 800 µL of 100% ethanol and 40 µL of sodium acetate 3M ph 5.2 (Life Technologies, #R1181). After spinning down the samples (5 minutes at 14,000 rpm, 4°C), the supernatant was discarded and pellets were washed with 800 µL of freshly made 70% ethanol. Samples were then centrifuged (5 minutes at 14,000 rpm, 4°C) and the DNA pellet was air dried. DNA was resuspended in 200 µL of UltraPure DNase/RNase-Free Distilled Water and incubated at 4°C overnight. DNA quality was assessed by NanoDrop Lite spectrophotometer. An absorbance 260/280 ratio of approximately 1.8 indicated uncontaminated DNA.

Library preparation for tumor barcoding sequencing

Libraries were prepared in a clean PCR hood and using DNA low binding, clean PCR tubes. DNA samples were amplified using Illumina compatible, dual indexing primers designed by the Winslow lab.

An initial test PCR was conducted on DNA samples to evaluate the amplification efficiency of the primer pairs targeting the barcoded region. This test PCR consisted of 800 ng of genomic DNA, 1.6 µL of a 5 µM index primer mix, 10 µL of NEBNext Ultra II Q5 Master Mix (New England Biolabs, #M0544S), and UltraPure DNase/RNase-Free Distilled Water to reach a final volume of 20 µL. The PCR program was as follows: 98°C for 3 minutes, followed by 25 cycles of 98°C for 10 seconds, 63°C for 30 seconds, and 72°C for 12 seconds, with a final extension step at 72°C for 5 minutes, and then holding at 4°C. The resulting amplicons were visualized by electrophoresis on a 2% agarose gel containing peqGreen DNA dye, applying a voltage of 120V. The target bands at 320 bp were captured using an Invitrogen iBright FL1500 Imaging System. In cases where no amplicon was observed, the PCR program was extended to 27 cycles.

Subsequently, upon obtaining positive results, a large-scale PCR library was generated. This involved replicating the same PCR parameters as described earlier, but with an increased scale, utilizing 32 µg of genomic DNA, 64 µL of primer mix, 400 µL of NEBNext Ultra II Q5 Master Mix, and UltraPure DNase/RNase-Free Distilled Water to achieve a final

volume of 800 µL. The final reaction mix was divided into 8 individual PCR tubes. Amplicons were then pooled into a clean centrifuge tube and stored at -20°C.

100 µL of the PCR product was transferred to a clean tube and mixed thoroughly with 70 µL of the AMPure XP beads (BECKMAN COULTER, # A63880) (DNA ratio 0.7x). Samples were incubated for 5 minutes and placed on a magnetic stand for 5 minutes. Supernatant was transferred to a clean tube and mixed thoroughly with 30 µL of AMPure XP beads (DNA ratio 1x). Samples were incubated for 5 minutes and placed on a magnetic stand for 5 minutes. Supernatant was discarded and beads were washed twice by resuspending the beads in 200 µL of 80% ethanol, incubated for 5 minutes and placed on a magnetic stand. Beads were then spun down and the residual ethanol was discarded. Beads were then air-dried and thoroughly resuspended in 23 µL of UltraPure DNase/RNase-Free Distilled Water. After 10 minutes incubation, beads were spun down and placed on a magnetic stand for 5 minutes. 21 µL of the clear supernatant were transferred to a PCR clean low binding tube. The quality of amplicons profiles was assessed using D1000 TapeStation system.

Tumor barcoding analysis

The following methods corresponding to tumor barcoding analysis were written by Emily Shuldiner, PhD student from Dr. Monte Winslow's laboratory (Stanford University).

Analysis of sgID-BC sequencing data

"Sequencing of Tuba-seq libraries produces reads that are expected to contain an 8-nucleotide sgID followed by a 30-nucleotide BC of the form GCNNNNNTANNNNNGCNNNNNTANNNNNGC, where each of the 20 Ns represents a random nucleotide. Each sgID has a one-to-one correspondence with an sgRNA in the viral pool; thus, the sgID sequence identifies the gene targeted in each tumor. Note that all sgID sequences in a viral pool differ from each other by at least three nucleotides such that incorrect sgID assignment (and thus, inference of tumor genotype) due to PCR or sequencing error is extremely unlikely. Distinct sets of sgIDs were used to tag each sgRNA in the V1 and V3 viral pools. The random 20-nucleotide BC tags all cells in a single clonal expansion. Note that the length of the BC ensures a high theoretical potential diversity (~420 > 1012 BCs per vector), with the actual diversity of each Lenti-sgRNA/Cre vector dictated by the number of bacterial colonies pooled during the plasmid barcoding step.

FASTQ files were parsed using regular expressions to identify the sgID and BC in each read. To minimize the effects of sequencing error on BC identification, we required the forward

and reverse reads to agree completely within the 30-nucleotide sgID-BC region. We also performed an analysis to identify BCs that were likely to have arisen from genuine tumors due to PCR or sequencing errors. Given the low rate of sequencing error, we expect these 'spurious tumors' to have read counts that are far lower than the read counts of the genuine tumors from which they arise. To minimize the impact of these 'spurious tumors', we identified small 'tumors' with BCs that were highly similar to the BCs of larger tumors in the same sample. Specifically, if a pair of 'tumors' within a sample had BCs that were within a Hamming distance of two, and if one of the tumors had fewer than 5% as many reads as the other, then the reads associated with the smaller tumor were attributed to the larger tumor.

After these filtering steps, the read counts associated with each BC were converted to absolute neoplastic cell numbers by normalizing to the number of reads from the 'spike-in' cell lines added to each sample before lung lysis and DNA extraction."

Removal of contaminating barcodes

"sgID-BC sequences that are not from genuine tumors in an individual tumor-bearing lung sample can none-the-less be present in sequencing libraries for several reasons including intra-experiment sample-to-sample cross-contamination during library preparation, external contamination (e.g. from samples and libraries from other experiments), and library-to-library misassignment during sequencing. These sgID-BC sequences have the potential to be identified as small tumors (i.e. 'spurious tumors') and thereby reduce the precision of our analyses. Both external contamination and sample-to-sample contamination result in the identification of the same sgID-BC in multiple samples. However, some sgID-BCs are expected to recur across samples in the absence of contamination due to the finite diversity of the sgID-BC region in each lenti-sgRNA/Cre vector. To minimize the effects of contamination, we examined patterns of sgID-BC recurrence across samples and removed barcodes that occurred in a number of samples that would be highly unlikely to occur by chance given the BC diversity of each vector.

To estimate the BC diversity associated with each sgID, we assume that the probability of observing a BC in i mice is Poisson distributed: $P(k=i; \lambda) = \lambda k\, e{-}\lambda / k!$, where λ is the mean number of mice that barcodes appear in for a given lenti-sgRNA vector. To estimate λr for each sgID r in the dataset we note that $\lambda r/(1 - e{-}\lambda r) = \mu$non-zero, where μnon-zero $= \Sigma i=1\infty P(k=i; \lambda r)$ is the mean number of occurrences of each BC that occurred once or more (a known quantity). Given the Poisson distribution defined for each sgID r, we calculated a lenti-sgRNA/Cre vector specific threshold Nr such that 99.9% of barcodes would be expected to

appear in Nr samples or fewer and identified and removed all 'tumors' with sgID-BCs that occurred in a number of samples exceeding Nr.

sgID-BCs can also recur across samples due to misassignment of reads during sample de-multiplexing. While misassignment of reads is expected to be extremely rare, it could result in sgID-BCs from genuine tumors with very large read counts in one sample (i.e., a very large, genuine tumor) appearing with low read counts in additional samples sequenced in the same lane. To guard against this possibility and ensure that very large tumors were not systematically discarded by the procedure described in the prior paragraph, we examined the distribution of reads across samples to identify sgID-BCs that appeared in >Nr samples but where >95% of sequencing reads were assigned to a single sample. These sgID-BCs were retained in the sample with the bulk of the sequencing reads and discarded in all other samples. All other barcodes appearing in > Nr samples were discarded from all samples."

Removal of mice with low tumor number

"After processing the sgID-BC sequencing data and performing the filtering steps described above the number of unique barcodes represents the number of genuine clonal tumors. Tumor number across mice was highly variable in all cohorts (i.e., the mean number of tumors in mice transduced with the Lenti-sgTSG^{75}-sgV1/Cre pool was 4,159 with a standard deviation of 3,553 and the mean number of tumors in mice transduced with the Lenti- sgTSG^{75}-sgV3/Cre pool was 9,403 with a standard deviation of 6,310). This is most likely driven by variability in lentiviral delivery and/or other factors that change overall transduction across mice. Samples with extremely low tumor number (fewer than 1,000 tumors detected) were deemed to not have been successfully transduced and were removed from the analysis. We removed one sample from the *Cas9-EGFP* cohort transduced with Lenti-sgTSG^{19}-sgV3/Cre, four samples from the *Cas9-EGFP* cohort transduced with Lenti- sgTSG^{75}-sgV1/Cre, one sample from the *Cas9-EGFP* cohort transduced with Lenti- sgTSG^{75}-sgV3/Cre, and one sample from the Cas9-negative *Kras$^{G12D/+}$;Trp53$^{flox/wt}$* cohort transduced with Lenti- sgTSG^{75}-sgV1/Cre."

Filtering of vectors with insufficient titer from analysis

"Each Lenti-sgRNA/Cre vectors was titered before pooling and pooled with goal of equal representation of each vector in the viral pool, however our analysis requires us to know the exact proportion of each vector in the pool. We therefore transduced cohorts of Cas9-negative control mice with each lentiviral pool to quantify the representation of each vector in each pool. These cohorts were composed of *Kras$^{LSL-G12D/+}$;p53$^{flox/wt}$* and *Kras$^{LSL-G12D/+}$; p53$^{flox/flox}$*

mice which do not express Cas9. Transduced cells, with unique sgID-BCs, will still expand into *Kras*-driven tumors, but all sgRNAs are functionally inert. In these mice the relative tumor number associated with each sgRNA reflects the proportion of that vector in that viral pool. Quantifying the number of tumors associated with each sgRNA in these Cas9-negative mice revealed a small number of vectors that were represented at a suboptimal proportion to enable further analysis. Vectors with an average of fewer than 15 unique barcodes per mouse in the Cas9-negative control cohorts were removed prior to analysis of tumor suppressive effects (*sgDnmt3a#1*, *sgp53#1*, *Nkx2-1#1 and sgKmt2c#1* were removed from analysis of the Lenti-sg*TSG*[75]-sg*V1*/Cre viral pool; *sgSmad4#2*, *sgSlc34a2#2* and *sgLats2#1* were removed from the analysis of the Lenti-sg*TSG*[75]-sg*V3*/Cre pools. No vectors were removed from analyses of the Lenti-sg*TSG*[19]-sg*V1*/Cre and Lenti-sg*TSG*[19]-sg*V3*/Cre viral pools)."

Adaptive sampling of tumors for statistical comparison of tumor genotypes

"We performed four independent screens of tumor suppressor function in EML4-ALK-driven lung cancer using different viral pools (Lenti- sg*TSG*[19]-sgV1/Cre, Lenti- sg*TSG*[19]-sgV3/Cre, Lenti- sg*TSG*[75]-sgV1/Cre, and Lenti- sg*TSG*[75]-sgV3/Cre). These experiments varied in several respects including technical differences such as sequencing depth, cohort size, and the titer and pooling of Lenti-sgRNA/Cre vectors, as well as intrinsic differences in the growth dynamics of V1- and V3-driven tumors. To mitigate the impact of these factors and ensure that an equivalent portion of the tumor size distribution was analyzed for each sgRNA i in each experiment j, we scaled the number of tumors analyzed from each dataset (combination of sgRNA and experiment) to account for differences in viral titer and pooling and then analyzed the largest $N_{i,j}$ tumors per vector.

This scaling procedure requires selecting a benchmark (basal) sgRNA and a benchmark (basal) experiment, and then selecting a defined number of tumors with that sgRNA from that experiment (N_(i=basal,j=basal)). The number of tumors sampled for each other sgRNA i in each experiment j (N_(i,j)) is then adjusted to take into account differences in both the overall viral titer delivered and in the representation of sgRNAs between the viral pool used in experiment j and the viral pool used in the basal experiment:

$$N_{i,j} = N_{i=basal,j=basal} * \frac{T_j}{T_{j=basal}} * \frac{p_{i,j}}{p_{i=basal,j=basal}}$$

where T_j denotes the total viral titer delivered in experiment j and $p_{i,j}$ denotes the proportion of the viral pool in experiment j allocated to sgRNA i. T_j is a known quantity determined during viral preparation which represents the sum of the viral titers delivered to

each mouse in experiment j. $P_{i,j}$ values were calculated using Tuba-seq data generated by transducing control *Kras*$^{LSL\text{-}G12D/+}$;*R26*$^{LSL\text{-}Tom}$;*p53*$^{flox/wt}$ and *Kras*$^{LSL\text{-}G12D/+}$;*R26*$^{LSL\text{-}Tom}$;*p53*$^{flox/flox}$ mice. As these mice lack Cas9 expression all Lenti-sgRNA/Cre vectors are functionally inert, and the observed tumor number associated with each sgRNA reflects the make-up of the viral pool. To account for variation in tumor number across mice the sample of $N_{i,j}$ tumors was distributed across all mice in the cohort in proportion to the total number of tumors in each mouse.

For analyses of data generated using the Lenti-sg*TSG*^{19}-sg*V1*/Cre and Lenti-sg*TSG*^{19}-sg*V3*/Cre viral pools, we used sgNT1 (a non-targeting control sgRNA) in the V1 cohort as the basal dataset. Likewise, for analyses of data generated using the Lenti-sg*TSG*^{75}-sg*V1*/Cre, and Lenti-sg*TSG*^{75}-sg*V3*/Cre viral pools we used sgNT1 in the V1 cohort as the basal dataset. Note that these choices were arbitrary, and identical results could be achieved by basing the sampling calculations on any sgRNA in any dataset."

Selection of $N_{i=basal,j=basal}$

"The parameter $N_{i=basal,j=basal}$ defines the portion of the tumor size distribution that we use in our calculations of tumor suppressive effects. In selecting $N_{i=basal,j=basal}$ for each analysis we sought to include as much data as possible while maintaining high data quality by excluding tumors with barcodes supported by very few reads. We sequenced samples to median depths of 35.2, 44.8, 15.5, and 16.0 cells per read for the cohorts transduced with Lenti-sgTSG^{19}-sgV1/Cre, Lenti-sgTSG^{19}-sgV3/Cre, Lenti-sgTSG^{75}-sgV1/Cre, and Lenti-sgTSG^{75}-sgV3/Cre, respectively. We reasoned that restricting our analysis to tumors above 250 cells in size (and therefore supported by an average of >5 reads in our lowest depth dataset) would minimize noise associated with the detection and measurement of very small tumors while maintaining high statistical power to detect tumor suppressive effects. We therefore selected an $N_{i=basal,j=basal}$ for each analysis that corresponded to the number of tumors with >250 cells for the basal sgRNA in the basal experiment. The values of $N_{i=basal,j=basal}$ used for each experiment are shown in the top row of the table below. To ensure that our findings were robust to a range of minimum tumor sizes and corresponding numbers of tumors sampled, we also performed our analyses using values of $N_{i=basal,j=basal}$ corresponding to the inclusion of tumors larger than 300, 350, and 400 cells and found similar results.

Table 23 | Number of sgNT1 tumors sampled in V1 cohort (Ni=basal,j=basal) rounded to the nearest hundred

Minimum size Threshold	Lenti-sgTSG[19]-sgV1/Cre and Lenti-sgTSG[19]-sgV3/Cre experiment	Lenti-sgTSG[75]-sgV1/Cre, and Lenti-sgTSG[75]-sgV3/Cre
250	700	700
300	600	700
350	500	600
400	400	600

The same logic was used to determine $N_{i=basal,j=basal}$ for the control Cas9-negative cohorts in each experiment. Because these cohorts contained both *Kras*$^{LSL\text{-}G12D/+}$;*R26*$^{LSL\text{-}Tom}$;*p53*$^{flox/wt}$ and *Kras*$^{LSL\text{-}G12D/+}$;*R26*$^{LSL\text{-}Tom}$;*p53*$^{flox/flox}$ mice, a given lentiviral titer may not initiate the same number of tumors in each cohort (although the proportion of each sgRNA should be the same as there is no Cas9). We therefore defined separate $N_{i=basal,j=basal}$ values for each control cohort (again using sgNT1 as our basal sgRNA) and performed the scaling calculation described above within each cohort. The $N_{i=basal,j=basal}$ sampled for these cohorts are shown in the table below."

Minimum size Threshold	Ni=basal,j=basal Lenti-sgTSG[19]-sgV1/Cre control cohort	Ni=basal,j=basal Lenti-sgTSG[19]-sgV3/Cre control cohort	Ni=basal,j=basal Lenti-sgTSG[75]-sgV1/Cre control cohort	Ni=basal,j=basal Lenti-sgTSG[75]-sgV3/Cre control cohort
250	1000	1100	100	400
300	900	1000	100	300
350	900	900	100	300
400	800	800	100	200

Summary statistics for impact of targeted genes on tumorigenesis

"After performing the adaptive sampling described above, we assessed the extent to which each targeted gene (X) affects tumor initiation and growth, by comparing the distribution of tumor sizes produced by vectors targeting that gene (sgX tumors) to the distribution produced by our negative control vectors (sgInert tumors). We relied on two statistics to characterize these distributions: the log-normal mean size (adaptively sampled LN mean or ASM) and the size of tumors at the 95th percentile of the distribution (adaptively sampled 95th percentile size). The LN mean is the maximum-likelihood estimate of mean tumor size assuming a log-normal distribution. Previous work found that this statistic represents the best parametric summary of tumor growth based on the maximum likelihood quality of fit of various common parametric distributions (Rogers et al. 2017). The 95th percentile size is a nonparametric summary statistic of the tumor size distribution. This metric corresponds to the right tail of the distribution and thus reflects the growth of larger tumors, thereby avoiding issues stemming from potential variation in cutting efficiency among guides.

Note that while these statistics are functions of the tumor size distribution, they are also sensitive to the effects of tumor suppressor gene inactivation on tumor initiation due to our use of adaptive sampling. For example, a gene which increases tumor burden when inactivated solely by increasing the number of tumors (i.e., without shifting the tumor size distribution) would still increase the LN mean and 95th percentile size of the adaptively sampled datasets and would therefore still be detectable as a tumor suppressor using these metrics. These statistics therefore integrate the impact of each targeted gene on the initiation and growth of tumors.

To quantify the extent to which each gene suppressed or promoted tumorigenesis, we normalized statistics calculated on tumors of each genotype to the corresponding inert statistic. The resulting ratios reflect the fitness advantage (or disadvantage) associated with each tumor genotype relative to the initiation and growth of sgInert tumors.

The adaptively sampled relative 95th percentile size for tumors of genotype X was calculated as:

$$Relative\ 95^{th}\ percentile\ size_{sgX} = \frac{95^{th}\ percentile\ of\ sgX\ distribution}{95^{th}\ percentile\ of\ sgInert\ distribution}$$

Likewise, the adaptively sampled relative LN mean size for tumors of genotype X was calculated as:

$$Relative\ LN\ mean\ size_{sgX} = \frac{LN\ mean\ of\ sgX\ distribution}{LN\ mean\ of\ sgInert\ distribution}$$

For both statistics the sgX and sgInert distributions were adaptively sampled as previously described and the sgInert statistic is the median value across all inert vectors."

Aggregating information across sgRNAs:

"Adaptive sampling and calculation of summary statistics was performed per sgRNA. To calculate statistics at the gene level, we aggregated information across all sgRNAs targeting the same gene. Specifically, the gene-level statistics reported are the weighted average of the per-sgRNA statistics, where the contribution of each sgRNA was proportional to the number of adaptively sampled tumors with that sgRNA."

Calculation of confidence intervals and P-values for tumor growth and number metrics

"Confidence intervals and *P*-values were calculated using bootstrap resampling to estimate the sampling distribution of each statistic. To account for both mouse-to-mouse variability and variability in tumor size and number within mice, we adopted a two-step, nested bootstrap approach where we first resampled mice, and then resampled tumors within each

mouse in the pseudo-dataset. 10,000 bootstrap samples were drawn for all reported P-values. 95% confidence intervals were calculated using the 2.5th and 97.5th percentile of the bootstrapped statistics. Because we calculate metrics of tumor growth that are normalized to the same metrics in sgInert tumors, under the null model where genotype does not affect tumor growth, the test statistic is equal to 1. Two-sided p-values were thus calculated as followed:

$$p = 2 * \min\{\Pr(T > 1), \Pr(T < 1)\}$$

Where T is the test statistic and Pr(T>1) and Pr(T<1) were calculated empirically as the proportion of bootstrapped statistics that were more extreme than the baseline of 1. To account for multiple hypothesis testing, p-values were FDR-adjusted using the Benjamini-Hochberg procedure as implemented in the Python package stats models."

Analyses of correlation in tumor suppressive effects across oncogenic contexts

"To assess the extent to which the effects of tumor suppressor gene inactivation were similar across oncogenic contexts, we calculated Spearman's rank correlation coefficient (ρ) of the effects of tumor suppressor inactivation between pairs of oncogenic contexts.

For comparison of our EML4-ALK V1 and V3 datasets (both V1 vs V3, and "self" comparisons of V1 vs V1 and V3 vs V3), we calculated ρ using the adaptively sampled log-normal mean tumor sizes (ASMs) for each putative tumor suppressor in each dataset. Confidence intervals around the point estimate of ρ were generated by bootstrapping each dataset using a two-step nested resampling approach (first resampling mice, then resampling tumors within each bootstrapped mouse), calculating the ASM for each gene in each pseudo-dataset, and then calculating ρ for the bootstrapped ASMs. 10,000 bootstrap samples were drawn and 95% confidence intervals were calculated using the 2.5th and 97.5th percentiles of the bootstrapped statistics.

For comparisons using data from (Blair et al. 2023) and the independently generated KRASG12D dataset (both cross-oncogene and "self" comparisons), ρ was calculated using the relative 95th percentile tumor size for each gene. Confidence intervals were generated by fitting normal distributions to the reported 95% confidence interval around the relative 95th percentile tumor size for each gene, repeatedly sampling statistics for each gene from these distributions, and then calculating ρ using the resampled statistics. 10,000 samples were drawn and 95% confidence intervals were calculated using the 2.5th and 97.5th percentiles of the resampled statistics.

For each set of tumor suppressor genes, we calculated the distribution of ρ under the null hypothesis (that there is no correlation in effects between two contexts) using a simulation that repeatedly measured the correlation between the list of genes and a randomly shuffled version of the list. The simulation was run 10,000 times for each gene set, and 95% confidence intervals were calculated using the 2.5th and 97.5th percentiles of the simulated statistics.”

Illustrations

Illustrations were made using Adobe Illustrator or Biorender. The cover was created with the help of Adobe Firefly's AI assistance and later modified in Adobe Illustrator.

ACKNOWLEDGMENTS

In this rollercoaster journey of my PhD odyssey, I extend my gratitude to my supervisor, Rocio Sotillo, who really fueled my seek for independence and self-motivation. Her mentorship has not only shaped my academic journey but has also played a pivotal role in immersing me into the scientific community. I appreciate her encouragement to navigate the challenges, fostering a sense of self-reliance. Thank you for supporting me, especially in the tumor suppressor gene project when some thought it would never work. Your support meant a lot and I appreciate your belief in my work.

I would like to express my gratitude to my Thesis Advisors and Committee Members: Prof. Dr. Rob Russel, Dr. Thomas Hoffer, and Dr. Darjus Tschaharganeh. I appreciate their valuable time, expertise, and engaging discussions throughout the thesis process. Their insightful comments and suggestions played an important role in enhancing the quality of this work. Special thanks to Prof. Sergio P. Acebron, Dr. Michael Milsom and Dr. Ana Banito for agreeing to participate in my PhD Examination Committee.

I would like to extend my thanks to the DKFZ Core Facilities, with special acknowledgment to the animal, microscopy, flow cytometry, and NGS Core Facilities. Their outstanding performance significantly contributed to enhancing the quality of my research.

Through thick and thin, my lab mates have made this journey not only bearable, but memorable. Thank you for being the exceptional team that you are. As my lovely friend Dr. Alicia said: ”When you are surrounded by excellent scientists and even better people, incredible science happens.” In the unpredictable and emotionally challenging landscape of a PhD, my lab mates have become my esteemed small family—witnesses to my growth, pillars of support, and part of the encouraging atmosphere that I will forever be grateful for. I would like to thank former lab members Dr. Charles, Dr. Kandala and Dr. Pan for their extensive discussions and enrichment of my cultural knowledge. I thank Dr. Sara for her help and support at the beginning of my project. Special thanks to my former student, organoid buddy and Mini-Me, Filizz Akkas. Your daily motivation and solid dedication made me a very proud mentor. I wish we could have continued working together for longer. I wish you the best of luck in your career and sincerely hope that our paths cross again soon. Special thanks to Hilary, whose dedication is essential to keep the lab running. Wishing you days free from the USA-Germany-Customs chaos. Kalman, the lab's superhero keeping things afloat. Thank you very much for supporting me during this long journey, not only scientifically but for being my personal cheerleader. These achievements would not have been possible without your constant

support. I will never forget your dedication and advices. I wish you all the best, and just like our days on the football field, may your path ahead be filled with exciting goals and victories. A big thanks to Mulham for making my days better with his positive energy. Good luck with your PhD project, and I hope you find the “EML4-ALK-world” as fascinated as I do. Keep being creative, full of ideas, and motivated. Thanks to former members Simone, Vanessa, Laura and Justin for their technical support. To the newcomers, Maria C. and Amelie, I extend my best wishes for your careers. Enjoy the journey ahead, it may be challenging, but it will be equally rewarding. Finally, a heartfelt thank you to my closest colleagues Alicia and Maria, you have made my experience unforgettable. Alicia, we lived through this experience together, and I am grateful for the journey. Thanks for showing me the beauty of APOBEC. I could not be prouder of all your achievements. You have been a true example of toughness and resilience specially during the most difficult times. Your motivation and self-drive are at the top of a long list of admirable qualities. Appreciating all the good times we shared, both inside and outside the lab. Thank you for making my time in Heidelberg warmer, even during the coldest winter. Maria, you are not only an incredible collaborator, but also an unforgettable friend. Your dedication has truly shaped our project, making it complete and meaningful. Thank you for the endless discussions and your invaluable assistance with the never-ending cell treatments and western blotting. Having you on board has been more rewarding and inspiring than words can express. You have revived my belief in teamwork and the power of collective effort.

I would like to thank Dr. Ursula Klingmüller, Dr. Barbara Helm, Dr. Dario Lucas Frey, and Dr. Junyan Lu for their support. I am grateful to them for sharing their extensive knowledge in proteomics, which was relevant to the progress of my research.

I would like to express my sincere appreciation to Monte Winslow and the members of his lab, Emily, Chris, Laura, and Mike. Monte is an outstanding collaborator whose belief in my project and support have been instrumental throughout my journey. Thank you for your continued coaching and mentorship from the distance. I would like to extend my thanks to Emily whose exceptional bioinformatics skills played a crucial role in the success of the Tuba-seq project. Wishing you the very best in your future endeavors. Finally, I am grateful not only for the opportunity to work with Monte and his lab, but also for the warm hospitality during my stay at Stanford.

I would not have reached this significant milestone without the invaluable support of my early mentors, to whom I extend my deepest gratitude. Dr. Mirna Perez-Moreno and Dr. Daniel Peña-Jimenez, thank you for providing me with an initial scientific opportunity and for introducing me to the forefront of scientific exploration. A heartfelt appreciation goes to Dr.

Angel R. Nebreda and Dr. Begoña Canovas for their dedicated mentorship during my internship in Barcelona. Their firm commitment and inspirational guidance have played a pivotal role in shaping my academic journey.

I will always appreciate the warmth and support of my dear Spanish friends, the greatest group of friends anyone ever had. To Mirian, the essence of a strong and independent woman. I am really thankful for her advice. It has shown me the importance of being strong and persistent. To Dominic, the Spanishized friend, I wish him a successful and fulfilling professional future. To Paula, the lively and spirited person, your enthusiasm for life has brought countless moments of joy and laughter. To Dani, although time is money and punctuality is not your strong suit, I really appreciate our friendship and the special things you bring to it. Finally, to Damian, my moustache-wearing, running and gym buddy, thanks for being a significant part of my journey in Germany. I appreciate all our after-hours talks, whether they were about science or not. More than just a friend, you have proven to be an amazing one, and for that, I will always be thankful. I appreciate the valuable lessons and values you have given me. Even though you are now in Switzerland and I am uncertain about my future location, I hope our paths will cross again someday.

A mi querida familia: papá, mamá, Alicia, abuelos, Brisa y los tres gatitos. Como dijo mamá cuando inicie este viaje en 2018: “Separados, que no distanciados”. Este es el mejor lema que define nuestra familia. Unión y apoyo incluso en la distancia. Mamá, papá, estaré eternamente agradecido por los innumerables sacrificios que hacéis por Alicia y por mí. Gracias por guiarme desde la distancia y por empujarme a lo más alto. Sois los mejores padres que alguien podría desear. Espero que sintáis un inmenso orgullo, ya que, sin vosotros, no habríamos alcanzado todo lo que hemos logrado.

A mi valiente hermana, Alicia. Coraje y perseverancia son tus cualidades más destacadas. No podría estar más orgulloso de tenerte como hermana. Sé que lograrás cualquier meta que te propongas, y junto con papá y mamá estaré ahí para celebrarlo. Siempre estaré a tu lado, apoyándote en cada paso de tu camino.

Nuria, mi huracán y mi calma. El camino no ha sido sencillo. Crecimos en la distancia, pero siempre estuvimos juntos. En este arduo viaje, reconozco los sacrificios que hemos realizado a lo largo de los años. Sin embargo, a tu lado, he encontrado aliento, apoyo, inspiración y tolerancia. Gracias por sostenerme en los momentos más difíciles y motivarme cuando más lo necesitaba. Aprecio profundamente tu paciencia durante mis largas noches frente al ordenador. Siempre había algo más por analizar o un párrafo más que redactar, pero de ahora en adelante, solo existirá un "nosotros". Estoy inmensamente agradecido por tu

apoyo incondicional y por caminar a mi lado no solo en este viaje, sino en todos los que nos esperan en el futuro. Tu fortaleza y tesón son admirables, estoy seguro que llegaras a lo más alto. Mi gratitud, de todo corazón.

Finally, thanks to me. Throughout my career, I have distinguished myself as a tireless worker who has dedicated all my efforts and perseverance to the success of the Lab. I am deeply proud of what I have achieved and confident of what is yet to come. With my eyes fixed on the horizon, I am ready to continue my journey with determination.

References

Alam H, Tang M, Maitituoheti M, Dhar SS, Kumar M, Han CY, Ambati CR, Amin SB, Gu B, Chen T-Y, Lin Y-H, Chen J, Muller FL, Putluri N, Flores ER, DeMayo FJ, Baseler L, Rai K, Lee MG (2020) KMT2D Deficiency Impairs Super-Enhancers to Confer a Glycolytic Vulnerability in Lung Cancer. Cancer Cell 37:599-617.e7. https://doi.org/10.1016/j.ccell.2020.03.005

Alberts B, Johnson A, Lewis J, Raff M, Roberts K, Walter P (2007) Molecular Biology of the Cell. https://doi.org/10.1201/9780203833445

Aldana CAF, Chang JC, Ptashkin R, Wang Y, Gedvilaite E, Baine MK, Travis WD, Ventura K, Bodd F, Yu HA, Quintanal-Villalonga A, Lai WVictoria, Egger JV, Offin M, Ladanyi M, Rudin CM, Rekhtman N (2022) Rb tumor suppressor in small cell lung cancer: Combined genomic and immunohistochemical analysis with a description of a distinct Rb-proficient subset. Clin Cancer Res 28:4702–4713. https://doi.org/10.1158/1078-0432.ccr-22-1115

Angeles AK, Christopoulos P, Yuan Z, Bauer S, Janke F, Ogrodnik SJ, Reck M, Schlesner M, Meister M, Schneider MA, Dietz S, Stenzinger A, Thomas M, Sültmann H (2021) Early identification of disease progression in ALK-rearranged lung cancer using circulating tumor DNA analysis. npj Precis Oncol 5:100. https://doi.org/10.1038/s41698-021-00239-3

Aronov AM, Tang Q, Martinez-Botella G, Bemis GW, Cao J, Chen G, Ewing NP, Ford PJ, Germann UA, Green J, Hale MR, Jacobs M, Janetka JW, Maltais F, Markland W, Namchuk MN, Nanthakumar S, Poondru S, Straub J, Haar E ter, Xie X (2009) Structure-Guided Design of Potent and Selective Pyrimidylpyrrole Inhibitors of Extracellular Signal-Regulated Kinase (ERK) Using Conformational Control. J Med Chem 52:6362–6368. https://doi.org/10.1021/jm900630q

Bilsland JG, Wheeldon A, Mead A, Znamenskiy P, Almond S, Waters KA, Thakur M, Beaumont V, Bonnert TP, Heavens R, Whiting P, McAllister G, Munoz-Sanjuan I (2008) Behavioral and Neurochemical Alterations in Mice Deficient in Anaplastic Lymphoma Kinase Suggest Therapeutic Potential for Psychiatric Indications. Neuropsychopharmacology 33:685–700. https://doi.org/10.1038/sj.npp.1301446

Blair LM, Juan JM, Sebastian L, Tran VB, Nie W, Wall GD, Gerceker M, Lai IK, Apilado EA, Grenot G, Amar D, Foggetti G, Carmo MD, Ugur Z, Deng D, Chenchik A, Zafra MP, Dow LE, Politi K, MacQuitty JJ, Petrov DA, Winslow MM, Rosen MJ, Winters IP (2023) Oncogenic context shapes the fitness landscape of tumor suppression. Nat Commun 14:6422. https://doi.org/10.1038/s41467-023-42156-y

Blasco MT, Navas C, Martín-Serrano G, Graña-Castro O, Lechuga CG, Martín-Díaz L, Djurec M, Li J, Morales-Cacho L, Esteban-Burgos L, Perales-Patón J, Bousquet-Mur E, Castellano E, Jacob HKC, Cabras L, Musteanu M, Drosten M, Ortega S, Mulero F, Sainz B, Dusetti N, Iovanna J, Sánchez-Bueno F, Hidalgo M, Khiabanian H, Rabadán R, Al-Shahrour F, Guerra C, Barbacid M (2019) Complete Regression of Advanced Pancreatic Ductal Adenocarcinomas upon Combined Inhibition of EGFR and C-RAF. Cancer Cell 35:573-587.e6. https://doi.org/10.1016/j.ccell.2019.03.002

Blasco RB, Francoz S, Santamaría D, Cañamero M, Dubus P, Charron J, Baccarini M, Barbacid M (2011) c-Raf, but Not B-Raf, Is Essential for Development of K-Ras Oncogene-Driven Non-Small Cell Lung Carcinoma. Cancer Cell 19:652–663. https://doi.org/10.1016/j.ccr.2011.04.002

Blasco RB, Karaca E, Ambrogio C, Cheong T-C, Karayol E, Minero VG, Voena C, Chiarle R (2014) Simple and Rapid In Vivo Generation of Chromosomal Rearrangements using CRISPR/Cas9 Technology. Cell Rep 9:1219–1227. https://doi.org/10.1016/j.celrep.2014.10.051

Bokhari AA, Lai W-Y, Le AT, Gabre JL, Chuang T-P, Fransson S, Bergman B, Djos A, Chen N, Martinsson T, Eynden JV den, Doebele RC, Palmer RH, Hallberg B, Umapathy G (2022) Novel human-derived EML4-ALK fusion cell lines identify ribonucleotide reductase RRM2 as a target of activated ALK in NSCLC. Lung Cancer 171:103–114. https://doi.org/10.1016/j.lungcan.2022.07.010

Bokhari AA, Lai W-Y, Le AT, Gabre JL, Chuang T-P, Fransson S, Bergman B, Djos A, Chen N, Martinsson T, Eynden JV den, Doebele RC, Palmer RH, Hallberg B, Umapathy G (2022) Novel human-derived EML4-ALK fusion cell lines identify ribonucleotide reductase RRM2 as a target of activated ALK in NSCLC. Lung Cancer 171:103–114. https://doi.org/10.1016/j.lungcan.2022.07.010

Boland JM, Wampfler JA, Jang JS, Wang X, Erickson-Johnson MR, Oliveira AM, Yang P, Jen J, Yi ES (2014) Pulmonary Adenocarcinoma With Signet Ring Cell Features. Am J Surg Pathol 38:1681–1688. https://doi.org/10.1097/pas.0000000000000280

Bresler SC, Weiser DA, Huwe PJ, Park JH, Krytska K, Ryles H, Laudenslager M, Rappaport EF, Wood AC, McGrady PW, Hogarty MD, London WB, Radhakrishnan R, Lemmon MA, Mossé YP (2014) ALK Mutations Confer Differential Oncogenic Activation and Sensitivity to ALK Inhibition Therapy in Neuroblastoma. Cancer Cell 26:682–694. https://doi.org/10.1016/j.ccell.2014.09.019

Brinkman EK, Chen T, Amendola M, van Steensel B (2014) Easy quantitative assessment of genome editing by sequence trace decomposition. Nucleic Acids Res 42:e168–e168. https://doi.org/10.1093/nar/gku936

Cai H, Chew SK, Li C, Tsai MK, Andrejka L, Murray CW, Hughes NW, Shuldiner EG, Ashkin EL, Tang R, Hung KL, Chen LC, Lee SYC, Yousefi M, Lin W-Y, Kunder CA, Cong L, McFarland CD, Petrov DA, Swanton C, Winslow MM (2021) A Functional Taxonomy of Tumor Suppression in Oncogenic KRAS–Driven Lung Cancer. Cancer Discov 11:1754–1773. https://doi.org/10.1158/2159-8290.cd-20-1325

Camidge DR, Bang Y-J, Kwak EL, Iafrate AJ, Varella-Garcia M, Fox SB, Riely GJ, Solomon B, Ou S-HI, Kim D-W, Salgia R, Fidias P, Engelman JA, Gandhi L, Jänne PA, Costa DB, Shapiro GI, LoRusso P, Ruffner K, Stephenson P, Tang Y, Wilner K, Clark JW, Shaw AT (2012) Activity and safety of crizotinib in patients with ALK-positive non-small-cell lung cancer: updated results from a phase 1 study. Lancet Oncol 13:1011–1019. https://doi.org/10.1016/s1470-2045(12)70344-3

Camidge DR, Doebele RC (2012) Treating ALK-positive lung cancer—early successes and future challenges. Nat Rev Clin Oncol 9:268–277. https://doi.org/10.1038/nrclinonc.2012.43

Camidge DR, Kim HR, Ahn M-J, Yang JCH, Han J-Y, Hochmair MJ, Lee KH, Delmonte A, Campelo MRG, Kim D-W, Griesinger F, Felip E, Califano R, Spira AI, Gettinger SN, Tiseo M, Lin HM, Liu Y, Vranceanu F, Niu H, Zhang P, Popat S (2021) Brigatinib Versus Crizotinib in ALK Inhibitor–Naive Advanced ALK-Positive NSCLC: Final Results of Phase 3 ALTA-1L Trial. J Thorac Oncol 16:2091–2108. https://doi.org/10.1016/j.jtho.2021.07.035

Camidge DR, Kim HR, Ahn M-J, Yang JC-H, Han J-Y, Lee J-S, Hochmair MJ, Li JY-C, Chang G-C, Lee KH, Gridelli C, Delmonte A, Campelo RG, Kim D-W, Bearz A, Griesinger F, Morabito A, Felip E, Califano R, Ghosh S, Spira A, Gettinger SN, Tiseo M, Gupta N, Haney J, Kerstein D, Popat S (2018) Brigatinib versus Crizotinib in ALK-Positive Non–Small-Cell Lung Cancer. N Engl J Med 379:2027–2039. https://doi.org/10.1056/nejmoa1810171

Chen J, Elfiky A, Han M, Chen C, Saif MW (2014) The Role of Src in Colon Cancer and Its Therapeutic Implications. Clin Color Cancer 13:5–13. https://doi.org/10.1016/j.clcc.2013.10.003

Chen Y, Takita J, Choi YL, Kato M, Ohira M, Sanada M, Wang L, Soda M, Kikuchi A, Igarashi T, Nakagawara A, Hayashi Y, Mano H, Ogawa S (2008) Oncogenic mutations of ALK kinase in neuroblastoma. Nature 455:971–974. https://doi.org/10.1038/nature07399

Chen Y, Toth R, Chocarro S, Weichenhan D, Hey J, Lutsik P, Sawall S, Stathopoulos GT, Plass C, Sotillo R (2022) Club cells employ regeneration mechanisms during lung tumorigenesis. Nat Commun 13:4557. https://doi.org/10.1038/s41467-022-32052-2

Childress MA, Himmelberg SM, Chen H, Deng W, Davies MA, Lovly CM (2018) ALK Fusion Partners Impact Response to ALK Inhibition: Differential Effects on Sensitivity, Cellular Phenotypes, and Biochemical Properties. Mol Cancer Res 16:molcanres.0171.2018. https://doi.org/10.1158/1541-7786.mcr-18-0171

Choi YL, Takeuchi K, Soda M, Inamura K, Togashi Y, Hatano S, Enomoto M, Hamada T, Haruta H, Watanabe H, Kurashina K, Hatanaka H, Ueno T, Takada S, Yamashita Y, Sugiyama Y, Ishikawa Y, Mano H (2008) Identification of Novel Isoforms of the EML4-ALK Transforming Gene in Non–Small Cell Lung Cancer. Cancer Res 68:4971–4976. https://doi.org/10.1158/0008-5472.can-07-6158

Christopoulos P, Kirchner M, Bozorgmehr F, Endris V, Elsayed M, Budczies J, Ristau J, Penzel R, Herth FJ, Heussel CP, Eichhorn M, Muley T, Meister M, Fischer JR, Rieken S, Lasitschka F, Bischoff H, Sotillo R, Schirmacher P, Thomas M, Stenzinger A (2018) Identification of a highly lethal V3+TP53+ subset in ALK+ lung adenocarcinoma. Int J Cancer 144:190–199. https://doi.org/10.1002/ijc.31893

Christova T, Ho SK, Liu Y, Gill M, Attisano L (2023) LTK and ALK promote neuronal polarity and cortical migration by inhibiting IGF1R activity. EMBO Rep 24:e56937. https://doi.org/10.15252/embr.202356937

Chuang T-P, Lai W-Y, Gabre JL, Lind DE, Umapathy G, Bokhari AA, Bergman B, Kristenson L, Thorén FB, Le A, Doebele RC, Eynden JV den, Palmer RH, Hallberg B (2023) ALK fusion NSCLC oncogenes promote survival and inhibit NK cell responses via SERPINB4 expression. Proc Natl Acad Sci 120:e2216479120. https://doi.org/10.1073/pnas.2216479120

Concepcion CP, Ma S, LaFave LM, Bhutkar A, Liu M, DeAngelo LP, Kim JY, Priore ID, Schoenfeld AJ, Miller M, Kartha VK, Westcott PMK, Sanchez-Rivera FJ, Meli K, Gupta M, Bronson RT, Riely GJ, Rekhtman N, Rudin CM, Kim CF, Regev A, Buenrostro JD, Jacks T (2021) SMARCA4 inactivation promotes lineage-specific transformation and early metastatic features in the lung. Cancer Discov 12:candisc.0248.2021. https://doi.org/10.1158/2159-8290.cd-21-0248

Consortium TIP-CA of WG, (2020) Pan-cancer analysis of whole genomes. Nature 578:82–93. https://doi.org/10.1038/s41586-020-1969-6

Cooper AJ, Sequist LV, Lin JJ (2022) Third-generation EGFR and ALK inhibitors: mechanisms of resistance and management. Nat Rev Clin Oncol 19:499–514. https://doi.org/10.1038/s41571-022-00639-9

Corte CMD, Viscardi G, Liello RD, Fasano M, Martinelli E, Troiani T, Ciardiello F, Morgillo F (2018) Role and targeting of anaplastic lymphoma kinase in cancer. Mol Cancer 17:30. https://doi.org/10.1186/s12943-018-0776-2

Costa DB, Kobayashi S, Pandya SS, Yeo W-L, Shen Z, Tan W, Wilner KD (2011) CSF Concentration of the Anaplastic Lymphoma Kinase Inhibitor Crizotinib. J Clin Oncol 29:e443–e445. https://doi.org/10.1200/jco.2010.34.1313

Crudele JM, Chamberlain JS (2018) Cas9 immunity creates challenges for CRISPR gene editing therapies. Nat Commun 9:3497. https://doi.org/10.1038/s41467-018-05843-9

Crystal AS, Shaw AT, Sequist LV, Friboulet L, Niederst MJ, Lockerman EL, Frias RL, Gainor JF, Amzallag A, Greninger P, Lee D, Kalsy A, Gomez-Caraballo M, Elamine L, Howe E, Hur W, Lifshits E, Robinson HE, Katayama R, Faber AC, Awad MM, Ramaswamy S, Mino-Kenudson M, Iafrate AJ, Benes CH, Engelman JA (2014) Patient-derived models of acquired resistance can identify effective drug combinations for cancer. Science 346:1480–1486. https://doi.org/10.1126/science.1254721

Cui JJ, Tran-Dubé M, Shen H, Nambu M, Kung P-P, Pairish M, Jia L, Meng J, Funk L, Botrous I, McTigue M, Grodsky N, Ryan K, Padrique E, Alton G, Timofeevski S, Yamazaki S, Li Q, Zou H, Christensen J, Mroczkowski B, Bender S, Kania RS, Edwards MP (2011) Structure Based Drug Design of Crizotinib (PF-02341066), a Potent and Selective Dual Inhibitor of Mesenchymal–Epithelial Transition Factor (c-MET) Kinase and Anaplastic Lymphoma Kinase (ALK). J Med Chem 54:6342–6363. https://doi.org/10.1021/jm2007613

Cully M, You H, Levine AJ, Mak TW (2006) Beyond PTEN mutations: the PI3K pathway as an integrator of multiple inputs during tumorigenesis. Nat Rev Cancer 6:184–192. https://doi.org/10.1038/nrc1819

Dagogo-Jack I, Kiedrowski LA, Heist RS, Lin JJ, Meador CB, Krueger EA, Do A, Peterson J, Sequist LV, Gainor JF, Lennerz JK, Digumarthy SR (2023) Efficacy and Tolerability of ALK/MET Combinations in Patients With ALK-Rearranged Lung Cancer With Acquired MET Amplification: A Retrospective Analysis. JTO Clin Res Rep 4:100534. https://doi.org/10.1016/j.jtocrr.2023.100534

Dagogo-Jack I, Rooney M, Lin JJ, Nagy RJ, Yeap BY, Hubbeling H, Chin E, Ackil J, Farago AF, Hata AN, Lennerz JK, Gainor JF, Lanman RB, Shaw AT (2019) Treatment with Next-Generation ALK Inhibitors Fuels Plasma ALK Mutation Diversity. Clin Cancer Res 25:6662–6670. https://doi.org/10.1158/1078-0432.ccr-19-1436

Dagogo-Jack I, Yoda S, Lennerz JK, Langenbucher A, Lin JJ, Rooney MM, Prutisto-Chang K, Oh A, Adams NA, Yeap BY, Chin E, Do A, Marble HD, Stevens SE, Digumarthy SR, Saxena A, Nagy RJ, Benes CH, Azzoli CG, Lawrence MS, Gainor JF, Shaw AT, Hata AN (2020) MET Alterations Are a Recurring and Actionable Resistance Mechanism in ALK-Positive Lung Cancer. Clin Cancer Res 26:2535–2545. https://doi.org/10.1158/1078-0432.ccr-19-3906

Dardaei L, Wang HQ, Singh M, Fordjour P, Shaw KX, Yoda S, Kerr G, Yu K, Liang J, Cao Y, Chen Y, Lawrence MS, Langenbucher A, Gainor JF, Friboulet L, Dagogo-Jack I, Myers DT, Labrot E, Ruddy D, Parks M, Lee D, DiCecca RH, Moody S, Hao H, Mohseni M, LaMarche M, Williams J, Hoffmaster K, Caponigro G, Shaw AT, Hata AN, Benes CH, Li F, Engelman JA (2018) SHP2 inhibition restores sensitivity in ALK-rearranged non-small-cell lung cancer resistant to ALK inhibitors. Nat Med 24:512–517. https://doi.org/10.1038/nm.4497

Davoli T, Xu AW, Mengwasser KE, Sack LM, Yoon JC, Park PJ, Elledge SJ (2013) Cumulative Haploinsufficiency and Triplosensitivity Drive Aneuploidy Patterns and Shape the Cancer Genome. Cell 155:948–962. https://doi.org/10.1016/j.cell.2013.10.011

Dick FA, Rubin SM (2013) Molecular mechanisms underlying RB protein function. Nat Rev Mol Cell Biol 14:297–306. https://doi.org/10.1038/nrm3567

Donepudi M, Resh MD (2008) c-Src trafficking and co-localization with the EGF receptor promotes EGF ligand-independent EGF receptor activation and signaling. Cell Signal 20:1359–1367. https://doi.org/10.1016/j.cellsig.2008.03.007

Drilon A, Sharma MR, Johnson ML, Yap TA, Gadgeel S, Nepert D, Feng G, Reddy MB, Harney AS, Elsayed M, Cook AW, Wong CE, Hinklin RJ, Jiang Y, Brown EN, Neitzel NA, Laird ER, Wu W-I, Singh A, Wei P, Ching KA, Gaudino JJ, Lee PA, Hartley DP, Rothenberg SM (2023) SHP2 Inhibition Sensitizes Diverse Oncogene-Addicted Solid Tumors to Re-treatment with Targeted Therapy. Cancer Discov 13:OF1–OF13. https://doi.org/10.1158/2159-8290.cd-23-0361

Drosten M, Barbacid M (2022) Targeting KRAS mutant lung cancer: light at the end of the tunnel. Mol Oncol 16:1057–1071. https://doi.org/10.1002/1878-0261.13168

DuPage M, Dooley AL, Jacks T (2009) Conditional mouse lung cancer models using adenoviral or lentiviral delivery of Cre recombinase. Nat Protoc 4:1064–1072. https://doi.org/10.1038/nprot.2009.95

Elshatlawy M, Sampson J, Clarke K, Bayliss R (2023) EML4-ALK biology and drug resistance in non-small cell lung cancer: a new phase of discoveries. Mol Oncol 17:950–963. https://doi.org/10.1002/1878-0261.13446

Eunice K, Yung-Jue B, Ross CD, T. SA, Benjamin S, G. MR, I. OS-H, J. DB, A. JP, B. CD, Marileila V-G, Woo-Ho K, J. LT, Panos F, Hannah S, A. EJ, V. SL, WeiWei T, Leena G, Mari M-K, C. WG, Martin SS, J. RM, Jeffrey S, G. CJ, A. HD, Keith W, Ravi S, I. SG, W. CJ, John IA (2010) Anaplastic Lymphoma Kinase Inhibition in Non–Small-Cell Lung Cancer. N Engl J Med 363:1693–1703. https://doi.org/10.1056/nejmoa1006448

Foggetti G, Li C, Cai H, Hellyer JA, Lin W-Y, Ayeni D, Hastings K, Choi J, Wurtz A, Andrejka L, Maghini DG, Rashleigh N, Levy S, Homer R, Gettinger SN, Diehn M, Wakelee HA, Petrov DA, Winslow MM, Politi K (2021) Genetic Determinants of EGFR-Driven Lung Cancer Growth and Therapeutic Response In VivoTumor Suppressor Genes and EGFR-Driven Lung Adenocarcinoma. Cancer Discov 11:1736–1753. https://doi.org/10.1158/2159-8290.cd-20-1385

Fujita S, Masago K, Katakami N, Yatabe Y (2016) Transformation to SCLC after Treatment with the ALK Inhibitor Alectinib. J Thorac Oncol 11:e67–e72. https://doi.org/10.1016/j.jtho.2015.12.105

Gadgeel SM, Gandhi L, Riely GJ, Chiappori AA, West HL, Azada MC, Morcos PN, Lee R-M, Garcia L, Yu L, Boisserie F, Laurenzio LD, Golding S, Sato J, Yokoyama S, Tanaka T, Ou S-HI (2014) Safety and activity of alectinib against systemic disease and brain metastases in patients with crizotinib-resistant ALK-rearranged non-small-cell lung cancer (AF-002JG): results from the dose-finding portion of a phase 1/2 study. Lancet Oncol 15:1119–1128. https://doi.org/10.1016/s1470-2045(14)70362-6

Gainor JF, Dardaei L, Yoda S, Friboulet L, Leshchiner I, Katayama R, Dagogo-Jack I, Gadgeel S, Schultz K, Singh M, Chin E, Parks M, Lee D, DiCecca RH, Lockerman E, Huynh T, Logan J, Ritterhouse LL, Le LP, Muniappan A, Digumarthy S, Channick C, Keyes C, Getz G, Dias-Santagata D, Heist RS, Lennerz J, Sequist LV, Benes CH, Iafrate AJ, Mino-Kenudson M, Engelman JA, Shaw AT (2016) Molecular Mechanisms of Resistance to First- and Second-Generation ALK Inhibitors in ALK-Rearranged Lung Cancer. Cancer Discov 6:1118–1133. https://doi.org/10.1158/2159-8290.cd-16-0596

Gavert N, Zwang Y, Weiser R, Greenberg O, Halperin S, Jacobi O, Mallel G, Sandler O, Berger AJ, Stossel E, Rotin D, Grinshpun A, Kamer I, Bar J, Pines G, Saidian D, Bar I, Golan S, Rosenbaum E, Nadu A, Ben-Ami E, Weitzen R, Nechushtan H, Golan T, Brenner B, Nissan A, Margalit O, Hershkovitz D, Lahat G, Straussman R (2022) Ex vivo organotypic cultures for synergistic therapy prioritization identify patient-specific responses to combined MEK and Src inhibition in colorectal cancer. https://www.nature.com/articles/s43018-021-00325-2. Accessed 10 Feb 2022

Gay CM, Stewart CA, Park EM, Diao L, Groves SM, Heeke S, Nabet BY, Fujimoto J, Solis LM, Lu W, Xi Y, Cardnell RJ, Wang Q, Fabbri G, Cargill KR, Vokes NI, Ramkumar K, Zhang B, Corte CMD, Robson P, Swisher SG, Roth JA, Glisson BS, Shames DS, Wistuba II, Wang J, Quaranta V, Minna J, Heymach JV, Byers LA (2021) Patterns of transcription factor programs and immune pathway

activation define four major subtypes of SCLC with distinct therapeutic vulnerabilities. Cancer Cell 39:346-360.e7. https://doi.org/10.1016/j.ccell.2020.12.014

Giglione C, Gonfloni S, Parmeggiani A (2001) Differential actions of p60c-Src and Lck kinases on the Ras regulators p120-GAP and GDP/GTP exchange factor CDC25Mm. Eur J Biochem 268:3275–3283. https://doi.org/10.1046/j.1432-1327.2001.02230.x

Golding B, Luu A, Jones R, Viloria-Petit AM (2018) The function and therapeutic targeting of anaplastic lymphoma kinase (ALK) in non-small cell lung cancer (NSCLC). Mol Cancer 17:52. https://doi.org/10.1186/s12943-018-0810-4

Gouzi JY, Moog-Lutz C, Vigny M, Carvalho NB (2005) Role of the subcellular localization of ALK tyrosine kinase domain in neuronal differentiation of PC12 cells. J Cell Sci 118:5811–5823. https://doi.org/10.1242/jcs.02695

Gridelli C, Rossi A, Carbone DP, Guarize J, Karachaliou N, Mok T, Petrella F, Spaggiari L, Rosell R (2015) Non-small-cell lung cancer. Nat Rev Dis Prim 1:15009. https://doi.org/10.1038/nrdp.2015.9

Guo C, Ma X, Gao F, Guo Y (2023) Off-target effects in CRISPR/Cas9 gene editing. Front Bioeng Biotechnol 11:1143157. https://doi.org/10.3389/fbioe.2023.1143157

Hallberg B, Palmer RH (2013) Mechanistic insight into ALK receptor tyrosine kinase in human cancer biology. Nat Rev Cancer 13:685–700. https://doi.org/10.1038/nrc3580

Han X, Li F, Fang Z, Gao Y, Li F, Fang R, Yao S, Sun Y, Li L, Zhang W, Ma H, Xiao Q, Ge G, Fang J, Wang H, Zhang L, Wong K, Chen H, Hou Y, Ji H (2014) Transdifferentiation of lung adenocarcinoma in mice with Lkb1 deficiency to squamous cell carcinoma. Nat Commun 5:3261. https://doi.org/10.1038/ncomms4261

Hanahan D (2022) Hallmarks of Cancer: New Dimensions. Cancer Discov 12:31–46. https://doi.org/10.1158/2159-8290.cd-21-1059

He L, Dar AC (2022) Targeting drug-resistant mutations in ALK. Nat Cancer 3:659–661. https://doi.org/10.1038/s43018-022-00390-1

Herbst RS, Morgensztern D, Boshoff C (2018) The biology and management of non-small cell lung cancer. Nature 553:446–454. https://doi.org/10.1038/nature25183

Heuckmann JM, Balke-Want H, Malchers F, Peifer M, Sos ML, Koker M, Meder L, Lovly CM, Heukamp LC, Pao W, Küppers R, Thomas RK (2012) Differential Protein Stability and ALK Inhibitor Sensitivity of EML4-ALK Fusion Variants. Clin Cancer Res 18:4682–4690. https://doi.org/10.1158/1078-0432.ccr-11-3260

Higuchi M, Ishiyama K, Maruoka M, Kanamori R, Takaori-Kondo A, Watanabe N (2021) Paradoxical activation of c-Src as a drug-resistant mechanism. Cell Rep 34:108876. https://doi.org/10.1016/j.celrep.2021.108876

Höijer I, Emmanouilidou A, Östlund R, Schendel R van, Bozorgpana S, Tijsterman M, Feuk L, Gyllensten U, Hoed M den, Ameur A (2022) CRISPR-Cas9 induces large structural variants at on-target and off-target sites in vivo that segregate across generations. Nat Commun 13:627. https://doi.org/10.1038/s41467-022-28244-5

Hrustanovic G, Olivas V, Pazarentzos E, Tulpule A, Asthana S, Blakely CM, Okimoto RA, Lin L, Neel DS, Sabnis A, Flanagan J, Chan E, Varella-Garcia M, Aisner DL, Vaishnavi A, Ou S-HI, Collisson EA, Ichihara E, Mack PC, Lovly CM, Karachaliou N, Rosell R, Riess JW, Doebele RC, Bivona TG (2015) RAS-MAPK dependence underlies a rational polytherapy strategy in EML4-ALK–positive lung cancer. Nat Med 21:1038–1047. https://doi.org/10.1038/nm.3930

Huang H (2018) Anaplastic Lymphoma Kinase (ALK) Receptor Tyrosine Kinase: A Catalytic Receptor with Many Faces. Int J Mol Sci 19:3448. https://doi.org/10.3390/ijms19113448

Huang S, Benavente S, Armstrong EA, Li C, Wheeler DL, Harari PM (2011) p53 Modulates Acquired Resistance to EGFR Inhibitors and Radiation. Cancer Res 71:7071–7079. https://doi.org/10.1158/0008-5472.can-11-0128

Huber W, Heydebreck A von, Sültmann H, Poustka A, Vingron M (2002) Variance stabilization applied to microarray data calibration and to the quantification of differential expression. Bioinformatics 18:S96–S104. https://doi.org/10.1093/bioinformatics/18.suppl_1.s96

Infarinato NR, Park JH, Krytska K, Ryles HT, Sano R, Szigety KM, Li Y, Zou HY, Lee NV, Smeal T, Lemmon MA, Mossé YP (2016) The ALK/ROS1 Inhibitor PF-06463922 Overcomes Primary Resistance to Crizotinib in ALK-Driven Neuroblastoma. Cancer Discov 6:96–107. https://doi.org/10.1158/2159-8290.cd-15-1056

Jackson EL, Olive KP, Tuveson DA, Bronson R, Crowley D, Brown M, Jacks T (2005) The Differential Effects of Mutant p53 Alleles on Advanced Murine Lung Cancer. Cancer Res 65:10280–10288. https://doi.org/10.1158/0008-5472.can-05-2193

Janoueix-Lerosey I, Lequin D, Brugières L, Ribeiro A, Pontual L de, Combaret V, Raynal V, Puisieux A, Schleiermacher G, Pierron G, Valteau-Couanet D, Frebourg T, Michon J, Lyonnet S, Amiel J, Delattre O (2008) Somatic and germline activating mutations of the ALK kinase receptor in neuroblastoma. Nature 455:967–970. https://doi.org/10.1038/nature07398

Ji H, Ramsey MR, Hayes DN, Fan C, McNamara K, Kozlowski P, Torrice C, Wu MC, Shimamura T, Perera SA, Liang M-C, Cai D, Naumov GN, Bao L, Contreras CM, Li D, Chen L, Krishnamurthy J, Koivunen J, Chirieac LR, Padera RF, Bronson RT, Lindeman NI, Christiani DC, Lin X, Shapiro GI, Jänne PA, Johnson BE, Meyerson M, Kwiatkowski DJ, Castrillon DH, Bardeesy N, Sharpless NE, Wong K-K (2007) LKB1 modulates lung cancer differentiation and metastasis. Nature 448:807–810. https://doi.org/10.1038/nature06030

Jia P, Zhao Z (2019) Characterization of Tumor-Suppressor Gene Inactivation Events in 33 Cancer Types. Cell Rep 26:496-506.e3. https://doi.org/10.1016/j.celrep.2018.12.066

Johnson TW, Richardson PF, Bailey S, Brooun A, Burke BJ, Collins MR, Cui JJ, Deal JG, Deng Y-L, Dinh D, Engstrom LD, He M, Hoffman J, Hoffman RL, Huang Q, Kania RS, Kath JC, Lam H, Lam JL, Le PT, Lingardo L, Liu W, McTigue M, Palmer CL, Sach NW, Smeal T, Smith GL, Stewart AE, Timofeevski S, Zhu H, Zhu J, Zou HY, Edwards MP (2014) Discovery of (10R)-7-Amino-12-fluoro-2,10,16-trimethyl-15-oxo-10,15,16,17-tetrahydro-2H-8,4-(metheno)pyrazolo[4,3-h][2,5,11]-benzoxadiazacyclotetradecine-3-carbonitrile (PF-06463922), a Macrocyclic Inhibitor of Anaplastic Lymphoma Kinase (ALK) and c-ros Oncogene 1 (ROS1) with Preclinical Brain Exposure and Broad-Spectrum Potency against ALK-Resistant Mutations. J Med Chem 57:4720–4744. https://doi.org/10.1021/jm500261q

Kang J, Chen H, Zhang X, Su J, Zhou Q, Tu H, Wang Z, Wang B, Zhong W, Yang X, Chen Z, Ding Y, Wu X, Wang M, Fu J, Yang Z, Zhang X, Shao YW, Wu Y, Yang J (2018) Heterogeneous responses and resistant mechanisms to crizotinib in ALK-positive advanced non-small cell lung cancer. Thorac Cancer 9:1093–1103. https://doi.org/10.1111/1759-7714.12791

Katayama R, Shaw AT, Khan TM, Mino-Kenudson M, Solomon BJ, Halmos B, Jessop NA, Wain JC, Yeo AT, Benes C, Drew L, Saeh JC, Crosby K, Sequist LV, Iafrate AJ, Engelman JA (2012) Mechanisms of Acquired Crizotinib Resistance in ALK-Rearranged Lung Cancers. Sci Transl Med 4:120ra17. https://doi.org/10.1126/scitranslmed.3003316

Kerr KM, López-Ríos F (2016) Precision medicine in NSCLC and pathology: how does ALK fit in the pathway? Ann Oncol 27:iii16–iii24. https://doi.org/10.1093/annonc/mdw302

Kersten K, Visser KE, Miltenburg MH, Jonkers J (2017) Genetically engineered mouse models in oncology research and cancer medicine. EMBO Mol Med 9:137–153. https://doi.org/10.15252/emmm.201606857

Kim Y, Hammerman PS, Kim J, Yoon J, Lee Y, Sun J-M, Wilkerson MD, Pedamallu CS, Cibulskis K, Yoo YK, Lawrence MS, Stojanov P, Carter SL, McKenna A, Stewart C, Sivachenko AY, Oh I-J, Kim HK, Choi YS, Kim K, Shim YM, Kim K-S, Song S-Y, Na K-J, Choi Y-L, Hayes DN, Kim J, Cho S, Kim Y-C, Ahn JS, Ahn M-J, Getz G, Meyerson M, Park K (2013) Integrative and Comparative Genomic Analysis of Lung Squamous Cell Carcinomas in East Asian Patients. J Clin Oncol 32:121–128. https://doi.org/10.1200/jco.2013.50.8556

Koivunen JP, Mermel C, Zejnullahu K, Murphy C, Lifshits E, Holmes AJ, Choi HG, Kim J, Chiang D, Thomas R, Lee J, Richards WG, Sugarbaker DJ, Ducko C, Lindeman N, Marcoux JP, Engelman JA, Gray NS, Lee C, Meyerson M, Jänne PA (2008) EML4-ALK Fusion Gene and Efficacy of an ALK Kinase Inhibitor in Lung Cancer. Clin Cancer Res 14:4275–4283. https://doi.org/10.1158/1078-0432.ccr-08-0168

Koopman B, Groen HJM, Schuuring E, Hiltermann TJN, Timens W, Dunnen WFA den, Berg A van den, Elst A ter, Kruchten M van, Kluiver JL, Hiddinga BI, Hijmering-Kappelle LBM, Groves MR, Vilacha JF, Kempen LC van, Wekken AJ van der (2022) Actionability of on-target ALK Resistance Mutations in Patients With Non-Small Cell Lung Cancer: Local Experience and Review of the Literature. Clin Lung Cancer 23:e104–e115. https://doi.org/10.1016/j.cllc.2021.06.011

Kron A, Alidousty C, Scheffler M, Merkelbach-Bruse S, Seidel D, Riedel R, Ihle MA, Michels S, Nogova L, Fassunke J, Heydt C, Kron F, Ueckeroth F, Serke M, Krüger S, Grohe C, Koschel D, Benedikter J, Kaminsky B, Schaaf B, Braess J, Sebastian M, Kambartel K-O, Thomas R, Zander T, Schultheis

AM, Büttner R, Wolf J (2018) Impact of TP53 mutation status on systemic treatment outcome in ALK-rearranged non-small-cell lung cancer. Ann Oncol 29:2068–2075. https://doi.org/10.1093/annonc/mdy333

Kuang S, Leighl NB (2021) Lorlatinib in ALK-Rearranged Lung Cancer. Cancer Cell 39:25–27. https://doi.org/10.1016/j.ccell.2020.12.017

LaFave LM, Kartha VK, Ma S, Meli K, Priore ID, Lareau C, Naranjo S, Westcott PMK, Duarte FM, Sankar V, Chiang Z, Brack A, Law T, Hauck H, Okimoto A, Regev A, Buenrostro JD, Jacks T (2020) Epigenomic State Transitions Characterize Tumor Progression in Mouse Lung Adenocarcinoma. Cancer Cell 38:212-228.e13. https://doi.org/10.1016/j.ccell.2020.06.006

Lee J-S, Han J-Y, Ahn M-J, Oh I-J, Kim H, Lee DH, Bertino EM, Ramirez SV, Pennell NA, Wozniak AJ, Schiller JH, Lin C, Keer HN, Azab M, Besse B, Camidge DR (2016) Addition of HSP90 inhibitor onalespib to crizotinib prior to progression in patients with ALK-pos NSCLC: Results of a randomized phase 2 study. J Clin Oncol 34:9059–9059. https://doi.org/10.1200/jco.2016.34.15_suppl.9059

Lee MC, Cai H, Murray CW, Li C, Shue YT, Andrejka L, He AL, Holzem AME, Drainas AP, Ko JH, Coles GL, Kong C, Zhu S, Zhu C, Wang J, Rijn M van de, Petrov DA, Winslow MM, Sage J (2023) A multiplexed in vivo approach to identify driver genes in small cell lung cancer. Cell Rep 42:111990. https://doi.org/10.1016/j.celrep.2023.111990

Lee Y-R, Chen M, Pandolfi PP (2018) The functions and regulation of the PTEN tumour suppressor: new modes and prospects. Nat Rev Mol Cell Biol 19:547–562. https://doi.org/10.1038/s41580-018-0015-0

Leung W, Teater M, Durmaz C, Meydan C, Chivu AG, Chadburn A, Rice EJ, Muley A, Camarillo JM, Arivalagan J, Li Z, Flowers CR, Kelleher NL, Danko CG, Imielinski M, Dave SS, Armstrong SA, Mason CE, Melnick AM (2022) SETD2 Haploinsufficiency Enhances Germinal Center–Associated AICDA Somatic Hypermutation to Drive B-cell Lymphomagenesis. Cancer Discov 12:1782–1803. https://doi.org/10.1158/2159-8290.cd-21-1514

Lin JJ, Zhu VW, Schoenfeld AJ, Yeap BY, Saxena A, Ferris LA, Dagogo-Jack I, Farago AF, Taber A, Traynor A, Menon S, Gainor JF, Lennerz JK, Plodkowski AJ, Digumarthy SR, Ou S-HI, Shaw AT, Riely GJ (2018) Brigatinib in Patients With Alectinib-Refractory ALK-Positive NSCLC. J Thorac Oncol 13:1530–1538. https://doi.org/10.1016/j.jtho.2018.06.005

Lin JJ, Zhu VW, Yoda S, Yeap BY, Schrock AB, Dagogo-Jack I, Jessop NA, Jiang GY, Le LP, Gowen K, Stephens PJ, Ross JS, Ali SM, Miller VA, Johnson ML, Lovly CM, Hata AN, Gainor JF, Iafrate AJ, Shaw AT, Ou S-HI (2018) Impact of EML4-ALK Variant on Resistance Mechanisms and Clinical Outcomes in ALK-Positive Lung Cancer. J Clin Oncol 36:JCO.2017.76.229. https://doi.org/10.1200/jco.2017.76.2294

Lipson D, Capelletti M, Yelensky R, Otto G, Parker A, Jarosz M, Curran JA, Balasubramanian S, Bloom T, Brennan KW, Donahue A, Downing SR, Frampton GM, Garcia L, Juhn F, Mitchell KC, White E, White J, Zwirko Z, Peretz T, Nechushtan H, Soussan-Gutman L, Kim J, Sasaki H, Kim HR, Park S, Ercan D, Sheehan CE, Ross JS, Cronin MT, Jänne PA, Stephens PJ (2012) Identification of new ALK and RET gene fusions from colorectal and lung cancer biopsies. Nat Med 18:382–384. https://doi.org/10.1038/nm.2673

Liu GY, Sabatini DM (2020) mTOR at the nexus of nutrition, growth, ageing and disease. Nat Rev Mol Cell Biol 21:183–203. https://doi.org/10.1038/s41580-019-0199-y

Maddalo D, Manchado E, Concepcion CP, Bonetti C, Vidigal JA, Han Y-C, Ogrodowski P, Crippa A, Rekhtman N, Stanchina E de, Lowe SW, Ventura A (2014) In vivo engineering of oncogenic chromosomal rearrangements with the CRISPR/Cas9 system. Nature 516:423–427. https://doi.org/10.1038/nature13902

Marino S, Vooijs M, Gulden H van der, Jonkers J, Berns A (2000) Induction of medulloblastomas in p53-null mutant mice by somatic inactivation of Rb in the external granular layer cells of the cerebellum. Genes Dev 14:994–1004. https://doi.org/10.1101/gad.14.8.994

Marjanovic ND, Hofree M, Chan JE, Canner D, Wu K, Trakala M, Hartmann GG, Smith OC, Kim JY, Evans KV, Hudson A, Ashenberg O, Porter CBM, Bejnood A, Subramanian A, Pitter K, Yan Y, Delorey T, Phillips DR, Shah N, Chaudhary O, Tsankov A, Hollmann T, Rekhtman N, Massion PP, Poirier JT, Mazutis L, Li R, Lee J-H, Amon A, Rudin CM, Jacks T, Regev A, Tammela T (2020) Emergence of a High-Plasticity Cell State during Lung Cancer Evolution. Cancer Cell 38:229-246.e13. https://doi.org/10.1016/j.ccell.2020.06.012

Marzec M, Kasprzycka M, Liu X, El-Salem M, Halasa K, Raghunath PN, Bucki R, Wlodarski P, Wasik MA (2007) Oncogenic tyrosine kinase NPM/ALK induces activation of the rapamycin-sensitive mTOR signaling pathway. Oncogene 26:5606–5614. https://doi.org/10.1038/sj.onc.1210346

McDermott U, Iafrate AJ, Gray NS, Shioda T, Classon M, Maheswaran S, Zhou W, Choi HG, Smith SL, Dowell L, Ulkus LE, Kuhlmann G, Greninger P, Christensen JG, Haber DA, Settleman J (2008) Genomic Alterations of Anaplastic Lymphoma Kinase May Sensitize Tumors to Anaplastic Lymphoma Kinase Inhibitors. Cancer Res 68:3389–3395. https://doi.org/10.1158/0008-5472.can-07-6186

Mok T, Camidge DR, Gadgeel SM, Rosell R, Dziadziuszko R, Kim D-W, Pérol M, Ou S-HI, Ahn JS, Shaw AT, Bordogna W, Smoljanović V, Hilton M, Ruf T, Noé J, Peters S (2020) Updated overall survival and final progression-free survival data for patients with treatment-naive advanced ALK-positive non-small-cell lung cancer in the ALEX study. Ann Oncol 31:1056–1064. https://doi.org/10.1016/j.annonc.2020.04.478

Mollaoglu G, Jones A, Wait SJ, Mukhopadhyay A, Jeong S, Arya R, Camolotto SA, Mosbruger TL, Stubben CJ, Conley CJ, Bhutkar A, Vahrenkamp JM, Berrett KC, Cessna MH, Lane TE, Witt BL, Salama ME, Gertz J, Jones KB, Snyder EL, Oliver TG (2018) The Lineage-Defining Transcription Factors SOX2 and NKX2-1 Determine Lung Cancer Cell Fate and Shape the Tumor Immune Microenvironment. Immunity 49:764-779.e9. https://doi.org/10.1016/j.immuni.2018.09.020

Montero JC, Seoane S, Ocaña A, Pandiella A (2011) Inhibition of Src Family Kinases and Receptor Tyrosine Kinases by Dasatinib: Possible Combinations in Solid Tumors. Clin Cancer Res 17:5546–5552. https://doi.org/10.1158/1078-0432.ccr-10-2616

Moore NF, Azarova AM, Bhatnagar N, Ross KN, Drake LE, Frumm S, Liu QS, Christie AL, Sanda T, Chesler L, Kung AL, Gray NS, Stegmaier K, George RE (2014) Molecular rationale for the use of PI3K/AKT/mTOR pathway inhibitors in combination with crizotinib in ALK-mutated neuroblastoma. Oncotarget 5:8737–8749. https://doi.org/10.18632/oncotarget.2372

Morris EJ, Jha S, Restaino CR, Dayananth P, Zhu H, Cooper A, Carr D, Deng Y, Jin W, Black S, Long B, Liu J, DiNunzio E, Windsor W, Zhang R, Zhao S, Angagaw MH, Pinheiro EM, Desai J, Xiao L, Shipps G, Hruza A, Wang J, Kelly J, Paliwal S, Gao X, Babu BS, Zhu L, Daublain P, Zhang L, Lutterbach BA, Pelletier MR, Philippar U, Siliphaivanh P, Witter D, Kirschmeier P, Bishop WR, Hicklin D, Gilliland DG, Jayaraman L, Zawel L, Fawell S, Samatar AA (2013) Discovery of a Novel ERK Inhibitor with Activity in Models of Acquired Resistance to BRAF and MEK Inhibitors. Cancer Discov 3:742–750. https://doi.org/10.1158/2159-8290.cd-13-0070

Morris SW, Kirstein MN, Valentine MB, Dittmer KG, Shapiro DN, Saltman DL, Look AT (1994) Fusion of a Kinase Gene, ALK, to a Nucleolar Protein Gene, NPM, in Non-Hodgkin's Lymphoma. Science 263:1281–1284. https://doi.org/10.1126/science.8122112

Mossé YP, Laudenslager M, Longo L, Cole KA, Wood A, Attiyeh EF, Laquaglia MJ, Sennett R, Lynch JE, Perri P, Laureys G, Speleman F, Kim C, Hou C, Hakonarson H, Torkamani A, Schork NJ, Brodeur GM, Tonini GP, Rappaport E, Devoto M, Maris JM (2008) Identification of ALK as a major familial neuroblastoma predisposition gene. Nature 455:930–935. https://doi.org/10.1038/nature07261

Mota I, Patrucco E, Mastini C, Mahadevan NR, Thai TC, Bergaggio E, Cheong T-C, Leonardi G, Karaca-Atabay E, Campisi M, Poggio T, Menotti M, Ambrogio C, Longo DL, Klaeger S, Keshishian H, Sztupinszki ZM, Szallasi Z, Keskin DB, Duke-Cohan JS, Reinhold B, Carr SA, Wu CJ, Moynihan KD, Irvine DJ, Barbie DA, Reinherz EL, Voena C, Awad MM, Blasco RB, Chiarle R (2023) ALK peptide vaccination restores the immunogenicity of ALK-rearranged non-small cell lung cancer. Nat Cancer 4:1016–1035. https://doi.org/10.1038/s43018-023-00591-2

Murray BW, Zhai D, Deng W, Zhang X, Ung J, Nguyen V, Zhang H, Barrera M, Parra A, Cowell J, Lee DJ, Aloysius H, Rogers E (2021) TPX-0131, a Potent CNS-penetrant, Next-generation Inhibitor of Wild-type ALK and ALK-resistant Mutations. Mol Cancer Ther 20:1499–1507. https://doi.org/10.1158/1535-7163.mct-21-0221

Murray CW, Brady JJ, Han M, Cai H, Tsai MK, Pierce SE, Cheng R, Demeter J, Feldser DM, Jackson PK, Shackelford DB, Winslow MM (2022) LKB1 drives stasis and C/EBP-mediated reprogramming to an alveolar type II fate in lung cancer. Nat Commun 13:1090. https://doi.org/10.1038/s41467-022-28619-8

Murray CW, Brady JJ, Tsai MK, Li C, Winters IP, Tang R, Andrejka L, Ma RK, Kunder CA, Chu P, Winslow MM (2019) An LKB1–SIK Axis Suppresses Lung Tumor Growth and Controls Differentiation. Cancer Discov 9:1590–1605. https://doi.org/10.1158/2159-8290.cd-18-1237

Muzumdar MD, Tasic B, Miyamichi K, Li L, Luo L (2007) A global double-fluorescent Cre reporter mouse. Genesis 45:593–605. https://doi.org/10.1002/dvg.20335

Nagaraj AS, Lahtela J, Hemmes A, Pellinen T, Blom S, Devlin JR, Salmenkivi K, Kallioniemi O, Mäyränpää MI, Närhi K, Verschuren EW (2017) Cell of Origin Links Histotype Spectrum to Immune Microenvironment Diversity in Non-small-Cell Lung Cancer Driven by Mutant Kras and Loss of Lkb1. Cell Rep 18:673–684. https://doi.org/10.1016/j.celrep.2016.12.059

Naranjo S, Cabana CM, LaFave LM, Romero R, Shanahan S-L, Bhutkar A, Westcott PMK, Schenkel JM, Ghosh A, Liao LZ, Priore ID, Yang D, Jacks T (2022) Modeling diverse genetic subtypes of lung adenocarcinoma with a next-generation alveolar type 2 organoid platform. Genes Dev 36:936–949. https://doi.org/10.1101/gad.349659.122

Neto JMF, Nadal E, Bosdriesz E, Ooft SN, Farre L, McLean C, Klarenbeek S, Jurgens A, Hagen H, Wang L, Felip E, Martinez-Marti A, Vidal A, Voest E, Wessels LFA, Tellingen O van, Villanueva A, Bernards R (2020) Multiple low dose therapy as an effective strategy to treat EGFR inhibitor-resistant NSCLC tumours. Nat Commun 11:3157. https://doi.org/10.1038/s41467-020-16952-9

Niederst MJ, Sequist LV, Poirier JT, Mermel CH, Lockerman EL, Garcia AR, Katayama R, Costa C, Ross KN, Moran T, Howe E, Fulton LE, Mulvey HE, Bernardo LA, Mohamoud F, Miyoshi N, VanderLaan PA, Costa DB, Jänne PA, Borger DR, Ramaswamy S, Shioda T, Iafrate AJ, Getz G, Rudin CM, Mino-Kenudson M, Engelman JA (2015) RB loss in resistant EGFR mutant lung adenocarcinomas that transform to small-cell lung cancer. Nat Commun 6:6377. https://doi.org/10.1038/ncomms7377

Nishio M, Yoshida T, Kumagai T, Hida T, Toyozawa R, Shimokawaji T, Goto K, Nakagawa K, Ohe Y, Seto T, Kudou K, Asato T, Zhang P, Yamamoto N (2021) Brigatinib in Japanese Patients With ALK-Positive NSCLC Previously Treated With Alectinib and Other Tyrosine Kinase Inhibitors: Outcomes of the Phase 2 J-ALTA Trial. J Thorac Oncol 16:452–463. https://doi.org/10.1016/j.jtho.2020.11.004

Noh K, Lee M, Lee SE, Song J, Shin H, Kim YJ, Oh DY, Jung K, Sung M, Kim M, An S, Han J, Shim YM, Zo JI, Kim J, Park W, Lee S, Choi Y (2017) Molecular breakdown: a comprehensive view of anaplastic lymphoma kinase (ALK)-rearranged non-small cell lung cancer. J Pathol 243:307–319. https://doi.org/10.1002/path.4950

Oikonomou N, Mouratis M-A, Tzouvelekis A, Kaffe E, Valavanis C, Vilaras G, Karameris A, Prestwich GD, Bouros D, Aidinis V (2012) Pulmonary Autotaxin Expression Contributes to the Pathogenesis of Pulmonary Fibrosis. Am J Respir Cell Mol Biol 47:566–574. https://doi.org/10.1165/rcmb.2012-0004oc

Olsen RR, Ireland AS, Kastner DW, Groves SM, Spainhower KB, Pozo K, Kelenis DP, Whitney CP, Guthrie MR, Wait SJ, Soltero D, Witt BL, Quaranta V, Johnson JE, Oliver TG (2021) ASCL1 represses a SOX9+ neural crest stem-like state in small cell lung cancer. Genes Dev 35:847–869. https://doi.org/10.1101/gad.348295.121

O'Regan L, Barone G, Adib R, Woo CG, Jeong HJ, Richardson EL, Richards MW, Muller PAJ, Collis SJ, Fennell DA, Choi J, Bayliss R, Fry AM (2020) EML4–ALK V3 oncogenic fusion proteins promote microtubule stabilization and accelerated migration through NEK9 and NEK7. J Cell Sci 133:jcs241505. https://doi.org/10.1242/jcs.241505

Ou S-HI, Ahn JS, Petris LD, Govindan R, Yang JC-H, Hughes B, Lena H, Moro-Sibilot D, Bearz A, Ramirez SV, Mekhail T, Spira A, Bordogna W, Balas B, Morcos PN, Monnet A, Zeaiter A, Kim D-W (2015) Alectinib in Crizotinib-Refractory ALK-Rearranged Non–Small-Cell Lung Cancer: A Phase II Global Study. J Clin Oncol 34:661–668. https://doi.org/10.1200/jco.2015.63.9443

Ou S-HI, Jänne PA, Bartlett CH, Tang Y, Kim D-W, Otterson GA, Crinò L, Selaru P, Cohen DP, Clark JW, Riely GJ (2014) Clinical benefit of continuing ALK inhibition with crizotinib beyond initial disease progression in patients with advanced ALK-positive NSCLC. Ann Oncol 25:415–422. https://doi.org/10.1093/annonc/mdt572

Ou S-HI, Zhu VW, Nagasaka M (2020) Catalog of 5' Fusion Partners in ALK-positive NSCLC Circa 2020. JTO Clin Res Rep 1:100015. https://doi.org/10.1016/j.jtocrr.2020.100015

Pailler E, Faugeroux V, Oulhen M, Mezquita L, Laporte M, Honoré A, Lecluse Y, Queffelec P, NgoCamus M, Nicotra C, Remon J, Lacroix L, Planchard D, Friboulet L, Besse B, Farace F (2019) Acquired Resistance Mutations to ALK Inhibitors Identified by Single Circulating Tumor Cell

Sequencing in ALK-Rearranged Non–Small-Cell Lung Cancer. Clin Cancer Res 25:6671–6682. https://doi.org/10.1158/1078-0432.ccr-19-1176

Palmer RH, Vernersson E, Grabbe C, Hallberg B (2009) Anaplastic lymphoma kinase: signalling in development and disease. Biochem J 420:345–361. https://doi.org/10.1042/bj20090387

Pan Y, Han H, Hu H, Wang H, Song Y, Hao Y, Tong X, Patel AS, Misirlioglu S, Tang S, Huang H-Y, Geng K, Chen T, Karatza A, Sherman F, Labbe KE, Yang F, Chafitz A, Peng C, Guo C, Moreira AL, Velcheti V, Lau SCM, Sui P, Chen H, Diehl JA, Rustgi AK, Bass AJ, Poirier JT, Zhang X, Ji H, Zhang H, Wong K-K (2023) KMT2D deficiency drives lung squamous cell carcinoma and hypersensitivity to RTK-RAS inhibition. Cancer Cell 41:88-105.e8. https://doi.org/10.1016/j.ccell.2022.11.015

Park B-J, Kang JW, Lee SW, Choi S-J, Shin YK, Ahn YH, Choi YH, Choi D, Lee KS, Kim S (2005) The Haploinsufficient Tumor Suppressor p18 Upregulates p53 via Interactions with ATM/ATR. Cell 120:209–221. https://doi.org/10.1016/j.cell.2004.11.054

Pelaz SG, Tabernero A (2022) Src: coordinating metabolism in cancer. Oncogene 41:4917–4928. https://doi.org/10.1038/s41388-022-02487-4

Pelish HE, Tangpeerachaikul A, Kohl NE, Porter JR, Shair MD, Horan JC (2021) Abstract 1468: NUV-655 (NVL-655) is a selective, brain-penetrant ALK inhibitor with antitumor activity against the lorlatinib-resistant G1202R/L1196M compound mutation. Cancer Res 81:1468–1468. https://doi.org/10.1158/1538-7445.am2021-1468

Platt RJ, Chen S, Zhou Y, Yim MJ, Swiech L, Kempton HR, Dahlman JE, Parnas O, Eisenhaure TM, Jovanovic M, Graham DB, Jhunjhunwala S, Heidenreich M, Xavier RJ, Langer R, Anderson DG, Hacohen N, Regev A, Feng G, Sharp PA, Zhang F (2014) CRISPR-Cas9 Knockin Mice for Genome Editing and Cancer Modeling. Cell 159:440–455. https://doi.org/10.1016/j.cell.2014.09.014

Playford MP, Schaller MD (2004) The interplay between Src and integrins in normal and tumor biology. Oncogene 23:7928–7946. https://doi.org/10.1038/sj.onc.1208080

Pyo KH, Lim SM, Kim HR, Sung YH, Yun MR, Kim S-M, Kim H, Kang HN, Lee JM, Kim SG, Park CW, Chang H, Shim HS, Lee H-W, Cho BC (2017) Establishment of a Conditional Transgenic Mouse Model Recapitulating EML4-ALK–Positive Human Non–Small Cell Lung Cancer. J Thorac Oncol 12:491–500. https://doi.org/10.1016/j.jtho.2016.10.022

Qin Z, Sun H, Yue M, Pan X, Chen L, Feng X, Yan X, Zhu X, Ji H (2021) Phase separation of EML4–ALK in firing downstream signaling and promoting lung tumorigenesis. Cell Discov 7:33. https://doi.org/10.1038/s41421-021-00270-5

Qin Z, Yue M, Tang S, Wu F, Sun H, Li Y, Zhang Y, Izumi H, Huang H, Wang W, Xue Y, Tong X, Mori S, Taki T, Goto K, Jin Y, Li F, Li F-M, Gao Y, Fang Z, Fang Y, Hu L, Yan X, Xu G, Chen H, Kobayashi SS, Ventura A, Wong K-K, Zhu X, Chen L, Ren S, Chen L-N, Ji H (2024) EML4-ALK fusions drive lung adeno-to-squamous transition through JAK-STAT activation. J Exp Med 221:e20232028. https://doi.org/10.1084/jem.20232028

Quintanal-Villalonga Á, Chan JM, Yu HA, Pe'er D, Sawyers CL, Sen T, Rudin CM (2020) Lineage plasticity in cancer: a shared pathway of therapeutic resistance. Nat Rev Clin Oncol 17:360–371. https://doi.org/10.1038/s41571-020-0340-z

Recondo G, Mezquita L, Facchinetti F, Planchard D, Gazzah A, Bigot L, Rizvi AZ, Frias RL, Thiery JP, Scoazec J-Y, Sourisseau T, Howarth K, Deas O, Samofalova D, Galissant J, Tesson P, Braye F, Naltet C, Lavaud P, Mahjoubi L, Lovergne AA, Vassal G, Bahleda R, Hollebecque A, Nicotra C, Ngo-Camus M, Michiels S, Lacroix L, Richon C, Auger N, Baere TD, Tselikas L, Solary E, Angevin E, Eggermont AM, Andre F, Massard C, Olaussen KA, Soria J-C, Besse B, Friboulet L (2020) Diverse Resistance Mechanisms to the Third-Generation ALK Inhibitor Lorlatinib in ALK-Rearranged Lung Cancer. Clin Cancer Res 26:242–255. https://doi.org/10.1158/1078-0432.ccr-19-1104

Redaelli S, Ceccon M, Antolini L, Rigolio R, Pirola A, Peronaci M, Gambacorti-Passerini C, Mologni L (2016) Synergistic activity of ALK and mTOR inhibitors for the treatment of NPM-ALK positive lymphoma. Oncotarget 7:72886–72897. https://doi.org/10.18632/oncotarget.12128

Redaelli S, Ceccon M, Zappa M, Sharma GG, Mastini C, Mauri M, Nigoghossian M, Massimino L, Cordani N, Farina F, Piazza R, Gambacorti-Passerini C, Mologni L (2018) Lorlatinib treatment elicits multiple on- and off-target mechanisms of resistance in ALK-driven cancer. Cancer Res 78:canres.1867.2018. https://doi.org/10.1158/0008-5472.can-18-1867

Richards MW, Law EWP, Rennalls LP, Busacca S, O'Regan L, Fry AM, Fennell DA, Bayliss R (2014) Crystal structure of EML1 reveals the basis for Hsp90 dependence of oncogenic EML4-ALK by

disruption of an atypical β-propeller domain. Proc Natl Acad Sci 111:5195–5200. https://doi.org/10.1073/pnas.1322892111

Richards MW, O'Regan L, Roth D, Montgomery JM, Straube A, Fry AM, Bayliss R (2015) Microtubule association of EML proteins and the EML4-ALK variant 3 oncoprotein require an N-terminal trimerization domain. Biochem J 467:529–536. https://doi.org/10.1042/bj20150039

Rikova K, Guo A, Zeng Q, Possemato A, Yu J, Haack H, Nardone J, Lee K, Reeves C, Li Y, Hu Y, Tan Z, Stokes M, Sullivan L, Mitchell J, Wetzel R, MacNeill J, Ren JM, Yuan J, Bakalarski CE, Villen J, Kornhauser JM, Smith B, Li D, Zhou X, Gygi SP, Gu T-L, Polakiewicz RD, Rush J, Comb MJ (2007) Global Survey of Phosphotyrosine Signaling Identifies Oncogenic Kinases in Lung Cancer. Cell 131:1190–1203. https://doi.org/10.1016/j.cell.2007.11.025

Rodig SJ, Mino-Kenudson M, Dacic S, Yeap BY, Shaw A, Barletta JA, Stubbs H, Law K, Lindeman N, Mark E, Janne PA, Lynch T, Johnson BE, Iafrate AJ, Chirieac LR (2009) Unique Clinicopathologic Features Characterize ALK-Rearranged Lung Adenocarcinoma in the Western Population. Clin Cancer Res 15:5216–5223. https://doi.org/10.1158/1078-0432.ccr-09-0802

Rogers ZN, McFarland CD, Winters IP, Naranjo S, Chuang C-H, Petrov D, Winslow MM (2017) A quantitative and multiplexed approach to uncover the fitness landscape of tumor suppression in vivo. Nat Methods 14:737–742. https://doi.org/10.1038/nmeth.4297

Rogers ZN, McFarland CD, Winters IP, Seoane JA, Brady JJ, Yoon S, Curtis C, Petrov DA, Winslow MM (2018) Mapping the in vivo fitness landscape of lung adenocarcinoma tumor suppression in mice. Nat Genet 50:483–486. https://doi.org/10.1038/s41588-018-0083-2

Roskoski R (2013) Anaplastic lymphoma kinase (ALK): Structure, oncogenic activation, and pharmacological inhibition. Pharmacol Res 68:68–94. https://doi.org/10.1016/j.phrs.2012.11.007

Rotow J, Bivona TG (2017) Understanding and targeting resistance mechanisms in NSCLC. Nat Rev Cancer 17:637–658. https://doi.org/10.1038/nrc.2017.84

Ruiz-Saenz A, Atreya CE, Wang C, Pan B, Dreyer CA, Brunen D, Prahallad A, Muñoz DP, Ramms DJ, Burghi V, Spassov DS, Fewings E, Hwang YC, Cowdrey C, Moelders C, Schwarzer C, Wolf DM, Hann B, VandenBerg SR, Shokat K, Moasser MM, Bernards R, Gutkind JS, Veer LJ van 't, Coppé J-P (2023) A reversible SRC-relayed COX2 inflammatory program drives resistance to BRAF and EGFR inhibition in BRAFV600E colorectal tumors. Nat Cancer 4:240–256. https://doi.org/10.1038/s43018-022-00508-5

Sabir SR, Yeoh S, Jackson G, Bayliss R (2017) EML4-ALK Variants: Biological and Molecular Properties, and the Implications for Patients. Cancers 9:118. https://doi.org/10.3390/cancers9090118

Sagawa R, Ohba T, Ito E, Isogai S (2018) ALK-Positive Squamous Cell Carcinoma Dramatically Responded to Alectinib. Case Rep Oncol Med 2018:4172721. https://doi.org/10.1155/2018/4172721

Sakamoto H, Tsukaguchi T, Hiroshima S, Kodama T, Kobayashi T, Fukami TA, Oikawa N, Tsukuda T, Ishii N, Aoki Y (2011) CH5424802, a Selective ALK Inhibitor Capable of Blocking the Resistant Gatekeeper Mutant. Cancer Cell 19:679–690. https://doi.org/10.1016/j.ccr.2011.04.004

Salgia R, Pharaon R, Mambetsariev I, Nam A, Sattler M (2021) The improbable targeted therapy: KRAS as an emerging target in non-small cell lung cancer (NSCLC). Cell Rep Med 2:100186. https://doi.org/10.1016/j.xcrm.2020.100186

Sampson J, Richards MW, Choi J, Fry AM, Bayliss R (2021) Phase-separated foci of EML4-ALK facilitate signalling and depend upon an active kinase conformation. EMBO Rep 22:e53693. https://doi.org/10.15252/embr.202153693

Sanclemente M, Francoz S, Esteban-Burgos L, Bousquet-Mur E, Djurec M, Lopez-Casas PP, Hidalgo M, Guerra C, Drosten M, Musteanu M, Barbacid M (2018) c-RAF Ablation Induces Regression of Advanced Kras/Trp53 Mutant Lung Adenocarcinomas by a Mechanism Independent of MAPK Signaling. Cancer Cell 33:217-228.e4. https://doi.org/10.1016/j.ccell.2017.12.014

Schmutz I, Mensenkamp AR, Takai KK, Haadsma M, Spruijt L, Voer RM de, Choo SS, Lorbeer FK, Grinsven EJ van, Hockemeyer D, Jongmans MC, Lange T de (2020) TINF2 is a haploinsufficient tumor suppressor that limits telomere length. eLife 9:e61235. https://doi.org/10.7554/elife.61235

Schneider JL, Lin JJ, Shaw AT (2023) ALK-positive lung cancer: a moving target. Nat Cancer 4:330–343. https://doi.org/10.1038/s43018-023-00515-0

Seto T, Kiura K, Nishio M, Nakagawa K, Maemondo M, Inoue A, Hida T, Yamamoto N, Yoshioka H, Harada M, Ohe Y, Nogami N, Takeuchi K, Shimada T, Tanaka T, Tamura T (2013) CH5424802 (RO5424802) for patients with ALK-rearranged advanced non-small-cell lung cancer (AF-001JP study): a single-arm, open-label, phase 1–2 study. Lancet Oncol 14:590–598. https://doi.org/10.1016/s1470-2045(13)70142-6

Settleman J, Neto JMF, Bernards R (2021) Thinking Differently about Cancer Treatment Regimens. Cancer Discov 11:1016–1023. https://doi.org/10.1158/2159-8290.cd-20-1187

Shaw AT, Bauer TM, Marinis F de, Felip E, Goto Y, Liu G, Mazieres J, Kim D-W, Mok T, Polli A, Thurm H, Calella AM, Peltz G, Solomon BJ, Investigators CT (2020) First-Line Lorlatinib or Crizotinib in Advanced ALK-Positive Lung Cancer. N Engl J Med 383:2018–2029. https://doi.org/10.1056/nejmoa2027187

Shaw AT, Engelman JA (2013) ALK in Lung Cancer: Past, Present, and Future. J Clin Oncol 31:1105–1111. https://doi.org/10.1200/jco.2012.44.5353

Shaw AT, Felip E, Bauer TM, Besse B, Navarro A, Postel-Vinay S, Gainor JF, Johnson M, Dietrich J, James LP, Clancy JS, Chen J, Martini J-F, Abbattista A, Solomon BJ (2017) Lorlatinib in non-small-cell lung cancer with ALK or ROS1 rearrangement: an international, multicentre, open-label, single-arm first-in-man phase 1 trial. Lancet Oncol 18:1590–1599. https://doi.org/10.1016/s1470-2045(17)30680-0

Shaw AT, Gandhi L, Gadgeel S, Riely GJ, Cetnar J, West H, Camidge DR, Socinski MA, Chiappori A, Mekhail T, Chao BH, Borghaei H, Gold KA, Zeaiter A, Bordogna W, Balas B, Puig O, Henschel V, Ou S-HI, investigators study (2016) Alectinib in ALK-positive, crizotinib-resistant, non-small-cell lung cancer: a single-group, multicentre, phase 2 trial. Lancet Oncol 17:234–242. https://doi.org/10.1016/s1470-2045(15)00488-x

Shaw AT, Solomon BJ, Besse B, Bauer TM, Lin C-C, Soo RA, Riely GJ, Ou S-HI, Clancy JS, Li S, Abbattista A, Thurm H, Satouchi M, Camidge DR, Kao S, Chiari R, Gadgeel SM, Felip E, Martini J-F (2019) ALK Resistance Mutations and Efficacy of Lorlatinib in Advanced Anaplastic Lymphoma Kinase-Positive Non–Small-Cell Lung Cancer. J Clin Oncol 37:1370–1379. https://doi.org/10.1200/jco.18.02236

Shiba-Ishii A, Johnson TW, Dagogo-Jack I, Mino-Kenudson M, Johnson TR, Wei P, Weinrich SL, McTigue MA, Walcott MA, Nguyen-Phuong L, Dionne K, Acker A, Kiedrowski LA, Do A, Peterson JL, Barth JL, Yeap BY, Gainor JF, Lin JJ, Yoda S, Hata AN (2022) Analysis of lorlatinib analogs reveals a roadmap for targeting diverse compound resistance mutations in ALK-positive lung cancer. Nat Cancer 3:710–722. https://doi.org/10.1038/s43018-022-00399-6

Shimizu Y, Okada K, Adachi J, Abe Y, Narumi R, Uchibori K, Yanagitani N, Koike S, Takagi S, Nishio M, Fujita N, Katayama R (2022) GSK3 inhibition circumvents and overcomes acquired lorlatinib resistance in ALK-rearranged non-small-cell lung cancer. Npj Precis Oncol 6:16. https://doi.org/10.1038/s41698-022-00260-0

Sies H, Jones DP (2020) Reactive oxygen species (ROS) as pleiotropic physiological signalling agents. Nat Rev Mol Cell Biol 21:363–383. https://doi.org/10.1038/s41580-020-0230-3

Skoulidis F, Heymach JV (2019) Co-occurring genomic alterations in non-small-cell lung cancer biology and therapy. Nat Rev Cancer 19:495–509. https://doi.org/10.1038/s41568-019-0179-8

Snyder EL, Watanabe H, Magendantz M, Hoersch S, Chen TA, Wang DG, Crowley D, Whittaker CA, Meyerson M, Kimura S, Jacks T (2013) Nkx2-1 Represses a Latent Gastric Differentiation Program in Lung Adenocarcinoma. Mol Cell 50:185–199. https://doi.org/10.1016/j.molcel.2013.02.018

Soda M, Choi YL, Enomoto M, Takada S, Yamashita Y, Ishikawa S, Fujiwara S, Watanabe H, Kurashina K, Hatanaka H, Bando M, Ohno S, Ishikawa Y, Aburatani H, Niki T, Sohara Y, Sugiyama Y, Mano H (2007) Identification of the transforming EML4–ALK fusion gene in non-small-cell lung cancer. Nature 448:561–566. https://doi.org/10.1038/nature05945

Soda M, Takada S, Takeuchi K, Choi YL, Enomoto M, Ueno T, Haruta H, Hamada T, Yamashita Y, Ishikawa Y, Sugiyama Y, Mano H (2008) A mouse model for EML4-ALK-positive lung cancer. Proc Natl Acad Sci 105:19893–19897. https://doi.org/10.1073/pnas.0805381105

Sodir NM, Pathria G, Adamkewicz JI, Kelley EH, Sudhamsu J, Merchant M, Chiarle R, Maddalo D (2023) SHP2: A Pleiotropic Target at the Interface of Cancer and Its Microenvironment. Cancer Discov 13:OF1–OF17. https://doi.org/10.1158/2159-8290.cd-23-0383

Solomon BJ, Bauer TM, Mok TSK, Liu G, Mazieres J, Marinis F de, Goto Y, Kim D-W, Wu Y-L, Jassem J, López FL, Soo RA, Shaw AT, Polli A, Messina R, Iadeluca L, Toffalorio F, Felip E (2023) Efficacy and safety of first-line lorlatinib versus crizotinib in patients with advanced, ALK-positive non-small-cell lung cancer: updated analysis of data from the phase 3, randomised, open-label CROWN study. Lancet Respir Med 11:354–366. https://doi.org/10.1016/s2213-2600(22)00437-4

Solomon BJ, Besse B, Bauer TM, Felip E, Soo RA, Camidge DR, Chiari R, Bearz A, Lin C-C, Gadgeel SM, Riely GJ, Tan EH, Seto T, James LP, Clancy JS, Abbattista A, Martini J-F, Chen J, Peltz G, Thurm H, Ou S-HI, Shaw AT (2018) Lorlatinib in patients with ALK-positive non-small-cell lung cancer: results from a global phase 2 study. Lancet Oncol 19:1654–1667. https://doi.org/10.1016/s1470-2045(18)30649-1

Solomon BJ, Mok T, Kim D-W, Wu Y-L, Nakagawa K, Mekhail T, Felip E, Cappuzzo F, Paolini J, Usari T, Iyer S, Reisman A, Wilner KD, Tursi J, Blackhall F, Investigators P 1014 (2014) First-Line Crizotinib versus Chemotherapy in ALK-Positive Lung Cancer. N Engl J Med 371:2167–2177. https://doi.org/10.1056/nejmoa1408440

Song MS, Salmena L, Pandolfi PP (2012) The functions and regulation of the PTEN tumour suppressor. Nat Rev Mol Cell Biol 13:283–296. https://doi.org/10.1038/nrm3330

Soria J-C, Ohe Y, Vansteenkiste J, Reungwetwattana T, Chewaskulyong B, Lee KH, Dechaphunkul A, Imamura F, Nogami N, Kurata T, Okamoto I, Zhou C, Cho BC, Cheng Y, Cho EK, Voon PJ, Planchard D, Su W-C, Gray JE, Lee S-M, Hodge R, Marotti M, Rukazenkov Y, Ramalingam SS, Investigators F (2017) Osimertinib in Untreated EGFR-Mutated Advanced Non–Small-Cell Lung Cancer. N Engl J Med 378:113–125. https://doi.org/10.1056/nejmoa1713137

Sun S, Schiller JH, Gazdar AF (2007) Lung cancer in never smokers — a different disease. Nat Rev Cancer 7:778–790. https://doi.org/10.1038/nrc2190

Sun X-J, Wei J, Wu X-Y, Hu M, Wang L, Wang H-H, Zhang Q-H, Chen S-J, Huang Q-H, Chen Z (2005) Identification and Characterization of a Novel Human Histone H3 Lysine 36-specific Methyltransferase*. J Biol Chem 280:35261–35271. https://doi.org/10.1074/jbc.m504012200

Sutherland KD, Song J-Y, Kwon MC, Proost N, Zevenhoven J, Berns A (2014) Multiple cells-of-origin of mutant K-Ras–induced mouse lung adenocarcinoma. Proc National Acad Sci 111:4952–4957. https://doi.org/10.1073/pnas.1319963111

Takegawa N, Hayashi H, Iizuka N, Takahama T, Ueda H, Tanaka K, Takeda M, Nakagawa K (2016) Transformation of ALK rearrangement-positive adenocarcinoma to small-cell lung cancer in association with acquired resistance to alectinib. Ann Oncol 27:953–955. https://doi.org/10.1093/annonc/mdw032

Takeuchi K, Choi YL, Soda M, Inamura K, Togashi Y, Hatano S, Enomoto M, Takada S, Yamashita Y, Satoh Y, Okumura S, Nakagawa K, Ishikawa Y, Mano H (2008) Multiplex Reverse Transcription-PCR Screening for EML4-ALK Fusion Transcripts. Clin Cancer Res 14:6618–6624. https://doi.org/10.1158/1078-0432.ccr-08-1018

Tangpeerachaikul A, Deshpande A, Kohl NE, Horan JC, Pelish HE (2021) Abstract P244: NVL-655 exhibits antitumor activity in lorlatinib-resistant and intracranial models of ALK-rearranged NSCLC. Mol Cancer Ther 20:P244–P244. https://doi.org/10.1158/1535-7163.targ-21-p244

Tanimoto A, Matsumoto S, Takeuchi S, Arai S, Fukuda K, Nishiyama A, Yoh K, Ikeda T, Furuya N, Nishino K, Ohe Y, Goto K, Yano S (2021) Proteasome Inhibition Overcomes ALK-TKI Resistance in ALK-Rearranged/TP53-Mutant NSCLC via Noxa Expression. Clin Cancer Res 27:1410–1420. https://doi.org/10.1158/1078-0432.ccr-20-2853

Tartari CJ, Gunby RH, Coluccia AML, Sottocornola R, Cimbro B, Scapozza L, Donella-Deana A, Pinna LA, Gambacorti-Passerini C (2008) Characterization of Some Molecular Mechanisms Governing Autoactivation of the Catalytic Domain of the Anaplastic Lymphoma Kinase*. J Biol Chem 283:3743–3750. https://doi.org/10.1074/jbc.m706067200

Thai AA, Solomon BJ, Sequist LV, Gainor JF, Heist RS (2021) Lung cancer. Lancet 398:535–554. https://doi.org/10.1016/s0140-6736(21)00312-3

Tsuboi M, Herbst RS, John T, Kato T, Majem M, Grohé C, Wang J, Goldman JW, Lu S, Su W-C, Marinis F de, Shepherd FA, Lee KH, Le NT, Dechaphunkul A, Kowalski D, Poole L, Bolanos A, Rukazenkov Y, Wu Y-L, Investigators A (2023) Overall Survival with Osimertinib in Resected EGFR-Mutated NSCLC. N Engl J Med 389:137–147. https://doi.org/10.1056/nejmoa2304594

Tsuji T, Ozasa H, Aoki W, Aburaya S, Funazo TY, Furugaki K, Yoshimura Y, Yamazoe M, Ajimizu H, Yasuda Y, Nomizo T, Yoshida H, Sakamori Y, Wake H, Ueda M, Kim YH, Hirai T (2019) YAP1 mediates survival of ALK-rearranged lung cancer cells treated with alectinib via pro-apoptotic protein regulation. Nat Commun 11:74. https://doi.org/10.1038/s41467-019-13771-5

Tulpule A, Guan J, Neel DS, Allegakoen HR, Lin YP, Brown D, Chou Y-T, Heslin A, Chatterjee N, Perati S, Menon S, Nguyen TA, Debnath J, Ramirez AD, Shi X, Yang B, Feng S, Makhija S, Huang B, Bivona TG (2021) Kinase-mediated RAS signaling via membraneless cytoplasmic protein granules. Cell 184:2649-2664.e18. https://doi.org/10.1016/j.cell.2021.03.031

Voena C, Menotti M, Mastini C, Giacomo FD, Longo DL, Castella B, Merlo MEB, Ambrogio C, Wang Q, Minero VG, Poggio T, Martinengo C, D'Amico L, Panizza E, Mologni L, Cavallo F, Altruda F, Butaney M, Capelletti M, Inghirami G, Jänne PA, Chiarle R (2015) Efficacy of a Cancer Vaccine against ALK-Rearranged Lung Tumors. Cancer Immunol Res 3:1333–1343. https://doi.org/10.1158/2326-6066.cir-15-0089

Walter DM, Venancio OS, Buza EL, Tobias JW, Deshpande C, Gudiel AA, Kim-Kiselak C, Cicchini M, Yates TJ, Feldser DM (2017) Systematic In Vivo Inactivation of Chromatin-Regulating Enzymes Identifies Setd2 as a Potent Tumor Suppressor in Lung Adenocarcinoma. Cancer Res 77:1719–1729. https://doi.org/10.1158/0008-5472.can-16-2159

Walter DM, Yates TJ, Ruiz-Torres M, Kim-Kiselak C, Gudiel AA, Deshpande C, Wang WZ, Cicchini M, Stokes KL, Tobias JW, Buza E, Feldser DM (2019) RB constrains lineage fidelity and multiple stages of tumour progression and metastasis. Nature 569:423–427. https://doi.org/10.1038/s41586-019-1172-9

Wang W-X, Xu C-W, Chen Y-P, Liu Wei, Zhong L-H, Chen F-F, Zhuang W, Huang Y-J, Huang Z-Z, Chen R-R, Guan Y-F, Yi X, Lv T-F, Zhu W-F, Lu J-P, Wang X-J, Shi Y, Lin X-D, Chen G, Song Y (2018) TP53 mutations predict for poor survival in ALK rearrangement lung adenocarcinoma patients treated with crizotinib. J Thorac Dis 10:2991–2998. https://doi.org/10.21037/jtd.2018.04.98

Werner M, Purta E, Kaminska KH, Cymerman IA, Campbell DA, Mittra B, Zamudio JR, Sturm NR, Jaworski J, Bujnicki JM (2011) 2′-O-ribose methylation of cap2 in human: function and evolution in a horizontally mobile family. Nucleic Acids Res 39:4756–4768. https://doi.org/10.1093/nar/gkr038

Winslow MM, Dayton TL, Verhaak RGW, Kim-Kiselak C, Snyder EL, Feldser DM, Hubbard DD, DuPage MJ, Whittaker CA, Hoersch S, Yoon S, Crowley D, Bronson RT, Chiang DY, Meyerson M, Jacks T (2011) Suppression of lung adenocarcinoma progression by Nkx2-1. Nature 473:101–104. https://doi.org/10.1038/nature09881

Winters IP, Murray CW, Winslow MM (2018) Towards quantitative and multiplexed in vivo functional cancer genomics. Nat Rev Genet 19:741–755. https://doi.org/10.1038/s41576-018-0053-7

Wolf J, Helland Å, Oh I-J, Migliorino MR, Dziadziuszko R, Wrona A, Castro J de, Mazieres J, Griesinger F, Chlistalla M, Cardona A, Ruf T, Trunzer K, Smoljanovic V, Novello S (2022) Final efficacy and safety data, and exploratory molecular profiling from the phase III ALUR study of alectinib versus chemotherapy in crizotinib-pretreated ALK-positive non-small-cell lung cancer. ESMO Open 7:100333. https://doi.org/10.1016/j.esmoop.2021.100333

Woo CG, Seo S, Kim SW, Jang SJ, Park KS, Song JY, Lee B, Richards MW, Bayliss R, Lee DH, Choi J (2016) Differential protein stability and clinical responses ofEML4-ALK fusion variants to various ALK inhibitors in advancedALK-rearranged non-small cell lung cancer. Ann Oncol 28:791–797. https://doi.org/10.1093/annonc/mdw693

Xiang Y, Zhang S, Fang X, Jiang Y, Fang T, Liu J, Lu K (2022) Therapeutic Advances of Rare ALK Fusions in Non-Small Cell Lung Cancer. Curr Oncol 29:7816–7831. https://doi.org/10.3390/curroncol29100618

Xie Y, Sahin M, Sinha S, Wang Y, Nargund AM, Lyu Y, Han S, Dong Y, Hsieh JJ, Leslie CS, Cheng EH (2022) SETD2 loss perturbs the kidney cancer epigenetic landscape to promote metastasis and engenders actionable dependencies on histone chaperone complexes. Nat Cancer 3:188–202. https://doi.org/10.1038/s43018-021-00316-3

Xie Y, Sahin M, Wakamatsu T, Inoue-Yamauchi A, Zhao W, Han S, Nargund AM, Yang S, Lyu Y, Hsieh JJ, Leslie CS, Cheng EH (2023) SETD2 regulates chromatin accessibility and transcription to suppress lung tumorigenesis. JCI Insight 8:e154120. https://doi.org/10.1172/jci.insight.154120

Yanagimura N, Takeuchi S, Fukuda K, Arai S, Tanimoto A, Nishiyama A, Ogo N, Takahashi H, Asai A, Watanabe S, Kikuchi T, Yano S (2022) STAT3 inhibition suppresses adaptive survival of ALK-

rearranged lung cancer cells through transcriptional modulation of apoptosis. npj Precis Oncol 6:11. https://doi.org/10.1038/s41698-022-00254-y

Yang D, Jones MG, Naranjo S, Rideout WM, Min KH (Joseph), Ho R, Wu W, Replogle JM, Page JL, Quinn JJ, Horns F, Qiu X, Chen MZ, Freed-Pastor WA, McGinnis CS, Patterson DM, Gartner ZJ, Chow ED, Bivona TG, Chan MM, Yosef N, Jacks T, Weissman JS (2022) Lineage tracing reveals the phylodynamics, plasticity, and paths of tumor evolution. Cell 185:1905-1923.e25. https://doi.org/10.1016/j.cell.2022.04.015

Yang JC-H, Liu G, Lu S, He J, Burotto M, Ahn M-J, Kim D-W, Liu X, Zhao Y, Vincent S, Yin J, Ma X, Lin HM, Popat S (2023) Brigatinib Versus Alectinib in ALK-Positive NSCLC After Disease Progression on Crizotinib: Results of Phase 3 ALTA-3 Trial. J Thorac Oncol 18:1743–1755. https://doi.org/10.1016/j.jtho.2023.08.010

Yang P, Patrick E, Humphrey SJ, Ghazanfar S, James DE, Jothi R, Yang JYH (2016) KinasePA: Phosphoproteomics data annotation using hypothesis driven kinase perturbation analysis. PROTEOMICS 16:1868–1871. https://doi.org/10.1002/pmic.201600068

Yang P, Patrick E, Tan S-X, Fazakerley DJ, Burchfield J, Gribben C, Prior MJ, James DE, Yang YH (2014) Direction pathway analysis of large-scale proteomics data reveals novel features of the insulin action pathway. Bioinformatics 30:808–814. https://doi.org/10.1093/bioinformatics/btt616

Yang X, Chen R, Chen Y, Zhou Y, Wu C, Li Q, Wu J, Hu W, Zhao W, Wei W, Shi J, Ji M (2022) Methyltransferase SETD2 inhibits tumor growth and metastasis via STAT1–IL-8 signaling-mediated epithelial–mesenchymal transition in lung adenocarcinoma. Cancer Sci 113:1195–1207. https://doi.org/10.1111/cas.15299

Yoda S, Lin JJ, Lawrence MS, Burke BJ, Friboulet L, Langenbucher A, Dardaei L, Prutisto-Chang K, Dagogo-Jack I, Timofeevski S, Hubbeling H, Gainor JF, Ferris LA, Riley AK, Kattermann KE, Timonina D, Heist RS, Iafrate AJ, Benes CH, Lennerz JK, Mino-Kenudson M, Engelman JA, Johnson TW, Hata AN, Shaw AT (2018) Sequential ALK Inhibitors Can Select for Lorlatinib-Resistant Compound ALK Mutations in ALK-Positive Lung Cancer. Cancer Discov 8:CD-17-1256. https://doi.org/10.1158/2159-8290.cd-17-1256

Yoshida R, Sasaki T, Minami Y, Hibino Y, Okumura S, Sado M, Miyokawa N, Hayashi S, Kitada M, Ohsaki Y (2017) Activation of Src signaling mediates acquired resistance to ALK inhibition in lung cancer. Int J Oncol 51:1533–1540. https://doi.org/10.3892/ijo.2017.4140

Young L, Sung J, Stacey G, Masters JR (2010) Detection of Mycoplasma in cell cultures. Nat Protoc 5:929–934. https://doi.org/10.1038/nprot.2010.43

Yousefi M, Boross G, Weiss C, Murray CW, Hebert JD, Cai H, Ashkin EL, Karmakar S, Andrejka L, Chen L, Wang M, Tsai MK, Lin W-Y, Li C, Yakhchalian P, Colón CI, Chew S-K, Chu P, Swanton C, Kunder CA, Petrov DA, Winslow MM (2022) Combinatorial Inactivation of Tumor Suppressors Efficiently Initiates Lung Adenocarcinoma with Therapeutic Vulnerabilities. Cancer Res 82:1589–1602. https://doi.org/10.1158/0008-5472.can-22-0059

Yu T, Chen X, Zhang W, Liu J, Avdiushko R, Napier DL, Liu AX, Neltner JM, Wang C, Cohen D, Liu C (2016) KLF4 regulates adult lung tumor-initiating cells and represses K-Ras-mediated lung cancer. Cell Death Differ 23:207–215. https://doi.org/10.1038/cdd.2015.85

Yuan H, Han Y, Wang X, Li N, Liu Q, Yin Y, Wang H, Pan L, Li L, Song K, Qiu T, Pan Q, Chen Q, Zhang G, Zang Y, Tan M, Zhang J, Li Q, Wang X, Jiang J, Qin J (2020) SETD2 Restricts Prostate Cancer Metastasis by Integrating EZH2 and AMPK Signaling Pathways. Cancer Cell 38:350-365.e7. https://doi.org/10.1016/j.ccell.2020.05.022

Yun MR, Choi HM, Lee YW, Joo HS, Park CW, Choi JW, Kim DH, Kang HN, Pyo K, Shin EJ, Shim HS, Soo RA, Yang JC, Lee SS, Chang H, Kim MH, Hong MH, Kim HR, Cho BC (2019) Targeting YAP to overcome acquired resistance to ALK inhibitors in ALK-rearranged lung cancer. EMBO Mol Med 11:e10581. https://doi.org/10.15252/emmm.201910581

Zacharias WJ, Frank DB, Zepp JA, Morley MP, Alkhaleel FA, Kong J, Zhou S, Cantu E, Morrisey EE (2018) Regeneration of the lung alveolus by an evolutionarily conserved epithelial progenitor. Nature 555:251–255. https://doi.org/10.1038/nature25786

Zhang S, Anjum R, Squillace R, Nadworny S, Zhou T, Keats J, Ning Y, Wardwell SD, Miller D, Song Y, Eichinger L, Moran L, Huang W-S, Liu S, Zou D, Wang Y, Mohemmad Q, Jang HG, Ye E, Narasimhan N, Wang F, Miret J, Zhu X, Clackson T, Dalgarno D, Shakespeare WC, Rivera VM (2016) The Potent ALK Inhibitor Brigatinib (AP26113) Overcomes Mechanisms of Resistance to

First- and Second-Generation ALK Inhibitors in Preclinical Models. Clin Cancer Res 22:5527–5538. https://doi.org/10.1158/1078-0432.ccr-16-0569

Zhang SS, Nagasaka M, Zhu VW, Ou S-HI (2021) Going beneath the tip of the iceberg. Identifying and understanding EML4-ALK variants and TP53 mutations to optimize treatment of ALK fusion positive (ALK+) NSCLC. Lung Cancer 158:126–136. https://doi.org/10.1016/j.lungcan.2021.06.012

Zhu Q, Yang Q, Lu X, Wang H, Tong L, Li Z, Liu G, Bao Y, Xu X, Gu L, Yuan J, Liu X, Zhu W-G (2021) SETD2-mediated H3K14 trimethylation promotes ATR activation and stalled replication fork restart in response to DNA replication stress. Proc Natl Acad Sci 118:e2011278118. https://doi.org/10.1073/pnas.2011278118

Zou HY, Friboulet L, Kodack DP, Engstrom LD, Li Q, West M, Tang RW, Wang H, Tsaparikos K, Wang J, Timofeevski S, Katayama R, Dinh DM, Lam H, Lam JL, Yamazaki S, Hu W, Patel B, Bezwada D, Frias RL, Lifshits E, Mahmood S, Gainor JF, Affolter T, Lappin PB, Gukasyan H, Lee N, Deng S, Jain RK, Johnson TW, Shaw AT, Fantin VR, Smeal T (2015) PF-06463922, an ALK/ROS1 Inhibitor, Overcomes Resistance to First and Second Generation ALK Inhibitors in Preclinical Models. Cancer Cell 28:70–81. https://doi.org/10.1016/j.ccell.2015.05.010

Zou HY, Li Q, Lee JH, Arango ME, McDonnell SR, Yamazaki S, Koudriakova TB, Alton G, Cui JJ, Kung P-P, Nambu MD, Los G, Bender SL, Mroczkowski B, Christensen JG (2007) An Orally Available Small-Molecule Inhibitor of c-Met, PF-2341066, Exhibits Cytoreductive Antitumor Efficacy through Antiproliferative and Antiangiogenic Mechanisms. Cancer Res 67:4408–4417. https://doi.org/10.1158/0008-5472.can-06-4443